

Micro-tubular Solid Oxide Fuel Cells with Nickelate Cathode-support

THÈSE N° 5315 (2012)

PRÉSENTÉE LE 25 MAI 2012

À LA FACULTÉ DES SCIENCES ET TECHNIQUES DE L'INGÉNIEUR
LABORATOIRE DE TECHNOLOGIE DES POUDRES
PROGRAMME DOCTORAL EN SCIENCE ET GÉNIE DES MATÉRIAUX

ÉCOLE POLYTECHNIQUE FÉDÉRALE DE LAUSANNE

POUR L'OBTENTION DU GRADE DE DOCTEUR ÈS SCIENCES

PAR

Henning LÜBBE

acceptée sur proposition du jury:

Prof. V. Michaud, présidente du jury
Prof. H. Hofmann, Dr J. Van Herle, directeurs de thèse
Prof. T. Graule, rapporteur
Prof. F. Mauvy, rapporteur
Dr L. Rodriguez Martinez, rapporteur



ÉCOLE POLYTECHNIQUE
FÉDÉRALE DE LAUSANNE

Suisse
2012

Acknowledgements

I would like to thank Dr. Jan Van herle for accepting me as a PhD student at the Industrial Energy Systems Laboratory (LENI), for being the Co-Director of this thesis, for his scientific help of great value and for making me a part of a well-motivated and very likeable group of fuel cell researchers.

I'd like to thank Prof. Heinrich Hofmann for welcoming me in his group, the Powder Technology Laboratory (LTP), for being the Director of this thesis, for his various scientific contributions and for providing a very friendly work environment.

I would like to thank Dr. Paul Bowen of LTP for numerous fruitful discussions, especially in the field of powder technology and characterisation. His expertise in powder technology helped me tremendously during the project.

I would like to thank my fellow-workers from LENI and LTP, who, too numerous to name them all, have often helped me to solve little and not so little problems in the laboratories and whose expertise has enriched my understanding and hence this project.

I'd also like to thank the students I had the pleasure to work with, who chose my project among the many exciting opportunities at EPFL. The contributions of Andreas Schuler, John Rossen, Rémy Tourvieille de Labrouhe, Delphine Marchon, Amelie Bazzoni, Selim Ben Mlouka, Myriam Ben Ameur and Ahlem Lamkarfed have brought this project substantially forward.

I'd further like to thank the collaborators of the scientific workshops of the materials and mechanics sections who have transformed my design ideas into functional workpieces within very short delays.

Moreover, I would like to thank collaborators from CIME and GGEC for their precious help, especially Andreas Schuler, Antonin Faes and Marco Cantoni from CIME for their help in preparing samples for electron microscopy, Vincent Laporte for his help in XPS analysis and Pietro Tanasini from GGEC for his help in serigraphy and fruitful discussions.

I am grateful for the various contributions from our collaborating partners concerning nicke-late powder characterisation and tube fabrication. I would like to especially mention

- Dr Aitor Larrañaga from the group of Prof Maribel Arriortua at the University of Bilbao, Spain for his immensely valuable contribution of quantitative phase analysis by XRD of the materials used in this work;

Acknowledgements

- Dr Cecile Lalanne from ICMCB, France for her ICP analysis of nickelate powders;
- Dr Frans Snijkers from VITO, Belgium for tube fabrication by cold-isostatic pressing (CIP);
- Dr Thomas Betz and Christian Muench from Kerafol AG, Germany for the tube fabrication by extrusion;
- Dr Vassilis Stathopoulos from Cereco, Greece for the preparation of nickelate tubes by slip-casting;
- Prof. Victor Orera, Dr Miguel Laguna and Dr Roberto Campana from the University of Zaragoza for their contributions to tube fabrication by CIP as well as many fruitful discussions.

I would like to thank my parents for their encouragement and support, not only during this thesis but throughout my life.

And finally I would like to thank Carmen who has been very understanding and encouraging all along this work and who I could always talk to and rely on, even though she had herself a thesis to cope with.

Lausanne, December 21, 2011

H. L.

Abstract

The shortage of natural resources, rising energy demands and global warming have created an urgent need for more efficient energy conversion devices and different energy resources to achieve a more sustainable and efficient economy. Solid Oxide Fuel Cells (SOFC) are one of the most promising devices for the direct conversion from chemical to electrical energy in conjunction with high system efficiencies. Micro-tubular SOFC have been investigated since roughly 15 years. In contrast to planar systems, which produce electricity in the kW to MW range and target utilisation in stationary applications such as CHP plants, micro-tubular SOFC systems can be envisaged for mobile application due to quick start-up/shutdown operation. While most micro-tubular cells are mechanically supported by the electrolyte or anode, only few researches have investigated cathode-supported cells due to challenging fabrication. In this work, the new cathode material neodymium nickelate (NNO), $\text{Nd}_{1.95}\text{NiO}_{4+\delta}$, was used as mechanical support, which is a novelty of this work, for micro-tubular SOFC. Different fabrication routes were used to create small tubes of 2-6 mm diameter. These tubes were evaluated with respect to their gas-diffusion properties by a new, self-manufactured diffusion setup and a complementary permeation setup.

In order to achieve an economical fabrication process, the low-cost dip-coating method was investigated for the deposition of thin films from wet-chemical suspensions to create entire SOFC single cells. As SOFCs require gas-tight electrolyte layers, cofiring of tubular substrates and thin films must be executed to allow sufficient shrinkage of the deposited electrolyte thin layers to full density. Various electrolyte and electrode powders were characterised in different solvents, dispersants and binders with respect to low-temperature sintering feasibility. The shrinkage of scandia-stabilised zirconia (ScSZ) powder was decreased to 18% to still deliver sufficient sintered density by optimisation of the green density (usually zirconia requires shrinkage of 25% and more for densification).

The cofiring temperature depends on the densification behaviour of powders but also on reactivity between adjacent layers. The reactivity between gadolinia-doped ceria (GDC)-interlayers and different zirconia materials was tested and showed lower compatibility of yttria-stabilised zirconia (YSZ) with GDC than for ScSZ/GDC reaction couples, which has not been reported so far. The interface of NNO cathodes and GDC interlayers was analysed by reactivity mapping and quantitative phase analysis. The performance optimisation of NNO/GDC interfaces by exchange current density measurement of NNO-cathodes sintered at different temperatures on GDC pellets is a further contribution of this work. The reactivity and performance investigations provide clear guidelines for maximum allowable cosintering temperature.

Acknowledgements

Some electrochemical single cell tests showed competitive area-specific resistances (ASR) of ca. $1 \Omega\text{cm}^2$ but were limited unfortunately by the counterelectrode microstructure and current collection methods, which were not the focus of this work. Open-circuit voltages (OCV) were 0.6-1.1 V at 700°C in dry hydrogen atmosphere for tubes prepared by extrusion but only 0.3 V for tubes prepared by slip-casting. The electrochemical performances were modest with only 0.035 W/cm^2 power density at 700°C for tubes prepared by extrusion due to the elevated resistances of the counterelectrode and current collection.

Key-words: SOFC; Neodymium nickelate cathodes; Micro-tubular; Dip-coating; Cathode-supported

Zusammenfassung

Ressourcenverknappung, steigende Energienachfrage und globale Erwärmung haben ein dringendes Bedürfnis nach effizienteren Energieumwandlern und anderen Rohstoffenquellen erzeugt, um nachhaltigeres und effizienteres Wirtschaften zu ermöglichen. Festoxidbrennstoffzellen (SOFC) sind eine der vielversprechendsten Technologien für die direkte Umwandlung von chemischer in elektrische Energie in Verbindung mit hoher System-Effizienz. Mikro-tubulare SOFC werden seit ca. 15 Jahren erforscht. Im Gegensatz zu planaren Systemen, die elektrische Energie im kW- bis MW-Bereich produzieren und für den Einsatz in stationären Anwendungen wie Kraft-Wärme gekoppelten Kraftwerken prädestiniert sind, können mikro-tubulare SOFC-Systeme aufgrund schneller Anfahr-/Abschalt-Vorgänge in mobilen Einsatzgebieten Anwendung finden.

Während die meisten mikro-tubularen Zellen mechanisch vom Elektrolyten oder der Anode getragen werden, haben nur wenige Forschungsarbeiten aufgrund der anspruchsvollen Herstellung kathoden-getragene Zellen untersucht. In dieser Arbeit wurde das neuartige Kathodenmaterial Neodymnickelat (NNO), $\text{Nd}_{1.95}\text{NiO}_{4+\delta}$, als mechanischer Support für mikro-tubulare SOFC verwendet, was ein Novum dieser Arbeit darstellt. Verschiedene Fabrikationsverfahren wurden benutzt um kleine Röhrchen von 2-6 mm Durchmesser herzustellen. Diese Röhrchen wurden in Bezug auf ihre Diffusionseigenschaften mit Hilfe eines neuem, selbst-hergestellten Diffusions-Setup und eines ergänzendem Permeations-Setup ausgewertet.

Um eine wirtschaftliche Herstellung zu gewährleisten, wurde die kostengünstige Dip-Coating Methode für das Abscheiden von Dünnschichten aus nass-chemischen Suspensionen untersucht, um komplette SOFC-Einzelzellen herzustellen. Da SOFC gasdichte Elektrolytschichten benötigen, muss das Kosintern von tubularen Substraten und Dünnschichten erfolgen um eine ausreichende Schwindung des Elektrolyten bis zu seiner vollständigen Dichte zu ermöglichen. Zahlreiche Elektrolyt- und Elektrodenpulver wurden in verschiedenen Lösemitteln, Dispergiermitteln und Bindern in Hinblick auf ihre Tieftemperatur-Sinterfähigkeit charakterisiert. Die Schwindung von Scandium-stabilisiertem Zirkonoxid (ScSZ) Pulver wurde auf 18% durch die Optimierung der Gründichte gesenkt, und erzielte dennoch eine genügende Verdichtung (normalerweise benötigt Zirkonoxid eine Schwindung von 25% oder mehr für seine Verdichtung).

Die Kosinter-Temperatur hängt vom Verdichtungsverhalten der Pulver, aber auch von der Reaktivität benachbarter Schichten ab. Die Reaktivität zwischen Gadolinium-dotierten Ceroxid (GDC)-Zwischenschichten und verschiedenen Zirkonoxid-Materialien wurde getestet und zeigte eine geringere Kompatibilität von Yttrium-stabilisiertem Zirkonoxid (YSZ) mit GDC als

für ScSZ/GDC Diffusionspaare, was bisher noch nicht publiziert wurde. Die Grenzfläche von NNO-Kathoden und GDC-Zwischenschichten wurde durch Elementverteilungsbilder und quantitative Phasenanalyse untersucht. Die Leistungsoptimierung von NNO/GDC Grenzflächen durch die Messung der Austauschstromdichte von bei verschiedenen Temperaturen auf GDC-Tabletten gesinterten NNO-Kathoden ist ein weiterer Beitrag dieser Arbeit. Die Analyse der Reaktivität und Leistung stellt klare Leitfäden für die maximal erlaubte Kosinter-Temperatur bereit.

Einige elektrochemische Einzelzell-Tests zeigten konkurrenzfähige flächen-spezifische Widerstände (ASR) von ca. $1 \Omega\text{cm}^2$, wurden aber durch die Mikrostruktur der Gegenelektrode und die Stromsammlung limitiert, die nicht im Fokus dieser Arbeit lagen. Leerlaufspannungen (OCV) von 0.6-1.1 V bei 700°C wurden unter trockener Wasserstoff-Atmosphäre für extrudierte Röhrchen, aber nur 0.3 V für schlicker-gegossene Röhrchen, gemessen. Die elektrochemische Effizienz war mit einer Leistungsdichte von 0.035 W/cm^2 bei 700°C für extrudierte Röhrchen recht gering aufgrund des hohen Widerstandes der Gegenelektrode und Stromsammlung.

Schlüsselworte: SOFC; Neodymnickelat-Kathoden; Mikro-tubular; Dip-coating; Kathoden-Support

Contents

Acknowledgements	iii
Abstract (English/Deutsch)	v
Table of symbols	xiii
1 Introduction	1
1.1 Context	1
1.2 Plan of the thesis	2
2 Theoretical Background	5
2.1 Colloidal Stability	5
2.1.1 Attractive interaction potential	5
2.1.2 Repulsive electrostatic interaction potential	6
2.1.3 Repulsive steric interaction potential	8
2.2 Dip-Coating	10
2.3 Drying and Green Density	11
2.3.1 Capillary forces	11
2.3.2 Drying Stages	12
2.3.3 Green Density	14
2.4 Sintering	14
2.4.1 Theory	14
2.4.2 Cosintering	16
2.5 Fuel Cells	17
2.5.1 Solid Oxide Fuel Cells(SOFC)	17
2.5.2 Nickelates	23
2.5.3 Approach of this project	25
3 Micro-tubular Fuel Cells - State of the Art	27
3.1 Introduction	27
3.2 Electrolyte-supported cells (First Generation)	28
3.3 Electrode-supported cells (Second Generation)	31
3.3.1 Anode-supported cells	31
3.3.2 Cathode-supported cells	35

Contents

3.4	Metal-supported cells (Third Generation)	37
3.5	Performance	38
4	Chemicals and Equipment	41
4.1	Equipment	41
4.1.1	Deposition of thin films and drying	41
4.1.2	Sintering	43
4.1.3	Pressure loss tests	45
4.1.4	Screen printing	46
4.1.5	Electrochemical tests	46
4.1.6	Slip-casting	46
4.2	Chemicals	48
4.2.1	Solvents	48
4.2.2	Dispersants	49
4.2.3	Binder	50
5	Powders	53
5.1	Cathode: Neodymium nickelate	53
5.1.1	Supply and Powder Characterisation	53
5.1.2	Chemical Stability	54
5.1.3	Si-Impurities	54
5.1.4	Dispersion and Shrinkage	55
5.2	Interlayer: Gadolinia-doped ceria (GDC)	58
5.2.1	Supply and Powder Characterisation	58
5.2.2	Dispersion and Shrinkage	59
5.2.3	Dip-Coating of GDC	68
5.3	Electrolyte: Scandia-stabilised zirconia (ScSZ)	73
5.3.1	10ScSZ from Praxair (ScSZ PR)	75
5.3.2	10ScSZ from DKKK (ScSZ DK)	84
5.3.3	10ScSZ from Treibacher (ScSZ TR)	86
5.3.4	Thermal expansion coefficient (TEC)	89
5.3.5	Chemical analysis(XRD, XPS, ICP)	91
5.3.6	Dip-Coating of ScSZ	92
5.4	Anode: NiO-electrolyte cermets	93
5.4.1	NiO-YSZ, premixed by Nextech	93
5.4.2	NiO-GDC, prepared at EPFL	94
5.4.3	Dip-Coating of anode powder suspensions	94
6	Nickelate Tubes	97
6.1	Tubes prepared by cold-isostatic pressing (CIP)	98
6.1.1	CIP from VITO (CIP-VITO)	98
6.1.2	CIP at Zaragoza (CIP-ZARA)	99
6.1.3	CIP at EPFL (CIP-EPFL)	101

6.2	Tubes prepared by Extrusion	103
6.2.1	Small Diameter (Ex-SD)	103
6.2.2	Bigger Diameter (Ex-BD)	104
6.3	Tubes prepared by slip-casting (T-SC)	106
6.4	Diffusion and Permeation Tests	106
6.5	Supports for Dip-Coating	111
7	Chemical Compatibility	115
7.1	GDC-NNO interfaces	115
7.1.1	Diffusion couples	115
7.1.2	Symmetrical 3-electrode cells	119
7.2	GDC-Zirconia interfaces	122
7.2.1	GDC-10ScSZ	124
7.2.2	GDC-10YSZ	126
7.3	ZrO ₂ -NNO interfaces	129
8	Electrochemical Characterisation of the used nickelate	131
8.1	Motivation	131
8.2	1 st series of measurements	132
8.3	2 nd series of measurements	137
8.4	Exchange current density	141
9	Fabrication and Testing of Single Cells	145
9.1	Fabrication of Complete Single Cells	145
9.1.1	Fabrication of cell with tubes of type CIP-VITO	145
9.1.2	Fabrication of cell with tubes of type CIP-ZARA	148
9.1.3	Fabrication of cells with tubes of type T-SC	149
9.1.4	Fabrication of cells with tubes of type CIP-EPFL	151
9.1.5	Fabrication of cells with tubes of type Ex-SD	151
9.2	Measurement Setup	153
9.3	Electrochemical Results	157
9.3.1	Cells based on extruded tubes (Ex-SD)	157
9.3.2	Cells based on tubes prepared by slip-casting(T-SC)	159
10	Summary, Conclusions and Outlook	163
10.1	Chemical Reactivity	163
10.2	Shrinkage	165
10.3	Exchange Current Density	165
10.4	Electrochemical Performance of Single Cells	166
10.5	Outlook	167
	Bibliography	185
	Curriculum Vitae	187

Contents

A Appendix	191
A.1 Diffusion-Test	191

Table of symbols

Symbol or Abbrev.	Explanation
Abbreviations	
ASC	Anode-supported cells.
ASR	Area-specific resistance [$\Omega \text{ cm}^2$].
BoP	Balance-of-Plant.
Cereco	Greek research organisation, www.cereco.gr , Greece.
CHP	Combined heat and power.
CIP	Cold-Isostatic Pressing.
CSC	Cathode-supported cells.
EDX	Energy-dispersive X-ray Spectroscopy.
EIS	Electrochemical Impedance Spectroscopy.
EMPA	Swiss Federal Laboratories for Materials Science and Technology.
ESA	Electrokinetic Sonic Amplitude.
ESC	Electrolyte-supported cells.
GDC	Gadolina-doped ceria (also: CGO for ceria gadolinia oxide), electrolyte and electrode material, MIEC.
ICMCB	Institute of condensed matter chemistry, France.
ICP	Inductively Coupled Plasma.
IEP	Iso-electric point, point of zero net-charge on the particle surface [-].
LBNL	Lawrence Berkeley National Lab, USA.
LSC	$\text{La}_{1-x}\text{Sr}_x\text{CoO}_{3-\delta}$, cathode material, MIEC.
LSCF	$\text{La}_{1-x}\text{Sr}_x\text{Co}_{1-y}\text{Fe}_y\text{O}_{3-\delta}$, cathode material, MIEC.
LSF	$\text{La}_{1-x}\text{Sr}_x\text{FeO}_{3-\delta}$, cathode material, MIEC.
LSGM	$\text{La}_{1-x}\text{Sr}_x\text{Ga}_{1-y}\text{Mn}_y\text{O}_{3-\delta}$, electrolyte material, ionic conductor.
LSM	$\text{La}_{1-x}\text{Sr}_x\text{MnO}_{3-\delta}$, cathode material, almost pure electronic conductor.
LSFN	$\text{La}_{1-x}\text{Sr}_x\text{Fe}_{1-y}\text{Ni}_y\text{O}_{3-\delta}$, cathode material, MIEC.
LTP	Laboratory of Powder Technology, EPFL.
MIEC	Mixed ionic electronic conductor.
MSC	Metal-supported cells.
MW	Molecular weight [$\text{g}\cdot\text{mol}^{-1}$].
NEDO	New Energy Development Organisation, Japan.

Continued on next page...

Contents

Symbol or Abbrev.	Explanation
NiO-GDC (and NiO-YSZ)	Anode cermet material, mixture of nickel oxide and electrolyte-material,
NNO	Neodymium nickelate, $\text{Nd}_{2-x}\text{NiO}_{4+\delta}$, cathode material, MIEC.
OCV	Open circuit voltage [V].
PAA	Polyacrylic Acid.
PSD	Particle size distribution.
RCP	Random Close Packing.
RH	Relative humidity [%].
RLP	Random Loose Packing.
ScSZ	Scandia-stabilised zirconia, $\text{Zr}_{1-x}\text{Sc}_x\text{Ce}_{0.01}\text{O}_{2-\delta}$, ionic conductor.
SDC	Samaria-doped ceria, MIEC, electrolyte and electrode material.
SOFC	Solid Oxide Fuel Cells.
SSA	Specific surface area [m^2g^{-1}].
SSC	$\text{Sm}_{1-x}\text{Sr}_x\text{CoO}_{3-\delta}$, cathode material, MIEC.
VITO	Flemish Institute for technological research.
XRD	X-ray diffraction.
YSZ	Yttria-stabilised zirconia, $\text{Zr}_{1-x}\text{Y}_x\text{O}_{2-\delta}$, ionic conductor.
Symbols	
a	Particle radius [m].
α	Constant of integration for diffusion measurement, cf. appendix.
β	Efficiency, as defined in the introduction section [-].
χ	Measure for solvent-adsorbate interactions [-].
D	Diffusion coefficient, defined in various contexts [$\text{m}^2\cdot\text{s}^{-1}$].
d	Distance, described in more detail in various contexts [m].
ΔV	Interaction potential between particles [eV].
δ	Oxygen nonstoichiometry, $\delta < 0$: vacancies, $\delta > 0$: interstitials [-].
e	Elementary charge [$1.6 \cdot 10^{-19}$ C].
ϵ	Fractional porosity [-].
ϵ_m	Relative electric permittivity of the suspension medium [-].
ϵ_0	Electric permittivity of vacuum [$8.85 \cdot 10^{-12}$ $\text{C}^2\cdot\text{N}^{-1}\cdot\text{m}^{-2}$].
$\phi_{(2)}$	Volume fraction (of polymer in the adsorbed layer) [-].
φ	Wetting angle of a liquid on a solid surface [°].
F	Permeability of a porous solid [$\text{mol}\cdot\text{m}^{-2}\cdot\text{Pa}^{-1}\cdot\text{s}^{-1}$].
G	Shear viscosity of the porous body drained by liquid, cf. drying stresses [Pas].
g	Gravitation constant [$9.81\text{m}\cdot\text{s}^{-2}$].
γ_{LV}	Liquid's surface tension [$\text{N}\cdot\text{m}^{-1}$].
$\eta_{g(s)[,m]}$	Viscosity of a gas (of a suspension)[of a suspension medium] [Pas].
h_∞	Limiting film thickness, Landau-Levich theory [m].

Continued on next page...

Symbol or Abbrev.	Explanation
i_0	Exchange current density [$\text{mA}\cdot\text{cm}^{-2}$].
I_c	Ionic strength of a liquid in [$\text{mol}\cdot\text{L}^{-1}$].
K	Bulk viscosity of drained network, context: drying stresses [Pas].
k_B	Boltzmann constant, [$1.38\cdot 10^{-23} \text{ J}\cdot\text{K}^{-1}$].
k_{chem}	Chemical oxygen surface exchange coefficient [$\text{m}\cdot\text{s}^{-1}$].
κ_{DH}^{-1}	Debye-Hueckel constant of exponential charge decay as a function of surface distance [m].
κ	exponential decay constant for pressure loss measurements [s^{-1}].
L	Length over which diffusion/permeation occurs [m].
M_j	Molar mass of gas species j , [$\text{kg}\cdot\text{mol}^{-1}$].
N	Poisson's ratio of the drained network, context: drying stresses [-].
N_A	Avogadro's number, [$6.02\cdot 10^{23} \text{ mol}^{-1}$].
P	Pressure, used in various contexts, in [Pa] if not otherwise indicated .
ϑ	Thickness of the adsorbed surface layer [m].
θ	Diffraction angle in XRD measurements [$^\circ$].
ρ	Suspension's density [$\text{g}\cdot\text{ml}^{-1}$].
$\rho_b (\rho_{green})$	Relative density of bulk solid network(=green density) [%].
ρ_s	Density of the solid skeleton [$\text{g}\cdot\text{cm}^{-3}$].
r	Radius, in various contexts [m].
$\langle r \rangle$	Average radius of pores contributing to diffusion [m].
σ	Electrical conductivity [$\text{S}\cdot\text{cm}^{-1}$].
$s(\bar{s})$	(Mean) Particles' surface-surface separation distance [m].
t	Time [s].
T	Temperature, in Kelvin [K] if not otherwise indicated.
$T_{s,max,e}$	Characteristic temperatures for dilatometry [K].
U	Withdrawal speed from the suspension bath, dip-coating, [$\text{mm}\cdot\text{min}^{-1}$].
V_0	Total volume of the pressure loss system [214 ml].
\dot{V}_E	The rate of evaporation of the liquid [$\text{m}^3\cdot\text{m}^{-2}\cdot\text{s}^{-1}$].
w_f	Film thickness [m].
w_s	Scaled film thickness [].
w_w	Wall thickness of the tube [m].
Ψ_i	Surface potential of particle i [eV].
ψ	Quotient of porosity and tortuosity, as defined in the appendix [-].
z	Number of carried charges [-].

1 Introduction

1.1 Context

In the global context of shortage of resources, global warming and pursuit of higher sustainability, Solid Oxide Fuel Cells (SOFC) are an attractive device due to high efficiencies of the chemical to electrical energy conversion. While SOFCs are typically used for systems in the upper kW or MW for stationary applications, investigations of small-sized SOFC have gathered strong interest in recent years. This was mainly caused by the development of small tubular SOFCs, which, due to their small thermal mass and tubular design, demonstrated quick start-up/shutdown operation while showing a high thermal shock resistance, as cells were shown to produce currents within ca. 10-20 seconds after initiation. As SOFC main challenges are costs, a low-cost fabrication method was sought and found in dip-coating, which conveniently allows the deposition of thin films on tubular substrates.

In dip-coating, a substrate is dipped inside a liquid and withdrawn from it at a constant withdrawal speed. The retention of a thin film on the substrate is controlled by gravitational and viscous forces. The deposition of thin films that consist of ceramic powders requires the dispersion of these powders in appropriate liquids and conditions. The colloidal stability of powder particles in the size range of a few hundred nanometers demands high control of the dispersion conditions. In this work, several powders were tested with respect to convenient dispersion conditions for dip-coating on tubular substrates, as different solvents, dispersants and binder were evaluated.

The fabrication of microtubular SOFC is achieved by a cofiring process, during which the substrates and deposited films of ceramic powders are cofired at high temperature in order to obtain gas-tight layers by sintering. Therefore, thermal shrinkages of both the tubular substrate and the deposited thin films have to be carefully matched, as thermal stresses can develop due to different shrinkage profiles. The density of the electrolyte is the key parameter for successful fabrication, particularly for cells mechanically supported by the cathode, which have a limited cosinter temperature due to chemical reactivity of adjacent layers. The reactivity of conterminal materials at different temperatures is consequently of great importance and was studied in this work, too.

Chapter 1. Introduction

As the new cathode material neodymium nickelate (NNO) was utilised for mechanical support, NNO tubes were fabricated by different means and their thermal and physical properties compared to each other. Special attention was paid to thermal shrinkage and properties of the porous tubes such as pore size and porosity, which influence the diffusivity of the tubular support.

Finally, electrochemical tests of complete cells were accomplished and the results compared to literature values. Suggestions are given for the further optimisation of the system.

1.2 Plan of the thesis

The present work, dealing with micro-tubular SOFC supported by a cathode tube made from a new material (neodymium nickelate), shall begin with a description of the theoretical background of the principle relevant subjects and utilised techniques, followed by a literature review on microtubular SOFC. Afterwards, the materials and devices, the powders that were used in this work and the tubes made from nickelate powder are detailed before investigating the reactivity between adjacent layers (nickelate and ceria as well as between ceria and zirconia). The electrochemical behaviour of nickelate cathode on GDC button cells is furthermore examined. Finally, electrochemical tests of complete cells are presented and a conclusion of this work is given. Chapter 2 to 10 will therefore contain the following information:

Chapter 2 The theoretical background of the main subjects and techniques that were used in this work are presented in this chapter. As this thesis deals with the fabrication and testing of micro-tubular solid oxide fuel cells, which are prepared by dip-coating of thin films on tubular substrates, these subjects and techniques involve colloidal stability of suspensions, dip-coating, drying, cosintering and solid oxide fuel cells.

Chapter 3 This chapter, entitled "Microtubular Fuel Cells - State of the Art" describes the work of other researchers in the field of micro-tubular SOFC. It is organised in different sections according to the supporting element of the single cell, which has seen shifts over the years. The sections are therefore named first, second and third generation as the chronological order of reports on different mechanical supports evidences the development and direction of research.

Chapter 4 The chemicals and equipment used in this work are detailed in this chapter. The equipment is presented first and the following part, chemicals, is divided into sections where solvent, dispersants and binder are introduced.

Chapter 5 In this chapter, the different powders for the nickelate cathode tube, ceria inter-layer, zirconia electrolyte layer and cermet anode layer are presented. The emphasis is on

powder characterisation by granulometry and surface area measurement as well as densification behaviour and shrinkage among other methods and properties.

Chapter 6 In Chapter 6, the nickelate tubes prepared by different fabrication routes are presented. The tubes are investigated with respect to diffusion properties as well as thermal shrinkage during sintering in order to evaluate their applicability as substrates for coating and cosintering processes.

Chapter 7 In this chapter, the reactivity between adjacent layers at different sintering temperatures is examined. Therefore, nickelate-ceria and ceria-zirconia powder diffusion couples are fabricated and analysed by XRD. The interfacial reaction between ceria and nickelate is furthermore investigated by cross-section SEM imaging of symmetrical 3-electrode button cells consisting of ceria pellets and nickelate thin film electrodes.

Chapter 8 The electrochemical characterisation of nickelate-ceria interfaces, especially with respect to exchange current densities, is presented in chapter 8. Parameters such as nickelate sintering temperature and granulometry, current collection and Cr-degradation were considered. Comparisons to other cathode materials are given.

Chapter 9 In this chapter, the electrochemical tests of complete cells are described. The fabrication of cells by thin films deposition via dip-coating is explained. The gas-tightness of electrolyte layers on each different tube type was evaluated by pressure loss measurements and observation of cross-sectional images. Complete cells were mounted in a measurement cell which is also presented. Parameters such as current collection method and anode porosity are addressed.

Chapter 10 This conclusive part will summarise the present work and its main results. Additionally, it points out directions to follow in order to further improve the electrochemical performance of the cells.

2 Theoretical Background

2.1 Colloidal Stability

The colloidal stability of a suspension is of utmost importance for any wet-chemical process involving a powder dispersed in a solvent. When powder particles are put into contact with the liquid medium of a solvent, attractive and repulsive interactions are created which define the state of the particles (e.g. well-dispersed, agglomerated). The state of dispersion, i.e. the colloidal stability, defines whether particles agglomerate, which influences critical parameters such as the suspension viscosity and the density of the ceramic green body, among others. The DLVO-theory, developed by Derjaguin, Landau, Verwey and Overbeek, states that the total interaction potential ΔV_{total} can be calculated as the sum of attractive interaction ΔV_{attr} and repulsive interaction. For the latter, electrostatic interaction ΔV_{elec} and steric repulsion ΔV_{ster} are considered in the current case, as shown in equation 2.1.

$$\Delta V_{total} = \Delta V_{elec} + \Delta V_{ster} + \Delta V_{attr} \quad (2.1)$$

While the DLVO theory has its shortcomings in complex systems, e.g. involving magnetic nano-materials, it is convenient to use and gives good estimates of colloidal stability for simple systems as in the present case, where only solvent, dispersant and powder particles are present in aqueous or organic solutions.

2.1.1 Attractive interaction potential

The attractive interaction between particles arises from the presence of van der Waals-dispersion forces. Dispersion forces, also often named London forces or London dispersion forces after Fritz London, arise from interactions of instantaneous dipoles-induced dipole forces. When an instantaneous dipole is created in particle A, its dipole oscillations are transferred from particle A to particle B by electromagnetic waves and induce a dipole in the latter. This coupling creates the attractive London forces. Different models were proposed and compared [1] with respect to their validity for different particle sizes and surface separation distances.

Chapter 2. Theoretical Background

For "large" spherical equal-sized particles with a radius a of $a \geq 100$ nm, the Gregory model [2] showed the best approximation for the complete range of separation distances s between particles' surfaces. Gregory's semi-empirical relation is shown in Equation 2.2

$$\Delta V_{attr} = \left(-\frac{A_H \cdot a}{12s} \right) \left[1 - \frac{bs}{\lambda_0} \ln \left(1 + \frac{\lambda_0}{bs} \right) \right] \quad (2.2)$$

where A_H is the effective Hamaker constant, which is a measure for the attractive force acting between two particles, of the dispersed material and the two parameters b and λ_0 , which account for retardation effects between the particles, are $b=5.32$ and $\lambda_0=100$ nm. The surface separation distance between particle surfaces, s , varies as the particles move due to Brownian motion. However, a mean value \bar{s} can be calculated as a function of particle volume fraction ϕ and particles' radius a by

$$\bar{s} = \left[\sqrt{\frac{1}{3\pi\phi} + \frac{5}{6}} - 1 \right] 2a \quad (2.3)$$

2.1.2 Repulsive electrostatic interaction potential

The electrostatic repulsive interaction arises from charged particle surfaces that can be attributed to dissociated, ionised surface groups, adsorbed charged groups at the surface or the preferential desorption or adsorption of ions at the surface. In an aqueous solution, the surface charge is controlled by the pH. The charged surface layer, also called Stern layer, leads to the formation of a diffuse layer of opposite charge, also called Gouy-Chapman layer, to balance the electric potential, which surrounds the particle surfaces. The diffuse layer comprises counter-ions of opposite charge that are attracted from the liquid medium towards the particle surface by coulomb force. The two layers of opposite charge are called double-layer. As the diffuse layer is composed of opposite charge to the surface layer, the total net charge decreases with increasing distance from the particle surface. This is schematically shown in Fig. 2.1. The decrease of charge as a function of distance, as shown in Fig. 2.1, follows approximately an exponential decay. The thickness of the double layer can hence be described with the distance from the particle surface at which the initial surface charge Ψ_S has dropped to $1/e^* \Psi_S$ ($\approx 37\%$). The constant of exponential decay, κ_{DH}^{-1} , is related to the ionic strength I_c of the solution by the Debye-Hueckel equation

$$\kappa_{DH}^{-1} = \left(\frac{\epsilon_s \epsilon_0 k_B T}{2e^2 I_c N_A} \right)^{\frac{1}{2}} \quad (2.4)$$

where ϵ_m is the relative electric permittivity of the suspension medium, $\epsilon_0 = 8.85 \cdot 10^{-12}$ C²·N⁻¹·m⁻² is the electric permittivity of vacuum, $k_B = 1.38 \cdot 10^{-23}$ J·K⁻¹ is the Boltzmann constant, $N_A = 6.02 \cdot 10^{23}$ mol⁻¹ is Avogadro's number, T is the temperature in Kelvin, $e = 1.6 \cdot 10^{-19}$ C is the elementary charge and I_c is the ionic strength of the solution in mol·L⁻¹. I_c depends on the concentration of ionic species, c , and their number of carried charges, z ,

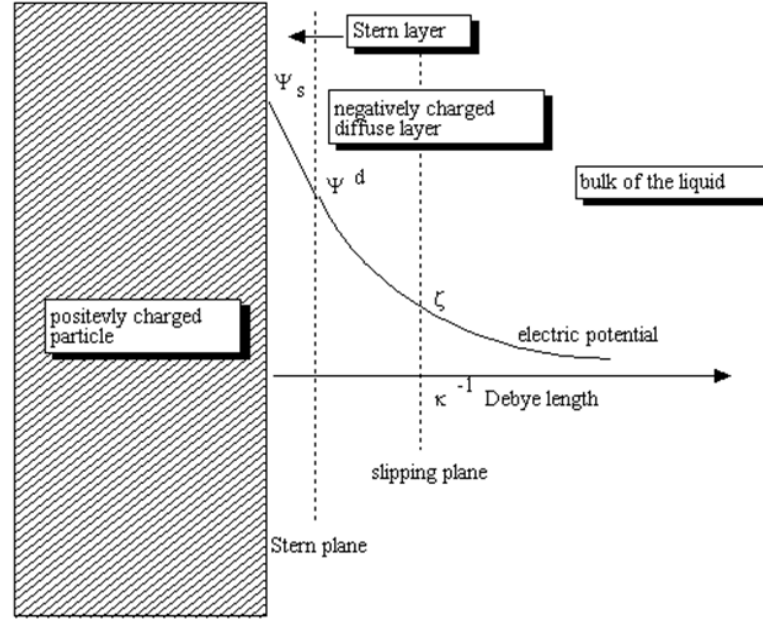


Figure 2.1: The total charge in a suspension as a function of distance from the charged particle surface. Source: [3]

following

$$I_c = \frac{1}{2} \sum_i c_i z_i^2 \quad (2.5)$$

For a symmetric two-species electrolyte, $\kappa^{-1} \approx 3.3\sqrt{I_c} \text{ nm}^{-1}$.

The DLVO model states that the electrostatic repulsion is created by interacting double layers of the particles. There are different approaches to describe the electrostatic interaction potential between particles. The Hogg-Healy Fuerstenau approach for two particles of equal particle radius a , which is used in this work, is presented in equation 2.6.

$$\Delta V_{elect} = \pi \cdot \epsilon_m \cdot \epsilon_0 \cdot \frac{a}{2} \left[(\Psi_1 + \Psi_2)^2 \ln(1 + \exp(-\kappa \cdot s)) + (\Psi_1 - \Psi_2)^2 \ln(1 - \exp(-\kappa \cdot s)) \right] \quad (2.6)$$

The surface potential of particle i is Ψ_i in equation 2.6 whereas all other parameters were already introduced. As the surface potential cannot be measured directly, it has to be calculated from the experimentally accessible zeta(ζ)-potential by

$$\Psi(d_s) = \frac{2kT}{ze} \ln \frac{1 + \left(\frac{\exp(ze\zeta/2kT) - 1}{\exp(ze\zeta/2kT) + 1} \right) \exp(-\kappa(d_s - d_\zeta))}{1 - \left(\frac{\exp(ze\zeta/2kT) - 1}{\exp(ze\zeta/2kT) + 1} \right) \exp(-\kappa(d_s - d_\zeta))} \quad (2.7)$$

where d_ζ is the distance between the particle surface and the zeta(ζ)-plane (cf Fig. 2.1) and

Chapter 2. Theoretical Background

d_s is the variable distance from the surface. Details about the ζ -potential and ζ -plane are introduced in the next paragraph.

ζ -potential The ζ -potential is the potential at the ζ -plane, a plane inside the double layer as shown in Fig. 2.1. It is defined as the plane where the diffuse layer stops to follow the movement of the charged particles, e.g. in an electric field. Its exact distance from the particle surface is unknown but generally assumed to be similar to the electrical double layer thickness. The zeta-potential was, in the scope of this work, measured by the acoustophoretic technic on an Acoustosizer II device by Colloidal Dynamics, USA.

The measurement technique is described in detail by Perche [4]. In the measurement, an electrical field of high frequency is applied to the suspension. This induces an oscillation of the charged particles in the suspension, which leads to an acoustic wave of the same frequency assuming the particles have a density different from the suspension medium. This measurement is repeated at 13 different frequencies and the results constitute the ESA spectrum ("Electrokinetic Sonic Amplitude"). In a second series of measurements, a sonic impuls of a certain frequency is conducted through the suspension. The amplitude of this signal is divided by the signal which should have been measured by using pure water as medium and the ration is calculated for all 13 frequencies. These ratios constitute the attenuation spectrum. The ESA spectrum is converted into a spectrum of dynamic mobility μ_d by

$$ESA = A(\omega)\phi \frac{\Delta\rho}{\rho_m} Z\mu_d \quad (2.8)$$

where $A(\omega)$ is a calibration function, ϕ is the volumetric fraction of particles, $\Delta\rho$ is the density difference between the particles and the suspension medium, Z is determined by the acoustic impedance of the suspension and automatically measured by the device and ρ_m is the density of the medium. The dynamic mobility is related to the size and ζ -potential of the particles in suspension by

$$\mu_d = \frac{2\epsilon_m\zeta}{3\eta_m} G(a, \omega)[1 + f] \quad (2.9)$$

for diluted suspensions ($\phi \leq 5\%$) where η_m is the viscosity of the suspension medium, $G(a, \omega)$ is a function depending on the particle radius a and frequency ω and f is a complex function. For particles size smaller than 10 μm , the Smoluchowski model is valid, in which the ζ -potential is independent of the particle size and is calculated by

$$\zeta = \frac{\mu_d\eta_m}{\epsilon_m} \quad (2.10)$$

2.1.3 Repulsive steric interaction potential

In the absence of electrostatic repulsion, e.g. in non-polar solvents, steric repulsion is needed to counterbalance the always present attractive interaction to achieve sufficient colloidal

stability. Steric stabilisation is achieved by adsorbed surface molecules such as polymers. The affinity between solvent and adsorbed surface group has to be high enough to form an elongated polymer layer that protrudes in the solvent in order to screen the attractive van der Waals interactions between particles. An expression used by Bergstroem [5] was employed in this work and reads

$$\Delta V_{ster} = \frac{\pi \cdot a \cdot k_B T}{\bar{V}} \phi_2^2 \left(\frac{1}{2} - \chi \right) (2\vartheta - s)^2 \quad (2.11)$$

In this equation, \bar{V} is the molar volume of the solvent, ϕ_2 is the volume fraction of polymer in the adsorbed layer and χ is a measure for solvent-adsorbate interactions. The thickness of the adsorbed surface layer is given by ϑ . The attractive and electrostatic repulsive interaction potential curves as well as the total summed interaction potential between two particles as a function of their surface separation distance are schematically shown in Fig. 2.2. The

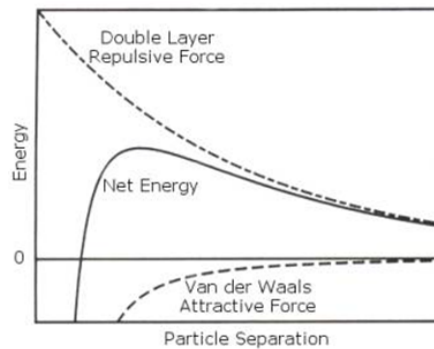


Figure 2.2: The interaction potential curves for attractive, electrostatic repulsive and the total summed interaction of particles as a function of their surface separation. Source: cite WDLV

repulsive interaction curve leads to a finite value for particle contact (separation=0), whereas the attractive potential energy diverges to minus infinity with decreasing particle separation. The effect on the total interaction potential can be seen in figure 2.2, as the net energy curve shows a maximum and decreases steeply with decreasing particle separation. Consequently, for very small separation distance particles will always attract each other and agglomerate. This state is called the primary minimum. If the energy barrier, which is the maximum of the net energy curve in Fig. 2.2, is much greater than the thermal energy, particles are prevented from approaching each other to separation distances smaller than the position of the energy barrier and hence cannot reach the primary minimum. Dispersants are used to increase the repulsive interaction, and therefore also the energy barrier, by electrostatic or steric or both repulsion mechanisms combined, which is termed electrosteric.

In this study, four different dispersants were used, namely triolein, triethanolamin, Triton-X 100 and polyacrylic acid. The first three dispersants were employed in the organic solvents ethanol and isopropanol and consequently stabilised particles by steric repulsion of their adsorbed polymer chains. Polyacrylic acid (PAA) was used as a dispersant in the polar solvent water and works by electrosteric stabilisation due to its long and charged polymer chains.

The configuration of PAA chains on the particle surface as well as the fraction of carboxylic functional groups that are charged due to dissociation ($\text{COOH} \rightarrow \text{COO}^- + \text{H}^+$) depend on the pH of the aqueous solution [6]. The pH of aqueous PAA-solutions is adapted by bases such as NaOH or NH_4OH . The R-value is defined as the molar amount of base divided by the molar amount of acrylic acid monomers in PAA. In this work, $R=1.5$ with NH_4OH as base was used, which leads to a pH of ca. 9.5 and almost entirely dissociated PAA-chains in brush-like configuration. The brush-configuration leads to almost completely elongated PAA polymer chains that protrude into the solution, with a total length of ca. 4-5 nm, which creates a repulsive steric contribution due to polymer chains' interaction as well as electrostatic repulsion due to almost completely dissociated and hence charged carboxylic groups along the PAA polymer chain.

2.2 Dip-Coating

Dip-Coating is used in this work as a low-cost fabrication method for the deposition of thin layers from wet-chemical state, i.e. as colloidal suspensions. In dip-coating processes, a substrate is lowered into a bath of colloidal suspension of the powder to be coated, immersed and withdrawn from the bath at defined conditions, i.e. immersion time and withdrawal speed. As the substrate is withdrawn from the suspension bath, a wet film of the material in the bath is formed on the substrate surface due to wettability of the substrate for the suspension (related to the liquid's surface tension), viscous drag of the liquid (related to its viscosity) and gravity. Different regimes can be distinguished and are shown in Fig. 2.3. There are two

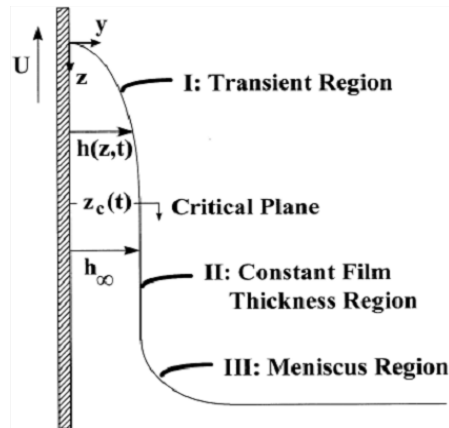


Figure 2.3: A schematic view of the different film regions formed during Dip-Coating.

principal models to describe the film formation on the substrate, the Jeffreys solution for transient coating and the Landau-Levich solution for steady-state coating [7, 8]. The principal prediction of the Landau-Levich model is the thickness in the constant film region shown in

Fig. 2.3, called the limiting film thickness h_∞

$$h_\infty = 0.944 \frac{(\eta_s U)^{\frac{2}{3}}}{\gamma_{LV}^{\frac{1}{6}} (\rho g)^{\frac{1}{2}}} \quad (2.12)$$

where η_s is the suspension's viscosity, U the withdrawal speed from the bath, γ_{LV} the interfacial energy between liquid and gas phase (also called the liquid's surface tension) ρ is the suspension's density and g the gravitation constant. It is common to introduce a scaled film thickness w_f and a capillary number Ca

$$w_f = h \left(\frac{\rho g}{\eta_s U} \right)^{\frac{1}{2}} \quad (2.13)$$

$$Ca = \frac{\eta_s U}{\gamma_{LV}} \quad (2.14)$$

so that the Landau-Levich equation can be written as

$$T_\infty = 0.944 Ca^{\frac{1}{6}} \quad (2.15)$$

This theory is valid for $Ca \ll 1$, when capillary forces are important with respect to the viscous drag and gravity. The calculations were done for water, ethanol and isopropanol and yielded values of $Ca < 0.02$. Therefore, the Landau-Levich equation was applied in this work to calculate film thicknesses of deposited electrolyte and anode layers. While the constant film thickness region covers the vast majority of the substrate's surface, edge effects of higher (Region III in Fig. 2.3) and lower (Region I in Fig. 2.3) film thickness were observed during the work.

2.3 Drying and Green Density

2.3.1 Capillary forces

When a solid body is covered by a liquid layer, a solid-liquid-gas triple point is created. At this triple-point, Young's equation

$$\gamma_{SV} = \gamma_{SL} + \gamma_{LV} \cos(\varphi) \quad (2.16)$$

is valid which says that the liquid film covers the solid surface when the interfacial energy of solid-gas γ_{SV} boundary is bigger than of solid-liquid interface γ_{SL} , which translates to the wetting angle $\varphi < 90^\circ$. A wetting angle of less than 90° generally indicates that the liquid wets the surface whereas $\varphi > 90^\circ$ means that the liquid does not wet the surface well. The interfacial energy γ_{LV} between the liquid and the gas phase is generally called the surface energy or surface tension of a liquid. Capillary forces arise from the presence of surface

Chapter 2. Theoretical Background

tensions. In a capillary tube of radius r_{cap} , a liquid will form triple-points at the edge of the tube with an equilibrium of energies described in equation 2.16. This leads to a curved liquid surface, where the curvature of the liquid leads to capillary pressure. The capillary pressure P_{cap} acting on the liquid is

$$P_{cap} = \frac{2\gamma_{LV}\cos(\varphi)}{r_{cap}} \quad (2.17)$$

When all the forces are balanced, the pressure difference on both sides of the curved surface is given by the Young-Laplace equation

$$\Delta P = \gamma_{LV} \left(\frac{1}{R_1} + \frac{1}{R_2} \right) \equiv \gamma_{LV} \zeta \quad (2.18)$$

where R_1 and R_2 are the radii of curvature of the interface in each of the axes parallel to the surface and ζ is the curvature. In a cylindrical capillary tube, $R_1 = R_2 = r_{cap}$ which leads to

$$\Delta P = \frac{2\gamma_{LV}}{r_{cap}} \quad (2.19)$$

2.3.2 Drying Stages

The different stages of drying were described in detail by Brinker [9] and experimentally applied by Juillerat [10]. Different periods were distinguished according to weight loss measurements of drying films. In the first stage, the constant rate period, the weight loss is constant as a function of drying time as solvent evaporates from the surface of the drying film. When the solvent's level decreases further and finally reaches the surface of particles, adsorption and capillary forces oppose exposure of the particles. This leads to meniscus formation of concave shape at the solid phase's surface. The curved surface leads to tension in the liquid equal to the radius of curvature r of the meniscus, which is given by equation 2.19 with $r = r_{cap}$. The tension of the liquid must be supported by the flimsy network of solid particles which goes into compression and rearranges into closer packing, forced by the rising capillary pressure as the network pore sizes, and therefore also r , decreases. The rearrangement of the particles causes shrinkage of the network, which starts at the surface as the solvent evaporates from there. The higher tension of the liquid at the surface causes the network to shrink more at the surface than in the interior which causes different shrinkages of the network and hence the build-up of tensile stresses. This is shown in Fig. 2.4. When the solid network reaches its densest configuration, the shrinkage and therefore the first stage is stopped. The step at the end of the first stage where r reaches its minimum value is called critical point of drying. Cracking is most likely to appear at this point starting from the surface, where the tensile stress is maximum. The tensile stress σ_x experienced by the network of a film dried on a flat, rigid surface is

$$\sigma_x = H_G \left(\frac{1-2N}{1-N} \right) \left(\frac{\dot{V}_E}{L} \right) \left[\frac{\chi(L) \cosh(\chi(L) \cdot u)}{\sinh(\chi(L))} \right] \quad (2.20)$$

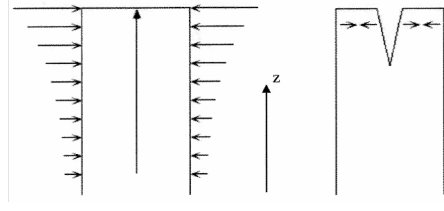


Figure 2.4: The distribution of tensile drying stresses in the drying film. z is the direction perpendicular to the film surface.

where $H_G = K + (4/3)G$ is a term that depends on K , the bulk viscosity of the drained network, and G , the shear viscosity of the porous body drained of liquid; \dot{V}_E is the rate of evaporation of the liquid; N is the Poisson's ratio of the drained network; $u = z/w_f$ is the normalized coordinate along the vertical axis z ; w_f is the thickness of the film and $\chi(w_f) = \sqrt{w_f^2 \eta_m / F_N H}$ where F_N is the permeability of the network. The two periods of falling rate after the constant rate period describe the final stages of drying, when liquid still covers partially the solid's surfaces inside the porous network but the surface is already completely exposed to the gas phase. More information can be found in the original source [10].

Viscosity of the drained network, H_G The maximum stress is present at the film surface, hence $u = 1$. At the critical point, the radius of curvature r is equal to $r = r_p = 2r_h$, where r_p is the pore radius and r_h is the hydraulic radius. These expressions lead to

$$\frac{2\gamma_{LV}}{r_p} \approx \frac{H_G \dot{V}_E}{w_f} \quad (2.21)$$

where $r_p = \frac{2(1-\rho)}{S_{BET}\rho\rho_s}$, $\rho = \frac{\rho_b}{\rho_s}$ is the relative density of the bulk solid network ρ_b (green density of the formed layer) with respect to the density of the solid skeleton ρ_s (theoretical density of the used powder) and S_{BET} is the specific surface area measured by BET. H_G is then calculated for different evaporation rates and a mean value is used.

Permeability, F For the permeability of the porous solid, the Carman-Kozny model

$$F = \frac{(1-\rho)^3}{5(\rho S_{BET}\rho_s)^2} \quad (2.22)$$

was used [9].

2.3.3 Green Density

The green density ρ_{green} of a ceramic is the density of a compacted ceramic green body before sintering. It is influenced by several parameters, among others particle size distribution (PSD), particle shape and the force that is applied during the compaction. In this work, two principal methods were used to fabricate green bodies, which are (a) the compaction of ceramic powder from the dry state by uniaxial or cold-isostatic pressing and (b) the casting of suspensions in specific shapes and subsequent solvent evaporation, which was done by slip-casting for pellet shaped ceramics and dip-coating for thin films.

While an external compaction pressure is applied in the former case, capillary pressure leads to compaction in the latter. Powder particles that were e.g. assembled without external pressure naturally have no defined long range order in the particle network and possess loose parts of surfaces without contact to other particles' surfaces. This conformation is called Random Loose Packing (RLP). When a powder is e.g. severely shaken or vibrated in a receptacle, the particles will glide along each other's surface until pores are filled and the density increased. The obtained conformation is called Random Close Packing (RCP). The green density for spherical particles of a single size and for log-normal distributed particle sizes is retaken from Hausonne et al. [11] and reprinted in Table 2.1. The results shown in Table 2.1 must be

Table 2.1: Green densities of ceramic green bodies according to different PSDs and conformations.

PSD	RLP	RCP
spheres of equal size	51.6%	64.2%
spheres with log-normal Distr.	54.0%	65.7%

considered an idealized guideline as the assumption of perfect spheres cannot be fulfilled with industrial powders. Further effects such as surface charges and multimodal distributions due to agglomeration complicate the situation in real systems. However, the measured green density gives a good indication of the green body's microstructure, mechanical stability and pore sizes.

2.4 Sintering

2.4.1 Theory

After the formation of a porous green body, sintering has to be performed to obtain consolidated and densified ceramics. Sintering is a high temperature treatment and its driving force is the reduction of overall free energy of the system which is achieved by reduction of the solid-vapour interface. The process can be broadly divided in 3 steps, where neighbouring particles will

1. form common necks
2. undergo complete coalescence and
3. display grain growth

to reduce the total surface area. Sintering takes place due to diffusion of atoms in one and vacancies in the inverse direction. Diffusion is mathematically described by Fick's first law

$$J = -D\nabla c \quad (2.23)$$

where J is mass flux, D is the diffusion coefficient and c the concentration. As solid state diffusion is a thermally activated process, D follows the Arrhenius equation

$$D = D_0 \exp\left(-\frac{Q}{RT}\right) \quad (2.24)$$

where D_0 is a temperature independent diffusion constant, Q the activation energy, R the ideal gas constant and T the absolute temperature in Kelvin. Different diffusion paths are possible and shown in Fig. 2.5. During the first sintering stage, necks between particles are

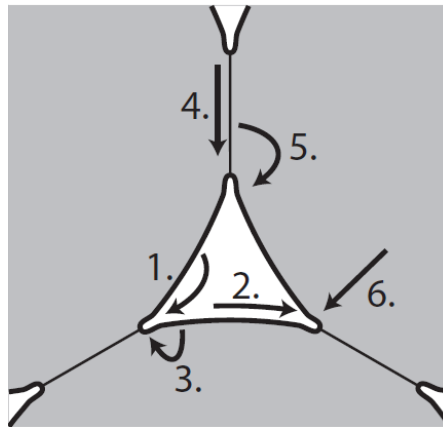


Figure 2.5: Schematic view of the different diffusion paths that are possible during sintering. 1. vapor phase transport, 2. surface diffusion, 3. volume diffusion from surface, 4. grain boundary diffusion, 5. volume diffusion from grain boundary and 6. volume diffusion [12]

formed. Diffusion takes place via surfaces, bulk, grain boundaries or in the gas phase. Only slight densification of <5% linear shrinkage is observed. The stage is considered finished when neck radii attain about half of the particle radii.

In the second stage, the porosity is still open and presents channels along polyhedral grains. Diffusion of matter principally occurs from the grain-boundaries toward pores via the bulk and grain boundaries. The majority of densification takes place during this stage which is considered ended when porosity changes from open to closed. At the end of the stage, 90-95% of theoretical density is reached. During the final sintering stage, the porous canals are cut

Chapter 2. Theoretical Background

off to form isolated pores at triple points, i.e. closed porosity. Grain boundary and volume diffusion towards the pores are the active transport mechanisms. Grain growth is observed by grain boundary migration. Pores may detach from grain boundaries and remain inside grains where there are difficult to clear away, as bulk diffusion is much slower than grain boundary diffusion. During grain growth, large grains grow to the detriment of smaller ones, due to the grain boundary curvature.

Sintering of a material can be monitored by dilatometric measurement of the ceramic body's linear length change with temperature. A typical shrinkage curve with the indicated characteristic temperatures and processes is shown in Fig. 2.6. The zones of existence of the noted

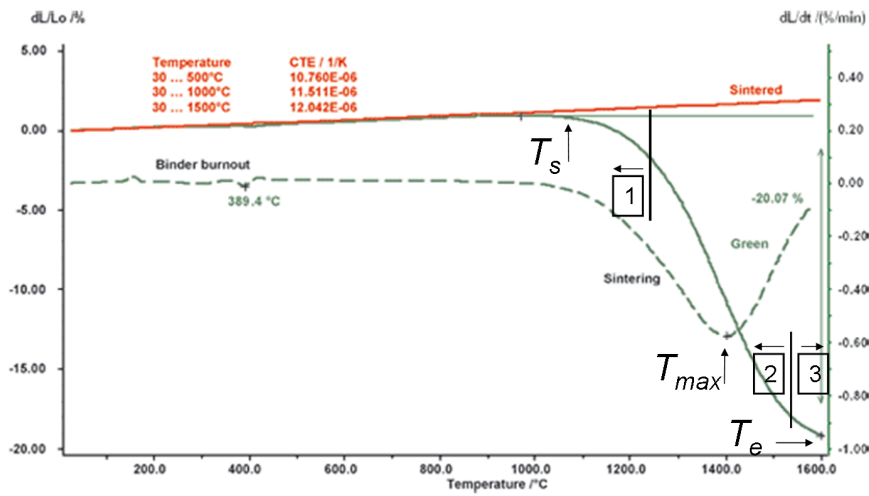


Figure 2.6: Typical shrinkage curve taken from [13] with indicated characteristic temperatures. T_s is the onset for densification, T_{max} the temperature of maximum shrinkage rate (first derivative of shrinkage with respect to time) and T_e the temperature at the end of the shrinkage curve, where shrinkage begins to level off into nearly a plateau.

processes 1, 2, and 3 are only rough estimates as the shrinkage depends on many parameters such as green density and heating rate among others.

2.4.2 Cosintering

Cosintering in a layered system is the simultaneous sintering process of more than one layer at the time. When different materials shrink at the same time, their shrinkages have to be matched to each other. In Fig. 2.7, idealised shrinkage curves of two powders A and B are presented. When used for cosintering, their sintering onset temperatures $T_s^{A,B}$, end or sintering temperature $T_e^{A,B}$ and the total relative shrinkage from $T_s^{A,B}$ to $T_e^{A,B}$ should be as close as possible. For example, during cosintering of materials A and B in a layered design, at temperatures $T_s^B < T < T_s^A$ material B should have started to shrink but is impeded by its contact to A, creating tensile stresses in B which can lead to failure mechanisms such as

cracking or delamination. The onset temperature T_s can be influenced to some extent by

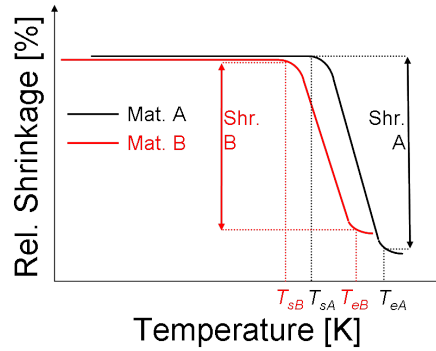


Figure 2.7: Shrinkage curves of materials A and B. For cosintering purposes, the shrinkage curves must be matched as closely as possible to minimise stresses.

the powder granulometry. However, if a distinct decrease of T_s is required, sintering aids can be added to trigger liquid phase sintering [11]. The end temperature T_e can be influenced by sintering aids and green density to some extent, as green bodies of poor green density need higher sintering temperatures to reach the same density as green bodies of higher green density. The total relative shrinkage between T_s and T_e can be influenced by the granulometry and the green density due to different dispersion systems (different solvents, dispersants, etc.) If the cosintering temperature T_{sint} is smaller than T_e , then the same conditions have to be fulfilled and the density at T_{sint} has to be sufficient for the application.

2.5 Fuel Cells

In the global context of shortage of fossil fuels and rising energy demands, research of more efficient energy systems and renewable energies is undertaken. Fuel Cells are efficient energy conversion devices due to their direct transformation of chemical to electrical energy and heat. While waste heat is generally a sign of conversion efficiencies less than 100%, it can be used for reforming of fuels or other heating applications in the case of high-temperature fuel cells. This application is abbreviated CHP for Combined Heat and Power. Fuel Cells were first conceived by Schoenbein in 1838 and experimentally validated by Grove in 1839. Different types of fuel cells exist and are commonly categorised by their operation temperature or the chemical nature of their electrolyte material. As this work deals with high temperature solid oxide fuel cells, only their principle of working will be introduced in the next section.

2.5.1 Solid Oxide Fuel Cells(SOFC)

Principle of working In Solid Oxide Fuel Cells (SOFC), the electrolyte is made of a ceramic oxide which becomes an ionic conductor for oxygen ions (O^{2-}) at high temperatures. The electrolyte is sandwiched between two electrodes, cathode and anode, and the ensemble of cathode, electrolyte and anode is termed PEN (positive-electrolyte-negative assembly) or

Chapter 2. Theoretical Background

MEA (membrane electrode assembly). At the cathode, oxygen from an air stream is reduced according to



and the oxygen ions are conducted through the ceramic oxide electrolyte to the anode side, where the oxygen ions recombine with a fuel, here for sake of simplicity represented by hydrogen H_2 , to water.



The electrons that are liberated by the anode reaction are conducted via an external electrical circuit to the cathode where they are consumed in the cathode reaction. It is therefore possible to power a consumer load by connecting it to the external circuit. A schematic cell design is shown in Fig. 2.8. As the power of a single cell is insufficient for application, cells are

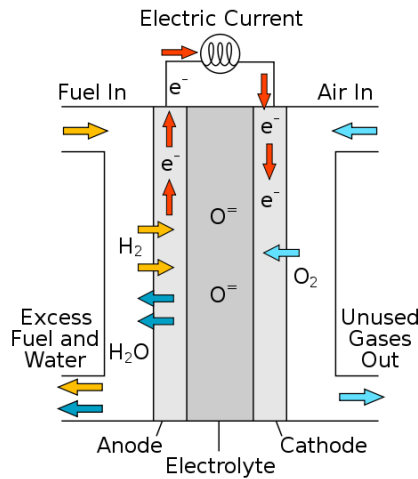


Figure 2.8: The schematic design of an SOFC single cell [14].

electrically connected and assembled into SOFC-stacks, which then can be integrated into SOFC-systems.

Theoretical and real cell voltage The overall cell reaction, the sum of anode and cathode reactions shown in equations 2.25 and 2.26, reads $H_2 + \frac{1}{2}O_2 \rightarrow H_2O$. The Gibbs energy ΔG of the reaction is -237 kJ/mol at 25°C. This corresponds to a standard voltage of E_0 given by

$$\Delta G = -zFE_0 \quad (2.27)$$

where z is the number of exchanged electrons, F is the Faraday constant and E_0 the reversible potential or electromotive force. The potential when no current is drawn and also termed OCV

(open circuit voltage) or Nernst-potential is calculated by the Nernst-equation

$$E_0(T) = E^0 - \frac{RT}{zF} \ln \frac{p_{O_2}^A}{p_{O_2}^C} \quad (2.28)$$

where E^0 is the standard electrode potential and $p_{O_2}^A$ and $p_{O_2}^C$ are the oxygen partial pressures at the anode and cathode side, respectively. At typical working temperatures of SOFCs, 800°C, the OCV is around 1080 mV as it decreases with temperature. When the fuel cell is operated, a current I is drawn from it. Due to its internal resistances R_i , the voltage decreases while the current is conducted. The voltage as a function of drawn current is given by

$$E(I) = E_0 - IR_i = E_0 - IR_{ohm} + \eta_C(I) - \eta_A(I) \quad (2.29)$$

where R_{ohm} is the ohmic resistance of the cell with $R_{ohm} = R_{ohm,C} + R_{ohm,E} + R_{ohm,A}$, where $R_{ohm,C,A,E}$ are the ohmic resistances of cathode, anode and electrolyte and $\eta_{C,A}$ are the overpotentials of cathode and anode, respectively. The cathode overpotential $\eta_C(I)$ is per definition negative in sign. The electrode overpotentials can be further split up into diffusion overpotentials, η_{Diff} , and activation overpotentials, η_{Act} , which will be important in chapters 8, 9 and 10.

Efficiency Different efficiency numbers are used to characterise the functioning of a fuel cell, the most common one [15] being the overall cell efficiency β which is defined as

$$\beta = \beta_g \beta_v \beta_f \quad (2.30)$$

where β_g is the Gibbs efficiency, β_v is the voltage efficiency, and β_f is the fuel efficiency, also called fuel utilisation, which is the fraction of fuel that is used in the conversion process. The former two efficiencies are defined as, β_g , effective work ΔG divided by the fuel's heatig value ΔH

$$\beta_g = \frac{\Delta G}{\Delta H} = \frac{nFE_0}{\Delta H} \quad (2.31)$$

and β_v is the relation of actual potential $E(I)$ divided by OCV E_0 , which is a measure for the internal resistance R_i of the cell.

$$\beta_v = \frac{E}{E_0} = \frac{(E_0 - IR_i)}{E_0} \quad (2.32)$$

Modern SOFC stacks and systems achieve more than 60% pure electrical efficiency and over 85% efficiency by CHP.

Designs There are a variety of different designs for SOFC cells, which can be attributed to the two principal designs of a) planar and b) tubular cells and different combinations thereof.

Chapter 2. Theoretical Background

These two designs are shown in Fig. 2.9. The planar design consists of thin-layered PENs which

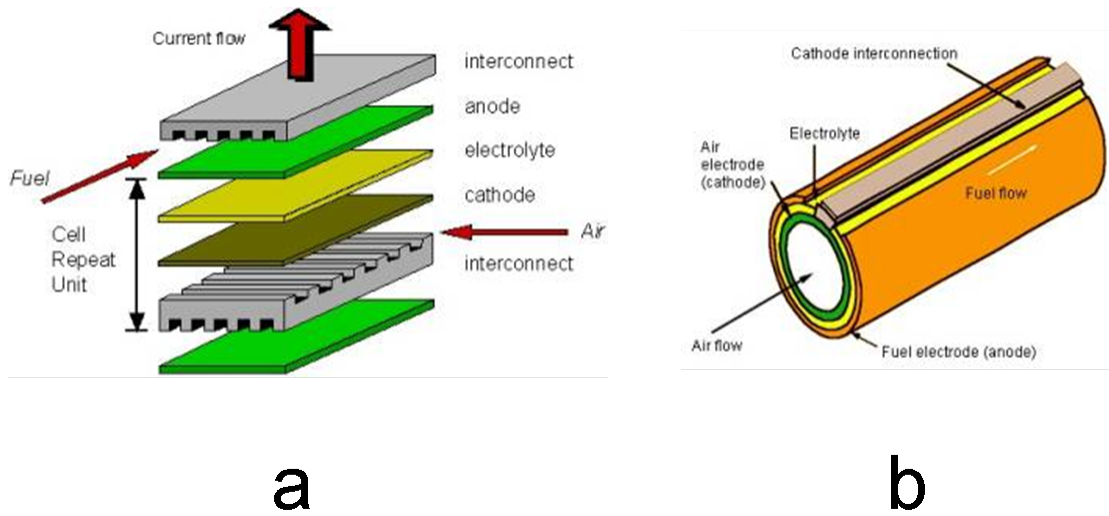


Figure 2.9: The Schematic design of planar(a) and tubular (b) SOFC single cells citeWCDS.

can easily be stacked and connected to increase the total power. Its advantages are ease of manufacturing and high power density, however planar cells require high temperature sealing materials and long start-up time. They also have poor thermal cycling ability, as thermal transients can lead to cell failure by delamination and cracking. The tubular design was mainly investigated and put forward by Siemens Westinghouse, who investigated cathode-supported tubes which were coated by electrochemical vapor deposition. Tubes of 1.5 m length and 22 mm diameter were bundled into stacks by Ni-felt connection. While the system ran for over 70,000 hours [16] with degradation of $<0.1\%/1000\text{h}$, it had a low power density and slow start-up time. Generally, as the tubes can be made longer than the furnace, the sealing on both ends of the tube can be done in the cold zone with low temperature sealings which are easier to apply. Higher manufacturing cost is a further disadvantage of tubular cells. Mixed designs such as the flat-tube concept, the mono-block layer concept or the integrated planar SOFC exist and are used by several companies and research facilities. A further design variation is the downsizing of the cell which leads to μ -SOFCs for planar cells and micro-tubular SOFCs, where the latter are the subject of this work. They are introduced in Chapter 3.

Electrolyte The most commonly used electrolyte is $92\text{mol}\%\text{ZrO}_2\text{-}8\text{mol}\%\text{Y}_2\text{O}_3$ (8YSZ), where the cubic high temperature phase of zirconia is stabilised at low temperatures by yttria-doping. As yttrium is trivalent and replaces tetravalent zirconium in its lattice, oxygen vacancies are created for charge compensation along which the oxygen ions are conducted. It is thrived [15] to keep the area specific resistance (ASR) of the electrolyte below $0.15\ \Omega\text{cm}^2$. Assuming thicknesses of ca. $15\ \mu\text{m}$, it means that the specific conductivity of the electrolyte should exceed $10^{-2}\ \text{Scm}^{-1}$. The specific conductivity of typical electrolyte materials is shown in Fig. 2.10. As the activation energy for ionic conduction of 8YSZ is rather high, it can only be used

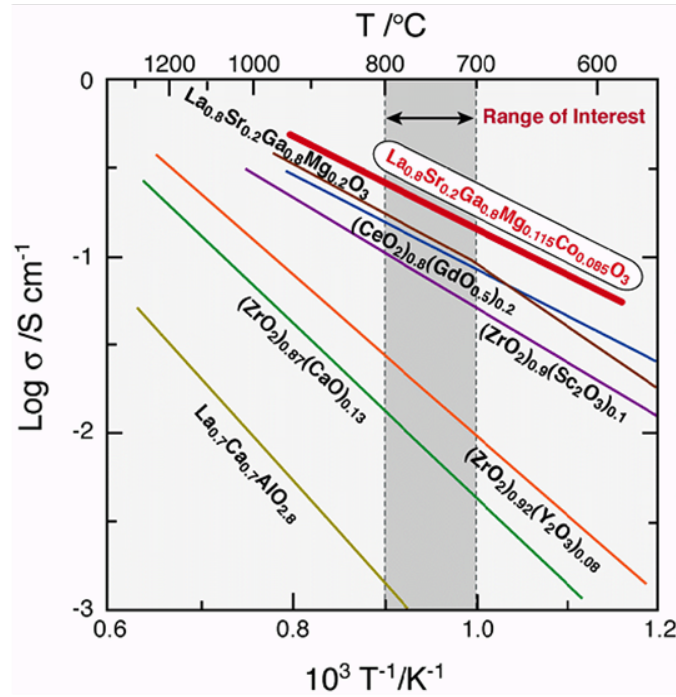


Figure 2.10: The specific conductivity of typical SOFC electrolyte materials [17].

below 700°C by decreasing its layer thickness [18]. Other materials were investigated and have shown higher conductivities than 8YSZ, especially at lower temperatures, however reactivity or chemical stability issues limit their applicability. The most popular alternative to 8YSZ is the fluorite structured $\text{Ce}_{0.9}\text{Gd}_{0.1}\text{O}_{1.95}$ (10GDC), which is stable in oxidising atmospheres but becomes an electronic conductor in fuel-rich, reducing atmospheres, as they prevail at the anode side, above 600°C, leading to internal short-circuits of the cell. Scandia-stabilised zirconia (ScSZ), of composition 92-88 mol% ZrO_2 , 8-12 mol% Sc_2O_3 , was another investigated fluorite-type material and has shown superior conductivity at lower temperatures [19]. However, scandia is more precious than yttria and the stabilisation of the cubic phase requires the addition of 1 mol% CeO_2 , which otherwise transforms from its cubic structure into lower conductive rhombohedral (high Sc-content) or tetragonal (low Sc-content) lattice symmetry at temperatures below 650°C [20].

Cathode The classical cathode material for SOFC is $\text{La}_{1-x}\text{Sr}_x\text{MnO}_{3-y}$ (LSM), a pure electronic conductor that has sufficient catalytic activity at 800°C, but suffers from high polarisation resistance at lower temperature. The thermal expansion coefficient (TEC) can be adapted by mixing electrolyte material with LSM to a composite cathode, which therefore becomes a two-phased mixed ionic and electronic conductor (MIEC). As LSM cannot conduct oxygen ions, the cathode reaction shown in equation 2.25 has to take place at intersections of cathode, electrolyte and gas phase, so-called triple-points, where oxygen ions after reduction are immediately incorporated in the oxygen vacancies of the electrolyte. The reaction in Kroeger-

Vink notation reads



where $V_O^{\bullet\bullet}$ represents an oxygen vacancy in the anion sublattice of the electrolyte and O_O^x an oxygen atom which is inserted in the electrolyte. Research in recent years has produced a number of alternatives, which are almost exclusively MIEC. The advantage of the latter is the extension of the reaction shown in 2.33 from the triple-phase boundary (TPB) areas to the complete surface of the cathode, as oxygen ions can be conducted insided the bulk of an MIEC cathode to the cathode-electrolyte interface. $La_{1-x}Sr_xCo_yFe_{1-y}O_{3-\delta}$ (LSCF) is the most popular material among new cathodes and has shown superior oxygen reduction kinetics at lower temperatures, however it suffers from reactivity with zirconia-based electrolytes and forms the pyrochlore-phase $La_2Zr_2O_7$ and the perovskite $SrZrO_3$ at the interface which are very poor conductors and deteriorate the cell performance. A thin GDC-interlayer is often inserted between zirconia electrolyte and LSCF to circumvent this problem. Nickelates are a new family of cathode materials and will be introduced later on. A comprehensive review of different cathode materials is given by Sun [21].

Anode The most frequently used anode material is the cermet Ni-YSZ. It is normally introduced as ceramic powder mixture NiO-YSZ and reduced to Ni-YSZ at high temperatures in a reducing fuel stream prior to utilisation. Ni is a good electronic conductor and low-priced hydrogen catalyst. It is mixed with electrolyte material YSZ to adapt the TEC to values close to the electrolyte. The decrease of Ni-content decreases its TEC, however, 30 vol% are needed for percolation of Ni grains where the TEC mismatch is still roughly 20%. The electrolyte addition provides a skeleton to inhibit sintering of the Ni particles. Stability issues arise in high oxygen partial pressures (Redox-stability), which may prevail during cool down in the absence of fuel and during high fuel utilitions, when the reaction kinetics of Equation 2.26 are slower than the O^{2-} transport across the electrolyte. The oxidation of Ni is associated with a substantial volume increase which induces stresses and leads to cracks in the electrolyte. Another disadvantage is the unwanted cracking of hydrocarbons under release of carbon, which deposits on the anode and blocks the diffusion paths (anode coking).

Balance-of-plant All remaining parts of an SOFC except cathode, electrolyte and anode are called the balance of plant (BoP) materials. As the costs of BoP account for up to 50% of the total system costs, substantial research is performed to optimised BoP materials as well. The function of BoP components ranges from current collection layers on either electrode, conductive cables to extract the electrical current (mostly made of costly noble metals), sealing materials for gas-tightness, gas-manifolds to direct the gas flow to achieve homogeneous gas and temperature distribution, inter-connectors, gas-filters, gas reforming units, heat exchangers etc.

Reforming and Fuel Flexibility Hydrogen is the most simple fuel in terms of research and is often used to explain the reaction mechanism of SOFC. However, pure hydrogen has a low volumetric energy density which limits the utility of SOFCs in space-limited, e.g. mobile, applications, where liquid hydrocarbons are often used. Furthermore, it is for the moment difficult to produce and store hydrogen from CO₂-neutral sources in large quantities, which leads to the utilisation in SOFCs of commonly applied hydrocarbon fuels such as steam-methane mixtures that are internally reformed.

At the high working temperatures of an SOFC, internal reforming of hydrocarbons such as methane allows for a wide range of different possible fuels and simplifies the system which leads to lowered costs. The working temperature of an SOFC should be at least 700°C to enable internal steam reforming of fuels such as diesel or propane to syngas (mixture of H₂ and CO). Problems are associated with the varying content of additives such as sulphur-containing odorants, which can lead to degradation of the anode.

Challenges The biggest challenges preventing SOFC from speedy commercialisation and market introduction are the high price and degradation issues. In the last years, substantial effort was undertaken to lower the working temperature to $\leq 700^\circ\text{C}$, which would enable the utilisation of more ordinary and hence less expensive materials such as low-cost steel as metallic interconnector, which suffers from Cr-evaporation and associated cathode-poisoning at higher temperatures. The price and degradation would potentially decrease with the working temperature which is therefore regarded as a very promising tactic for further SOFC development. As the temperature decreases, the two main challenges are

1. Ohmic loss of the electrolyte
2. Cathodic polarization resistance

where the electrolyte layer has to be made either thinner or of a more conductive material. The cathode polarisation can be decreased by its impregnation with nano-materials or by changing the material and optimisation of its microstructure. Nickelates are presented as an alternative material for intermediate temperature SOFC (IT-SOFC) cathodes in the next section.

2.5.2 Nickelates

Structure Nickelates are Ruddlesden-Popper compounds with stoichiometry $A_{n+1}M_nO_{3n+1}$ ($n = 1, 2, 3$), where $M = \text{Ni}$, the A-position is occupied by rare earth elements, most commonly La, Nd or Pr, and $n = 1, 2, 3$. They possess the so-called K_2NiFe_4 -structure. The structure can be described as an assembly of alternating layers in vertical direction of rock salt (AO) and perovskite (AMO_3) crystal units. Ni is coordinated 6-fold by oxygen to form MO_6 octahedral units, which share corners with each other in the horizontal x-y plane forming a two-dimensional

network of MO_2 square planes. The structure, which is shown in Fig. 2.11, is therefore also described in the literature as an alternating sequence of MO_2 - and A_2O_2 -layers. Additional

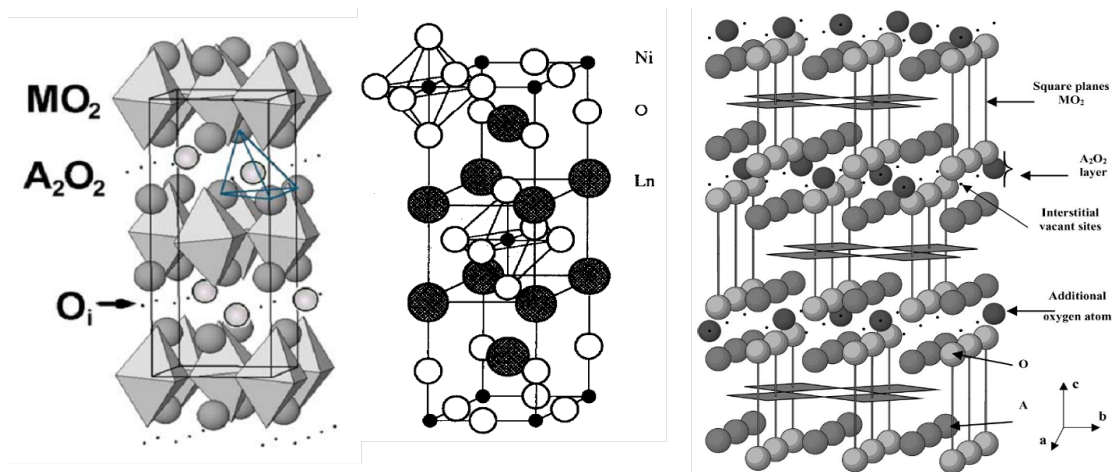


Figure 2.11: The crystal structure of nickelates showing the MO_2 -square planes and the position of vacant interstitial sites that can be occupied by oxygen. $\text{A}=\text{Ln}=\text{La, Nd, Pr}$, $\text{M}=\text{Ni}$. Sources: [22, 23, 24].

oxygen ions can be incorporated at empty interstitial sites in the A_2O_2 -layers. This leads to an oxygen overstoichiometry of δ in $\text{A}_2\text{NiO}_{4+\delta}$ for nickelates, where the excess oxygen ions are the mobile species in the ionic conduction process. This means that the oxygen conduction mechanism differs fundamentally from cathode materials LSM and LSCF, where oxygen is incorporated and conducted along vacancies of the oxygen sublattice. As the interstitial sites are exclusively situated in the A_2O_2 -layers, the conductivity as well as magnetic exchange interactions are much higher within the Ni-O basal plane than perpendicular to them, leading to anisotropic properties such as ionic conductivity.

History Since the lanthanum cuprate-family of $\text{La}_{2-x}\text{M}_x\text{CuO}_{4+\delta}$ ($\text{M}=\text{alkaline earth metals}$) compounds were found to be high-temperature superconductors and lanthanum nickelate was similar in terms of structure, nickelates have been investigated since the late 1980's in order to understand their structure and physical properties. As structural, electric and magnetic properties were thought to be strongly influenced by the amount or overstoichiometry of oxygen, several studies were carried out to investigate structural transitions, oxygen content, low-temperature magnetic transitions, nature of the lanthanide cation among others [23, 25, 26]. As SOFC-cathode material, nickelates have been investigated since roughly ten years [27, 28]. An important fraction of the development was performed at ICMCB in Bordeaux, France, and characterisation of relevant properties for SOFC-application was mainly done and reported by ICMCB and Skinner from Imperial College London, UK.

Nickelates as SOFC-Cathode Nickelates have shown interesting properties as a potential IT-SOFC cathode material. Different compositions were tested [24], among which slightly substoichiometric neodymium nickelate (NNO), $\text{Nd}_{1.95}\text{NiO}_{4+\delta}$, and praseodymium nickelate, $\text{Pr}_2\text{NiO}_{4+\delta}$, have shown the most promising electrical conductivities and oxygen diffusion and surface exchange coefficients.

Oxygen exchange kinetics, characterised by its diffusion coefficient D^* and its chemical surface exchange coefficient k_{chem} , are higher than for commonly used IT-SOFC cathode materials LSCF and $\text{La}_{1-x}\text{Sr}_x\text{Fe}_{1-y}\text{Ni}_y\text{O}_{3-\delta}$ (LSFN) [24, 28, 22].

The electrical conductivities of substoichiometric neodymium nickelate $\text{Nd}_{1.95}\text{NiO}_{4+\delta}$ showed a maximum of ca. 120 S/cm at ca. 500°C and 100 S/cm at 700°C, which is considered the limit for SOFC cathode application.

The stability in wet and CO_2 -containing air atmospheres, a property lacking in potential cathode material $\text{Ba}_{1-x}\text{Sr}_x\text{Co}_{1-y}\text{Fe}_y\text{O}_{3-\delta}$ (BSCF), was found to be reasonable in the case of nickelates even though a decrease of k_{chem} was reported [29].

The influence of Cr-evaporation from metallic interconnects on the kinetics of NNO cathodes was reported by Yang [30]. It showed that the degradation of k_{chem} under deliberate Cr-evaporation and sedimentation on cathode surfaces was much more pronounced for $\text{La}_{0.6}\text{Sr}_{0.4}\text{CoO}_{3-x}$ (LSC) than for NNO cathodes.

Reactivity with common electrolytes YSZ and GDC was reported and showed differing results. For the improvement of electrochemical results, a ceria-interlayer is inserted between nickelate cathode and zirconia electrolyte [31]. However, interaction between ceria and nickelate were shown to start at 900-1000°C already [31, 32, 33] depending on the exact conditions. The reactivity between these two materials is therefore tested in this work again and correlated with electrochemical properties (cf. chapters 7 and 8).

Polarisation resistances of neodymium nickelate cathode layers on YSZ electrolyte pellets at different temperatures, voltages and oxygen pressures were reported by Mauvy [22, 34]. Impedance spectroscopy of symmetrical NNO/YSZ/NNO 3-electrode cells showed a medium frequency (MF)-contribution, which belonged to the charge-transfer at the electrode-electrolyte interface, and two low frequency (LF)-contributions, where the first one represented oxygen reduction on the cathode surface and the second one, which depended strongly on oxygen partial pressure, probably represented oxygen dissociation phenomena.

Exchange current densities were reported for NNO/YSZ interfaces [34] and showed 10 mA/cm² at 700°C. As no data for NNO/GDC interfaces were available, exchange current densities for NNO/GDC were consequently measured in the present work, too (cf chapter 8), as the insertion of a ceria-interlayer leads to the charge-transfer reaction taking place at the NNO/GDC interface.

2.5.3 Approach of this project

In this project, cathode-supported micro-tubular SOFC will be fabricated and characterised. The cathode support was chosen to highlight a new cathode material of the family of nickelates, namely sub-stoichiometric neodymium nickelate (NNO) of chemical composition

Chapter 2. Theoretical Background

$\text{Nd}_{1.95}\text{NiO}_{4+\delta}$. As the degradation and price are driving factors of SOFC development, the cathode as support was furthermore chosen as cathode-supported cells by Siemens have shown the lowest degradation rate of any SOFC system so far. Besides, nickelates allow for a decrease in working temperature to 700°C , where they are more effective than conventionally used LSM [35, 36]. Furthermore, cathode-supported cells are supposed to withstand redox-cycling much better than anode-supported cells, as the anode is only a thin layer and consequently does not harm the mechanical integrity of the whole cell by volume changes during redox processes. In order to adress electrolyte ohmic resistance limitations of IT-SOFC, ScSZ is used as electrolyte material. GDC is inserted between ScSZ and nickelate as interlayer to circumvent reactivity between ScSZ and NNO [31]. Classical cermets of Ni-electrolyte are used as anode material. The schematic design of the single cell is shown in Fig. 2.12. The outer diameter of the tube is

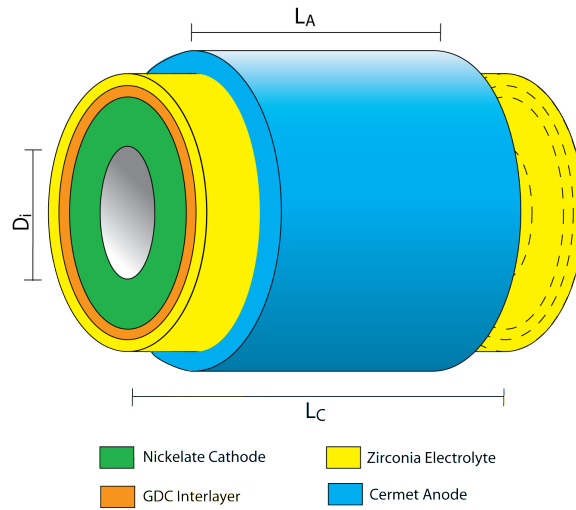


Figure 2.12: The schematic design of a cathode-supported micro-tubular SOFC single cell targeted in this project.

aimed at ca. 5 mm. Several aspects of the fabrication and characterisation of single cells will be adressed and are pointed out in the plan of the thesis in the next chapter.

3 Micro-tubular Fuel Cells - State of the Art

In this chapter, important contributions to the development of micro-tubular SOFC that were reported in the literature are summarised. The sources are mainly journal papers but also proceedings of oral and poster presentations from conferences as well as information published on the internet.

3.1 Introduction

Although the name suggests cells in the micrometer range, microtubular SOFC have no clear-cut definition in terms of size. They are tubular cells with a diameter of generally less than 5 mm and can be mechanically supported by either electrode, the electrolyte or by a metallic tube, which also takes the function of current collector. As the cell diameter decreases, the active surface area per volume unit increases which addresses one weak point of the tubular Siemens-Westinghouse design. Moreover, the smaller cell diameter allows for thinner layers which increases the specific energy density per active unit area due to reduced ohmic and diffusion resistances. Micro-tubular SOFC were shown to start-up from ambient temperatures in the range of seconds [37], as they possess very low thermal mass, which opened a whole new range of mobile and portable applications previously inaccessible for SOFC. The choice of supporting cell element largely influences the cell characteristics as the supporting layer has to be thick enough to mechanically support the load of the other layers. The different cell designs are schematically shown in Fig. 3.1. An electrolyte-supported cell for example will be mechanically robust due to a thick electrolyte layer of high density, however its ohmic loss is relatively elevated to its higher electrolyte thickness. An electrode-supported cell has a thinner



Figure 3.1: The schematic design of (a) electrolyte supported, (b) anode supported, (c) cathode supported and (d) metal-supported microtubular cells.

electrolyte layer and hence better performance, but can suffer from mass-transport limitations due to the thicker support-electrode and specific problems such as redox-stability (especially for anode-supported cells) and lower conductivity (especially for cathode-supported cells). The advantages and disadvantages of each cell configuration is presented in Table 3.1.

Table 3.1: Specific advantages and disadvantages of micro-tubular SOFC supported by different cell elements

Cell-support	Advantages	Disadvantages
	Self-supporting	
Electrolyte supported	<ul style="list-style-type: none"> - Gas-tightness - Less risk of anode reoxidation - Mechanical robustness 	<ul style="list-style-type: none"> - Ohmic losses - High working temperature - current collection from cathode
Anode Supported	<ul style="list-style-type: none"> - Lower working temp. - Co-sintering at higher temperature leads to good electrolyte gas-tightness 	<ul style="list-style-type: none"> - Anode Redox Stability - Mass transport of 2 species requires high porosity - Cathode current collection
Cathode Supported	<ul style="list-style-type: none"> - Lower working temperature - Less risk of anode reoxidation - Cathode current collection 	<ul style="list-style-type: none"> - Lower conductivity - Sintering temperature limitations due to solid state reactions
	External supporting	
Porous Metal Support	<ul style="list-style-type: none"> - Thin layers leading to higher performance - Integrated solution for current collection 	<ul style="list-style-type: none"> - Fabrication more difficult (low temp.) as new material is added - Reactivity of metal with cell and sealing materials

3.2 Electrolyte-supported cells (First Generation)

Micro-tubular SOFC were first prepared with electrolyte support and reported by Kilbride et al. [38] in 1996. An electrolyte-supported cell was prepared by extrusion of 3YSZ and 8YSZ electrolyte tubes of 2.4 mm outer diameter. The anode layer, consisting of NiO-YSZ in organic solvent and additives, was deposited with a syringe on the inside and cosintered with the tube at 1300°C/1h. LSM/YSZ was used as cathode functional layer and LSM as cathode current collecting layer. Both were deposited subsequently by brush-painting and fired at 1100-1300°C. Ag- and Ni/Cr-wires were used as cathode current collector and Ni-wires on the anode side. A current of 179 mA/cm² was measured at 0.7 V and 800°C for 5 mm long cells. The specific current density dropped distinctly with increasing cell length which is explained with in-plane currents on the cathode due to potential differences during the operation. The cell survived

3.2. Electrolyte-supported cells (First Generation)

more than 30 thermal cycles between 200 and 900°C with 100 K/min heating and cooling rate without distinct degradation. Following this paper, a large number of reports from the group of Prof. Kendall at the University of Keele, UK, was published which used electrolyte-supported cells to investigate (a) the possibilities of different fuel sources and their reforming and (b) new applications and materials.

Fuels and Reforming Staniforth [39, 40] has investigated the performance of electrolyte-supported cells powered by three different types of biogas. The cell consisted again of an extruded 8YSZ tube of 2 mm internal diameter with 200 µm wall thickness which was fired at 1450°C and afterwards painted with Ni-YSZ cermet anodes on the inside and with LSM cathode on the outside of the tube and sintered again at 1300°C. Ni- and Ag-wires were used for current collection on the anode and cathode side, respectively. The cell could be heated to 800°C in a few seconds. Synthetic biogas made from methane/carbon dioxide mixtures showed stable production in the range of several hours before coking of the anode set in. The injection of air into the biogas before it entered the cell anode proved to circumvent this problem and the power rose to almost hydrogen level, for some air flow rates even higher. Low methane rates of 1:5 methane to CO₂ still led to significant power output which would not be possible in combustion engines, as they would fail to ignite. One remaining issue, the poisoning of the catalytic nickel-anode surface due to sulphur present in biogas in different compositions, was met by desulphurisation, where the gas passed through a sodium carbonate solution before entering the cell. Further improvement was achieved by air reforming, as the carbon dioxide level in the biogas was not high enough to achieve complete reforming. The greater longevity was also attributed to the oxidation of hydrogen sulphide to sulphur dioxide, the former being a well-known poison for the nickel catalyst.

Finnerty [41, 42, 43] has developed a system that permits to investigate and link the catalytic behaviour of the fuel reforming anode, its surface chemistry and the electrochemical performance of the cell with each other. The cell had the same characteristics as the one used by Staniforth. Methane/steam mixtures were used as fuel in different experimental conditions (anode formulations, flow rates etc.). Ni/YSZ anodes showed good activity as methane steam reforming catalysts. The formation of carbon on the anode increased with temperature and could be reduced by adding 5% of steam to methane. Further decrease was achieved by adding small amounts of molybdenum or ceria (<1%) to the anode. As current is drawn from the cell, the flux of oxygen ions through the electrolyte increased the methane conversion and decreased the carbon deposition. A complete system of integrated catalytic fuel processing was built and could be heated to 800°C in less than 5 minutes running on methane and butane fuel. Methane was more effective as fuel when diluted with inert gas or carbon dioxide [44], as it is the case in biogas, and showed minimal carbon deposition. Further fuels tested successfully involved methanol [45], methanoic acid and ammonia [46] and methyl formate and dimethoxymethane whereas other hydrocarbons had to be diluted with steam or carbon dioxide to prevent carbon deposition. It was reasoned that hydrocarbons without C-C bond deposit less carbon and are potential fuels for internal combustion engine (ICE)-SOFC hybrids.

The reduction temperature of Ni-cermet anodes also has shown to influence the mechanism of anode coking [47].

Since the fabrication of cells was outsourced to the start-up company Adelan [48], the produced cells were also tested by other researchers. Buchinger investigated compatibility of wood gas as SOFC fuel and the influence of hydrogen chloride (HCl) and hydrogen sulfide (H₂S) on the performance using the same electrolyte-supported cell as mentioned before. A nearly stable operation of the cell over 200 min was possible with nearly 50 ppm HCl whereas H₂S degraded the performance at low contents. Sammes [49] used Adelan's cell with two different anodes, cermets with and without addition of ceria, where the electrodes were both sintered at 1300°C for 1h. Butane was used as fuel but led to quick coking by soot formation on the anode for both anode formulations. Partial oxidation was demonstrated over the Ce/Ni/YSZ anode.

Materials and Applications As the current collection from the cathode limited the cell performance, Hatchwell [50] investigated Ag inks and wires and perovskite-coated Ni-wires (Nimonic 90). Ag-wires and contacted inks showed less resistance than the coated Ni-wire, where the coating delaminated partially from the metallic wire as verified by SEM after the test. As silver is known to evaporate at high temperatures due to its low melting point, Ag-containing current collectors were proposed for intermediate- and low-temperature SOFC. Metallic Cr₅Fe₁Y₂O₃ interconnects also improved current collection upon coating of ceramic perovskites, where the TEC mismatch has to be kept small in order to avoid delamination of the coating [51]. However, Ag-wires still showed the least polarisation resistance and were consequently also used as interconnects for 20-cell ministacks [52] that were modeled for optimum temperature distribution.

Micro-tubular SOFC allow for smaller power outputs in reasonable conditions, where previous planar and tubular systems have aimed at the 10 kW to multi-MW range. Kendall [53] has demonstrated a 3 cell ministack, which was made from the same cell as mentioned before with cermet anode and LSM cathode both sintered at 1300°C/1h on an already densified 8YSZ tube prepared by extrusion. Butane gas was used as fuel and cell heating device as the combustion took place close to the tube entry. It was possible to heat the individual cells to 700°C in a few seconds and the cells also survived 12 thermal cycles, while generating between 0.1-1 W of electric power at 700°C operating temperature which was used to power electric devices such as an electronic calculator.

A 1000-cell reactor was built [54], using the same cells as described before, that were grouped into 40 individual racks of 25 tubes each and then assembled in modular fashion. Natural gas was used as fuel for the start-up and after ignition, the air ratio was slowly increased to allow for partial oxidation. The tubes in each rack were connected in parallel while the racks were connected in series to achieve a useful voltage. The specific power density of the reactor was 82 mW/cm² at 850°C, which was smaller than for individual cells as irregular gas flow and

3.3. Electrode-supported cells (Second Generation)

non-uniform temperatures may have led to extra resistances. Possible applications of sub-kW micro-SOFCs were listed by Tompsett [55], who named micro-hybrid vehicle applications such as electric golf-trolleys and bicycles as well as micro-CHP devices such as camping gas burners, which were tested with cells supplied by Adelan.

Electrolyte-supported cells using commercial and synthesized 8YSZ and $\text{La}_{0.8}\text{Sr}_{0.2}\text{Ga}_{0.8}\text{Mg}_{0.2}\text{O}_{2.8}$ (LSGM) electrolyte powders were reported by Sammes [56]. Synthesized LSGM powder was only single-phased within a small range of Mg-and Sr-content. The electrolyte powders were mixed with organic additives to form pastes that were extruded to form tubes of 2-4 mm outer diameter and 200-550 μm wall thickness dried and sintered under air. The quantity of organic additives to the extrudate paste, the material and shape of the drying support as well as the extrusion die designs greatly influence the quality of the tubes. After completed sintering, burst strength was measured by feeding pressurised water into the tube and registering the pressure when the tube burst. Room temperature burst strengths of 8YSZ and LSGM tubes were 127 and 40 MPa, respectively. The anode and cathode were deposited by dip-coating and brush-painting respectively. LSGM based single cells of 220 μm wall thickness with Ni-SDC (samaria-doped ceria) anode and LSC cathode achieved 0.482 W/cm^2 at 800°C whereas YSZ-based single cells with Ni-YSZ anode and LSM cathode only achieved 0.22 W/cm^2 at 850°C .

3.3 Electrode-supported cells (Second Generation)

As the power densities for electrolyte supported cells remained limited and the working temperatures generally above 800°C , electrode-supported cells were investigated as they featured a thin-layered electrolyte and hence reduced ohmic losses. The first feasibility study on electrode-supported micro-tubular SOFC was published by Van herle [57] in 2000. It involved mechanical tests of extruded electrolyte tubes, oxygen reduction studies on the cathode side by testing dense LSC layers on doped ceria substrates by impedance spectroscopy. The cell concept was validated on planar anode-plate supported cells and reached 0.47 and 0.89 W/cm^2 at 700°C and 800°C respectively.

3.3.1 Anode-supported cells

The first report on prepared half cells of electrode-supported micro-tubular SOFC was published in 2004 by Du [58], using an anode-supported design and thin layered electrolyte and cathode that were deposited by dip-coating and brush-painting respectively. An NiO-YSZ cermet powder was mixed with organic binders and extruded. Following a pre-firing of the anode tubes, YSZ coating was deposited by vacuum-assisted dip-coating with different submersion times. Cracks and pinholes were the main electrolyte layer failures. Cracks were found to appear in the middle to late drying stages and were circumvented by using thin layers and slow drying, which mirrors the introduction given on drying stresses in Equation 2.20 and Fig. 2.4. Electrolyte thicknesses were between 10-50 μm . First electrochemical

results on anode-supported cells were reported by Nguyen [59]. NiO-3YSZ anode pastes were used for the fabrication of tape-casted slurry tapes, which were wound to form tubes. The tubes were fired at 900°C before a zirconia layer of either 10ScSZ or 3 YSZ was deposited by a modified dip-coating technique and cosintered at 1300°C. GDC interlayers were deposited on the already sintered half cell and fired at a lower temperature in order to suppress solid state reactions between zirconia and GDC. LSC was deposited by brush-painting and fired at 1000°C/1h. The tubes had an outer diameter of 6-10 mm and 1 mm wall thickness. Gaseous diffusion resistance which was attributed to the thick anode substrate was determined by impedance spectroscopy. The measured power density for 3YSZ electrolyte layers was 0.17 W/cm² at 600°C and 0.22 W/cm² at 700°C and did not increase further with rising temperature. Sammes [60] used the same half-cell as reported by Du [58] and applied an LSM cathode by brush-painting followed by sintering. Current collectors made of nickel 200 were built to assemble cells to planar multi-cell arrays and connected to the cells by a brazing technique involving silver wires as brazing material. A concept of 40 cells stacked together in planar arrays was presented. Power densities attained were 0.1 W/cm² at 800°C.

Sarkar [61] investigated one-end-closed cells fabricated by electrophoretic deposition (EPD) on graphite rods. The anode consisted of a structural layer of 250 µm thickness for mechanical stability, with a powder mixture of coarse NiO and 8YSZ, and a <10 µm thick functional layer with fine NiO and 8YSZ. After the deposition of a <10 µm 8YSZ electrolyte layer, the half-cells were dried over night and cosintered at 1380-1400°C/4h. Cathode layers of LSM-YSZ were applied by brush-painting on the sintered half cells. The cell attained 0.44 W/cm² peak power density at 800°C and a cell with Sm_{0.6}Sr_{0.4}CoO_{3-δ} (SSC) cathode achieved 0.45 W/cm² peak power density at 650°C. Cells heated by the open flame of a gas burner started to produce power within seconds. Tests of 550 thermal cycles showed no signs of degradation. Small stacks of 12 W total power were tested.

Gil [62, 63] has investigated microtubular cells on porous Ni-GDC support prepared by cold-isostatic pressing with GDC electrolyte and LSCF-GDC cathode. Electrolyte and cathode were deposited by dip-coating. Grain agglomeration of GDC electrolyte proved to be a key parameter and was decreased by attrition milling, as the majority of particles after attrition milling were smaller than 100 nm. OCVs of complete cells at 450 °C and 500 °C were only 0.78 V and 0.74 V respectively although SEM cross-section images suggested a dense electrolyte layer of 15-20 µm thickness, which was attributed to the electronic conductivity of GDC. Maximum power densities at 450°C were 0.066 W/cm².

Campana [64, 65, 66, 67] has fabricated and analysed anode-supported SOFCs with Ni-zirconia cermet support, zirconia electrolyte and LSM cathode. Anode-supports of 2.4 mm inner diameter and 400 µm thickness were made by cold-isostatic pressing. The electrolyte layer was deposited by wet powder spraying. Anode and electrolyte were cosintered at 1400C/2h. Afterwards, the cathode layer was dip-coated and sintered, where the layer thickness and the sinter temperatures were varied. Power densities of 0.6 W/cm² were measured for wet hydrogen fuel at 850°C. The cells were also operated in electrolysis mode (cite Cam4).

Zhang [68] has prepared Ni-YSZ anode cermet tubes by extrusion and applied 8YSZ coatings by dip-coating. After drying at room temperature for 24h, the coated tubes were cosintered at

3.3. Electrode-supported cells (Second Generation)

1400°C/5h. The cathode was a composite of LSCM-SDC-YSZ, where SDC is samarium-doped ceria and LSCM is $\text{La}_{0.75}\text{Sr}_{0.25}\text{Cr}_{0.5}\text{Mn}_{0.5}\text{O}_{3-\delta}$, and painted onto the surface and sintered at 1200°C/5h. The complete cell had an outer diameter of 1.3 mm and 240 μm wall thickness. The thickness of electrolyte and cathode were 10 and 25 μm respectively. Peak power densities using wet hydrogen fuel were 0.513, 0.408 and 0.278 W/cm^2 at 850, 800 and 750°C respectively.

Anode-supported micro-tubular cells are used by companies in the USA such as Protonex [69, 70], Ultra-Ami [71] and Acumentrics [72, 73] to market small off-grid power for leisure, portable and military applications. In Japan, companies such as TOTO, Toho Gas, Mitsubishi Heavy Industries and Kyocera have been working on tubular and flat-tubular SOFC for years [74, 73]. The flat-tubular concept was used by Kyocera and Siemens-Westinghouse [73] and adapted by researchers at the Korean Institute of Energy Research (KIER) [75] as well.

Toho Gas [76] has recently attempted to downsize the cell diameter and investigated also small tubular anode-supported cells of 2 mm outside diameter and 500 μm wall thickness in collaboration with academic partners in the Advanced Ceramic Reactor Project. Ni-GDC was used as anode material and its ceramic paste extruded to tubes that were dip-coated with GDC electrolyte. After cosintering, an LSCF cathode was brush-painted on the half-cell and sintered. Pt-wires were used as current collector. The cell showed maximum power densities of 0.46 and 0.62 W/cm^2 at 550°C and 600°C respectively. No degradation was observed during 300 hours of operation. At higher fuel utilisations, higher polarisation resistances were observed and attributed to anode diffusion resistances. The performance of a 6-cell short stack was inferior to single cells due to poor gas distribution and current collection. Stagnant air was used on the cathode side which caused shortage of oxygen in 6-tube and 36-tube bundles.

Advanced Ceramic Reactor Project The Advanced ceramic reactor project, financed by the New Energy Development Organisation (NEDO), Japan, aimed at the fabrication of high performance anode-supported microtubes in the low temperature region (450-550°C) by using electrochemically very active materials [77]. Tubes with a diameter smaller than 1 mm were targeted for the construction of bundled cell modules that could achieve power densities of $\geq 2 \text{ W}/\text{cm}^3$ at temperatures of 500-650°C. Ni-GDC was selected as anode material, GDC as electrolyte and LSCF-GDC as composite cathode material to ensure sufficient performance at the working temperatures. Several authors as Suzuki, Funahashi, Hashimoto, Awano, Sin and Yamaguchi reported the fabrication and testing surrounding micro-tubular Ni-GDC supported cells.

Yamaguchi [78] prepared Ni-GDC supported cells for low-temperature (450-550°C) application with dip-coated GDC electrolyte and LSCF-GDC cathode. The linear shrinkage of the cofired samples was found to be decisive for the densification of the GDC electrolyte layer. Shrinkages >15% led to well-densified layers whereas shrinkages <10% led to constrained sintering of the GDC-electrolyte and hence porous microstructure. The calcination temperature influenced the shrinkage during cosintering and the GDC film thickness through capillary pressure, the latter due to the decrease of fine pores in the support for higher calcination temperatures. Cells achieved 0.1, 0.2 and 0.4 W/cm^2 at 450, 500 and 550°C respectively.

Suzuki investigated extruded Ni-GDC tubes of 1.6 mm [79, 80, 81] and 0.8 mm external diameter [82, 83] and achieved 1017 mW/cm^2 at 550°C for the latter with controlled high anode tube porosity of 46 vol% before reduction. GDC-electrolyte layers of ca. $10 \mu\text{m}$ thickness were dip-coated from suspensions with organic solvent and additives, dried and sintered at $1400^\circ\text{C}/1\text{h}$ in air. LSCF-GDC cathode were dip-coated on the sintered half-cells and sintered at $1050^\circ\text{C}/1\text{h}$. Current collection [81] from both ends of the tube limited the efficiency losses to values 2-4 times smaller than for current collection from only one end.

Sin [84] measured the performance of 1.6 mm outer diameter cells with silver wires and silver paste current collectors for the cathode side and nickel paste for the anode side respectively. The cells were vertically mounted for even fuel concentration over the cross-section and air was pumped to facilitate convective air flow. Ceramabond 552 was used as ceramic sealant. The power densities using wet hydrogen as fuel attained 0.263 , 0.518 and 1.31 W/cm^2 at 450 , 500 and 550°C respectively. These values represent the highest power densities measured so far for ceria-based electrolyte systems. However, the OCV of the cells fell in the range of 0.8 - 0.9 V , which means that the electronic conductivity of ceria in the reducing atmosphere of the fuel side led to a leaking current through the electrolyte and decreased the potential.

Funahashi [85, 86] reported the possibility of using matrices of LSCF cathode material to stack sintered half-cells together to cube-shaped arrays. Permeation calculations proved the feasibility of the concept whereas MgO as porous matrix material showed more homogeneous temperature distribution than LSCF matrices due to higher thermal conductivity [87]. Estimated power losses in short stacks mainly originated from ohmic losses of the anode tubes and current collectors.

Suzuki also reported results on cells with zirconia electrolyte at $\leq 600^\circ\text{C}$. At these low temperatures, 8YSZ has conductivities below 0.01 S/cm [15], which would severely increase the ohmic resistance of the cell for common electrolyte thicknesses. Consequently, in two studies Suzuki used [18] single-grain-thick electrolyte layers of 8YSZ (thickness of ca. $1 \mu\text{m}$) and [88] scandia-stabilised zirconia electrolyte (ScSZ). In both cases, zirconia electrolyte layers were cosintered with NiO-zirconia (either YSZ or ScSZ) support tubes between 1250°C and 1400°C . A GDC interlayer was deposited and sintered at 1100°C and a LSCF-GDC cathode layer was dip-coated and sintered at 1000°C to complete the cell in both cases. For single-grain-thick 8YSZ-electrolyte, pores were observed at the 8YSZ grain boundaries for sintering temperatures below 1350°C . The OCV was 1.0 V , indicating a slightly porous 8YSZ electrolyte layer. Maximum power densities were 0.2 W/cm^2 at 550 and 0.39 W/cm^2 at 600°C respectively. For scandia-stabilised zirconia, increasing sintering temperature led to lower anode tube porosities, higher electrical conductivities due to enhanced Ni-grain connectivity and overall lower electrochemical performance, thus indicating the importance of support tube porosity, especially at lower working temperatures. Furthermore, the OCV also decreased slightly from 1.1 to 1.0 V for decreasing cofiring temperature from 1400°C to 1250°C indicating some residual porosity of the electrolyte. This could prove critical in long-term degradation experiments. Hashimoto [89, 90] reported enhanced performance of Ni-ScSZ/ScSZ/GDC/LSCF-GDC cells under pressurised conditions. The peak power density at 650°C increased from 0.68 to 1.48 W/cm^2 by increasing the pressure of both fuel and air side from atmospheric pressure to 0.7

MPa. A combination of two different ceramic hard sealings and control of the differential pressure between cathode and anode side proved to be effective enough as sealing method to obtain stable OCVs close to the theoretical value. Further increase in performance of the above mentioned cells was achieved by more efficient current collection methods, where two different methods led to drastically different ohmic losses, especially at higher current densities as the ohmic loss is associated with a development of heat and hence a change of temperature. EIS measurements showed that the ohmic loss varied for current densities ≥ 0.1 A/cm² as the temperature at the cell changed due to the generation of heat. The deposition of Pt-paste over the whole cathode surface plus a net-shaped current collector increased the maximum power density of the cell from 0.3 W/cm² (without Pt-paste and net) to 0.68 W/cm² (with Pt-paste and net) at 650°C.

The highest power densities were observed for small-diameter (<2 mm) tubes at low temperatures (<600°C) for cells with ceria-based electrolyte or thin-layered zirconia electrolyte of some residual porosity. However, these cells generally are challenged with respect to degradation [91, 92] and heat removal mechanisms [90], as high power densities also lead to great heat generation, which is difficult to remove especially from very narrow tubes as used in the Advanced Ceramic Reactor Project.

3.3.2 Cathode-supported cells

Cathode-supported micro-tubular cells were investigated slightly after anode-supported cells and are to this day scarcely reported due to the difficulties in fabrication. As cathode-supports are cosintered with electrolyte layers, chemical interaction between the two and coarsening/-densification of the cathode material dictate the limitations in sintering temperature.

Liu [93, 94] reported results on cathode-supported cells with LSCF-GDC cathode support, a 12-15 μ m thin GDC electrolyte layer and equally thick Ni-GDC anode layer, both deposited by dip-coating from organic suspensions. In the first study [93], cathode and electrolyte, whose shrinkages were highly tailored, were cosintered at 1200°C/10h. As the GDC was nano-sized (SSA: 30 m²/g), densities of $\geq 92\%$ were achieved at 1200°C. The Ni-GDC anode was then deposited on the sintered half-cell and fired at 1100°C/1h. Pt-mesh was wrapped around the outer anode side as current collector, whereas Pt-wires were twisted around the two terminals of the cathode tube. 30% wet H₂/70%He was used as fuel, air as gas on the cathode side and both gases were flown in counter-flow arrangement at 100 ml/min. The outer diameter of the complete cell was 2.26 mm and its wall thickness 460 μ m.

Peak power densities for 1.5 cm total length of the cell reached 0.11, 0.13 and 0.16 W/cm² at 500, 550 and 600°C and decreased with total cell length due to cathode current collection losses. OCVs were 0.7-0.8 V which indicates pressure or electronic current leakage across the GDC electrolyte layer.

In the second report [94], an increase in anode sintering temperature to 1200°C led to a single cofiring step for the entire cell which was accompanied by slightly improved power densities due to improved anode/electrolyte interfacial properties. However, the OCVs remained as

low as described before. Switching from air to pure oxygen drastically increased the power densities to 0.58 W/cm^2 at 600°C for 2 cm cell length.

Zhao [95] reported the fabrication and characterisation of cathode-supported cells with in-house produced, A-site deficient, LSM as cathode material. The cell consisted of a LSM cathode support, a cathode activation layer of LSM-ScSZ mixture, an ScSZ electrolyte and NiO-ScSZ as anode layer. The complete cell was fabricated by dip-coating of a one-end-closed glass rod into suspensions which consisted of the ceramic powders, organic solvents ethanol and butanone, methyl ethyl ketone as dispersant, PVB as binder and polyethylene glycol (PEG) as plasticizer. For the creation of sufficient porosity, graphite was added to the suspension as pore former for cathode support and active layers. The layers were successively deposited and dried, after the ScSZ electrolyte layer, the green tube was rolled out from the glass tube and pre-fired at 1150°C . Afterwards, the anode was deposited on the electrolyte surface and all layers were co-sintered at $1250^\circ\text{C}/4\text{h}$. At this temperature, no interaction between A-site deficient LSM and ScSZ was observed. The complete cell had a length of ca. 60 mm, a diameter of ca. 10 mm and a wall thickness of ca. $800\text{--}900 \mu\text{m}$. The ScSZ electrolyte layer had a thickness of ca. $14 \mu\text{m}$. The ScSZ layer, with powder form Daiichi Kigenso, still showed some closed pores after sintering but adhered well, which was attributed to the great shrinkage of the supporting tube, which was 26% linear shrinkage from ambient temperature to 1250°C , helping the densification of the electrolyte, even at these low temperatures.

The cell performance was tested between $750\text{--}850^\circ\text{C}$ and wet hydrogen and oxygen as fuel and oxidant, respectively. OCV values of 1.10, 1.08 and 1.06 V at 750, 800 and 850°C respectively indicated good gas-tightness of the electrolyte layer. Peak power densities were 157, 272 and 358 mW/cm^2 at the temperatures mentioned above. Impedance spectroscopy indicated strong limitations of the LSM support at temperatures below 800°C due to its low oxygen kinetics, which led to the suggestion of alternative cathode materials at lower working temperatures.

Yamaguchi [96] reported electrochemical results of LSM supported tubes of 1.6 mm outer diameter and $400 \mu\text{m}$ wall thickness. All layers were deposited by dip-coating from organic suspensions with diamine dispersant and PVB binder in an ethanol-based solvent. An LSM-GDC activation layer was optionally deposited before one GDC- and ScSZ-layers and all were co-fired at $1300^\circ\text{C}/2\text{h}$. Afterwards, Ni-GDC anode layers were deposited and again sintered at $1300^\circ\text{C}/2\text{h}$. The film thicknesses were 10, 20 and $15 \mu\text{m}$ for LSM-GDC activation layer, GDC layer and ScSZ layer respectively. Stepwise sintering after GDC-layer and again after ScSZ-layer led to weakly connected GDC/ScSZ interfaces and delamination of ScSZ. Particle sizes of LSM, GDC, ScSZ and NiO were 3, 0.3, 0.6 and $1 \mu\text{m}$ respectively.

XRD analysis found a reaction product at the GDC-ScSZ interface which was assumed to be a solid solution of GDC and ScSZ according to the peak positions, so that a decrease of the sintering temperature was suggested. Ag-wire and paste were used for current collection, where Ag-wire was wrapped around the edges of the cathode tubes. Wet hydrogen was used as fuel and pure oxygen as oxidant. Peak power densities for cells with LSM-GDC activation layer were 15, 73, 230 and 378 mW/cm^2 at 500, 600, 700 and 750°C respectively, showing roughly twice the peak power output of the cell without activation layer, which were ca. 130 mW/cm^2 at 700°C [97]. Without GDC-interlayer and with LSM-GDC activation layer, the peak power

density was increased to 0.45 W/cm^2 at 750°C [98]. Rapid start-up of the cell was demonstrated [99], as cells were heated at 60°C/min and operational within less than 5 minutes of start-up. Yamaguchi also investigated cathode-supported honeycomb structures [100, 101]. LSM was used as cathode material and extruded to form the supporting structure, and coated with LSM-GDC, ScSZ and NiO-GDC layers as activation layer, electrolyte and anode layer respectively. The cosintering after the deposition of the electrolyte layer as well as the second sintering step were both carried out at 1300°C/2h . The OCV at 600°C was ca. 1.0 V [102] which suggests some gas leakage. A two-unit stack was also tested and yielded 1.17 W maximum power, which translated to 0.6 W/cm^3 considering the honeycomb volume. Impedance spectroscopy indicated that ohmic resistances of two-unit stacks were elevated due to the interface resistance of honeycomb and interconnect. Improvements on electrolyte gas-tightness (OCV $>1.0 \text{ V}$ at 600°C) and volumetric power density (1.2 W/cm^3 at 600°C) were also reported [103].

3.4 Metal-supported cells (Third Generation)

Metal-supported microtubular cells were investigated in recent years, mainly in order to decrease the detrimental influence of thick layers and to integrate current collection components into the single cell design. The design was used by Ikerlan [104, 105]. In their cell, the metal support was prepared from metal powders by scaleable routes. A diffusion barrier layer was deposited to prevent Cr, Fe and Ni interdiffusion. An anode- and electrolyte-layer was deposited respectively by dip-coating and cofired at 1350°C in non-oxidising atmosphere to protect the metallic support from oxidation. The composite cathode was deposited and fired in situ prior to electrochemical characterisation. Pt-paste and mesh were used on the cathode side and four Ni-wires were welded at several points around the anode. Zirconia based seals or alumina felts were used on the cathode side. Fuels such as humidified hydrogen, methane, propane and liquid fuels such as ethanol or bio-oil were used for tests. Power densities of 0.45 W/cm^2 at 800°C and 0.7 V were obtained (State: April 2008, [104]), whereas maximum power densities exceeded 0.6 W/cm^2 . The stack concept was based on bundles of 10 tubes connected in parallel and the bundles connected in series to create domestic power generator systems of $< 3 \text{ kW}$ electrical power output. Degradation issues mainly arose from machining of the tubes prior to testing, anodic interconnects and sealing.

Further metal-supported cells involve mainly the planar button-cell design used e.g. by Risoe [106] and Lawrence Berkeley National Labs (LBNL [107]). An extensive review of progress made on metallic substrates, electrolyte materials etc. is given by Tucker [108] from LBNL. Main challenges involve chromia scale formation on the surface of stainless steel supports, cathode processing routes due to the reducing atmosphere during sintering and long-term demonstrations of low degradation rates. The rather narrow window for operation temperature of $650\text{--}700^\circ\text{C}$ is caused by the requirements for internal reforming and low oxidation rates or chromia scale thicknesses.

This literature summary does not claim to be complete. For comprehensive reviews of progress on microtubular SOFC, the reader is also referred to reviews by Mizutani [74], Lawlor [109],

Kendall [110] and Howe [111]. Further activities in the field of microtubular cells were and are conducted, e.g. on protonic conductor electrolytes [112], enhanced pressurisation experiments [113], tube fabrication techniques [114, 115], improved efficiencies of current collectors [116], infiltration of the cathode with nano-particles [117] and more efficient stack designs [118], among other subjects.

3.5 Performance

In most cases, the performances are reported as a complete voltage-current density-power density diagram with all relevant information. In some reports however, the peak power density or the power density at 0.7 V is simply indicated as a number without graphical representation. The former is the maximum power density that occurs generally at rather low voltages of ca. 0.4-0.5 V, and is associated with high ohmic losses due to high current densities, whereas the latter represents a condition of only limited ohmic losses and is therefore considered realistic as SOFC operation condition as the efficiency is higher. Since the maximum power density is the number that is reported most regularly, it is used here for a comparison of the measured performances of the different supporting designs, which is shown in Figure 3.2.

Anode-supported cells generally show the highest power densities, especially at low temperatures with ceria electrolyte or at intermediate temperatures with ScSZ electrolyte. However, all reported performances are of unaged, freshly installed cells, which means that degradation or redox-stability issues, which are typically problematic for ASC, are not taken into account.

At temperatures between 700-750°C, the cathode-supported cells fabricated by Yamaguchi [96, 98] have shown the highest power densities of all reported cells, which is emphasized in Fig. 3.2 by the rectangular inset as this temperature range seems particularly interesting for improved cathode materials. At 800°C, metal-supported cells by Ikerlan [104] performed better than ASC. Electrolyte-supported cells are generally inferior in terms of power density but mechanically very robust due to the thick electrolyte layer, however they gain in competitiveness at 800°C or at lower temperatures with alternative electrolyte materials such as LSGM as prepared by Sammes [56].

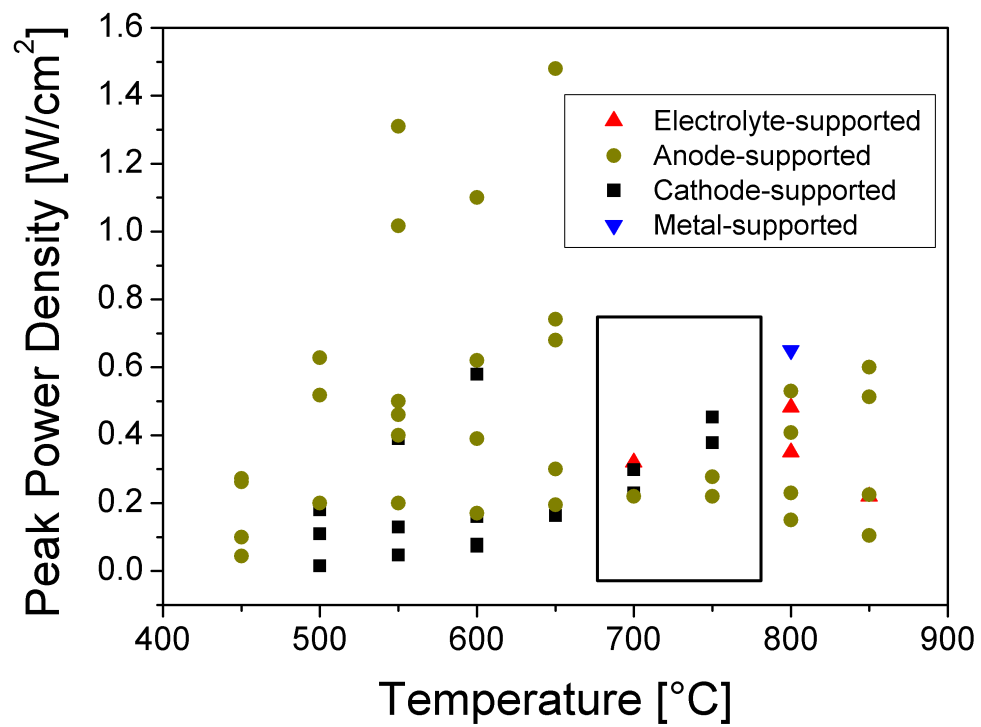


Figure 3.2: A review of all reported maximum power densities as a function of working temperature.

4 Chemicals and Equipment

In this chapter, the equipment and chemicals that were regularly used in most parts of this work will be detailed. Other non-specific products or devices will be described in the respective chapter.

4.1 Equipment

4.1.1 Deposition of thin films and drying

The principal technological step for the fabrication of complete micro-tubular single cells is the controlled deposition and drying of thin films. The thin films are deposited on the tubular substrates in the wet-chemical state by dip-coating the tubes in powder suspensions. The dip-coater used in this work (Speedline Technologies, Model PL3201) is shown in Figure 4.1. The vertical displacement of the horizontal lift arm is realized by an oil-pressure driven system which enables the dip-coater to work in a range of ca. 30-1600 mm/min of vertical displacement velocity. It is however not possible with this device to perform complex displacements, such as hold times at the same height. As it is an open system, depositions can solely be realized at atmospheric conditions. When it was necessary to change the temperature and/or relative humidity of the atmosphere surrounding the drying sample, coated tubes were moved from the dip-coater to the drying chamber immediately after coating and dried vertically by attaching the sample to the support. The drying chamber used in this work (Rhumed, Model 4001) is shown in Figure 4.2a and the sample support in Figure 4.2b.

The drying chamber is operational in the range of 25-60°C and 20-95 % of relative humidity (hereafter abbreviated RH). As it is placed very closely to the dip-coater as shown in Figure 4.3, the transfer of freshly coated substrates can be realized in less than 30 seconds. This limits the time of exposure of wet thin layers to uncontrolled drying conditions to values which are very low compared to the total time of the drying process, which is on the scale of hours (see Fig. 4.4). The total drying time is a function of the evaporation rate and hence the RH in the drying chamber. Tubes freshly coated with aqueous GDC-suspensions were placed on a balance inside the drying chamber. The balance had a serial port which made it possible to register the



Figure 4.1: The Dip-Coater used in this work (a); the inset(b) shows the enhanced alligator-clip which is used to fix the sample.

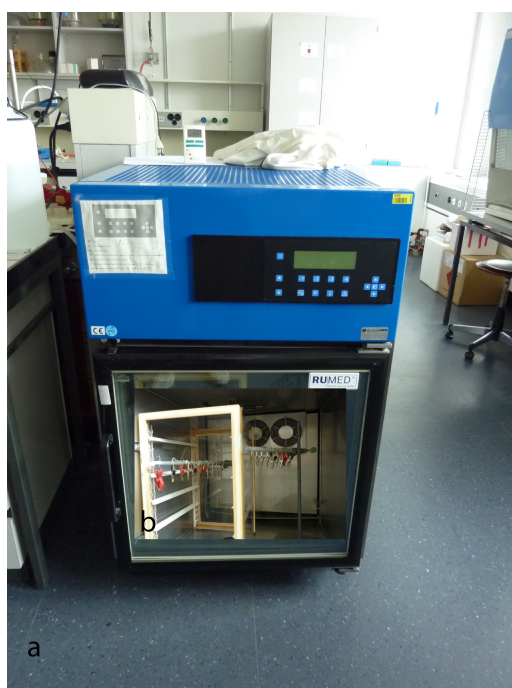


Figure 4.2: The Drying Chamber used in this work (a); the inset(b) shows the enhanced sample-support with alligator-clips which are used to dry the sample in a free hanging vertical way.

weight loss as a function of time. In Fig. 4.4, the weight loss and evaporation rate for steady state evaporation is shown for 60%, 75% and 90% of RH. It can be seen that the weight loss,



Figure 4.3: The Placing of the Dip-Coater (a) and the Drying Chamber(b)in the laboratory; the short distance allows for durations of uncontrolled drying below 30 seconds after the deposition.

and hence the drying speed as well, is linear until it sharply deviates into a plateau. The break of slope indicated in Fig. 4.4 shows that the drying time is proportional to RH, as expected. With the geometry of the tube being known, the evaporation rates were calculated and are also shown. These are somewhat lower than the evaporation rates of free water surfaces measured by Juillerat (cf. Table 4.3, [10]). It is hence possible that the drying process is only controlled in the very beginning by free surface evaporation and for the most part by evaporation from the interface.

As the hollow tubular substrates should be exclusively coated on the outer surface by dipping them in a liquid suspension, a tight sealing of the tubes' upper and especially lower extremities has to be realized in order to avoid the liquid's penetration inside the tube. As thin-walled, porous ceramic tubes can be fragile, the force applied on the tube by the sealing material must be kept as small as possible while still ensuring tightness against liquid's penetration. Modelling clay was found to work most conveniently as sealing material for all types of substrates involved. In order to attach the sealed substrates to the alligator clips of the dip-coater and of the support inside the drying chamber, a copper rod of 1 mm diameter and ca. 10cm of length is inserted into the tube and the tube-sealing clay is attached to both the tubular substrates and the copper rod. Tubular substrates, which are sealed on both extremities and attached to the copper rod by modelling clay, represent the standard samples for dip-coating and are shown in Figure 4.5.

4.1.2 Sintering

The sintering in this work, if not otherwise indicated, is carried out in stagnant air atmosphere in two different furnaces. For all tasks in this work which involve temperatures $\leq 1300^{\circ}\text{C}$, a

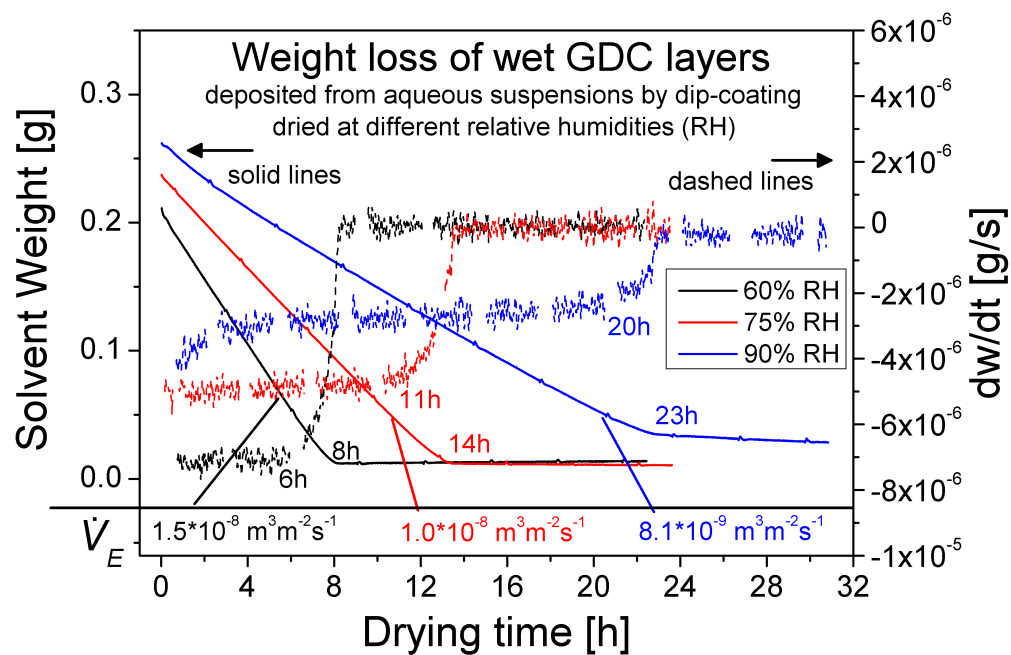


Figure 4.4: The time necessary for complete drying of aqueous suspensions as a function of RH.

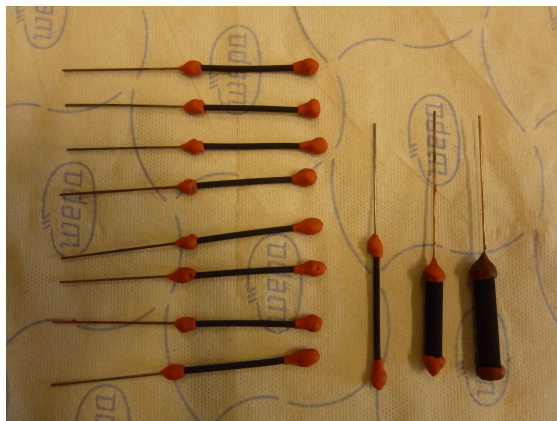


Figure 4.5: Different substrates after the standard preparation for dip-coating.

Naber L08/14 furnace was used. For all tasks which involve temperatures $>1300^{\circ}\text{C}$, a Naber HT10/18 furnace was used. As the latter was furthermore equipped with a second thermocouple to control the temperature during the operation, it was also used for all thermal treatments where high precision was required (e.g. reaction temperatures of diffusion couples, cf. chapter 7). If not otherwise indicated, the sintering was done in alumina crucibles, which were filled with supports or sinter beds in order to inhibit solid state reaction at high temperatures. Further details such as sintering position of tubes and the composition of sinter beds to avoid solid state reactions etc. are given in the respective sections.

4.1.3 Pressure loss tests

The gas-tightness of sintered half-cells with GDC-ScSZ double electrolyte layer was tested by measuring the pressure loss across the tube. One side of the tube was connected via plastic hoses and a closeable valve to an air supply and the other tube extremity was blocked by closing the plastic hose connected to the tube. When the air was conducted into the tube, the pressure inside the tube rose since the air could not leave the tube via the blocked exit. When the pressure inside the tube reached 100-120 mbar, the valve was closed and hence the air supply disconnected from the tube. The pressurised air inside the tube consequently had to diffuse through the porous cathode tube wall and across the sintered electrolyte layers. The setup is shown in Figure 4.6a and the process schematically drawn in Figure 4.6b. The pressure

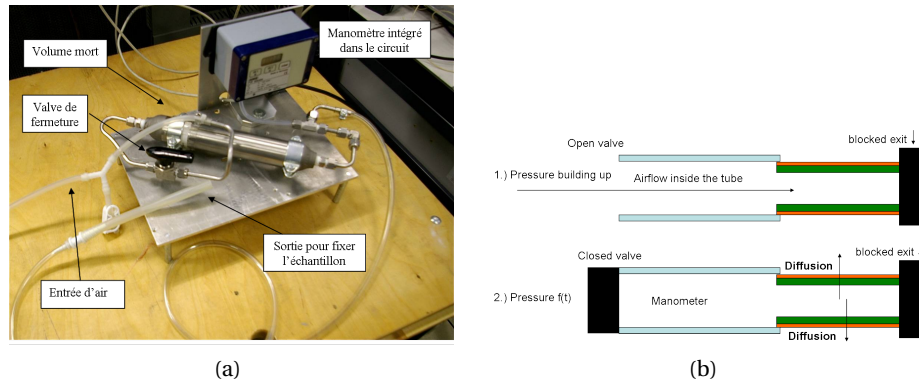


Figure 4.6: The used setup for pressure loss measurements. (a) Photograph of the used equipment. (b) Schematic representation of the principle of the measurement

inside the tube was measured as a function of time and followed exactly an exponential decay function of the shape

$$P(t) = P_0 e^{-\kappa * t} \quad (4.1)$$

where P_0 is ca. 100-120 mbar, t is time in seconds and κ is the exponential decay constant, for which lower values indicate slower pressure loss. The decay of pressure over time, which was registered by a manometer, was slower for increasing thickness and density of the sintered layers. It is therefore a direct measure for the gas-tightness of the electrolyte layers. The

permeability F of the tubes was calculated by developing the ideal gas law to

$$F = \frac{V_0}{2\pi L r_m} \frac{\kappa}{RT} \quad (4.2)$$

where V_0 is the total volume of the system which was measured beforehand, L is the tube length along which gas flow occurs and r_m is the mean tube radius, taken as the arithmetic mean of outer and inner tube radii. R and T are the ideal gas constant and the absolute temperature in Kelvin respectively.

4.1.4 Screen printing

Screen-printing was used to deposit electrodes on GDC pellets for the electrochemical characterisation of nickelate cathodes (cf. chapter 8 on page 131). The layers are deposited from a suspension in an organic solvent, the nickelate powder was dispersed in a 3 wt% solution of ethyl cellulose in terpineol, where the former acts as a binder and the latter as the solvent. The exact mixing ratios are presented in chapter 8. After the dispersion was completed, the paste was printed through a circular screen of 8 mm diameter and yielded electrodes of equal diameter and a thickness of ca. 5-10 μm .

4.1.5 Electrochemical tests

Electrochemical tests were performed on two different systems in this work. Firstly, completed microtubular single cells were characterised electrochemically (cf. chapter 9). Secondly, planar cells were tested in order to characterise nickelate cathodes (cf. chapter 8). For both setups, the cells have to be contacted and connected to the measurement devices. Gold wires and meshes were used to contact the cells. Specific parameters such as wire and mesh diameters are given in the respective chapters. In the case of symmetrical cells, the nickelate acting as "counter-electrode" was furthermore coated with a LSC ($\text{La}_{0.7}\text{Sr}_{0.3}\text{CoO}_3$) contacting layer for better current collection. LSC was commercially obtained from Praxair, USA. Measurements of the current-voltage characteristics (I-V curves) of single cells were done with a Potentiostat-Galvanostat measuring device from Tacussel, type PJT 35-2 in galvanostatic mode. Impedance spectroscopy was performed with a IM6 impedance analyser with Thales 2.15 software, from Zahner, DE.

4.1.6 Slip-casting

Slip-casting of pellets was performed by casting suspensions into a natural rubber mold which contained multiple holes of a diameter of ca. 15 mm and a thickness of 11-15 mm. Below the mold, a porous gypsum plate was placed as a support. A cellulose nitrate filter of 0.2 μm pore size was inserted between the mold and the gypsum plate. When the suspensions were cast into the mold's holes, the solvent was extracted from the suspension through the filter into

the porous gypsum plate due to the capillary pressure of the latter. Furthermore, the solvent's content was reduced by evaporation through the uncovered liquid-gas interface on the liquid's surface. The pellet in the green state was formed after the drying process was complete. The drying of slip-casted pellets generally took 24 hours and could be slowed down by inserting the slip-casting setup into the drying chamber shown in Fig. 4.2 at high humidities. The slip-casting setup is shown in Figure 4.7. Slip-casting was used in order to determine the

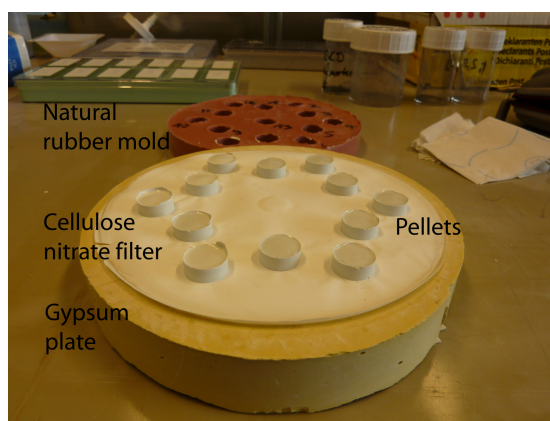


Figure 4.7: The different components of a slip-casting setup.

green density, density after sintering and the shrinkage during the sintering process of the powders in suspensions that were used for dip-coating. As these parameters are impossible to access for thin layers on substrates, slip-casting was used as the most similar shaping process to evaluate these properties. Contrary to forming methods in the dry powder state such as uniaxial or isostatical powder compaction, the densities and shrinkage of slip-casted green bodies depend on wet-chemical properties such as colloidal stability which are of utmost importance for the dip-coating process, too.

In commonly applied slip-casting, a suspension of high solid load is used in order to extract thick green bodies of high mechanical stability.

Here, it was attempted to use suspension formulations which were as similar as possible to the formulations that were used for dip-coating. It was found that suspensions of a solid load <10 vol% did not yield pellets of regular shape as the pellet's curvature was too big with respect to the pellet's thickness. For a suspension of 10 vol% solid load, a final pellet thickness after grinding, polishing and sintering of typically only 0.8-1 mm was attained. As the suspensions used for dip-coating generally had a solid load of 5 vol% in order to attain a layer thickness of a few micrometers after sintering (cf. sections 5.2.3 and 5.3.6), a small difference in the composition of suspensions prepared for slip-casting and dip-coating could not be avoided. The mentioned solid loads of both slip-casting and dip-coating were however low enough to consider the suspensions dilute and their difference in solid load were assumed to be small for the powder's shrinkage and green density.

4.2 Chemicals

4.2.1 Solvents

In the scope of this work, the three different solvents water, ethanol and isopropanol were used for suspension preparation. Water was triple distilled before utilisation, its conductivity was routinely checked and attained values smaller than 5 μS . Absolute ethanol of A15 grade had a purity $\geq 99.8\%$ (based on denaturant-free substance) and was denaturated with 2% MEK; Isopropanol was analytical grade with 99+% purity. Different considerations play into the choice of a solvent used for suspensions in dip-coating. The surface tension γ is important for wettability (cf. equation 2.16) and drying stresses (cf. equation 2.21). Another important parameter for the liquid coating of a substrate, especially with a significant surface roughness, is the liquid's viscosity. The surface tensions and viscosities of water, ethanol and isopropanol at 25°C are presented in Table 4.1. A good wettability of the substrate with the solvent has to be assured. The wetting angle φ , which can be measured to evaluate the wettability, is linked to the surface tension γ by equation 2.16. An example of wetting angle measurements is shown in Figure 4.8. A drop of respective liquid was dripped on a flat surface of a neodymium nickelate pellet. The measurement was repeated for pure water, aqueous PAA-solution (cf. section 4.2.2) and aqueous PVA-solution (cf. section 4.2.3). The results are shown in Table 4.2.

Table 4.1: Surface energies γ and viscosities of water, ethanol and isopropanol at 25°C, given in $[\text{J}/\text{m}^2]$ and $[\text{Pa}\cdot\text{s}]$ respectively

	Water	Ethanol	Isopropanol
γ $[\text{J}/\text{m}^2]$	$7.2 \cdot 10^{-2}$	$2.2 \cdot 10^{-2}$	$2.1 \cdot 10^{-2}$
η $[\text{Pa}\cdot\text{s}]$	$0.9 \cdot 10^{-3}$	$1.1 \cdot 10^{-3}$	$2.0 \cdot 10^{-3}$

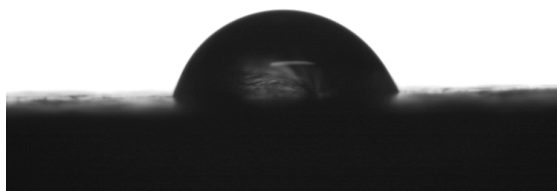


Figure 4.8: Measurement of the wetting angle φ .

As PVA-solution has a lower surface tension than pure water (cf. Fig. 4.10), equation 2.16 predicts that the wetting angle φ of PVA-solution should be smaller than for pure water. This is confirmed by the results from Table 4.2. Besides the surface tension, a further important

Table 4.2: Wetting angles of water, PAA-solution and PVA-solution in contact with neodymium nickelate

	Water	PAA-solution	PVA-solution
φ	$87 \pm 1^\circ$	$78 \pm 1^\circ$	$68 \pm 1^\circ$

parameter of a solvent is its rate of evaporation \dot{V}_E , as it influences strongly the maximum drying stress of a deposited layer (cf. section 5.2.3). The evaporation rate \dot{V}_E of water can be influenced by the temperature and the relative humidity (RH) of its surrounding atmosphere. Juillerat [31] has measured \dot{V}_E of water at different temperatures and humidities, his values are presented here. In this work, the experiments were performed at ambient conditions for ethanol and isopropanol and the values of \dot{V}_E for different solvents compared. The results are shown in Table 4.3. Water evaporates at a higher rate than both ethanol and isopropanol at low humidities but decreases proportionally with rising humidity. The evaporation rate of isopropanol at ambient conditions of 22°C and 24%RH is only half that of ethanol.

Table 4.3: Evaporation rates of water, ethanol and isopropanol at different conditions, given in $[\text{m}^3/\text{m}^2\text{s}]$

Temp.	RH	Evaporation Rates $[\text{m}^3/\text{m}^2\text{s}]$		
		Water	Ethanol	Isopropanol
22°C	24%		$6 \cdot 10^{-8}$	$3 \cdot 10^{-8}$
20°C	30%	$11 \cdot 10^{-8}$		
20°C	50%	$8 \cdot 10^{-8}$		
20°C	70%	$5 \cdot 10^{-8}$		
20°C	90%	$3 \cdot 10^{-8}$		

4.2.2 Dispersants

Different dispersants were studied in this work. The dispersant's primary function is to disperse the powder in the suspension and deny the particles' agglomeration. Consequently, the dispersant has to be soluble in the solvent.

For water-based systems, polyacrylic acid (hereafter abbreviated PAA) of a molecular weight of ca. 2000 g/mol was used as dispersant. This molecular weight corresponds to 27 repeat units of 73 g/mol monomer weight and hence a total length of 4-5 nm of the polymer chain. A 63 wt% aqueous solution of PAA, commercially obtained from Acros Organics, was diluted and filtered to yield a 10 wt% stem solution, from which all further dispersant solutions were made. The R-value (see Introduction, section 2.1) of the stem solution was set to 1.5 (pH=9) by the addition of a 25 wt% aqueous solution of ammonia, commercially obtained from Reactolab, CH.

For the organic solvents isopropanol and ethanol, three different dispersants were used, namely

- Triethanolamine (hereafter abbreviated TEA),
- Triolein (hereafter abbreviated Tl) and
- Triton-X 100 (hereafter abbreviated Tx).

The molecular structure of all four dispersants is shown in Figure 4.9.

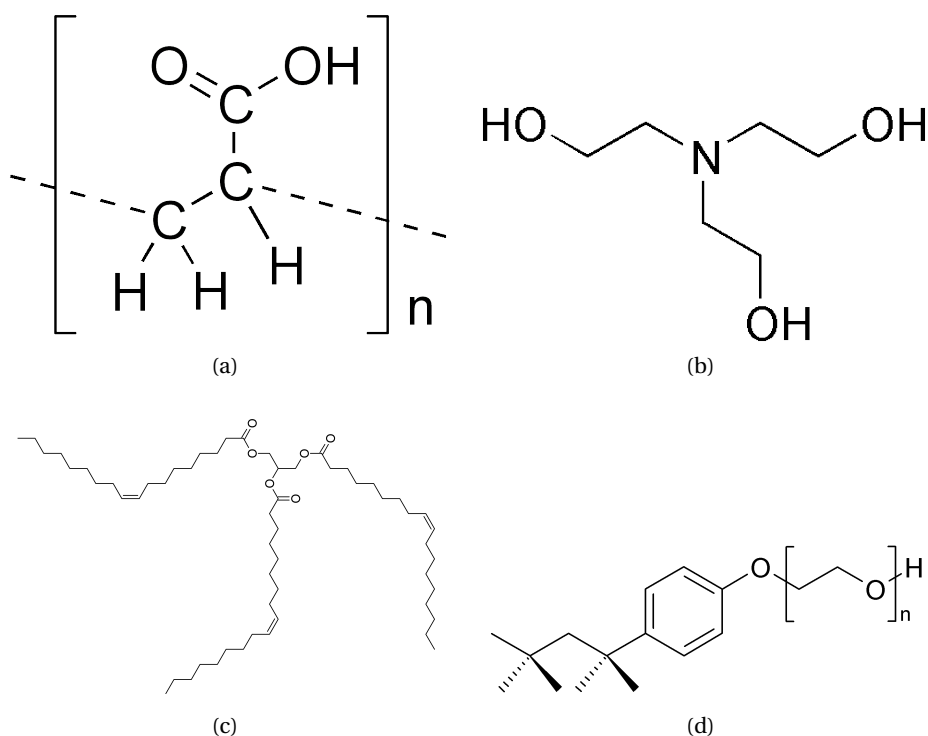


Figure 4.9: The molecular structure of the used dispersants. (a)PAA (b)TEA (c)Tl (d)Tx

4.2.3 Binder

The binder's principle function is to hinder the formation of cracks during drying by providing a soft, flexible matrix around the particles. As it has to surround homogeneously the particles in suspension, the binder has to be soluble in the solvent as well. In this work,

- Polyvinylalcohol (hereafter abbreviated PVA) was used for water-based suspensions
- Polyvinylbutyral (hereafter abbreviated PVB) was used for suspensions of organic solvents.

For both binders, 10 wt% stem solutions were made and filtered, and all subsequent binder solutions were derived from it. For the preparation of 10 wt% solutions, the respective amount of PVA powder was heated in the solvent to 95°C and stirred during several hours. A clear solution was obtained and its density measured for the preparation of suspensions. The commercial PVA-product Mowiol 8-88 of molecular weight 67'000 g/mol, and hence a polymerisation degree of 1400, was used as binder. As it is only partially hydrolysed (degree of hydrolysis 88 ± 1 mol%), it can be stocked during longer periods of time (some months) without precipitation; for fully hydrolysed grades precipitation of the hydroxyde is observed in less than 2 weeks after the preparation. The viscosity of a binder solution, even at low concentrations, is generally higher than the solvent's viscosity. A 4 wt% PAA 8-88 aqueous solution at 20°C for example has a viscosity of 8 mPas as opposed to 1 mPas for pure water at 20°C. Hence, the binder content influences the total suspension viscosity. Furthermore, the addition of PVA decreases the surface tension of water. This is shown as a function of PVA-concentration in Fig. 4.10. The

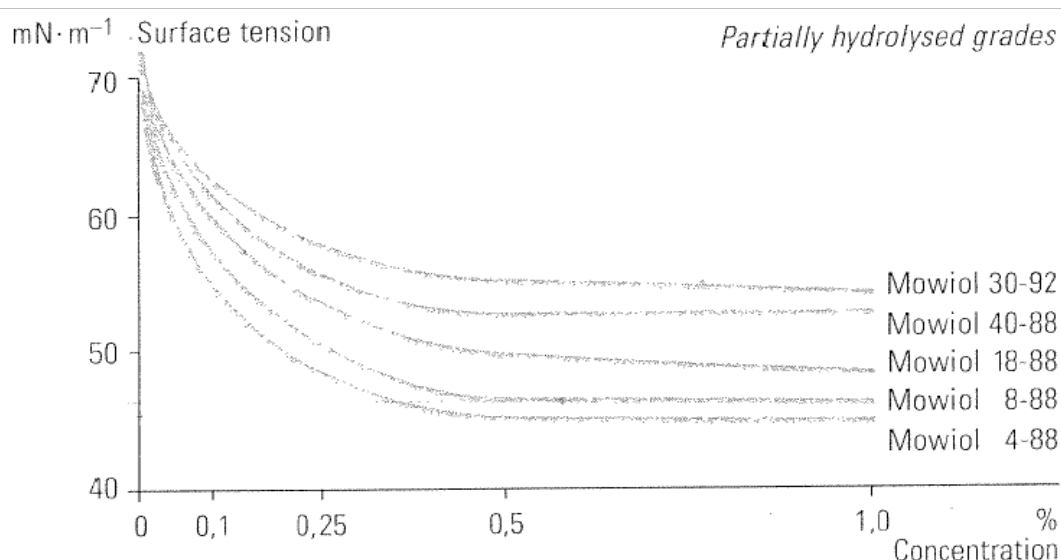


Figure 4.10: The surface tension of water upon the addition of PVA 8-88, Source: [119].

commercial PVB-product Mowital B20H, Lot-Nr: DEBC106048 was used as binder for organic solvents. Its molecular weight was ca. 22'000 g/mol, and hence its polymerisation degree ca. 360. The dynamic viscosity of a 10 wt% solution of PVB B20H in ethanol at 20°C is 25 mPas as opposed to 1.2 mPas for pure ethanol at the same temperature. The molecular structure of the two used binders is shown in Fig. 4.11.

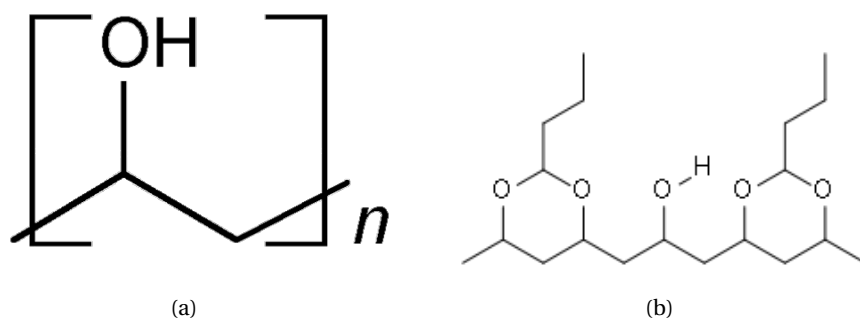


Figure 4.11: The molecular structure of the two used binders. (a)PVA 8-88 for aqueous suspensions. (b)PVB B20H for organic solvents

5 Powders

In this chapter, the different powders used in this work are described. The properties presented here to characterise the powders are their particle size distribution, which was measured by laser diffraction on a Malvern Mastersizer S, UK, and their specific surface area, which was measured by nitrogen adsorption on a Micromeritics Gemini 2375, USA. For particle size distribution, either the full curve is shown or two critical parameters, the median volume diameter ($d_{v,50}$) and its span, are reported. The span is defined as $\text{span} = \frac{d_{v,90} - d_{v,10}}{d_{v,50}}$ and indicates the width of the particle size distribution.

5.1 Cathode: Neodymium nickelate

5.1.1 Supply and Powder Characterisation

The powder used for the application as cathode and hence the support for the fabricated tubes was sub-stoichiometric neodymium nickelate of theoretical composition $\text{Nd}_{1.95}\text{NiO}_{4+\delta}$. It was commercially ordered at Marion Technologies, FR. Different batches of powder were obtained and tested at the ICMCB, FR and at LTP. The Nd/Ni ratio was measured by ICP at ICMCB whereas powder characteristics such as specific surface area and granulometry were measured at LTP. A summary is shown in Table 5.1. The nickelate powder batch Nr. 1 was used to study

Table 5.1: Powder characteristics of different batches of nickelate powder.

$\text{Nd}_{1.95}\text{NiO}_{4+\delta}$		Characteristics				
Batch Nr.	Amount	$d_{v,50}$ [nm]	Span	SSA [m^2/g]	$R_{\text{Nd/Ni}}$	Specifics
1	1 kg	580	0.8	4.3	1.98	Si-impurities
2	1 kg	280	1.8	8.2	1.97	Precursor
3	1 kg	550	1.0	5.2	1.95	Si-impurities
4	10 kg	640	1.0	5.4	1.96	Si-impurities

the powder's densification and to prepare the first tubes by cold-isostatic pressing (see page 98). In order to achieve higher electrochemical activity of the cathode support, the second batch consisted of a precursor to neodymium nickelate of finer particle size. However, the lacking controllability of the phase crystallisation as well as poor compactability by pressing has led to the decision to use the crystalline nickelate phase again. The third batch was used for powder fabrication by extrusion. The higher quantity of powder in the fourth batch was chosen in order to achieve better reproducibility. Slip-casting and cold-isostatic pressing was performed with fourth powder batch. Furthermore, all electrochemical tests of nickelate cathodes on ceria pellets (see chapter 8) were made with the fourth powder batch.

5.1.2 Chemical Stability

When sintered layers, tubes and pellets of the neodymium deficient $\text{Nd}_{1.95}\text{NiO}_{4+\delta}$ were analysed by energy-dispersive X-ray spectroscopy (EDX) in both scanning electron microscopy (SEM) and transmission electron microscopy (TEM), the presence of NiO was evidenced, especially when the sintering temperature exceeded 1300°C . One example of these measurements is shown in Fig. 5.1. It was suggested by coworkers from ICMCB that the substoichiometric

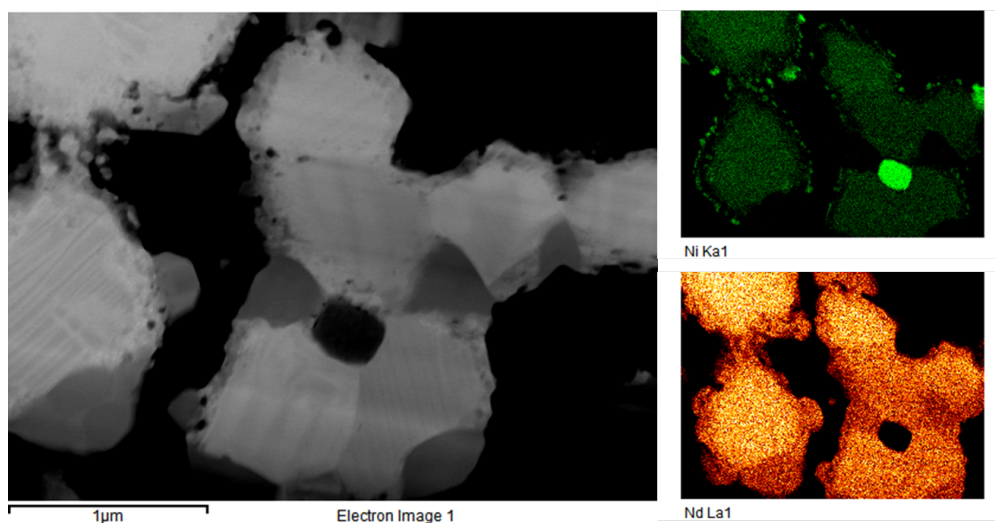
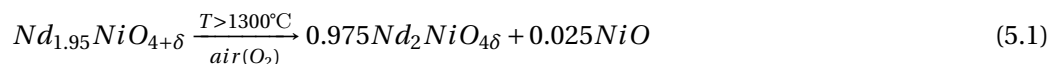


Figure 5.1: TEM-EDX analysis of a $\text{Nd}_{1.95}\text{NiO}_{4+\delta}$ thin film showing the formation of NiO.

neodymium nickelate transforms to the stoichiometric phase by creation of NiO, hence:

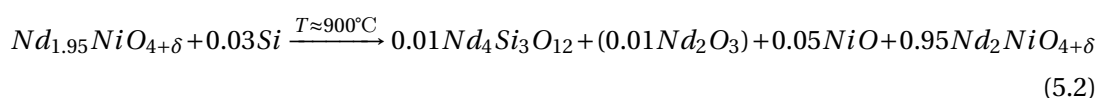


5.1.3 Si-Impurities

During the scope of almost the entire work, Si-traces were found in different batches of nickelate powder prepared by Marion Technologies. During the fabrication of the crystalline

neodymium nickelate phase, Si-impurities were introduced, most probably during a cost-cutting milling process with Si-based milling media in order to attain a defined granulometry. The Si-impurities are present in the powder in an amorphous or partially-crystallised state, as they are hardly detectable by XRD in the as-received powder, shown in Fig. 5.2. However, when the powder is heated to temperatures above 700-900°C, Si reacts with Nd from the nickelate phase to form neodymium silicates.

The stoichiometry of these silicates is unknown but may be $\text{Nd}_4\text{Si}_3\text{O}_{12}$, as this composition (ICCD 00-042-0171) gives the best fit for the obtained spectra. Furthermore, traces of Nd_2O_3 were found, however, the peak positions (ICCD 00-013-0176) either coincide with $\text{Nd}_4\text{Si}_3\text{O}_{12}$ or with $\text{Nd}_{1.95}\text{NiO}_{4+\delta}$ and are therefore difficult to distinguish. Further proof of the existence of neodymium silicate was found by TEM-EDX analysis of nickelate thin layers on GDC pellets after electrochemical tests (cf. chapter 8). The analysis of local chemical composition at different locations at a nickelate particle surface is shown in Fig. 5.3. In local quantifications of Nd- and Si, a stoichiometry of Si:Nd=1:2 was never exceeded in any spectrum. It is hence reasonable to assume that the Si-contamination induced reaction happens according to



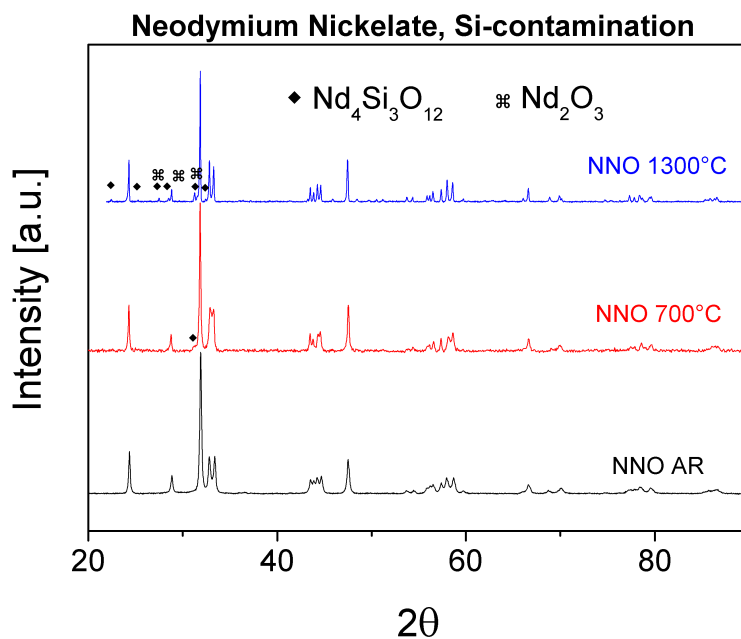
where the formation of Nd_2O_3 is difficult to evidence, hence the parentheses in equation 5.2. From equations 5.1 and 5.2 we can see that Si-impurities trigger and decrease the temperature of the decomposition of the neodymium deficient phase $\text{Nd}_{1.95}\text{NiO}_{4+\delta}$ to the less conductive [24] stoichiometric $\text{Nd}_2\text{NiO}_{4+\delta}$ phase by formation of neodymium silicate $\text{Nd}_4\text{Si}_3\text{O}_{12}$.

5.1.4 Dispersion and Shrinkage

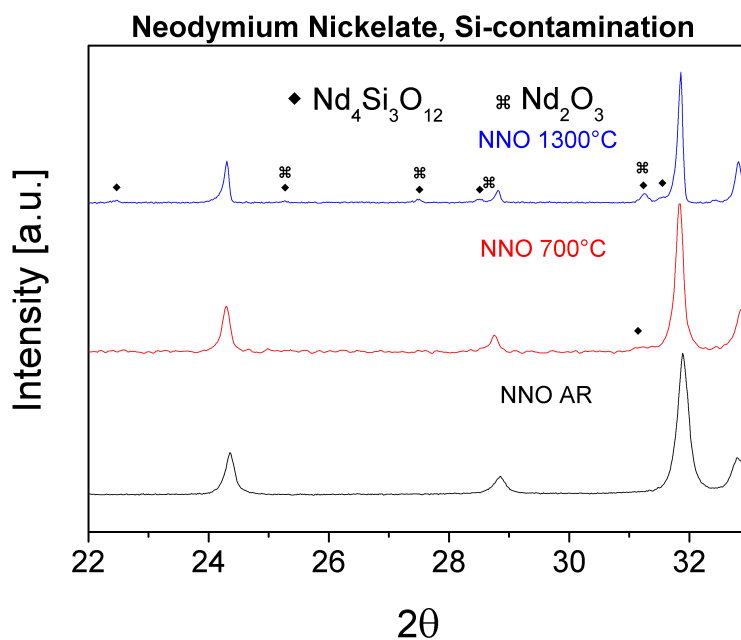
The shrinkage of nickelate material was investigated by measuring the thermal contraction of pellets prepared by uniaxial and isostatic compaction as well as slip-casting of nickelate suspensions, either by geometrical measurements or by dilatometry.. Furthermore, nickelate tubes were also prepared and investigated with respect to shrinkage (see chapter 6). The sintering temperature depends on many parameters and is generally a balanced compromise of reactivity limitations (see chapter 7), sinterability and grain growth as well as electrochemical performance (see chapter 8), among others.

Based on such a compromise, 1300°C was chosen as the target maximum sintering temperature at the beginning of this work. Nickelate pellets of the 4th powder lot were prepared by cold-isostatic pressing at different pressures. The holding time at each pressure was 2 minutes and the pressure increase and decrease rate 1 kN/sec. The green and sinter density of the pellets and its shrinkage to 1300°C were determined geometrically and by Archimedes method. In Fig. 5.4, the nickelate pellet's green density as well as sintering shrinkage is shown as a function of compaction pressure.

It can be seen that the green density increases and the sinter shrinkage slightly decreases with rising CIP pressure. This is due to the lower green density at lower pressure and hence



(a)



(b)

Figure 5.2: Results for XRD measurements of as-received and heat-treated neodymium nickelate powder after dwelling at 700°C and 1300°C. (a) Whole range of measurements. (b) Zoom on low angle part to highlight peak formation of impurities

5.1. Cathode: Neodymium nickelate

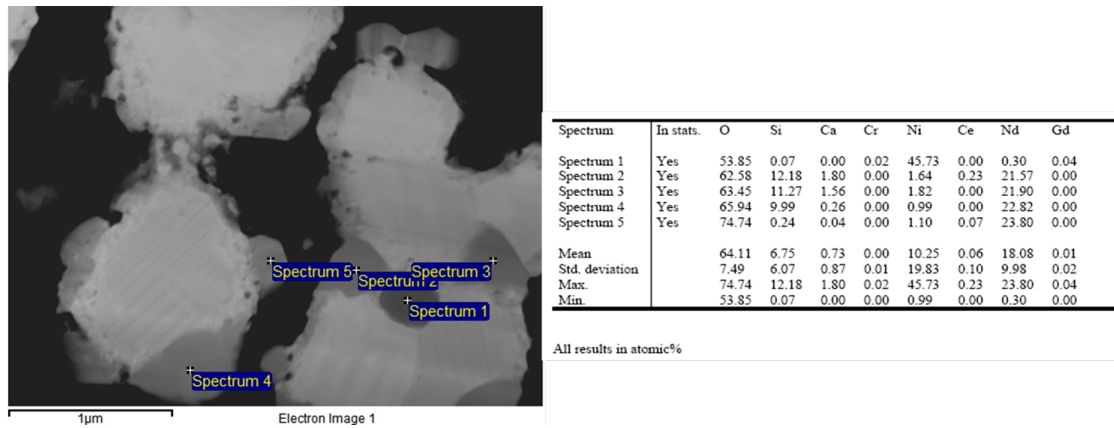


Figure 5.3: Local chemical analysis of a $\text{Nd}_{1.95}\text{NiO}_{4+\delta}$ thin film.

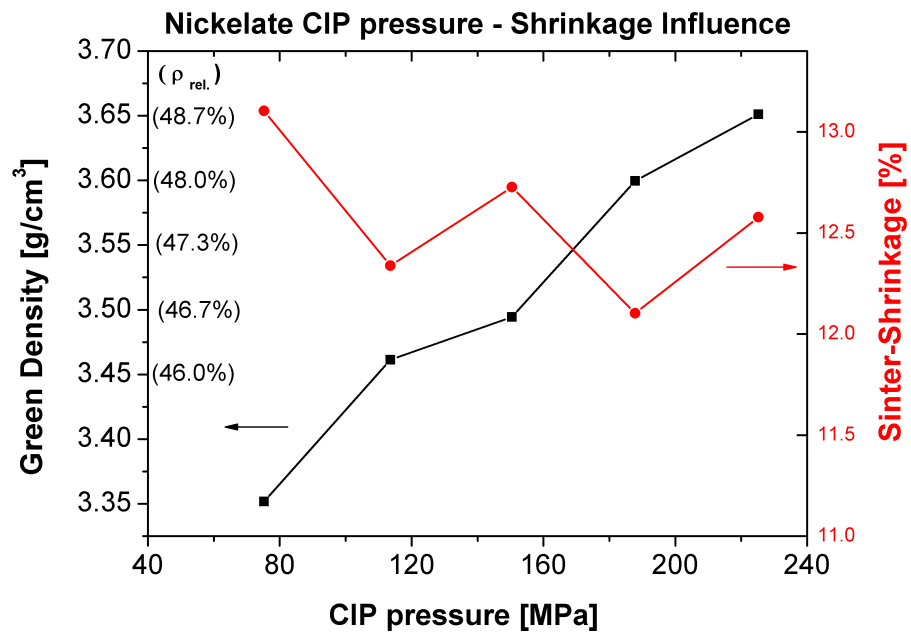


Figure 5.4: The green densities and sinter shrinkages of nickelate pellets prepared by CIP.

less particle contact, which leads to higher shrinkage during sintering. Pellets of neodymium nickelate were used for dilatometric measurements at EMPA, Duebendorf. A typical shrinkage curve for the NNO powder is shown in Figure 5.5.

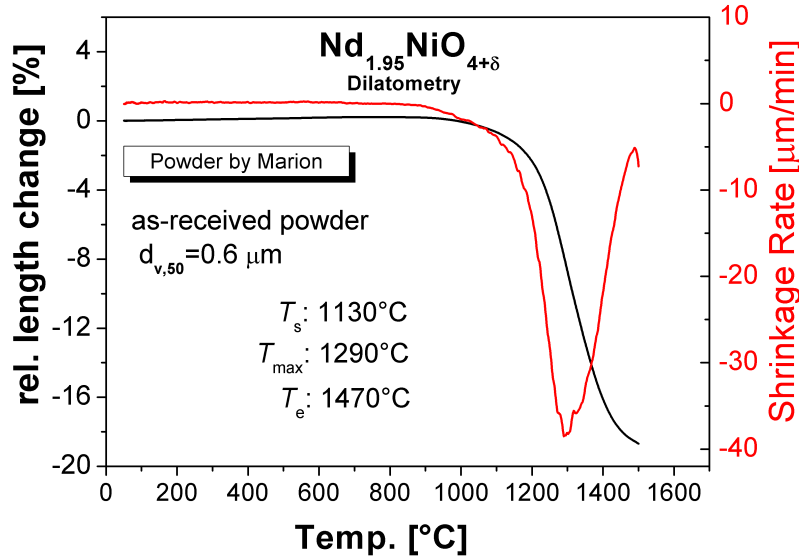


Figure 5.5: The shrinkage of neodymium nickelate pellets prepared by CIP.

5.2 Interlayer: Gadolinia-doped ceria (GDC)

5.2.1 Supply and Powder Characterisation

During the scope of this work, different GDC powders were used. All of them were 90 mol% CeO_2 - 10 mol% $\text{GdO}_{1.5}$, leading to the stoichiometry of $\text{Ce}_{0.9}\text{Gd}_{0.1}\text{O}_{1.95}$ which will be abbreviated 10GDC in this manuscript. The powder characteristics of the different 10GDC powders are summarised in Table 5.2. All GDC powders were received from SOFCPower, IT. The GDC

Table 5.2: Summary of different GDC-Powders used in this work.

$\text{Ce}_{0.9}\text{Gd}_{0.1}\text{O}_{1.95}$		Characteristics					
Supplier	Batch Nr.	Doping	used from	used until	$d_{v,50}$ [nm]	Span	SSA [m^2/g]
Nextech	159-064	-	07/2007	07/2009	960	4.3	16.9
Fuel Cell Materials	338-018	-	08/2009	11/2011	250	6.2	11.0
Fuel Cell Materials	338-018	1% Co	07/2011	11/2011	230	3.08	10.3
Fuel Cell Materials	338-018	2% Co	11/2010	11/2011	1870	61.6	10.0

powder from Nextech was only used until July 2009 as their fuel cell component segment, and hence powders as well, was taken over by Fuel Cell Materials and the powder no longer produced. The follow-up product to Nextech's 159-064 GDC powder by Fuel Cell Materials, Lot-Nr. 338-018, was used until the end of the work but has shown less sinter-activity than the former (cf. section 5.2.2), due to a lower specific surface area. It was therefore mixed at SOFCPower with different amounts of Cobalt as dopant to decrease its sinter temperature as reported in the literature [120]. As can be seen from Table 5.2, the Cobalt-doping process resulted in some agglomeration leading to poor dispersion and thin layers of poor packing. Ball-milling was used to break up the particle agglomerates, which will be described in more detail in the following section.

5.2.2 Dispersion and Shrinkage

In this section, results of particle dispersion, green and sinter densities as well as sinter shrinkage of the respective powders will be given for each powder individually as these parameters are key to successful fabrication.

10GDC 159-064, Nextech

For the first ca. two years of this project, 10GDC from Nextech Materials was used. It was first attempted to disperse 10GDC as an aqueous suspension with PAA dispersant.

In a first step, the PSD of 10GDC 159-064 was measured by Laser diffraction in the presence of water (solvent) and PAA-dispersant in excess with respect to values reported later. The result is shown in Fig. 5.6. A bimodal PSD was evidenced, with primary particles having a mode volume diameter of $d_{v,50}=210$ nm and agglomerates' of ca. $2.5\ \mu\text{m}$. The zeta-potential of 10GDC was measured in a 10^{-3}M solution of KNO_3 as a function of pH by titration. The titration agents to rise and lower the pH were $1\text{M NH}_4\text{OH}$ and 1M HNO_3 , respectively. The result is shown in Fig. 5.7.

The Isoelectric point (IEP) of ca. 8.1 coincides almost perfectly with results obtained on Ce-ZrO₂ solid solutions, which showed an IEP of 7.9 [121]. The pH in the range of 9-10 leads to effective negative surface charges. While a zeta-potential of -10 mV is rather low at pH=9.5 in terms of stabilisation, the addition of optimised amounts of PAA-dispersant increased the absolute value of the zeta-potential to up to -30 mV, the exact value however depended on the powder source, as different surface charges may have been present. As PAA at pH=9.5 has shown great ability to stabilise particles in suspension [122, 123, 124, 125], a 2.5 wt% suspension of 10GDC in 10^{-3}M solution of KNO_3 was titrated with 0.75 wt% PAA-solution. The suspension was adapted to the same pH as the PAA-solution before the addition of the latter. Results are shown in Figure 5.8. The specific surface coverage of PAA on GDC particles was calculated by using the specific surface area of 10GDC and the concentrations of 10GDC-suspension and PAA-solution. It can be seen that the adsorption of PAA significantly decreases the zeta-potential as it adds a negative charge to the GDC-surface. For PAA amounts $>1.15\ \text{mg PAA/m}^2$, the GDC surfaces are already completely covered by PAA polymer chains and its

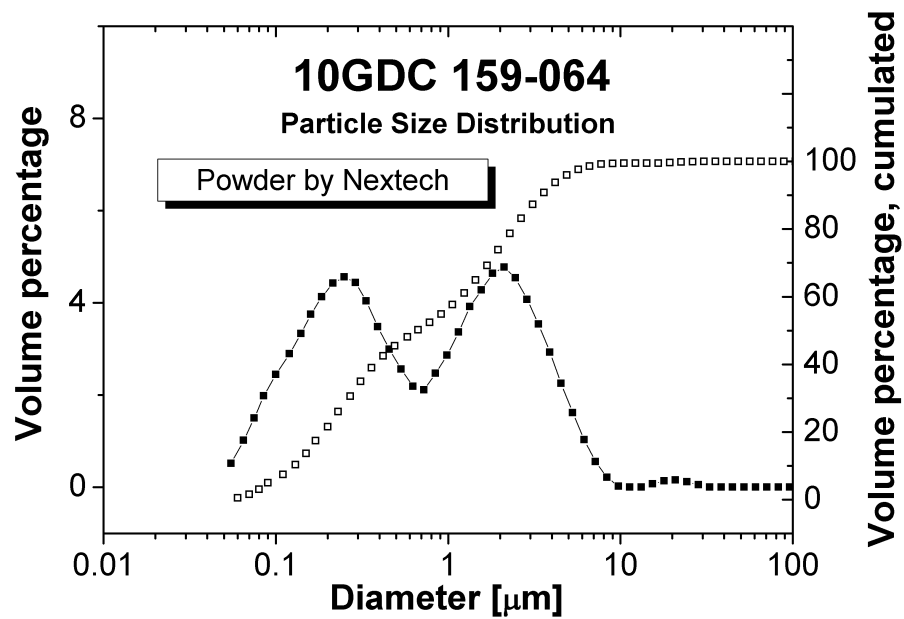


Figure 5.6: Particle size distribution (PSD) of 10GDC 159-064.

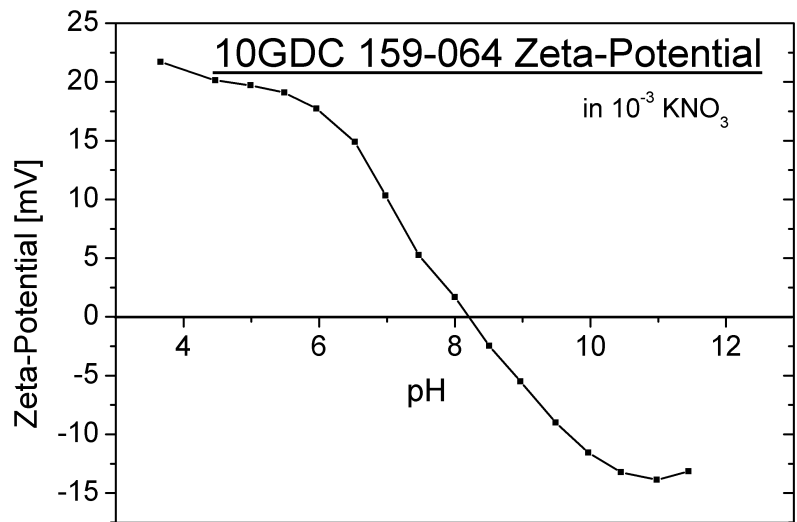


Figure 5.7: The zeta-potential of 10GDC as a function of pH, measured by Acoustosizer.

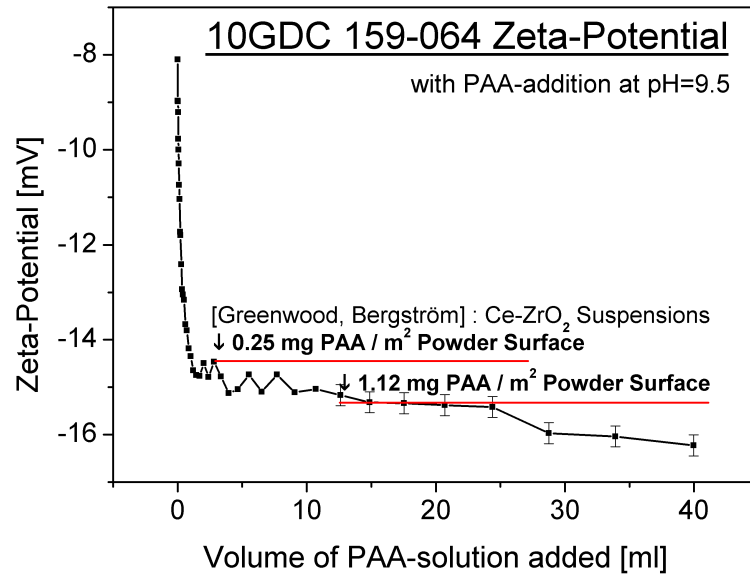


Figure 5.8: The zeta-potential of 10GDC under the addition of PAA-solution at pH=9.5, as measured by the Acoustosizer.

further addition doesn't alter the zeta-potential significantly anymore as the curve becomes a plateau, albeit somewhat sloped.

Greenwood et al. [121] investigated 13 mol%Ce-Zirconia suspensions and found specific PAA surface coverages of 0.25 mg/m² which coincides almost perfectly with the first signs of a plateau formation. For simulation purposes, a zeta-potential of -16 mV was assumed. This value was used for a simulation of colloidal stability following DLVO theory with the Hamaker software code. It included electrostatic attraction using the semi-empirical Gregory model, electrostatic repulsion using Hogg-Healy Fuerstenau equation and steric repulsion following Bergstrom's approach (cf. section 2.1). The parameters used for the simulation are shown in Table 5.3 and results of the simulation for 10GDC are shown in Fig. 5.9.

As the primary GDC-particles had a median volume diameter of 210 nm, it was chosen as the basis for the simulation. The unpublished Hamaker constant for 10GDC was assumed to be in the range of 10⁻²⁰ - 10⁻¹⁹ J, which is the typical range of Hamaker constants for inorganic solids [126]. However, the influence of the Hamaker constant on the results was found to be minimal. As one can see, the volume fraction of polymer in the adsorbed layer ϕ_2 in the range of 30-54 vol% doesn't change the shape of the curve significantly either. The results indicate that 10GDC is well-protected against agglomeration as the adsorbed PAA chains create a potential wall at ca. 10 nm of particle surface separation distance without the appearance of a potential minimum which would enable agglomeration. Pellets of 10GDC 159-064 were made by slip-casting of aqueous suspensions. The amount of added PAA-dispersant was 1.15 mg/m²

Table 5.3: Simulation parameters for colloidal stability of 10GDC using Hamaker V.2-2.

10GDC 159-064	attractive interaction, Gregory equation				
	A _H	a	b	λ ₀	ζ
	1*10 ⁻¹⁹ J	150 nm	5.32	100 nm	-16mV
	repulsive electrostatic interaction, HHF				
	I _C	d _ζ			
	10 ⁻² mol/l	4 nm			
	repulsive steric interaction, Bergstrom				
ϑ	ϕ ₂	χ			
5 nm	0.30-0.54	0.35			

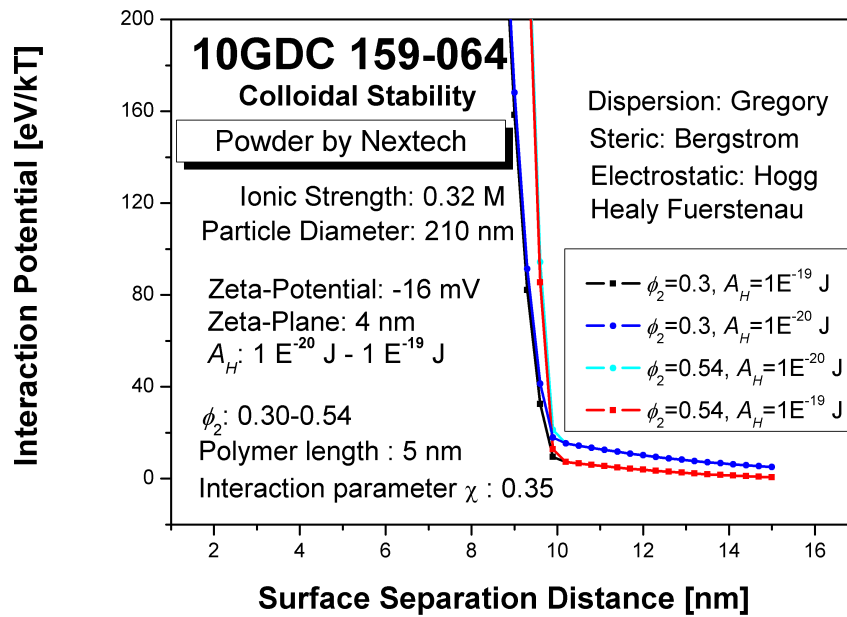


Figure 5.9: The total interaction potential of 10GDC particles including electrostatic and steric contributions.

5.2. Interlayer: Gadolinia-doped ceria (GDC)

as determined by the adsorption measurements mentioned before. 5 wt% of PVA-binder was added to achieve durable pellets by slip-casting. The green density, sinter density at 1300°C and sinter shrinkage are shown in Table 5.4. Green pellets prepared by cold-isostatic pressing were used for dilatometric measurements. The results are shown in Figure 5.10.

Table 5.4: Green and sinter density at 1300°C as well as shrinkage during sintering of 10GDC 159-064 pellets made by slip-casting of aqueous suspensions with PAA-dispersant and PVA-binder.

10GDC 159-064	Green density	Sinter density	Sinter Shrinkage
	55%	91%	12%

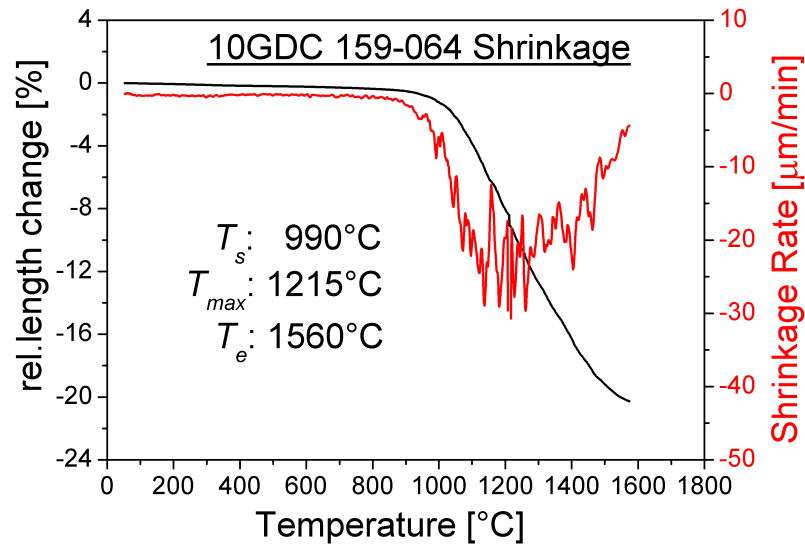


Figure 5.10: The sinter shrinkage of 10GDC 159-064 pellets measured by dilatometry.

10GDC 318-033, Nextech

After GDC 159-064 was no longer available, the work was continued with the follow-up product GDC 318-033 from Nextech. The dilatometric result for GDC 318-033 is shown in Fig. 5.11. For the sake of comparison, the shrinkage curve of GDC 159-064 is shown, too. GDC 318-033 is less sinter-active and shows consequently lower densities at sintering temperatures. The green and sinter density as well as sinter shrinkage of slip-cast pellets are shown in Table 5.5 on page 66. The amount of used PAA-dispersant was the same as for 10GDC 159-064, as their PAA-surface coverages were assumed to be equal. From table 5.5 it can be seen that the shrinkage during sintering as well as the final sintering density are rather low. While in cells with GDC/zirconia

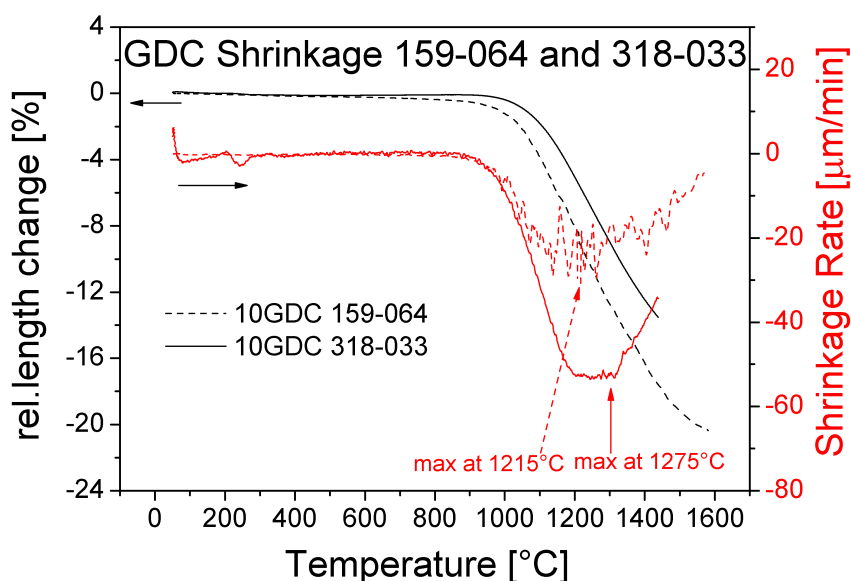


Figure 5.11: The sinter shrinkage of 10GDC 318-033 pellets measured by dilatometry. The shrinkage of 10GDC 159-064 is shown for comparison

double electrolyte layer structure the GDC interlayer does not necessarily need to be dense, substantial porosity can lead to enhanced degradation phenomena by diffusion through the porous interlayer [127].

Furthermore, the sinter shrinkage of 12% was much smaller than for scandia-stabilised zirconia (ScSZ, cf. section 5.3), which is inconvenient for cosintering. It was hence attempted to increase the sinter-activity by attrition-milling. Therefore, batches of ca. 100 g of powder with ca. 100 ml of aqueous PAA-solutions were milled for 3 hours at 1500 rpm. The change of the particle size distribution is shown in Figure 5.12. The attrition-milled powder was slip-cast to measure densities and shrinkage again. The results are shown in Table 5.5 on page 66. From Figure 5.12 and Table 5.5, it becomes clear that the attrition-milled (AM) powder yields higher green and sinter densities as the agglomerates are broken down by the milling process. However, the sinter shrinkage does not increase significantly as both green and sinter density are simply shifted to higher values. The shrinkage of slip-cast pellets of both as-received and attrition-milled GDC is shown in Figure 5.13. The temperature of maximum shrinkage rate decreased from 1275 to 1200°C for attrition-milled powder. In order to obtain higher sinter densities, doping with Cobalt was performed at SOFCPower, Italy. As 2wt% Co-doped powder was received first, it will be presented in the next section.

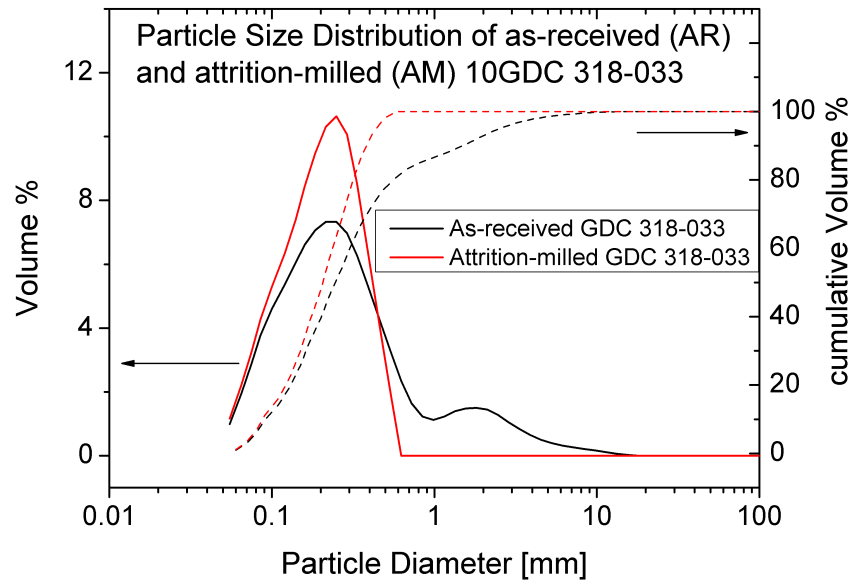


Figure 5.12: The particle size distribution of 10GDC 318-033 in as-received and attrition-milled state.

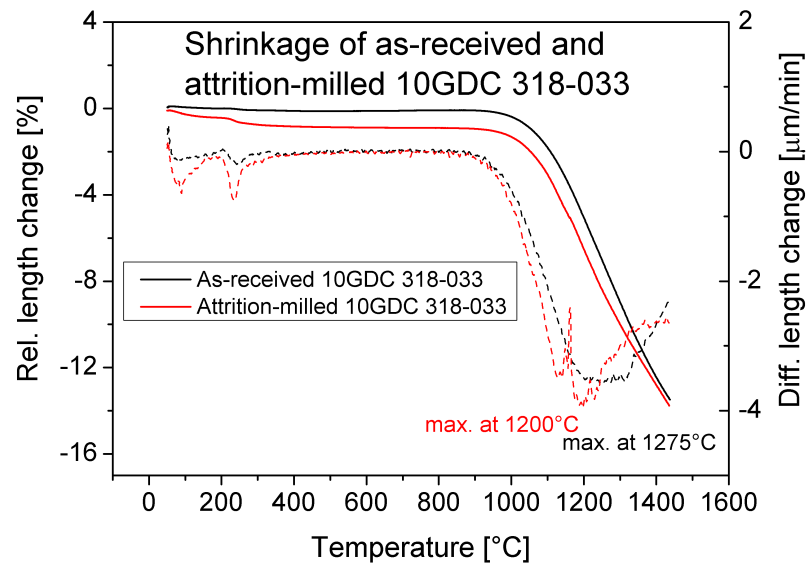


Figure 5.13: The shrinkage of 10GDC 318-033 in as-received and attrition-milled state, measured by dilatometry (at EMPA).

10GDC 318-033, Nextech + 2wt% Co(GDC-2CD)

The particle size distribution of as-received powder is shown in Figure 5.14. As-received powder shows primary particle sizes of ca. 250 nm as well as smaller agglomerates of ca. 1-30 μm particle size and larger agglomerates of a particle diameter of 50-200 μm . The shrinkage

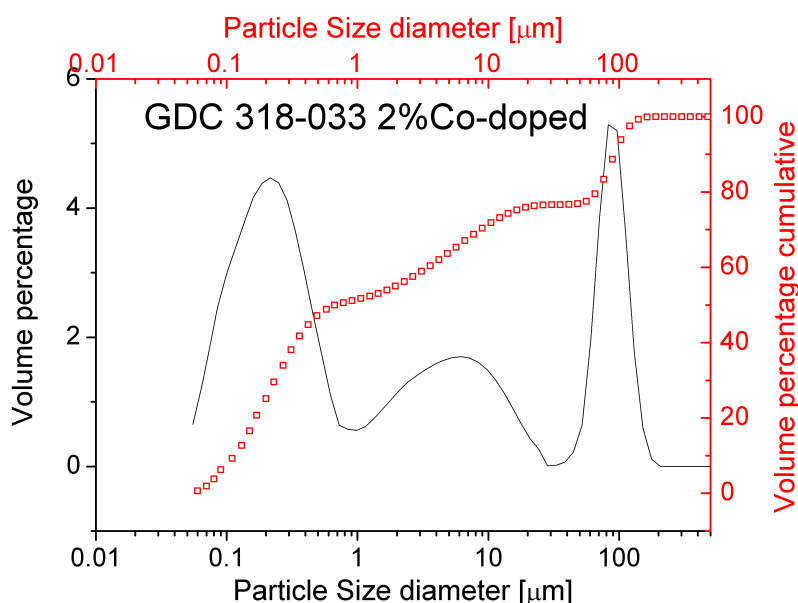


Figure 5.14: The particle size distribution of as-received 2 wt% Cobalt-doped GDC.

of compacted GDC-2CD pellets is shown in Fig. 5.15 and compared to undoped GDC. The sintering temperature drastically decreased for the Cobalt-doped powder. This phenomenon is already described in the literature as being related to transient liquid phase sintering of Co_3O_4 and subsequent formation of a Co-Ce solid solution [120]. The green and sinter density as well as sinter shrinkage of pellets of 2 wt% cobalt-doped and undoped 10GDC prepared by CIP is shown in Table 5.5. From Table 5.5 and Figure 5.15 it becomes clear that while Co-

Table 5.5: Green and sinter density at 1300°C as well as shrinkage during sintering of undoped and 2 wt% Cobalt-doped 10GDC pellets made by slip-casting of aqueous suspensions with PAA-dispersant and PVA-binder.

10GDC 318-033	Green density	Sinter density	Sinter Shrinkage
undoped AR	47%	86%	12%
undoped AM	50%	90%	13%
2 wt% Co-doped AR	55%	95%	13%

doping does decrease the sintering temperature of 10GDC, its total sinter shrinkage in water

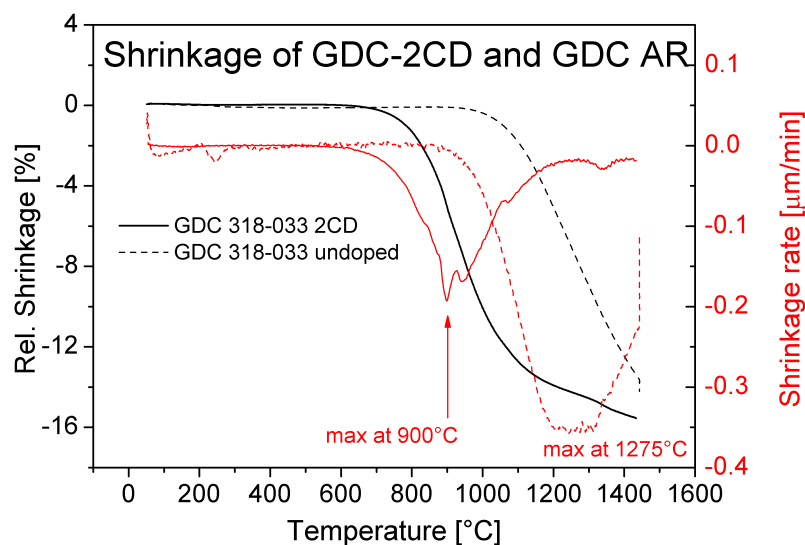


Figure 5.15: The shrinkage of 2 wt% cobalt-doped and undoped 10GDC 318-033, measured by dilatometry (at EMPA).

solvent with PAA-dispersant is not altered significantly. Therefore, it was attempted to lower the green density by choosing a less efficient dispersant in order to slightly "destabilise" the powder particles and to increase the total sinter shrinkage. Slip-casting was performed again with GDC-2CD with the three dispersants TEA, TX and TI for organic solvents. Suspensions of 10 vol% solid load with 2 wt% dispersant content and 2 wt% of PVB binder with ethanol and isopropanol respectively were made and slip-cast. The green and sinter densities were again measured, the results are shown in Table 5.6. Triton X 100(Tx) and Triolein(TI) are poor

Table 5.6: Green and sinter density at 1300°C as well as shrinkage during sintering of 2wt% Cobalt-doped 10GDC pellets made by slip-casting of suspensions in organic solvents with different dispersants.

GDC-2CD	Green density	Sinter density	Sinter Shrinkage
Tx - Eth	36%	75%	24%
Tx - Iso	39%	78%	22%
TI - Eth	39%	73%	22%
TI - Iso	36%	66%	19%
TEA - Eth	42%	85%	20%
TEA - Iso	49%	91%	18%

dispersants as the densities before and after sintering are rather low. For all three dispersants in both organic media, the sinter shrinkage is much greater than for water-based suspensions.

The sinter shrinkage of 10GDC was tried to match with the shrinkage of ScSZ-powder. As ScSZ from Treibacher, dispersed in aqueous PAA-solution, shrinks ca. 18% until 1300°C (cf. section 5.3.3), this very shrinkage was targeted for GDC as well. TEA-dispersant in isopropanol was chosen as the most promising candidate as the shrinkage coincided well and the green and sinter density were the highest among the candidates tested. The measurements were repeated for different amounts of PVB binder. Results are shown in Table 5.7. The density and shrinkages do not vary significantly in the tested range of binder concentration. This is important for dip-coating of GDC, where different amounts of binder generally ≤ 5 wt% were used.

Table 5.7: Green and sinter density at 1300°C as well as shrinkage during sintering of 2 wt% Cobalt-doped 10GDC pellets made by slip-casting of suspensions in isopropanol with 2 wt%TEA-dispersant and different amounts of PVB-binder.

GDC-2CD	Green density	Sinter density	Sinter Shrinkage
TEA-Iso-2%PVB	49%	92%	18%
TEA-Iso-3%PVB	48%	91%	18%
TEA-Iso-4%PVB	49%	92%	19%

10GDC 318-033, Nextech + 1 wt% Co(GDC-1CD)

The difference between the temperatures T_s of the sintering process of GDC- and ScSZ-layers should be as small as possible in order to minimise thermal stresses. In Figure 5.16, the shrinkage curves of ScSZ TR, 10GDC318-033 AR and GDC-2CD are presented. It can be seen that T_s of ScSZ is between those of 10GDC318-033 AR and GDC-2CD. In order to further approach the temperatures T_s of GDC and ScSZ, another batch of 10GDC 318-033 with 1 wt% Co-doping was prepared by SOFCPower. The shrinkage curve of GDC-1CD is shown and compared to the shrinkage of GDC-2CD, undoped 10GDC 318-033 and ScSZ TR in Figure 5.17. The lower doping amount of 1 wt% of Cobalt visibly only shifted the shrinkage curve to slightly higher temperatures.

Still, GDC-1CD was the closest material to ScSZ TR in terms of shrinkage behaviour and was therefore used in the preparation of single cells for cells with GDC/ScSZ double layer electrolyte (cf. chapter 9).

5.2.3 Dip-Coating of GDC

GDC-suspensions were dip-coated directly onto the tubular nickelate substrates and typically consisted of 5 vol% particles, 2 wt% dispersant and ca. 5 wt% binder. For the most part of the work, aqueous suspensions of GDC with PAA-dispersant and PVA-binder were used. An example of a deposited and sintered GDC-layer from an aqueous suspension is shown in Fig. 5.18. Even though green and sintered layers seemed well-deposited and densified in

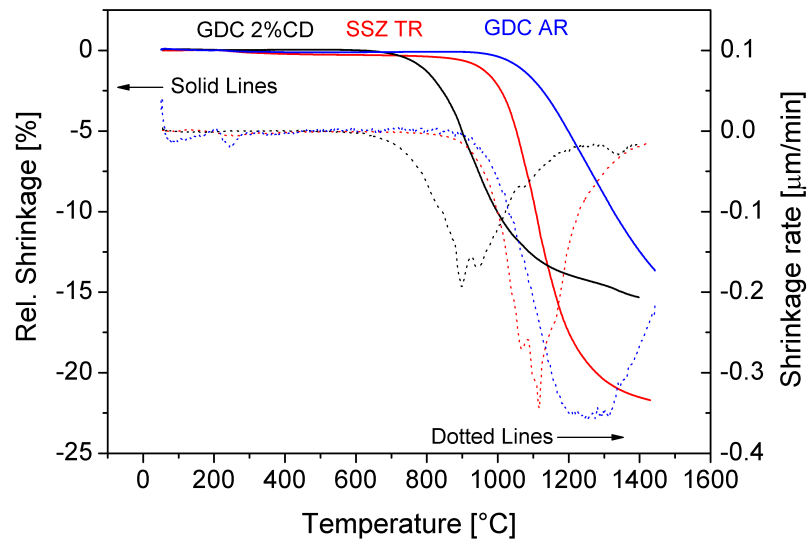


Figure 5.16: The shrinkage of 10GDC 318-033, GDC-2CD and SCSZ TR, all measured by dilatometry at EMPA.

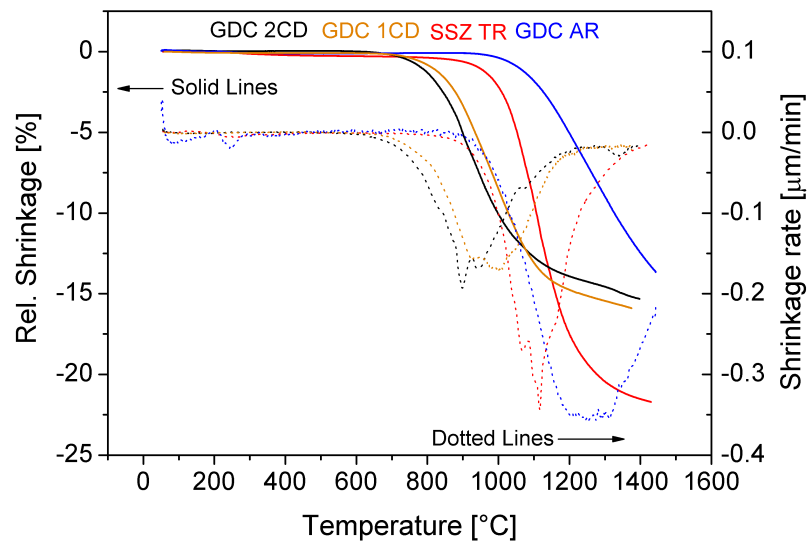


Figure 5.17: The shrinkage of GDC-1CD, compared to GDC-2CD, 10GDC 318-033 AR and ScSZ TR, measured by dilatometry (at EMPA).

cross-section images (Fig. 5.18a), surface cracks were found for different amounts of binder (Fig. 5.18b) and could not be completely eliminated. Consequently, pressure loss results

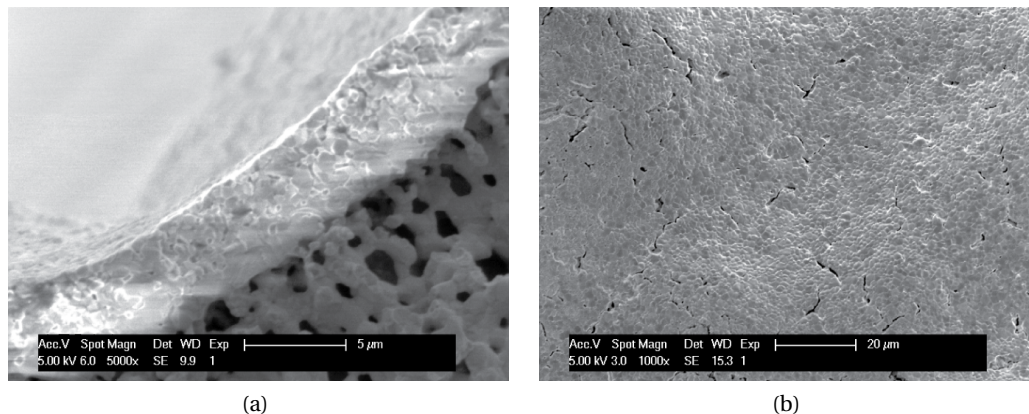


Figure 5.18: A typical GDC layer deposited from an aqueous suspension. (a) Cross-section of the layer. (b) Surface cracks of the GDC layer

stayed modest. Deposited ScSZ-layers on top of GDC-layers possessing surface cracks were themselves cracked or at least disturbed in their particle packing which led to insufficient pressure loss results of GDC/ScSZ double layers. Typically, the pressure loss constant κ of sintered GDC/ScSZ double layers was higher(worse) than for single GDC-layers due to perpetuation of surface cracks into the next layer and due to differences in sinter temperatures which led to reduced sinter shrinkage and hence substantially constrained sintering.

It was found in the latter part of this work that GDC-layers dip-coated from suspensions with organic solvents were deposited more homogeneously and were less cracked. This may be a result of lower surface tension of ethanol and isopropanol compared to water, which leads to lower drying stresses. The higher viscosity of isopropanol with respect to water may also play an important role as different tube types possessed surface roughness on the scale of the thickness of the deposited layer, i.e. several micrometers.

Calculations of the stresses of a drying GDC-layer were made for the three different solvents water, ethanol and isopropanol by using the equations 2.20 to 2.22. The median particle size diameter $d_{v,50}$ and the specific surface area (SSA) were taken as 250 nm and 11 m²/g respectively in the calculation (as shown in Table 5.2). The surface tensions of the solvents are taken from Table 4.1 and the evaporation rates from Table 4.3. The green densities of particles in the respective solvent were taken from the measured green densities of slip-casted pellets. The Poisson ratio N was estimated to be 0.2. The ratio of pore radius to particle diameter was taken as 0.47, as it is given for random loose packed particle of log-normal distribution [11]. The green layer thickness was taken as 10 μm. The calculation results are shown in Table 5.8. The drying stress of layers dip-coated from isopropanol-based suspensions and dried at even relatively dry conditions is equal to the drying stress of layers coated from water-based suspensions and dried at 20°C and 90%RH. While it cannot be excluded that cracks formed

5.2. Interlayer: Gadolinia-doped ceria (GDC)

Table 5.8: Drying stresses of a GDC-layer of 10 micrometer thickness for different solvents.

Temp.	RH	System	ρ_{green}	$\sigma_{\text{drying}}[\text{Pa}]$
22°C	24%	TEA-Isopropanol	49%	$6.8 \cdot 10^5$
20°C	30%	PAA-Water	55%	$2.5 \cdot 10^6$
20°C	50%	PAA-Water	55%	$1.8 \cdot 10^6$
20°C	70%	PAA-Water	55%	$1.1 \cdot 10^6$
20°C	90%	PAA-Water	55%	$6.8 \cdot 10^5$

during the short transition time between dip-coating and completed transfer of the tubes to the drying chamber, it seems more likely that the cracks visible on the surface of GDC-layers dipped from water-based suspensions are linked to the higher viscosity and lower surface tension of isopropanol compared to water, especially in view of the tube surface roughness.

In Figure 5.14, the particle size distribution of GDC-2CD was shown. The consequence of this multimodal distribution for dip-coating can be seen in Figure 5.19. During the preparation of GDC-suspension for dip-coating, particles of different sizes separate as bigger agglomerates sink to the bottom, see Fig. 5.19a. The tubes that were dip-coated in this suspension type and afterwards sintered were curved which indicates that the layer's green density was not homogeneously distributed and hence the layer shrank differently at different positions along the tube axis as can be seen in Fig. 5.19b.

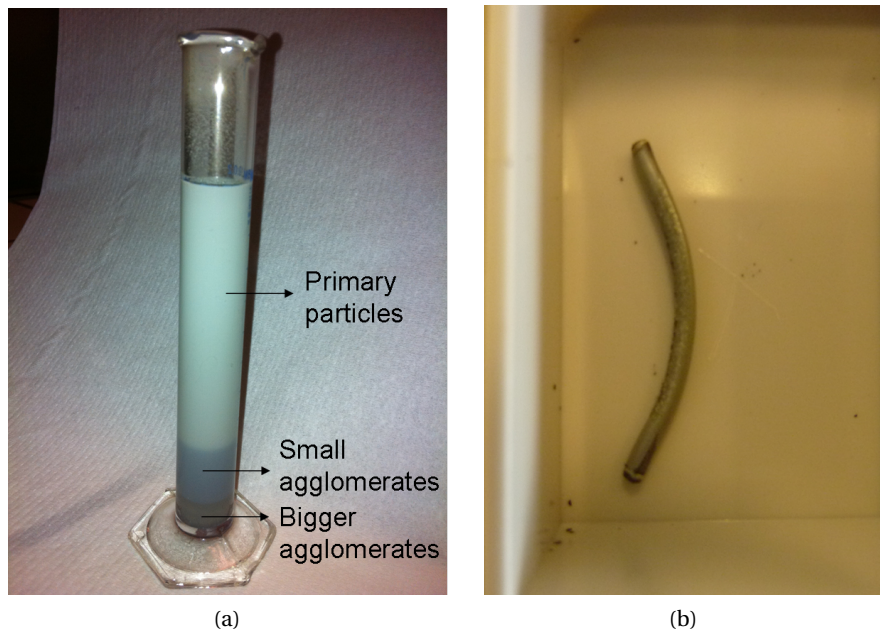


Figure 5.19: Co-doped 10GDC with differently sized agglomerates. (a) Sedimentation effect due to broad particle size distribution. (b) Resulting curved tubes due to different shrinkages

This problem was resolved by performing ball-milling for ca. 24 hours prior to dip-coating. The wet ball-milling was performed in isopropanol and 2 wt% TEA-dispersant with spherical zirconia milling media of 5 and 10 mm diameter. The particle size distribution and specific surface area of as-received, shortly milled (1 hour) and 24h-milled GDC-2CD is shown in Figure 5.20.

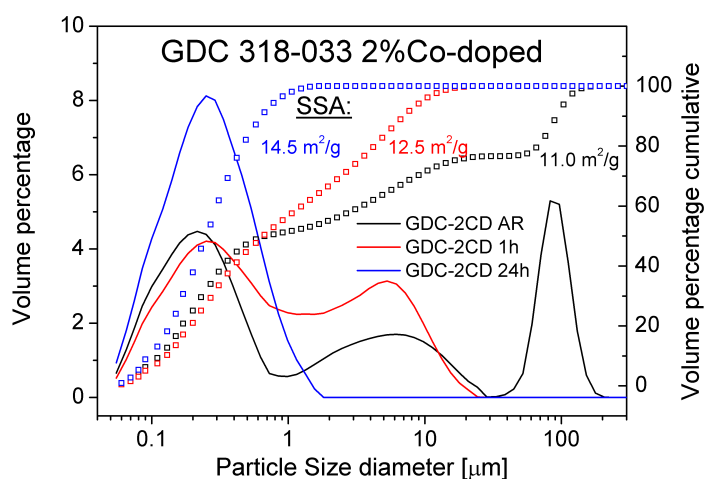


Figure 5.20: The particle size distributions and specific surface areas of GDC-2CD in as-received and different milling states.

GDC-2CD and GDC-1CD powders that were milled for 24 h in 5 and 10 mm zirconia milling media showed a monomodal size distribution whereas short milling durations only removed the biggest agglomerates. Tubes dip-coated in suspensions with sufficiently milled powder particles were no longer curved after sintering, or to a much lesser extent. Furthermore, the pressure loss constants κ were much reduced (slower pressure loss) for layers of ball-milled ceria powders than for layers of as-received powders when both were deposited from the same isopropanol-based suspension. Typically the milling was performed with both GDC-1CD and GDC-2CD powders in isopropanol with TEA-dispersant. The PVB-binder was only added after the milling process as milling media can damage the lengthy polymer chains of the binder.

The specifics of the suspensions that were finally used for dip-coating of GDC suspensions were:

- GDC particles, milled for 16-24 h in 2 wt% of TEA-dispersant and isopropanol with spherical zirconia milling media of 5 and 10 mm sphere diameter
- 5 wt% of PVB-binder which was added only after the milling but prior to dip-coating and
- additional isopropanol to adapt the amount of GDC particles to 5-7 vol%.

The dip-coating was performed only once per tube with 300 mm/min of withdrawal speed. The cross-section of a typical GDC-layer deposited in this manner is shown in Figure 5.21. Its thickness after sintering was approximately 6-8 μm and its microstructure appeared to

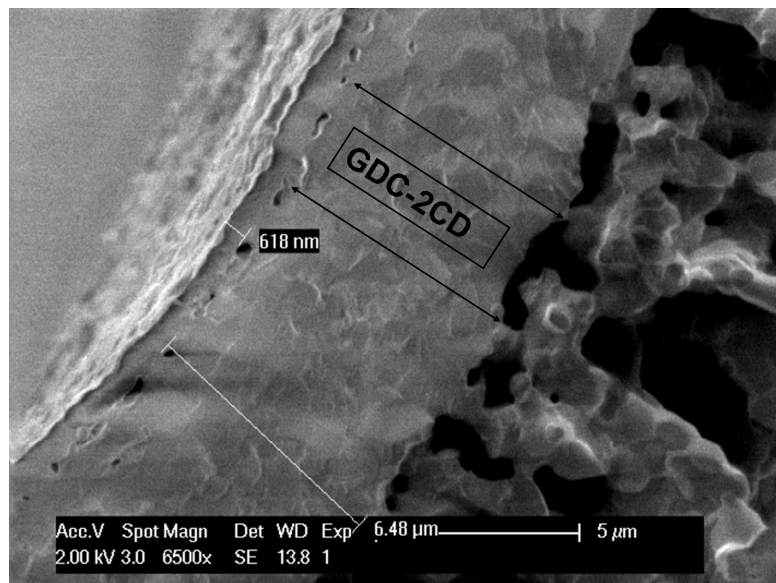


Figure 5.21: A cross-section of a typical deposited and sintered GDC-2CD layer from an isopropanol-based suspension.

be rather dense. While the median volume diameter $d_{v,50}$ of milled particles was slightly smaller than the average surface pore diameter of most tube types (cf. chapter 6), they did not penetrate significantly into the pores when isopropanol-based suspensions were used except for tubes of type CIP-ZARA, which had distinctly greater surface pores of ca. 3 μm diameter and hence twice as big as the biggest particles after milling.

This may be due to the higher viscosity of isopropanol compared to water, as penetration into pores was observed for all tube types using water-based suspensions. This penetration endangers the homogeneity of the deposited green layer and may lead to defects such as pinholes and cracks. Pressure loss results of a single GDC-layer deposited from water-based and isopropanol-based GDC-2CD suspension are shown in Figure 5.22. It can be seen that the pressure loss for isopropanol-based suspensions is much slower and hence the layer has higher density and less defects.

5.3 Electrolyte: Scandia-stabilised zirconia (ScSZ)

In this section, the different ScSZ-powders that were used in this work are described. While the GDC interlayer was targeted to be as dense as possible, a residual porosity is acceptable. The zirconia electrolyte layer imperatively needs to be gas-tight after cofiring for the cell to establish a correct OCV due to successful gas compartment separation. Therefore, the shrinkage of the ScSZ-layer is of utmost importance for the fabrication route of single cells

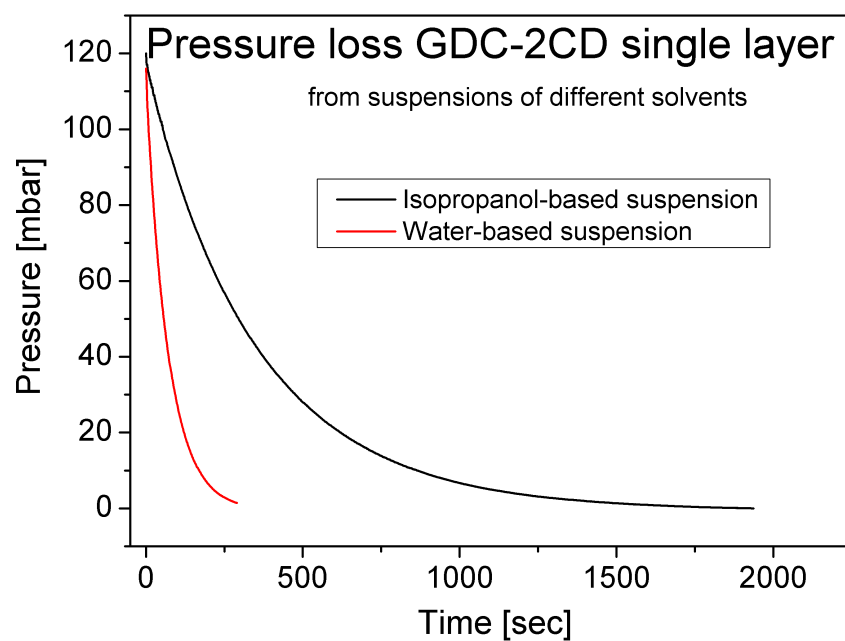


Figure 5.22: Pressure loss of GDC-2CD layer from an isopropanol-based suspension.

5.3. Electrolyte: Scandia-stabilised zirconia (ScSZ)

and the shrinkage of GDC-interlayers was adapted as described to match the shrinkage of ScSZ layers as accurately as possible.

For all powders, the nominal composition is 89 mol% ZrO_2 - 10 mol% Sc_2O_3 - 1 mol% CeO_2 , which is equivalent to the stoichiometry $\text{Zr}_{0.81}\text{Sc}_{0.18}\text{Ce}_{0.01}\text{O}_{1.91}$. The different powders and their principal characteristics are shown in Table 5.9. DKKK is an abbreviated form of Daiichi Kigenso Kagaku Kogyo, Japan. The ScSZ powder from Praxair had been used for the most part of the thesis until it was determined inapplicable for co-sintering at 1300°C as shown further below. Afterwards, ScSZ-powders from DKKK and Treibacher were obtained and tested, of which especially the Treibacher powder was used.

Table 5.9: Summary of different ScSZ-Powders used in this work.

$\text{Zr}_{0.81}\text{Sc}_{0.18}\text{Ce}_{0.01}\text{O}_{1.91}$		Characteristics				
Supplier	Batch Nr.	used from	used until	$d_{v,50}[\text{nm}]$	Span	SSA [m^2/g]
Praxair	03-P5978BM	07/2007	12/2010	1030	1.2	11.8
DKKK	B2203	02/2011	11/2011	770	1.9	10.0
Treibacher	EA80/10.1	02/2011	11/2011	210	1.7	14.7

5.3.1 10ScSZ from Praxair (ScSZ PR)

The particle size distribution of as-received powder is shown in Fig. 5.23. A monomodal size distribution of particles centered around a peak at ca. $1\ \mu\text{m}$ of particle diameter can be seen. The particles are reported to be presintered agglomerates [128] which were probably

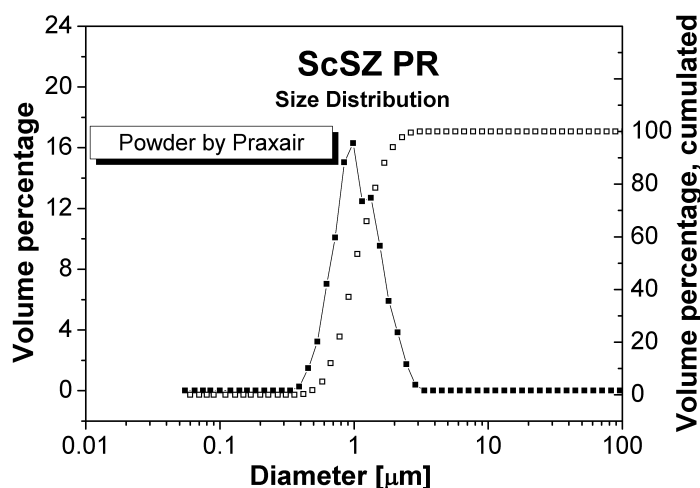


Figure 5.23: The particle size distribution of as-received ScSZ PR.

formed during Praxair's combustion spray pyrolysis process. An SEM-image of particles of the as-received ScSZ PR-powder is shown in Fig.5.24. It can be seen that it mainly consists of flake-like particles of irregular edged shape. The green and sinter density as well as sinter

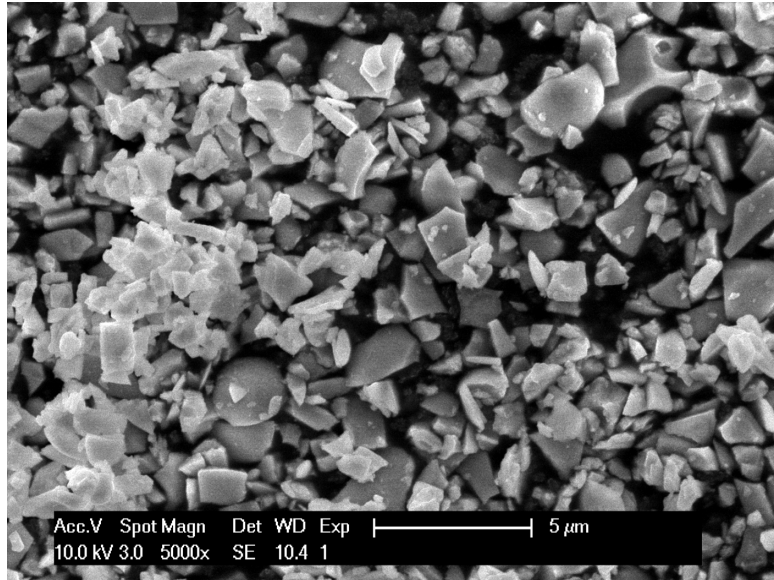


Figure 5.24: SEM-Image of as-received ScSZ PR particles.

shrinkage is shown in Table 5.10. As the powder densified poorly, ways to increase the sinter-activity were investigated.

Table 5.10: Green and sinter density at 1300°C as well as shrinkage during sintering of as-received ScSZ PR made by slip-casting of aqueous suspensions with PAA-dispersant and PVA-binder.

ScSZ PR	Green density	Sinter density	Sinter Shrinkage
AR	47%	78%	17%

Attrition-milling was used to decrease the particle size and to increase the specific surface area. For attrition-milling, the correct amount of dispersant had to be added to the slurry before the milling process in order to help to stabilise newly created surfaces. PAA-adsorption measurements were performed to measure the zeta-potential as a function of particle surface coverage. Therefore, a pH had to be defined as working condition. The zeta-potential of ScSZ PR in a 2.5 wt% suspension in 10^{-3} M KNO_3 as a function of pH is shown in Fig. 5.25. Here, the pH was changed by the addition of 1M HNO_3 and 1M KOH . The natural IEP of ScSZ PR is at pH=8, which is slightly higher than what Shojai et al. [122] have reported for 3Y-ZrO₂ powders in water. As PAA at R=1.5 has pH=9, the ScSZ-particle surfaces are slightly negatively charged. The adsorption of PAA-molecules then shifts the IEP to the acidic region, as reported elsewhere [129], and the zeta-potential is changed to strongly negative values in the examined region of pH=8-12, as can be seen in Fig. 5.26.

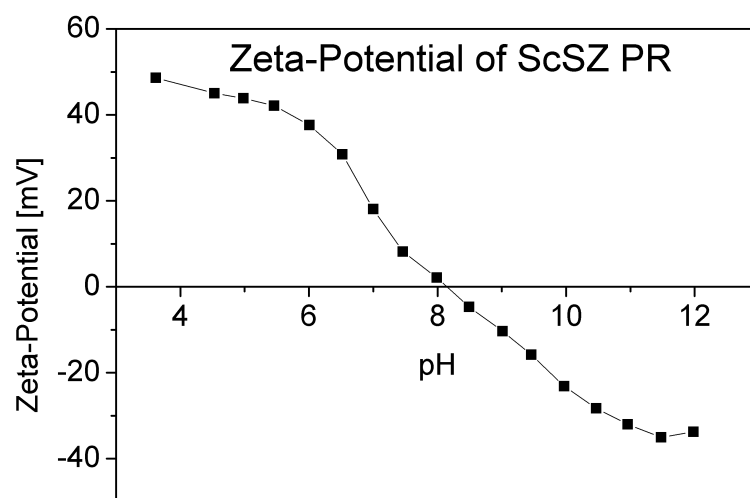


Figure 5.25: The zeta-potential of ScSZ PR in KNO₃-solution as a function of pH.

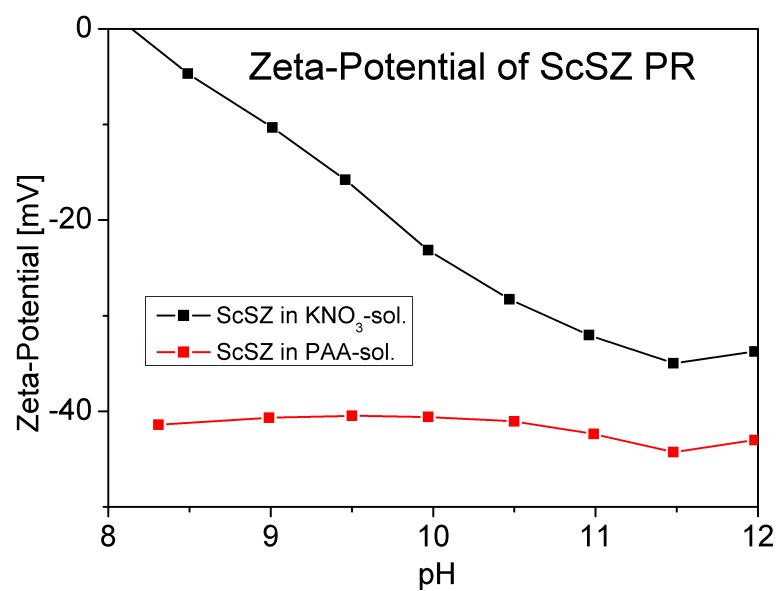


Figure 5.26: The zeta-potential of ScSZ PR in PAA-solution as a function of pH.

As a next step, the amount of PAA necessary to stabilise the particles by complete surface coverage was measured. Therefore, a 2.5 wt% suspension of ScSZ PR in KNO_3 -solution was brought to the natural pH of a 0.5 wt% aqueous PAA-solution with $R=1.5$, hence $\text{pH}=9$. After both liquids were at the same pH, the ScSZ-PR suspension was titrated with PAA-solution and the zeta-potential monitored. The results are shown in Fig. 5.27. A plateau is reached

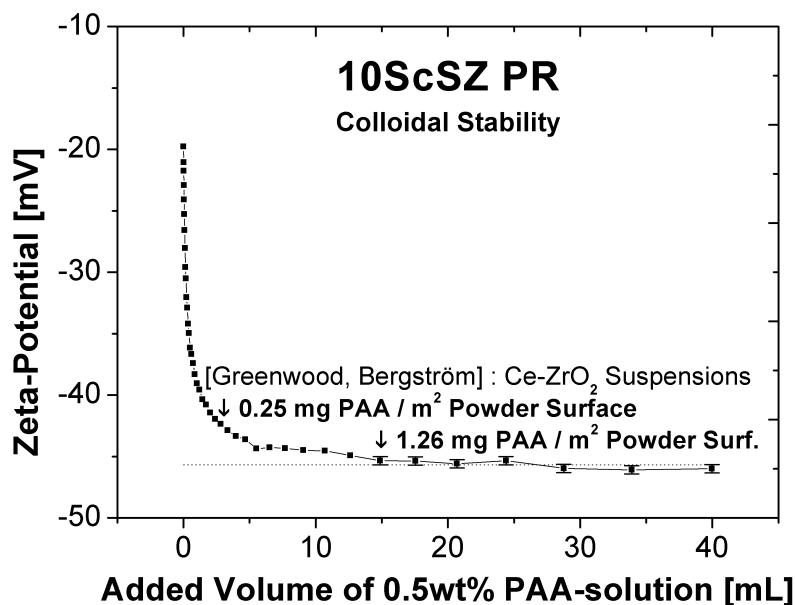
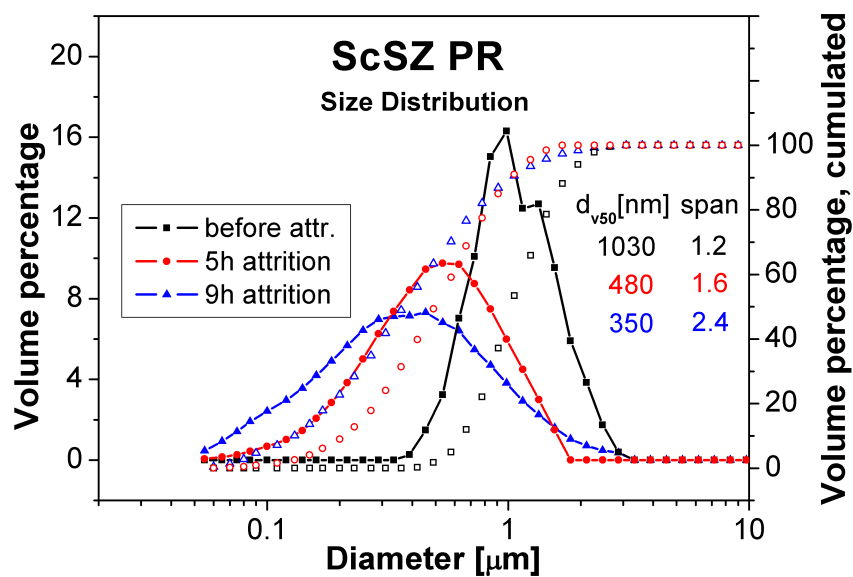


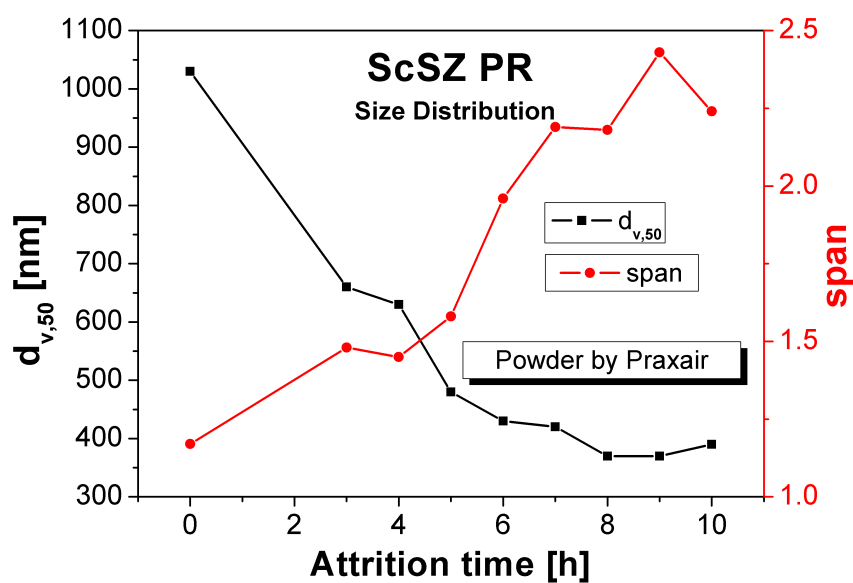
Figure 5.27: The zeta-potential of aqueous ScSZ PR-suspension with added PAA-solution.

after all the available adsorption sites are covered with PAA-molecules. The necessary specific PAA-concentration is 1.26 mg of PAA / m^2 of particle surface area and therefore higher than the 0.25 mg/m^2 that Greenwood [121] found for Ce-ZrO₂ suspensions.

The PAA-concentration to stabilise ScSZ PR-surface was used to perform attrition-milling. Per batch, 100-150 g of powder were milled with the respective amount of PAA. Water was added to bring the solid load to 50 wt%. After different times of milling, samples were taken and the particle size distribution measured. The results are shown in Fig. 5.28. Suspensions of attrition-milled ScSZ after 5 and 9 hours were slip-cast to pellets to monitor the development of densities and shrinkage as a function of milling duration and sinter temperature. The results are shown in Table 5.11. Milling durations of 9 hours were necessary to achieve sufficient densities for gas-tight layers. The shrinkage generally increased with the sintering temperature and reaches 20% for 1300°C and 9h milled particles. Cross-sections of slip-cast and sintered pellets of 5h and 9h milled ScSZ PR powder particles are shown in Figure 5.29. The theoretical density of ScSZ PR was taken as 5.76 g/cm^3 , which is based on theoretical cell occupation and lattice parameter. However, as the real composition of the powder can deviate from the theoretical one [128], this may be a source of error. Ray [128] has investigated several aspects



(a)



(b)

Figure 5.28: Particle size distribution of attrition-milled ScSZ PR (a) Distribution before and after 5 hours and 9 hours of attrition-milling. (b) Development of d_{v50} and span with the milling process.

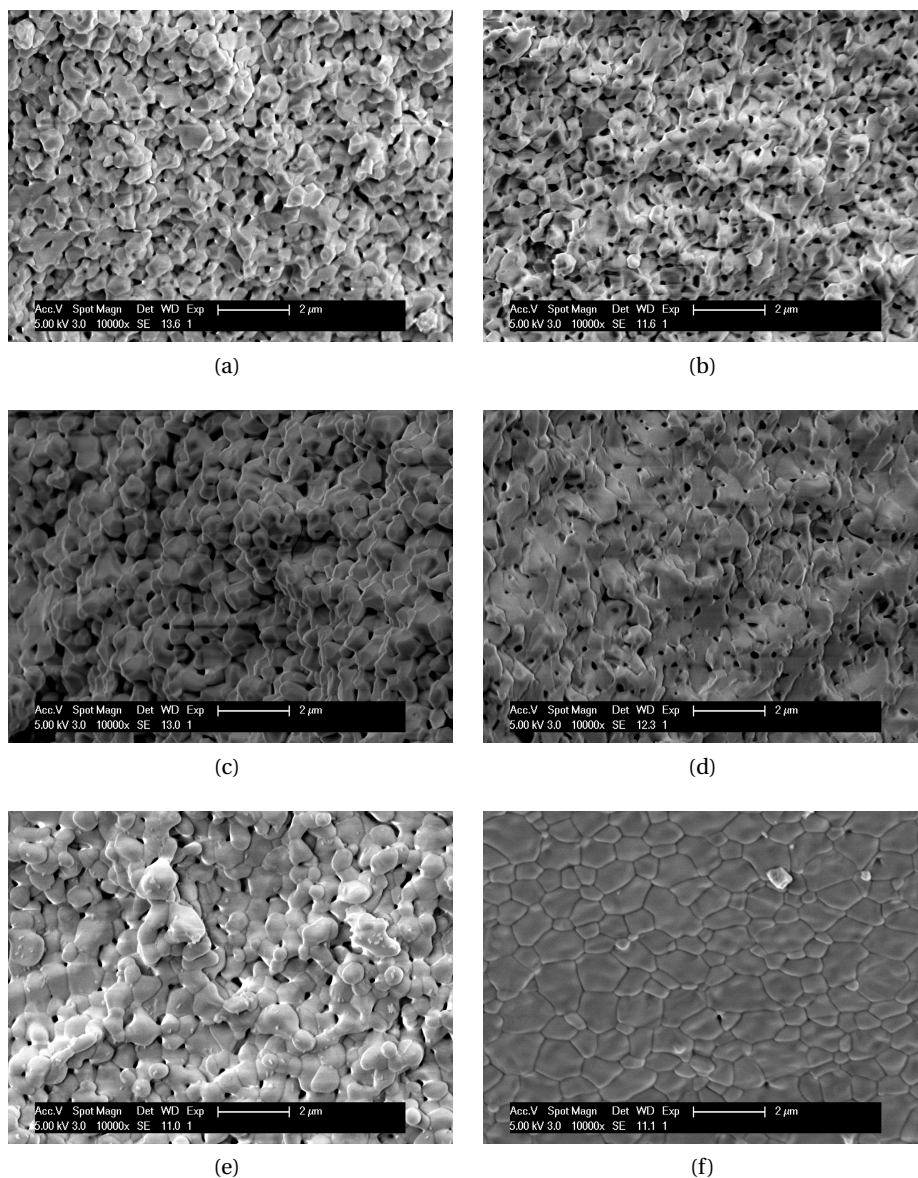


Figure 5.29: SEM cross-section images of attrition-milled ScSZ PR (a)5h milled, sintered at 1200°C. (b)9h milled, sintered at 1200°C. (c)5h milled, sintered at 1250°C. (d)9h milled, sintered at 1250°C. (e)5h milled, sintered at 1300°C. (f)9h milled, sintered at 1300°C.

5.3. Electrolyte: Scandia-stabilised zirconia (ScSZ)

Table 5.11: Green and sinter density at 1200-1300°C as well as shrinkage during sintering of as-received ScSZ PR made by slip-casting of aqueous suspensions with PAA-dispersant and PVA-binder.

ScSZ PR	ρ_{green}	$\rho_{1200^\circ\text{C}}$	$\rho_{1250^\circ\text{C}}$	$\rho_{1300^\circ\text{C}}$	Sinter Shrinkage
AR	47%			78%	17%
5h	51%	82%			16%
5h	51%		85%		17%
5h	51%			86%	17%
9h	50%	92%			18%
9h	50%		93%		19%
9h	50%			96%	20%

of ScSZ powders by Praxair and DKKK and found differences in chemical composition between the two powders leading to calculated full densities of 5.48 gcm^{-3} for powder by Praxair due to higher concentration of scandia and 5.76 gcm^{-3} for powder from DKKK.

The intense mechanical treatment in chemical aggressive conditions due to the presence of NH_4OH to establish the pH for PAA-solution can induce reactivity of the zirconia surfaces. In Figure 5.30, the dilatometric curves of as-received and attrition-milled ScSZ PR are shown. It can be seen that an abnormal shrinkage at temperatures below the sintering process exists for milled powder and shifts to lower temperatures with increasing milling duration. Already in the as-received powder, interaction with PAA seems to cause some shrinkage starting at $T_s=630^\circ\text{C}$. This is supplemented by some additional shrinkage from ambient temperature to 400°C for powder milled for 5 hours. For powder milled during 9 hours, a first steep mass decline until 400°C can be seen, followed by a steady decrease from 400°C to 1000°C before the sintering begins. As the decline clearly increases with the milling duration, it must be some zirconia surface reaction product which is formed during the milling process and decomposes at low temperatures.

The sintering of attrition-milled powder is also associated with an abnormal mass loss. A thermo-gravimetric analysis (TGA) further investigated this phenomenon. The result is shown in Fig. 5.31. The different regions, weight losses and possible explanations are shown in Table 5.12. It is very likely that the attrition-milling triggers a surface reaction according to equation 5.3.



The instability of ScSZ in PAA leading to abnormal shrinkage at low temperatures is problematic for cosintering, as the deposited ScSZ layer tries to shrink at temperatures where the adjacent layers do not shrink which leads to delaminations and cracks. An example is shown in Fig. 5.32. It was consequently tried to calcine the powder before and after attrition-milling at different temperatures to decompose surface species and to redisperse the powder after-

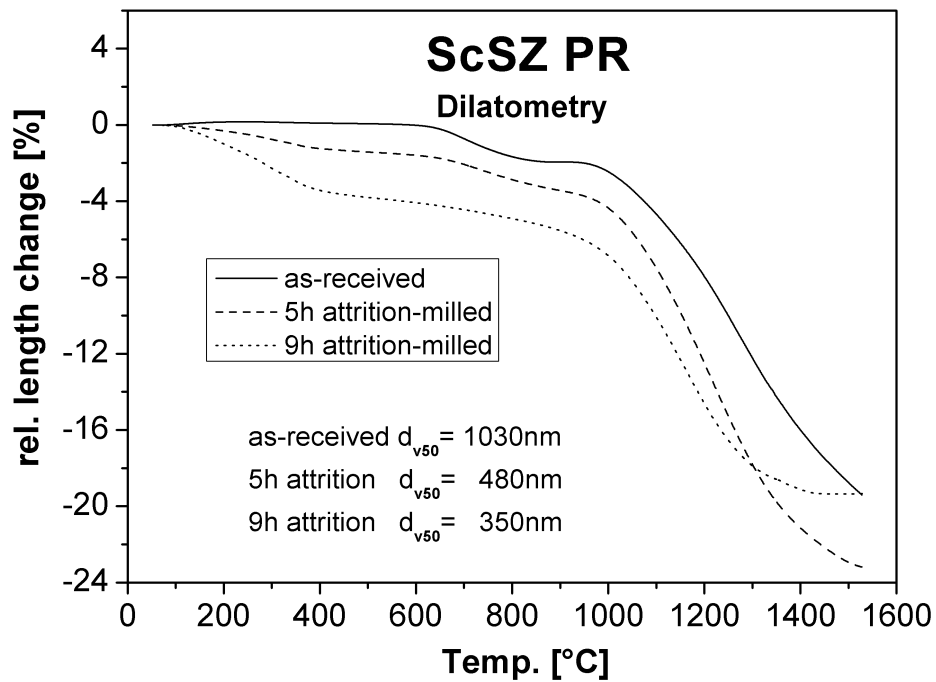
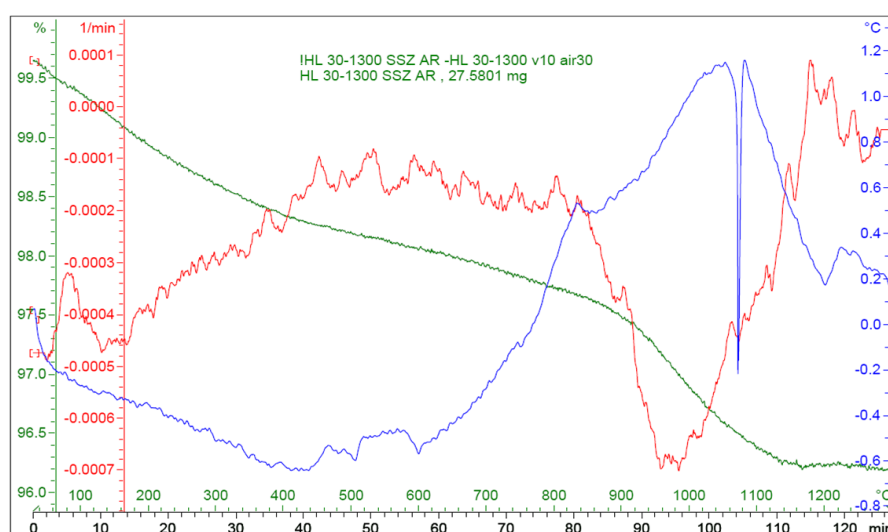


Figure 5.30: Dilatometric curves of slip-cast pellets of ScSZ PR-suspension before and after attrition-milling.

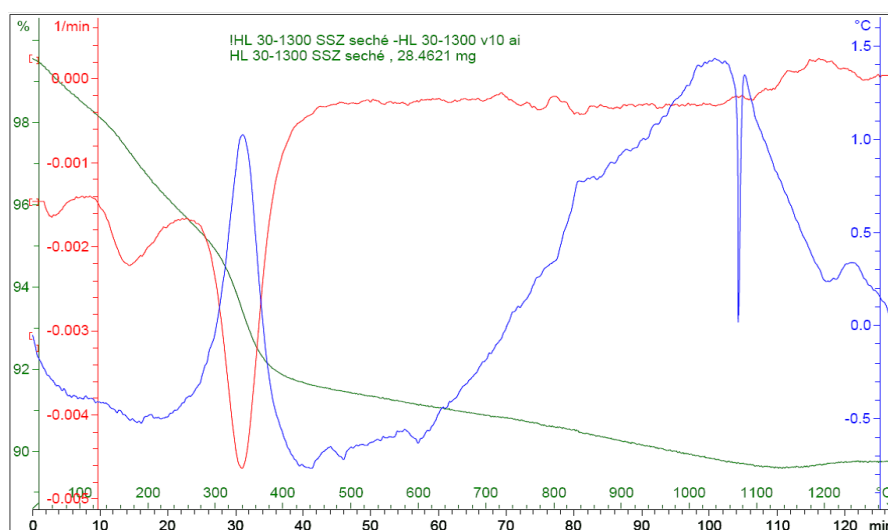
Table 5.12: Analysis of TGA data.

Powder	Start.Temp.	End Temp.	weight loss	Explanation
ScSZ PR AR	25°C	400°C	1.0%	Water and Surface Polymer Species
ScSZ PR AR	400°C	900°C	1.0%	Surface Species e.g. $\text{Zr}(\text{CO}_3)_2$
ScSZ PR AR	900°C	1150°C	1.3%	Phase Transition
ScSZ PR AM	25°C	120°C	1.6%	Water
ScSZ PR AM	120°C	280°C	3.3%	Water+ $\text{Zr}(\text{OH})_4$
ScSZ PR AM	280°C	410°C	2.0%	PAA-decomposition
ScSZ PR AM	410°C	900°C	2.0%	Surface Species e.g. Carbonates
ScSZ PR AM	900°C	1150°C	0.9%	Phase Transition

5.3. Electrolyte: Scandia-stabilised zirconia (ScSZ)



(a)



(b)

Figure 5.31: TGA of both as-received and attrition-milled ScSZ PR powders (a)TGA of as-received powder. (b)TGA of attrition-milled powder.

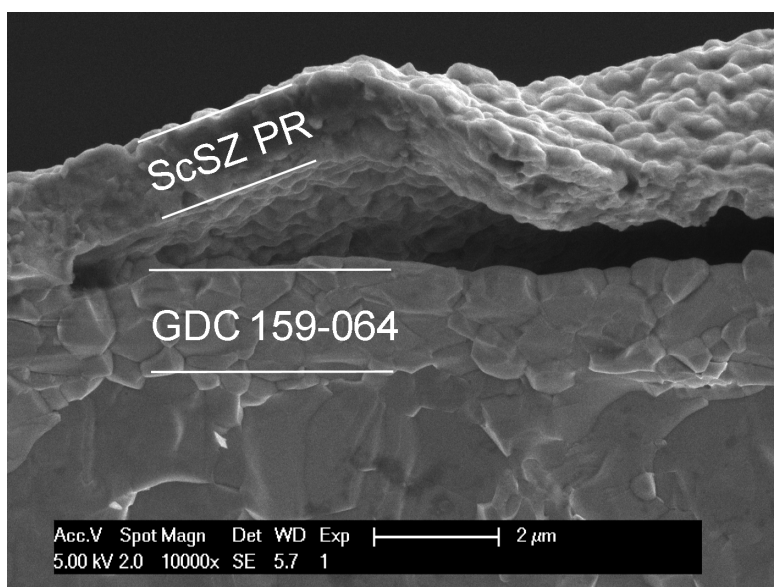


Figure 5.32: A delaminated ScSZ PR layer due to irregular shrinkage.

wards in PAA-solution again. However, it proved to be difficult to find the right calcination temperature. For powder calcined before attrition-milling, a lot of active surface was lost after calcination. Once it was lost due to particle agglomeration, it was impossible to recover by attrition-milling. For dried powders after attrition-milling, calcination at 400°C led to agglomeration and the weight losses of slip-cast pellets were still high. It was therefore decided to work with different ScSZ powders.

5.3.2 10ScSZ from DKKK (ScSZ DK)

The particle size distribution is shown in Fig. 5.33 and shows two modes. The primary particles' size peaked around 750 nm and granulates were seen in a size range of 10-70 μm. These granulates stem from the synthesis process. They can be easily seen by SEM-imaging as shown in Fig. 5.34. The powder was dispersed in different conditions (solvents, dispersants) and pellets were prepared by slip-casting. The results concerning green and sinter density as well as sinter shrinkage are shown in Table 5.13. It can be seen that for no dispersant-solvent combination, high green and sinter densities were obtained. The presence of granulates was considered to be the main reason inhibiting better particle packing. Therefore, ball-milling was performed to break the agglomerates. After 24 hours at 200 rpm with 1.25 mm milling media in water and isopropanol respectively, the suspensions were slip-cast and sintered. The results are shown in Table 5.14.

It became obvious that only water-based systems came close to gas-tightness after sintering at 1300°C, as the green density was generally the highest by far. This is associated with the more efficient combination of electrostatic and steric mechanisms for particle stabilisation as compared to only steric contributions from organic solvents/dispersants. However, even for

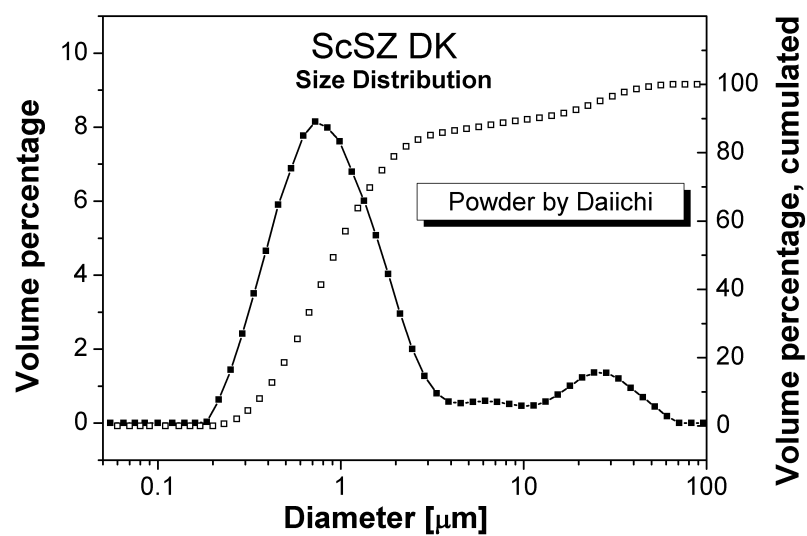


Figure 5.33: The PSD of ScSZ DK in PAA-solution.

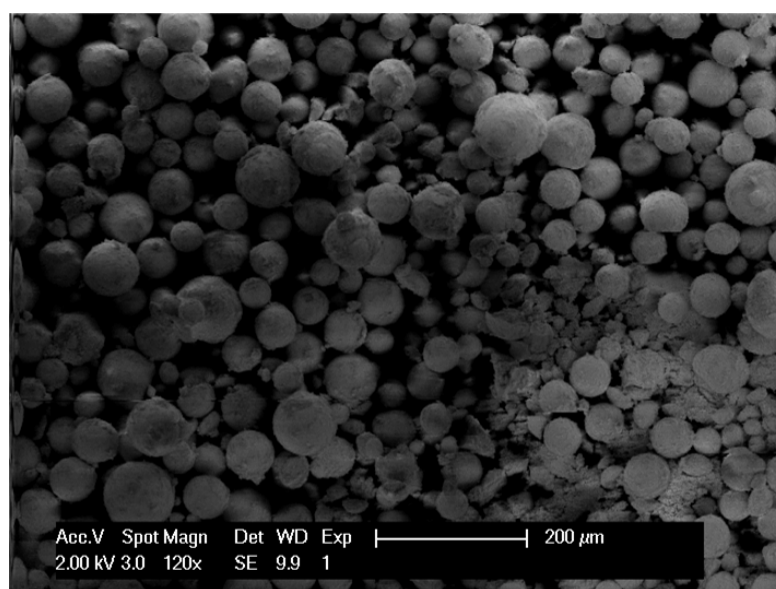


Figure 5.34: SEM-image of ScSZ DK particles.

Table 5.13: Green and sinter density at 1300°C as well as shrinkage during sintering of as-received ScSZ DK made by slip-casting of suspensions of different dispersant-binder-solvent systems.

ScSZ DK	Green density	Sinter density	Sinter Shrinkage
in PAA-PVA-Water	36-39%	84%	27%
in TEA-PVB-Ethanol	34%	78%	26%
in TEA-PVB-Isopropanol	32%	70%	24%
in all other org.	32-36%	76-89%	23-29%

water-based systems only 85% of relative density were attained. While it may be possible to densify this powder by longer dwell times at sintering temperatures, it was decided to look at another powder.

Table 5.14: Green and sinter density at 1300°C as well as shrinkage during sintering of ball-milled ScSZ DK made by slip-casting of suspensions in water and isopropanol.

ScSZ DK	Green density	Sinter density	Sinter Shrinkage
BM in PAA-Water	52%	85%	17%
BM in TEA-Iso.	36%	80%	25%

5.3.3 10ScSZ from Treibacher (ScSZ TR)

The particle size distribution of as-received ScSZ TR dispersed in aqueous PAA-solution at pH=9 is shown in Fig. 5.35. As it can be seen, the distribution is monomodal, more narrow and shifted to smaller sizes than for ScSZ DK powder. The powder was dispersed in different solvent-dispersant-binder systems and pellets were prepared by slip-casting. Results for densification behaviour of these pellets are shown in Table 5.15. Clearly, water-based systems with PAA-dispersant are able to produce pellets with high green densities and closed porosity after sintering at 1300°C.

Interestingly, 2 wt% of PAA-dispersant, considering the specific surface area of ScSZ TR, corresponds to 1.36 mg PAA/m² particle surface and therefore almost exactly the value calculated for ScSZ PR. As optimised dispersant content leads to optimal particle suspension, the highest green density is achieved under these conditions as the packing of particles is the most ordered. Adding more PAA will only increase the ionic strength of the liquid, as the particle surfaces are already covered. The stabilisation of ScSZ was also modelled by the Hamaker software code. The results and the used models are shown in Fig. 5.36, the parameters used in the models are all shown in Table 5.16. The zeta-potential of -45 mV was taken from ScSZ PR. The ionic strength was calculated as the actual amount of charged particles in the suspensions and hence the sum of charged AA-monomers in the PAA chain as well as completely dissociated

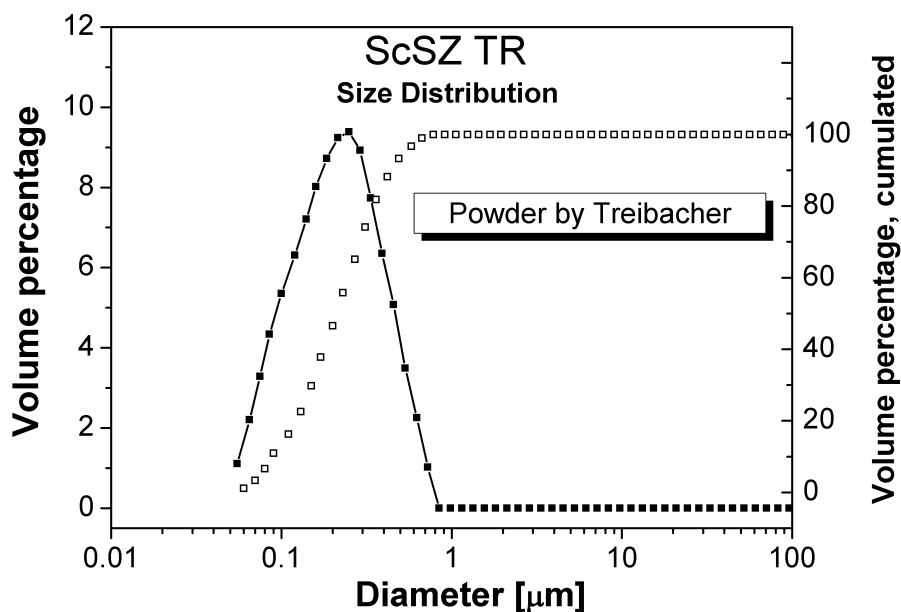


Figure 5.35: The PSD of ScSZ TR in PAA-solution.

Table 5.15: Green and sinter density at 1300°C as well as shrinkage during sintering of as-received ScSZ TR made by slip-casting of suspensions in water and isopropanol.

System	Green density	Sinter density	Sinter Shrinkage
2%TEA, 1%PVB, Isoprop.	38%	78%	22%
2%TEA, 2%PVB, Isoprop.	35%	71%	21%
2%TEA, 4%PVB, Isoprop.	31%	67%	18%
2%PAA, 1%PVA, Water	59.8±0.4%	95±1%	17.8±0.4%
2%PAA, 2%PVA, Water	59.1±0.2%	95.8±0.3%	18.0±0.2%
3%PAA, 1%PVA, Water	58.8±0.1%	92.6±0.1%	17.9±0.1%
3%PAA, 2%PVA, Water	57.8±0.2%	94.1±0.9%	19.2±0.1%

NH₄OH-solution. The Hamaker constant of $6 \cdot 10^{-20}$ J as it was used as the value reported for the closest material to ScSZ found in the literature, which were tetragonal zirconia with 3 mol% yttria (3YSZ, [126]) and monoclinic zirconia [130]. As this powder seemed the most promising

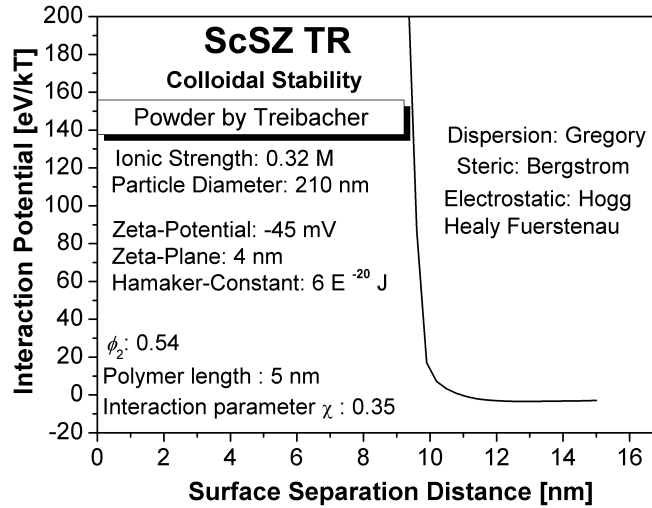


Figure 5.36: Simulation of interaction potential of ScSZ TR as a function of particle surface separation by Hamaker.

Table 5.16: Simulation parameters for colloidal stability of ScSZ using Hamaker V.2.1.

ScSZ	attractive interaction, Gregory equation				
	A_H 6*10 ⁻²⁰ J	a 105 nm	b 5.32	λ_0 100 nm	ζ -45mV
	repulsive electrostatic interaction, HHF				
	I_C 3*10 ⁻¹ mol/l	d_ζ 3-4 nm			
	repulsive steric interaction, Bergstrom				
	δ 5 nm	ϕ_2 0.54	χ 0.35		

by far in terms of densification and ease of handling, it was chosen as ScSZ-powder to prepare single cells by dip-coating. The shrinkage as a function of temperature was measured by dilatometry (at EMPA, Duebendorf) and is shown in Fig. 5.37. The shrinkage of ScSZ DK is also shown for comparison.

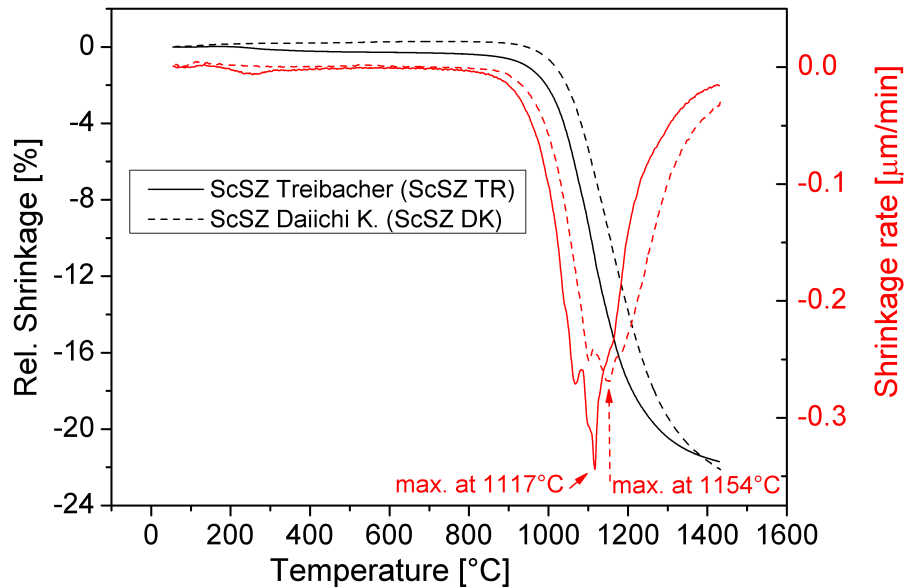


Figure 5.37: Sinter Shrinkage of ScSZ TR and comparison to ScSZ DK.

5.3.4 Thermal expansion coefficient (TEC)

The TEC of ScSZ was not published so far. It was therefore measured for all three different ScSZ-powders and is shown in Figure 5.38. It can be seen that the TEC is quite similar for all three tested powders. Deviations between ScSZ PR and the other two are probably related to differences in density, as the Praxair powder needed 1700°C of sinter temperature to attain 91% of density whereas ScSZ TR and ScSZ DK pellets were already >95% dense at 1300°C. The TECs of the other materials used in this work were also measured and are shown in Figure 5.39. 8YSZ and 10YSZ as typical electrolyte materials were also used for TEC measurements and coincided very well with published values in the literature [131]. It can be seen that their TEC-curves coincide almost perfectly with each other, which can be expected as they both have the same crystalline structure and differ only slightly in the dopant's amount.

The three different ScSZ powders however consistently show smaller TECs than YSZ as they differ in the dopant's nature. The greater differences in TEC between ScSZ and the other materials involved will result in higher compressive stresses in the ScSZ-layer during cooling than it would occur in YSZ-layers. These stresses may be helpful to close cracks in the ScSZ layer, however if they become too big, buckling or delamination may occur. The difference in TECs can lead to thermo-mechanical stresses during temperature changes of the complete cells. A study of post-sintering cooling stresses of the single cell is planned (cf. Publication list).

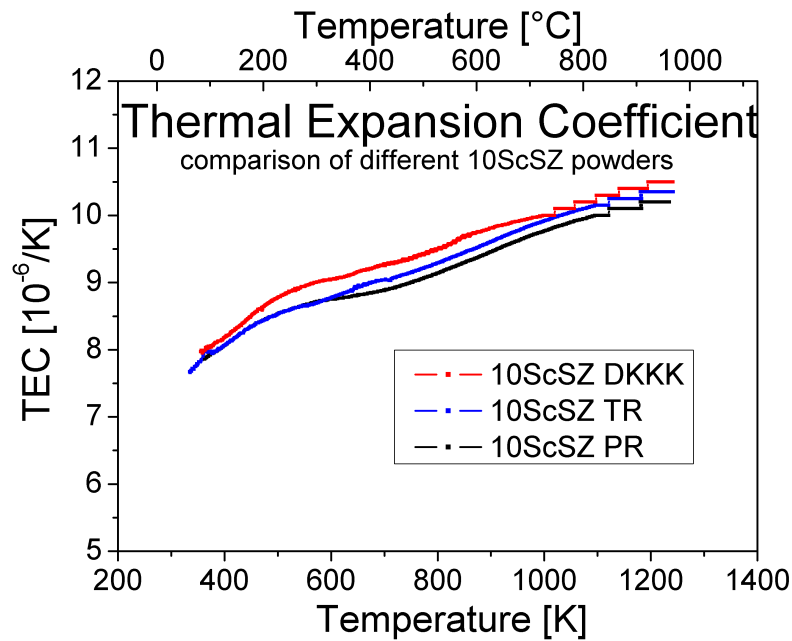


Figure 5.38: The TEC of the different ScSZ powders.

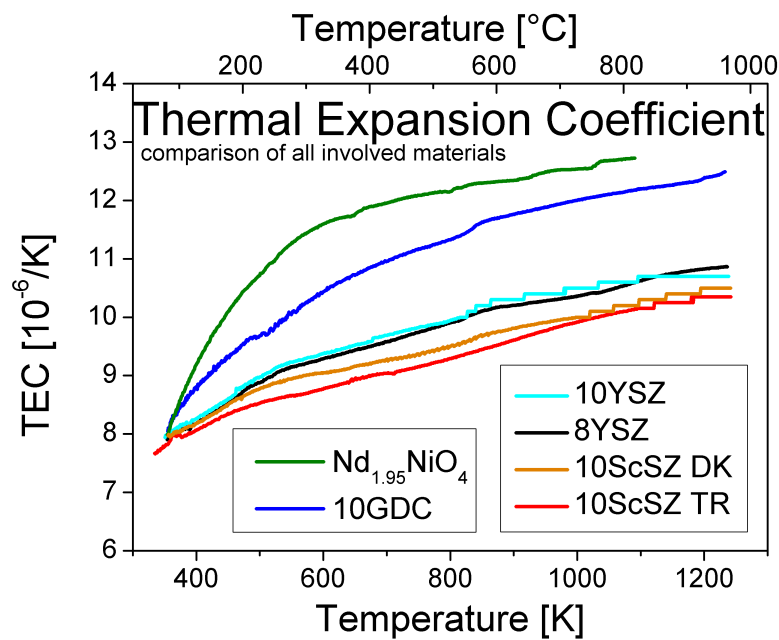


Figure 5.39: The TEC of all used materials.

5.3.5 Chemical analysis(XRD, XPS, ICP)

All three ScSZ powders were tested by XRD for phase purity. The results are shown in Figure 5.40. In Figures 5.40a to 5.40c, the diffractograms of the individual powders are shown. Fig. 5.40d is a close-up on the (112)-peak around $2\theta=50.8^\circ$. While ScSZ PR peaks are slightly shifted with respect to the other two ScSZ-powders, it is also poorly crystallized which can be seen by the broad peak width. The peak positions of ScSZ DK and ScSZ TR coincide

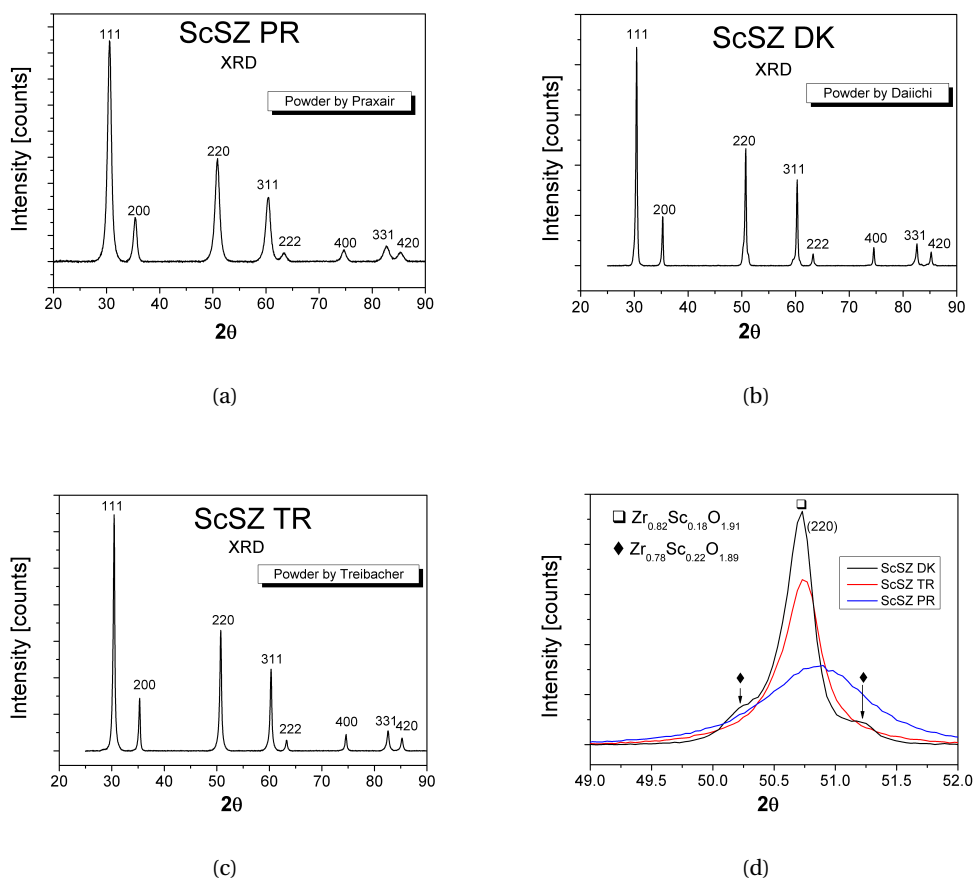


Figure 5.40: The XRD pattern of the used ScSZ powders. (a)ScSZ PR (b)ScSZ DK (c)ScSZ TR (d)comparison

while ScSZ DK clearly shows the presence of some secondary phase, which was identified as $Zr_{0.78}Sc_{0.22}O_{1.89}$ (ICCD 00-051-1604). The main crystalline phase was identified as cubic $Zr_{0.82}Sc_{0.18}O_{1.91}$ (ICCD 01-089-5483). The crystallite size was calculated according to the Debye-Scherrer equation for all peaks and averaged. The results are shown in Table 5.17. Further investigations were done to determine the exact composition of ScSZ powders by XPS and ICP. These analyses were done as multiple results suggested that there were differences in composition, which were:

Table 5.17: Crystallite size of the different ScSZ powders

	ScSZ PR	ScSZ DK	ScSZ TR
$d_{\text{cryst.}} [\text{nm}]$	10.0	28.9	21.3

- Firstly, the appearance of peaks of a secondary phase in XRD.
- Secondly, the difference in the temperature of the supposed phase transition (cf. TGA-graphs Fig. 5.31).
- Thirdly, the substantial difference in density between ScSZ PR and the other two ScSZ powders may be related to a different chemical composition, which would lead to a different theoretical density as well.

5.3.6 Dip-Coating of ScSZ

The Dip-Coating was performed with ScSZ TR powder in as-received state. The powder was dispersed during 15 minutes in an ultrasonic horn in 2 wt% PAA-solution and water. The water was added to yield suspensions of 5 vol% solid load. PVA-binder of 5 wt% content was added after the dispersion was finished and only immediately before the coating to minimise the risks of bubble formation or PAA-PVA interactions. Tubes that were already coated with GDC-suspensions and had dried GDC-layers, were dipped in ScSZ-suspensions and withdrawn with 300 mm/min. The tubes were immediately transferred to the drying chamber which was preset to 25°C and 90 % of relative humidity in order to reduce the evaporation rate and hence the drying stresses.

After drying for at least 24 hours at these conditions the humidity was slowly decreased to atmospheric conditions. A single layer of ScSZ coated in this manner on a tube already coated with a GDC-layer and cosintered at 1300°C is shown in Fig. 5.41. The single layer has a thickness of ca. 2-4 μm , but showed slight variations due to the presence of porosity on the substrate, which changed the deposition mechanism from pure dip-coating by Landau-Levich (cf. section 2.2) to a combined dip-coating/cake-filtration mechanism due to the presence of capillary pressure in the tube and GDC-layer (cf. section 2.3). For sintering conditions of 1300°C / 2 hours, the voids at the GDC/ScSZ interface due to a Kirkendall-effect of different cation diffusion speeds are already visible (see chapter 7).

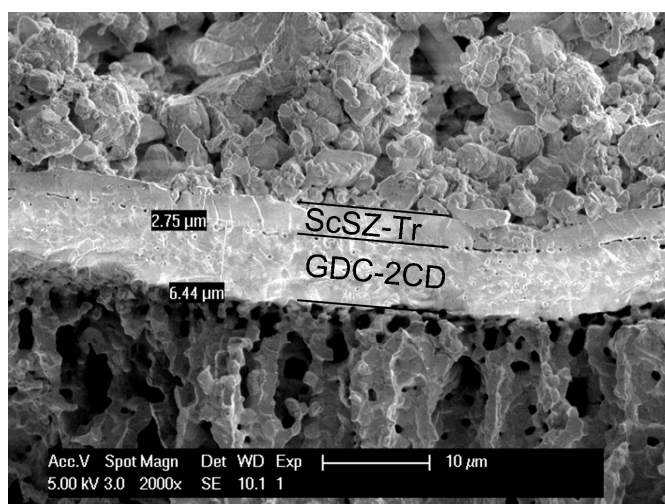


Figure 5.41: SEM cross-section image of single ScSZ TR layer.

5.4 Anode: NiO-electrolyte cermets

The two different anode formulations used in this work are presented in this section and shown in Table 5.18. Both anode powders are mixtures of NiO powder and electrolyte powder. In both cases, the quantities of the individual powders are calculated so that the final volume fraction of metallic Ni-particles in the cermet is 44 vol%. Both powders show a rather broad distribution of particle sizes in the as-mixed state, as can be seen from the great values of span in Table 5.18. This is due to the different sizes of electrolyte and anode, where the latter is the coarser powder.

Table 5.18: Summary of different Anode-Powders used in this work. FCM: Fuel Cell Materials.

Anode cermets				Characteristics			
	NiO	Electrolyte	mixed	NiO wt%	$d_{v,50}$ [nm]	Span	SSA [m ² /g]
NiO-YSZ	unknwon	unknown	at Nextech	60wt%	6150	114	3.4
NiO-GDC	J.T.Baker B24159	GDC FCM 318-033	at EPFL	55wt%	560	66	5

5.4.1 NiO-YSZ, premixed by Nextech

The particle size distribution of as-received powder mixture is shown in Figure 5.42. A bimodal size distribution can be seen. It became clear from filtering experiments that YSZ is the finer powder (peak around 300 nm) whereas the NiO powder is the coarser one (peak around 5 μm).

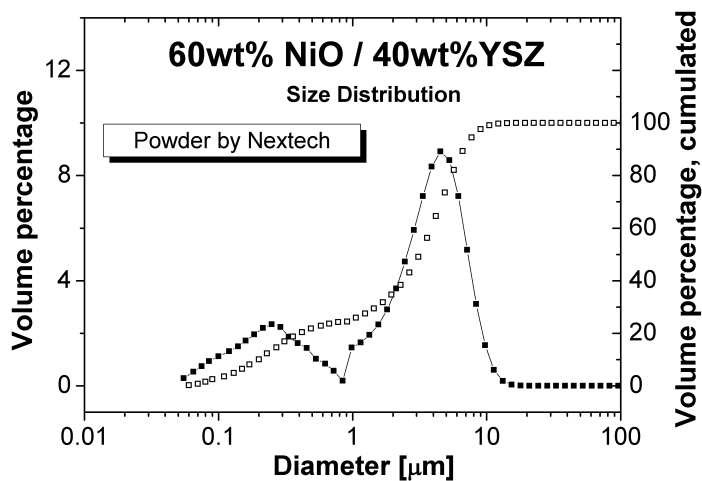


Figure 5.42: The particle size distribution of NiO-YSZ anode powder.

5.4.2 NiO-GDC, prepared at EPFL

The NiO powder was obtained from Baker, Lot-Nr. B24159 and the GDC powder was from Fuel Cell Materials, Lot-Nr. 318-033. The respective quantities were added and rolled for 24h to ensure homogenised mixtures. Afterwards, the particle size distribution was measured by Laser Diffraction. Therefore, the powder was dispersed in aqueous PAA-solution at pH=9. The results are shown in Fig. 5.43. It can be seen that the mixture of NiO powder from JT Baker and GDC from Fuel Cell Material has monomodal particle size distribution around a mode volumetric diameter of 400 nm with a small agglomeration up until ca. 20 μm. The granulometry of NiO powder from Baker was also measured individually and is shown in Figure 5.44. By comparing Fig. 5.43 and 5.44, it follows that the small agglomeration peak around 6 μm in Fig. 5.43 is due to GDC-particles.

5.4.3 Dip-Coating of anode powder suspensions

Anode powder suspensions were, due to their easier handling, prepared with isopropanol solvent, TEA-dispersant and PVB-binder. As a thickness of 30 μm was targeted for the anode, higher volume fractions of particles in the suspensions had to be used. Suspensions with 2 wt% TEA and 5 wt%PVB, where PVB was added as a 10 wt% solution in isopropanol, had solid fractions of 19 vol%. A single anode layer, dip-coated and sintered at 1100°C for 2 hours on top of an already sintered cathode+electrolyte half cell is shown in Fig. 5.45. The NiO-GDC anode is shown in Fig 5.45a and the NiO-YSZ anode is shown in Fig. 5.45b. It can be seen in Fig. 5.45a that the grain size of NiO and GDC is very homogeneous and similar to each other as opposed to the NiO-YSZ layer shown in Fig. 5.45b, where NiO grains of ca. 10 μm size alternate with submicrometric YSZ particles. The anode layer thickness is between 11-15 μm.

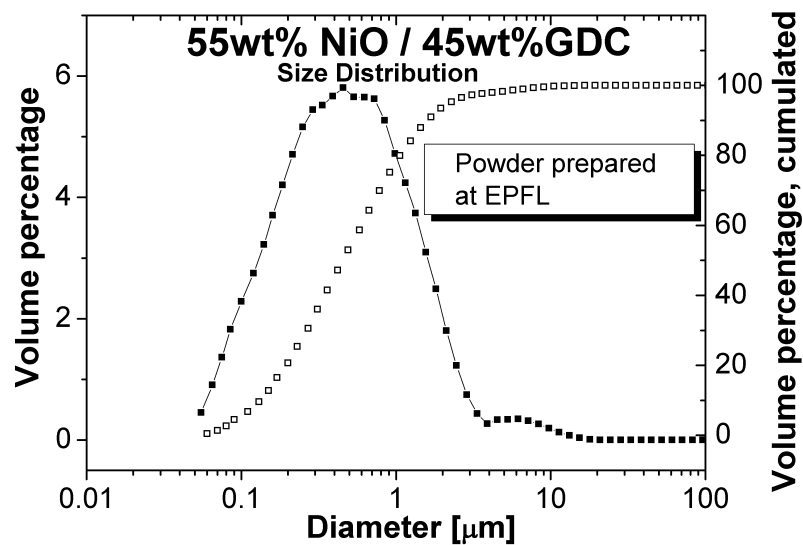


Figure 5.43: The particle size distribution of NiO-GDC anode powder.

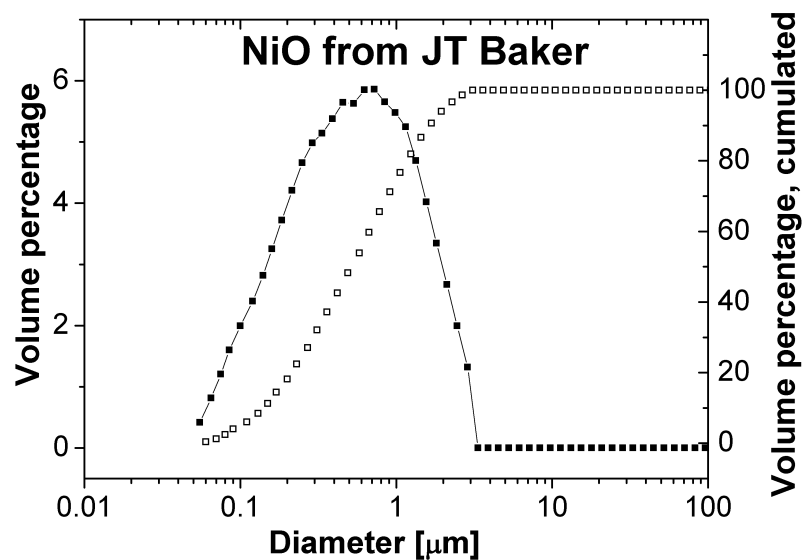


Figure 5.44: The particle size distribution of NiO-powder from JT Baker.

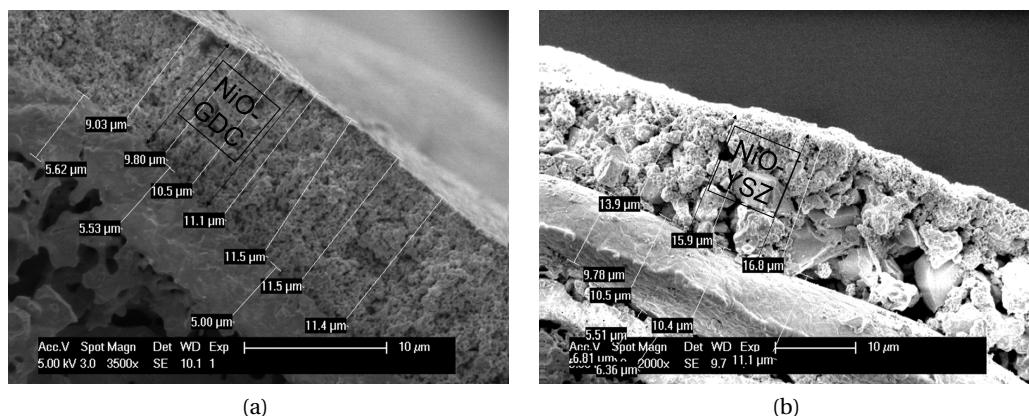


Figure 5.45: Cross-section SEM-images of single anode layers deposited by dip-coating. (a) Dip-Coated in a suspension of NiO-GDC powder. (b) Dip-Coated in a suspension of NiO-YSZ powder.

Therefore, 2 layers were deposited by dip-coating with the already mentioned parameters. The dip-coating speed was 300 mm/min. As anode layers could be removed by scratching from the electrolyte surface after being sintered at 1100°C/2 h, the anode sintering temperature was increased to 1300°C/2 h and rice starch was added as pore former for the preparation of complete single cells (cf. chapter 9). The anode was not deposited over the whole length of the tube but only in the middle over ca. 60% of the total length. The tube surface towards the extremities was sealed with teflon tape when the tube was dipped into the anode suspension. A tube prepared for dip-coating in anode suspension is shown in Fig. 5.46.

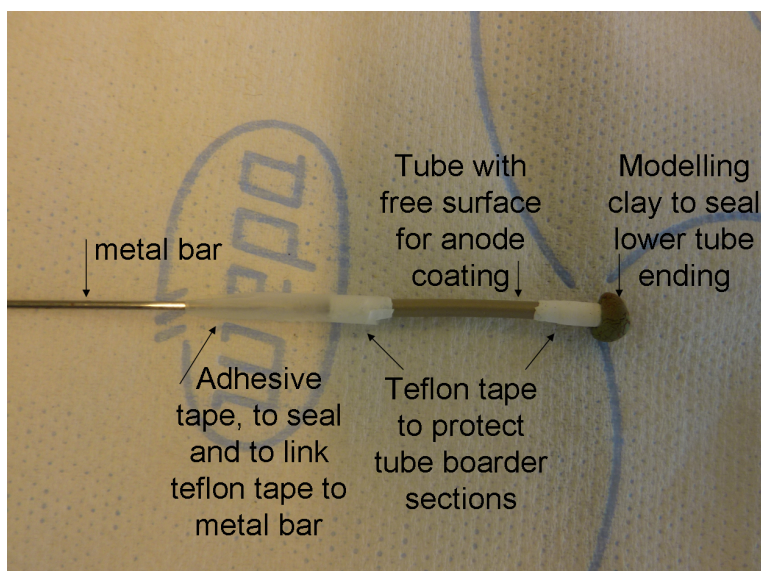


Figure 5.46: A prepared tube for dip-coating in anode suspension.

6 Nickelate Tubes

In this chapter, the different tubes used in this work are presented. Before their fabrication is described for each tube type individually, some basic characteristics are shown in Table 6.1. All tubes were prepared from nickelate powder Lots Nr. 3 and 4. For the measurement of the tube's pore size, SEM imaging of tube surfaces and mercury intrusion were performed at EPFL. The tubes principally have three different states.

- The green state immediately after fabrication.
- The presintered state after the first thermal treatment used to adapt shrinkages and additive-burnout.
- The sintered state after firing at the sinter temperature, typically 1300°C.

Table 6.1: Characteristics of the different nickelate tubes used in this work. The inner and outer diameter are measured after sintering of the tube at 1300°C/2h. Ex-SD stands for "Extrusion-Small Diameter", Ex-BD for "Extrusion-Big Diameter", T-SC for "Tubes, Slip-Casted".

Nd _{1.95} NiO _{4+δ} -Tubes		Characteristics				
Type	Poreformer	D _{ext} [mm]	D _{in} [mm]	Porosity	Shrinkage from	to 1300°C
CIP-VITO	Rice Starch	6.8	4.4	43%	1000°C	10-12%
CIP-ZARA	Maize Starch	3.4	2.6	51%	25°C	11%
CIP-EPFL	Rice Starch	4.8	3.6	40%	25°C	14%
Ex-SD	-	1.8	1.2	62%	1000°C	18%
Ex-BD	-	3.7	3.2	45%	900°C	15%
T-SC	-	5.4	3.8	36%	1000°C	12-14%

Tubes prepared by cold-isostatic pressing (CIP-VITO), extrusion (Ex-SD) and slip-casting (T-SC) that were sintered at 1300°C/2h are shown in Fig. 6.1.

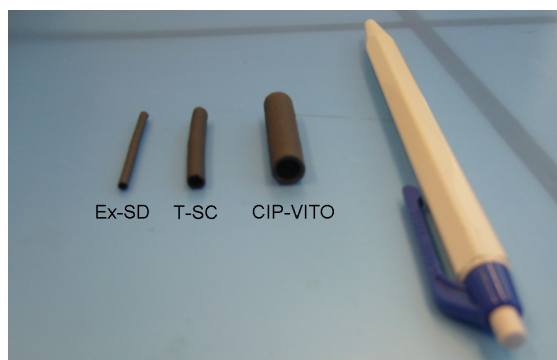


Figure 6.1: Sintered tubes prepared by different fabrication processes.

6.1 Tubes prepared by cold-isostatic pressing (CIP)

6.1.1 CIP from VITO (CIP-VITO)

At the beginning of this work, tubes were compacted at the Flemish Institute for Technological Research, VITO, Belgium. Nickelate powder was mixed with rice starch pore former, Remyline AX-DR, Remy Industries, in quantities to yield tubes of ca. 35% porosity. Powder mixtures were homogenised by mixing in 150 ml acetone in a planetary ball mill with a polymer jar and YSZ milling media for 3 minutes. After milling, the acetone was evaporated and the dry powder mixture sieved over a 500 μm mesh. The powder was compacted by cold isostatic pressing (CIP) in a tubular rubber mould at different pressures. The green tubes had an outer diameter of 7.8 mm and could be easily processed. The green tubes were then calcined by heating up with 30°C/h to 500°C, followed by a dwell of 1 hour, then 100°C/h to the presintering temperature, 900-1060°C. The shrinkage from the presintering temperature to 1300°C was ca. 10-12%, depending on presintering temperature and compaction pressure.

Rice starch and graphite were tested as pore formers. Graphite-added powder mixtures could be compacted only at pressures ≥ 240 MPa. The tubes showed less green density which led to higher sintering shrinkages (ca. 15% until 1300°C), however the mechanical stability was poor and the tubes showed black spots at the surface after presintering at 1000°C, which indicates that graphite was still present. Pore former which was still present after presintering evaporates during the cosintering process, where the created gas-molecules may endanger the layer's integrity by evaporation through the layer, thereby creating pinholes. For these reasons, graphite was abandoned as pore former and the effort concentrated on rice starch. In Figure 6.2, the surface pore size of tubes prepared with rice starch and graphite as measured by mercury porosimetry is shown. It can be seen that the pore size is quite similar and therefore not an important indicator for the choice of pore former. A tube fabricated with rice starch pore former is shown in cross-section in Fig. 6.3b. It can be seen that the porosity is distributed homogeneously throughout the volume. The surface pore size by SEM is furthermore shown in Fig. 6.3a.

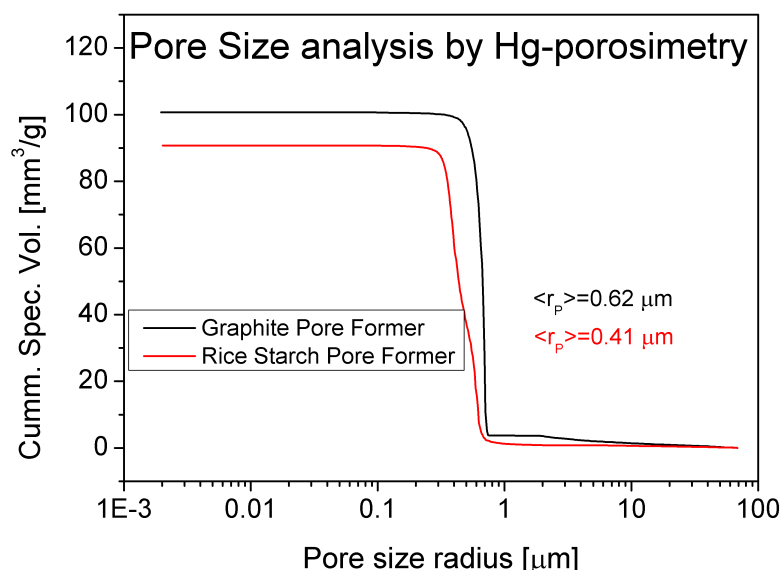
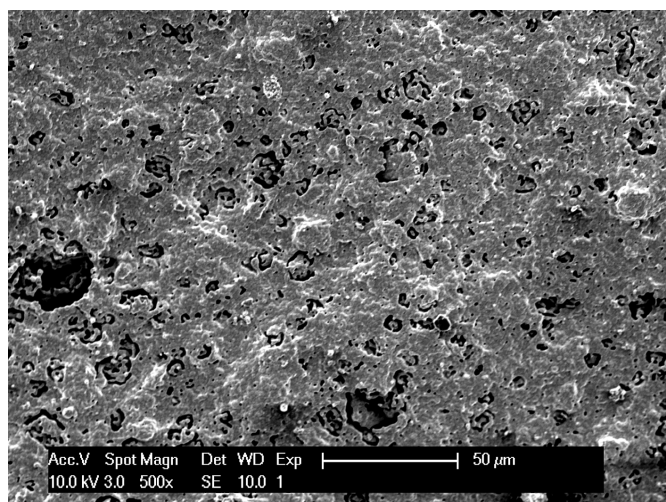


Figure 6.2: Pore size distribution of CIP-Vito tubes with Graphite and Rice Starch pore former.

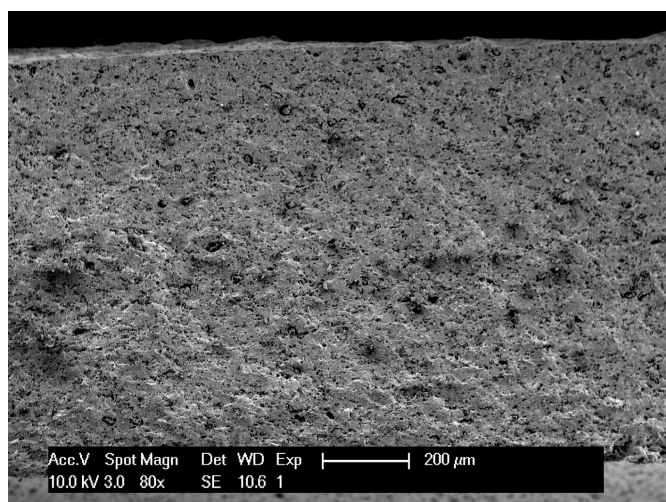
The compaction pressure for NNO-rice starch powder mixture was varied between 80-240 MPa and led to intact tubes over the whole pressure range. The influence of isostatic pressure during CIP on sinter shrinkage and densities was studied. It became clear that green and sinter density generally increased with the compaction pressure. The sinter shrinkage however, did vary only to a very small extent, i.e. between 10-12% until 1300°C. At the end, it was decided to use pressures of 240 MPa to receive well compacted, robust tubes.

6.1.2 CIP at Zaragoza (CIP-ZARA)

Nickelate powder was mixed with maizena pore former in different quantities and furthermore treated with PVA as binder. The PVA-binder was added dropwise from an aqueous solution and intensively mixed with the powder in a mortar. The tube shape was realised by a latex-hose surrounding a cylindrical metal rod which can be closed at both extremities by cable ties. The latex hose was 5 mm of inner diameter and the metal rod had a diameter of exactly 3 mm. The tubes were cold-isostatically pressed in oil at 200 MPa for 5 minutes before the cable ties were removed by cutters, the latex hose was heated to dilate and reduce the contact to the tube before it was carefully removed. The size of the green tube was ca. 3.8 mm external diameter. After sintering, the dimensions were 3.4 mm external and 2.6 mm of inner diameter. The readily sintered tubes were tested for pore size distribution by mercury intrusion, a typical result is shown in Fig. 6.4. It can be seen that the pores of tubes made with commercial maize starch (maizena) are bigger than with rice starch, as the former had coarser grains.



(a)



(b)

Figure 6.3: The pore size of CIPed tubes with rice starch pore former (a) Surface pores. (b) Cross-section through the tube volume.

6.1. Tubes prepared by cold-isostatic pressing (CIP)

Furthermore, the distribution is much broader, as the particle size distribution of commercial maize starch is less controlled than for the used rice starch. SEM surface and cross-section

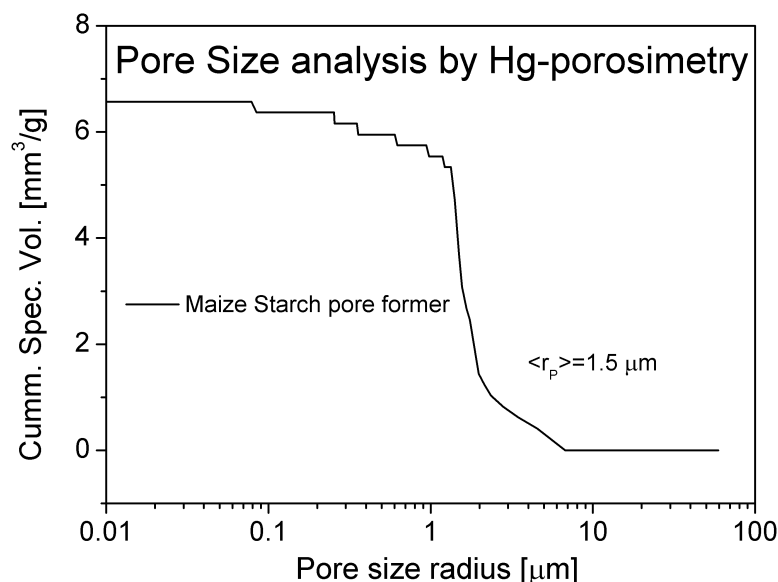


Figure 6.4: Surface pore size distribution of compacted tubes with maizena, measured by mercury intrusion.

images of tubes with maizena pore former after sintering at 1300°C are shown in Fig. 6.5. It can be seen that the pore size attained with commercial maize starch pore former is bigger than with rice starch by Remyline. Furthermore it appears to be bimodal, where larger pores of up to 20 μm diameter, frequently in the shape of horseshoes, are present next to small pores of ca. 1-2 μm diameter.

The shrinkage of tubes prepared in this manner was still relatively small, 10-11% from room temperature to 1300°C. However, it was believed that the combination of PVA-binder and smaller compaction pressures may lead to higher sinter shrinkages, which are necessary to fully densify the electrolyte layers (cf. sections 5.2.2 and 5.3.3).

6.1.3 CIP at EPFL (CIP-EPFL)

Powder mixtures of NNO and rice starch were compacted using the same setup type as in Zaragoza, but adapted for bigger tubes. The setup used for cold-isostatic compaction is shown in Fig. 6.6. The latex hose had an inner diameter of 6 mm and the metal bar had a diameter of exactly 4 mm. PVA of MW=146.000-186.000 g/mol from Sigma-Aldrich, Cat.:36,306-5 was drop-wise added to NNO-rice starch powder mixtures in a mortar and homogenised. In order to increase the sinter shrinkage, different amounts of PVA were tried until the maximum sinter

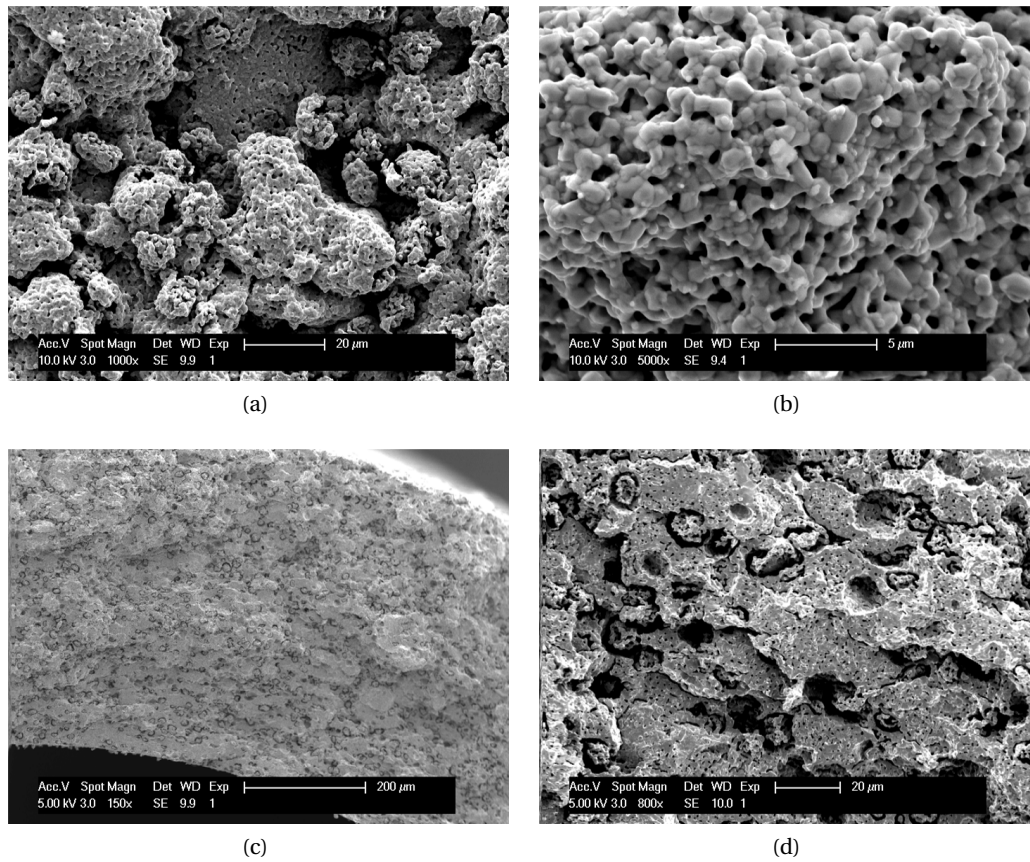


Figure 6.5: The pore size of CIPed tubes with maizena pore former (a) overview of the pore size at the tube's surface. (b) detailed view on small pores. (c) overview of the pore structure in cross-section. (d) detailed view on the small pores in cross-section.

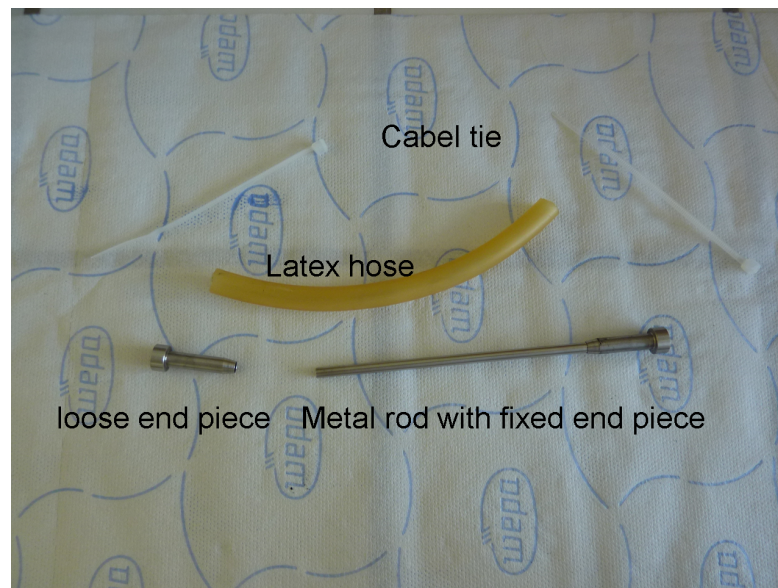


Figure 6.6: The setup used for the compaction of tubes at EPFL.

shrinkage was found. The compaction pressure of the tubes was kept at 80 MPa, maintained for 5 minutes. The tubes extracted from the compaction setup after CIP were fragile but could generally be processed. The shrinkage was in the region of $14 \pm 1\%$ from room temperature to 1300°C .

6.2 Tubes prepared by Extrusion

Powder batches of 600-3000 g according to the extrudates' diameter were mixed with ca. 18 wt% of organic and extruded through a circular opening at Kerafol, Germany. The exact nature of the organic additive as well as specifics about how the green extrudates were dried were not disclosed (confidential receipe, Kerafol). The green extrudates were cut to tubes of ca. 60 cm length.

6.2.1 Small Diameter (Ex-SD)

Batches of 600 g were mixed with organic additive and extruded to form extrudates of 2.7 mm external diameter. The extrudates did have some surface defects due to the extrusion process such as grooves. After sintering at 1300°C , the external diameter of the tubes was 1.8 mm with ca. $300\text{ }\mu\text{m}$ wall thickness. A cross-section of a sintered tube is shown in Fig. 6.7. As can be seen, the porosity is not distributed homogeneously throughout the tube volume but shows two distinct regions. Until ca. $20\text{ }\mu\text{m}$ of depth from the inner and outer tube surface, the pore sizes are between $1\text{--}10\text{ }\mu\text{m}$ and the structure appears rather dense. Starting at depths $\geq 20\text{ }\mu\text{m}$, the pores become bigger and attain pore sizes of up to $100\text{ }\mu\text{m}$ in the innermost section of the tube wall. The shape of the big pores is elongated and more or less perpendicular to the tube

surface. The surface pore size was examined as well by mercury intrusion. The result is shown

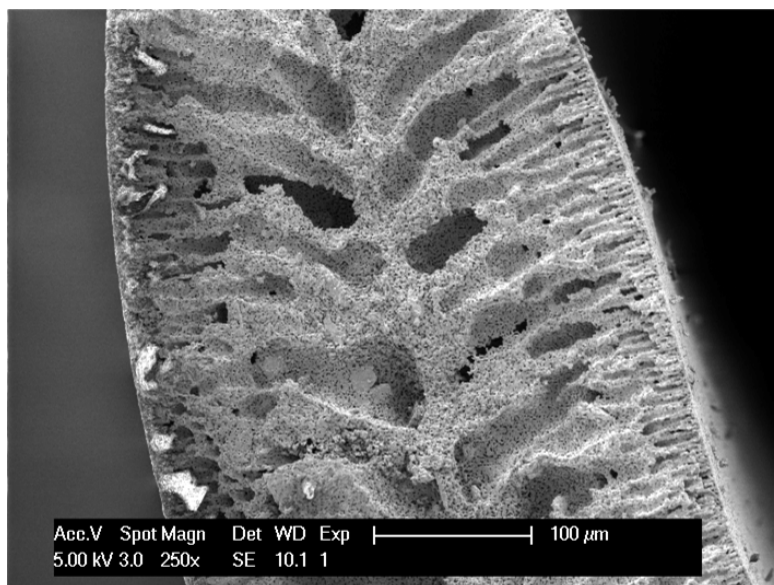


Figure 6.7: A cross-section of extruded tubes delivered by Kerafol.

in Fig. 6.8.

It can be seen that the surface pores are on the submicrometer scale and hence represent the bottleneck of the much bigger pores in the interior of the tubes. This is convenient for the utilisation, as oxygen diffusion capitalises on the bigger inner pore size whereas the deposition process only deals with the surface pores of ca. 1 μm size, which circumvents penetration of the particles into the pores. The surface pores are again shown by SEM-imaging in Fig. 6.9. The shrinkage of extruded tubes, measured by dilatometry in tube-axis direction, is shown in Fig. 6.10. Substantial shrinkage occurs below 500°C, where the organic binder desintegrates and leads to tubes of rather high porosity (61% after sintering at 1300°C). A tube had to be cooled down after being heated to 400°C, as the shrinkage exceeded the limitations of the dilatometer. In total, up to 40% in linear shrinkage are obtained, however, a majority of the shrinkage occurs at temperatures below 500°C due to binder burnout. Tubes presintered at temperatures $\geq 500^\circ\text{C}$ shrank ca. 18% between 1000°C and the cosintering temperature of 1300°C.

6.2.2 Bigger Diameter (Ex-BD)

Batches of 3000 g were mixed with organic additive and extruded to form tubes of 5.0 mm external diameter. The extrudates did have surface defects due to the extrusion process such as grooves and were generally more fragile than the small-diameter tubes due to the lower wall thickness to diameter ratio. After sintering at 1300°C, the external diameter of the tubes was 3.7 mm with ca. 260 μm wall thickness. The fragile tubes were difficult to prepare for dip-coating as they often broke in the presintered state. As it was not possible to increase

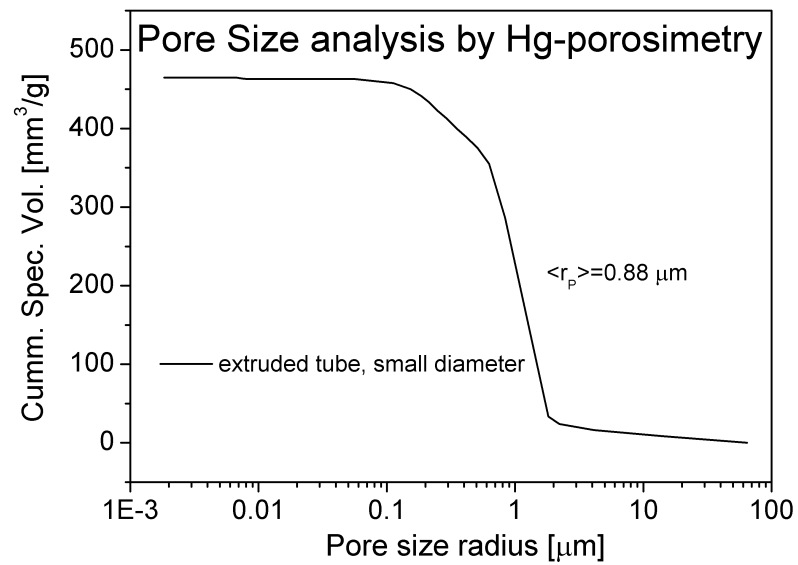


Figure 6.8: Mercury intrusion result of the pore size of extruded tubes.

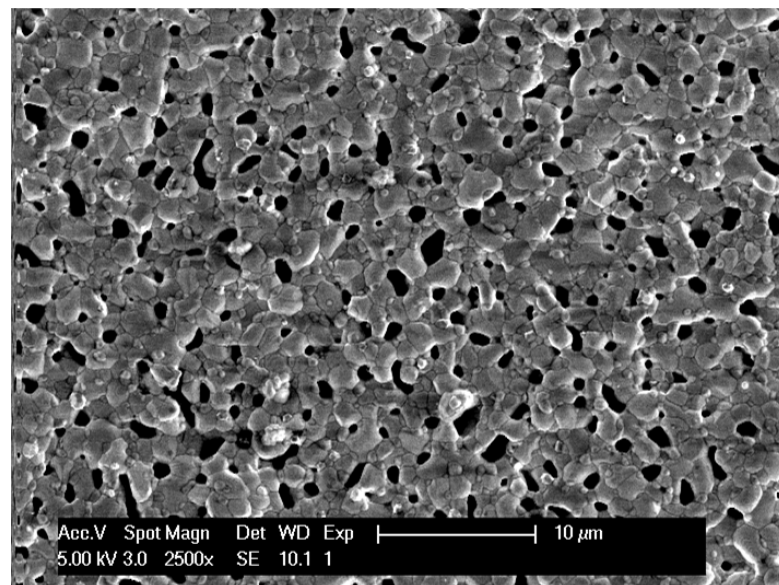


Figure 6.9: Surface pore size of extruded tubes.

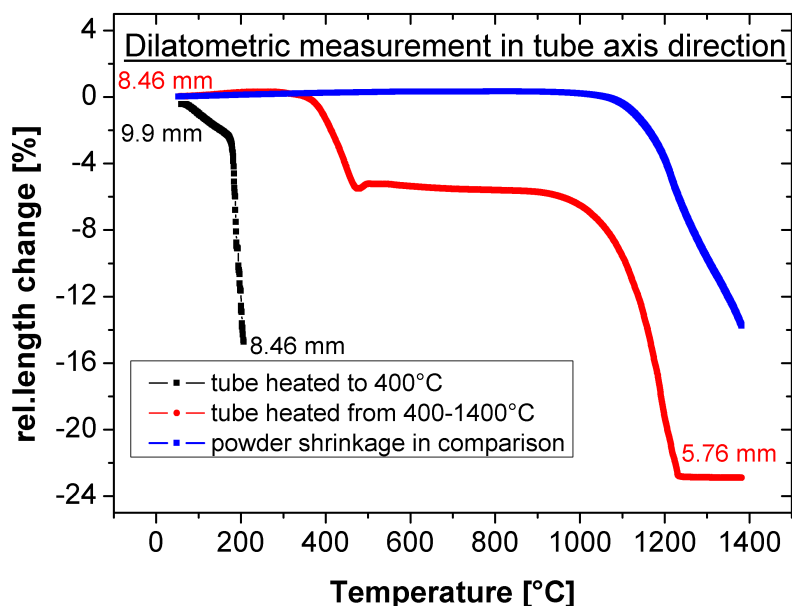


Figure 6.10: The thermal shrinkage of extruded tubes.

the wall thickness according to the fabrication process used at Kerafol, their utilisation was abandoned.

6.3 Tubes prepared by slip-casting (T-SC)

Nickelate tubes prepared by slip-casting were fabricated at Cereco, Greece. Nickelate powder was dispersed in water with binder of unknown origin to form suspensions. The suspensions were slip-cast in a tubular mould. After the mould was withdrawn, tubes of an outer diameter of ca. 6.5 mm were obtained. The tubes were presintered between 800-1000°C and the wall thickness of the tubes was varied in order to look for a compromise between electrochemical performance, i.e. low diffusion losses, and mechanical stability. The tubes were cut to sample lengths of ca. 3 cm before the deposition of thin films. The presintered tubes were rather solid and withstood the mechanical pressure exercised on them during the cutting and sealing process as preparation for dip-coating. The surface roughness of tubes prepared by slip-casting was substantial and required polishing prior to dip-coating.

6.4 Diffusion and Permeation Tests

The diffusion properties of the different tubes, namely average pore size and tortuosity of the porous solid network, were measured by two different methods, i.e. a permeation test and

a diffusion test. For the permeation test, the tortuosity τ can be calculated from the results but the average pore size has to be determined independently, e.g. from mercury intrusion experiments. The diffusion test allows to calculate the tortuosity of the porous network and the average size of the pores contributing to diffusion simultaneously.

Permeation test The setup of the permeation test is shown in Fig. 6.11. When gas is conducted into the blocked tube, its only path to escape from the tube is across the porous tube wall. As the permeation across the tube wall is not infinitely fast, an equilibrium between gas entering the tube through the connections and gas leaving the tubes through the porous wall is created. Consequently, a finite and constant pressure is established inside the tube. For different flow rates, this pressure changes. If the pressure varies linearly with the flow rate,

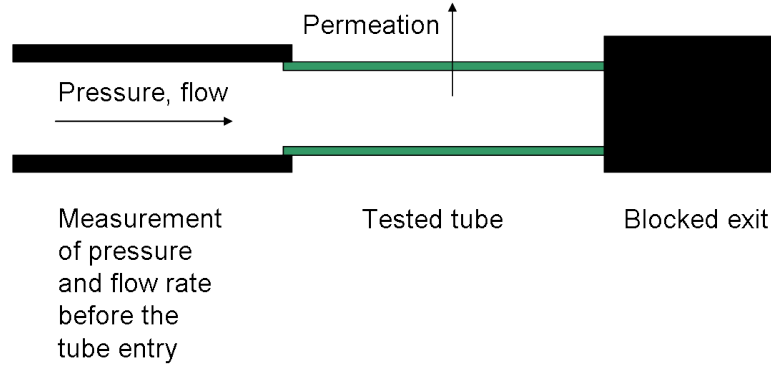


Figure 6.11: Setup of the permeation test.

then the permeability is independent of the overpressure inside the tube. Using equation 6.1 for the permeability of gases [66] across porous media

$$F = \frac{4}{3} \sqrt{\frac{2}{\pi}} \frac{\epsilon \langle r \rangle}{w_w \tau \sqrt{RTM}} + \frac{\epsilon \langle r \rangle^2}{8 w_w \tau \eta_g RT} P \quad (6.1)$$

where F is the permeability, P the pressure, ϵ the porosity, $\langle r \rangle$ the mean pore radius that has to be determined independently, τ the tortuosity of the porous network, w_w the wall thickness, η_g the gas viscosity and M its molecular mass, R the gas constant and T the temperature, equation 6.1 can be rearranged with respect to the tortuosity τ , yielding

$$\tau = \frac{4}{3} \sqrt{\frac{2}{\pi}} \frac{\epsilon \langle r \rangle}{w_w F \sqrt{RTM}} \quad (6.2)$$

A typical plot of flow rate against the pressure inside the tubes is shown in Fig.6.12. A direct proportionality is evidenced by a straight line over the whole range of pressure, which proves that the permeability, which is the slope of the straight line, is pressure-independent and hence the second term in equation 6.1 can be omitted.

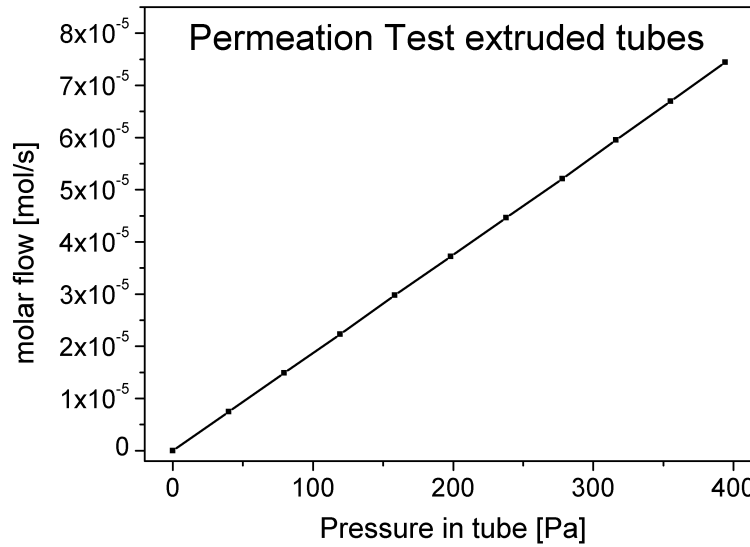


Figure 6.12: Variation of flow with the pressure inside the tubes during the permeation test, Sample: Ex-SD.

Diffusion test The diffusion setup is schematically shown in Fig. 6.13. A gas-mixture of inert gas, in this case argon, and oxygen is conducted inside the tube and pure inert gas is conducted outside of the tube. The concentration of oxygen in the gas mixture is changed by adapting the flow rates. The pressure of both gas compartments at the entry of the tube is measured (P^+ and P^-) and equilibrated by adjusting the pressure of the inner gas mixture using a fine control needle valve which is placed at the outlet of the inner gas compartment. Since the pressure is equilibrated, only diffusion due to concentration differences occurs while permeation due to pressure differences is prevented. Due to the concentration difference of oxygen across the tube, oxygen molecules diffuse through the porous tube wall. The composition of the gas at the outlet of the outer gas compartment is analysed by a gas chromatograph (GC) and the overall flow is measured by a flowmeter. During the diffusion experiment, atmospheric temperature and pressure in the laboratory are monitored. The mathematical deduction of the equations presented here is given in the annex. The main equation for the diffusion measurement is

$$\frac{2\pi L}{f} = A' \cdot \frac{1}{\Delta x_1} + A'' \quad (6.3)$$

where L is the length of the tube accessible to the diffusion process and Δx_1 is the difference between oxygen concentration outside and inside the tube. A' and A'' are defined in the annex.

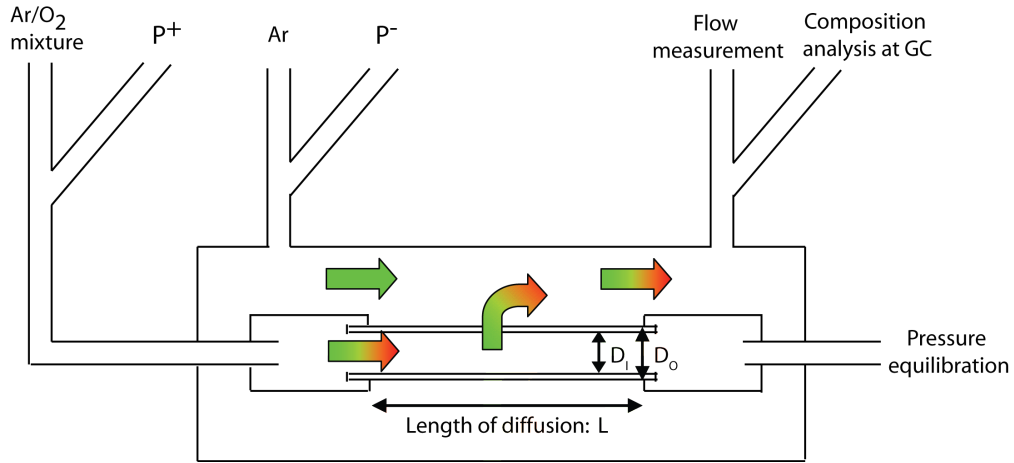


Figure 6.13: Setup of the diffusion test.

The average pore radius contributing to the diffusion process $\langle r \rangle$ is calculated by

$$\langle r \rangle = D_{12} \left[\left(\frac{A'}{2A''} + x_{1,ext} - 1 \right) (D_{1,K}^* - D_{2,K}^*) \right]^{-1} \quad (6.4)$$

and the tortuosity τ is determined by

$$\tau = \frac{\epsilon}{\psi} \quad (6.5)$$

where ϵ is the porosity and ψ is defined in the appendix. A typical result of a diffusion test is shown in Fig. 6.14, where the inverse flow is plotted against the inverse concentration gradient according to equation 6.3 and the slope A' and y-axis intercept A'' can be determined from the straight line. The indicated error bars stem from experimental errors of the flow meters, gas chromatograph and geometrical measurement of the diffusion length L among others. Errors in the measurement of the slope A' and y-axis intercept A'' , the sample's inner and outer radius and the ambient temperature and pressure during the experiment were further error sources leading to the confidence regions of the measured pore sizes $\langle r \rangle$ and tortuosities τ that are presented in Table 6.2.

The extruded tubes of big diameter were not tested. Tubes of type CIP-ZARA were only analysed by the permeation test. As the tubes of type CIP-EPFL used the same pore former and similar compaction pressures as the tubes prepared by VITO, it was assumed that the porous network had the same pore size and tortuosity. The compaction pressure may slightly influence the pore size in early stages of the sintering, but should not change it significantly after sintering at 1300°C.

The values in Table 6.2 show that the pore sizes measured by the diffusion test were systematically smaller than the surface pore sizes measured by mercury porosimetry. This can be caused by the tortuosity of the porous network, as curved pathways of the gas diffusion may restrict the actual cross-sectional area accessible to the diffusion process. Furthermore, mercury intrusion determines the surface pore size which is in the case of irregular shaped pores not

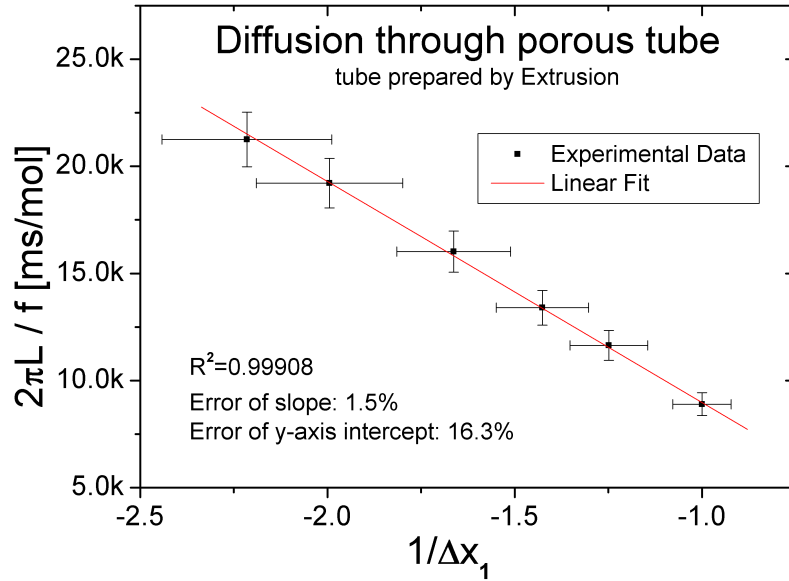


Figure 6.14: Plot of the inverse flow over the inverse concentration gradient according to equation 6.3 of the diffusion test.

Table 6.2: Characteristics of the porous network of the different nickellate tubes that were sintered at 1300°C and afterwards measured by the permeation and the diffusion setup. The pore sizes for the permeation test were determined by mercury intrusion.

Nd _{1.95} NiO _{4+δ} -Tubes		Geometry		Permeation Test		Diffusion Test	
Type	Poreformer	D _{ext} [mm]	D _{in} [mm]	<r _p > [μm]	τ	<r _p > [μm]	τ
CIP-Vito	Rice Starch	6.8	4.4	0.4	2	0.12±0.02	6±3
CIP-Vito	Graphite	6.5	4.2	0.6	1	0.12±0.02	6±3
CIP-Zar	Maize Starch	3.4	2.6	1.5	5		
CIP-EPFL	Rice Starch	4.8	3.6	0.4	1	0.12±0.02	6±3
Ex-SD	-	1.8	1.2	0.9	1	0.22±0.05	14±8
T-SC	-	5.2	4.0	0.4	2	0.5±0.2	13±10

necessarily the same as the volume averaged pore size contributing to diffusion. The tortuosity τ measured by the diffusion test is generally higher than the value measured by the permeation test. However, it can be seen in Table 6.2 that the difference between both tests seems to decrease with increasing diameter of the tubular samples. Metallic tubular samples from a collaborating institute were also tested and the pore size and tortuosity exactly reproduced by the test. Pressure loss inside the tubes during the diffusion test is a plausible explanation for the different results, as the pressures of both gas compartments were equilibrated at the tube entry. The diffusion test showed reasonable results and is a practical tool as it

- determines tortuosity and pore size at the same time and only needs the total porosity as input parameter
- yields directly effective diffusion parameters measured by an application-related process, in contrast to mercury porosimetry or SEM imaging which consider only surface pore sizes
- is applicable to multi-layered systems if the total porosity is known

The results of diffusion tests for tubes of type CIP-VITO and Ex-SD were published [132].

6.5 Supports for Dip-Coating

All types of tubes had surface roughness and grooves on the micrometer-scale. Before dip-coating, all tube types made by slip-casting and CIP were mechanically polished with SiC 800, 2400 and 4000 polishing paper to smoothen the surface. Extruded tubes showed worse results during power loss tests when they were treated mechanically before dip-coating, therefore they were used in as-received state. All tube types were cleaned by compressed air shortly before dip-coating.

As the shrinkage necessary to densify ScSZ TR could not be decreased below 18% until 1300°C (see 5.3.3), the tubular supports must theoretically shrink the exact same amount to allow densification of ScSZ TR during cosintering. With the exception of extruded tubes of small diameter, no tube type disposed of this high shrinkage as the investigated nickelate with a particle size of $d_{v,50}=0.6\ \mu\text{m}$ particle size shrunk only 12-13% until 1300°C. The extruded tubes shrank more due to the presence of substantial amounts of organic additives which decomposed during heating.

When nickelate tubes are used as substrates for cathode-supported SOFC application with zirconia-electrolyte, the tubes have to be made from wet-chemical fabrication processes such as extrusion or dip-coating [95], which enables sufficient shrinkage until 1300°C in order to allow densification of the cosintered zirconia electrolyte layer. Tubes made by CIP (CIP-VITO and CIP-ZARA) and slip-casting (T-SC) showed only 10-13% of shrinkage. The shrinkage curves, measured by dilatometry, of GDC 318-033 AR (GDC AR in table 6.3), GDC-1CD and GDC-2CD and ScSZ TR pellets and tubes prepared by extrusion are shown in Fig. 6.15.

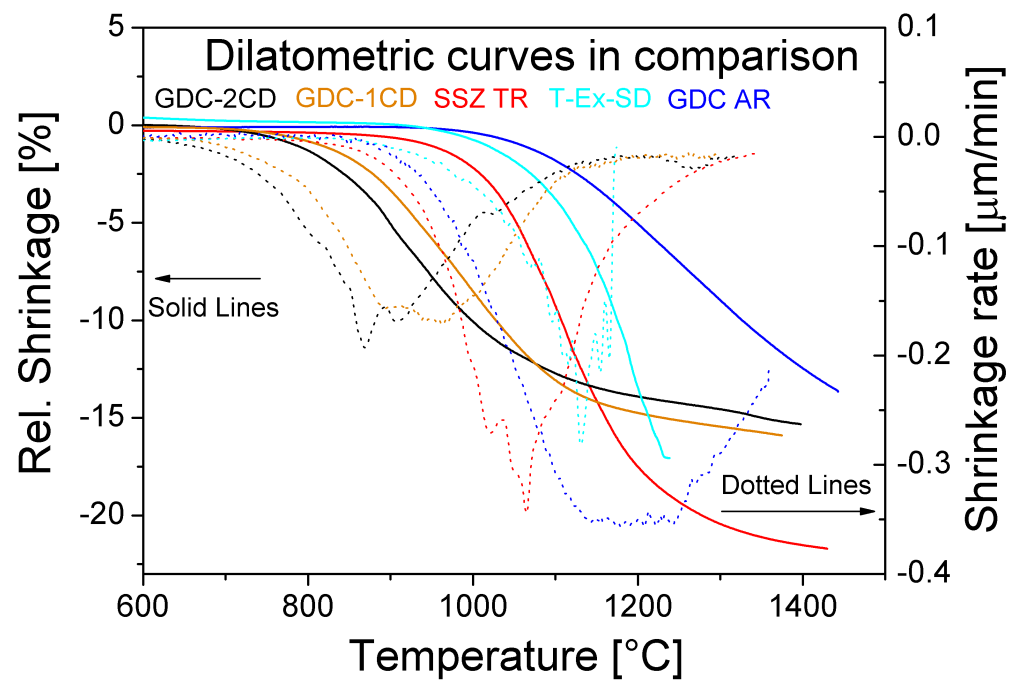


Figure 6.15: Shrinkage curves of extruded nickelate tubes and GDC and ScSZ-powders.

For each curve, the suggested offset-temperature T_s for beginning shrinkage due to sintering, the temperature of maximum densification rate T_{max} and the temperature offset for ending densification T_e is shown in Table 6.3.

Table 6.3: Characteristic temperatures for the shrinkage process of different GDC and ScSZ powders and extruded tubes.

Temp.	GDC-2CD	GDC-1CD	ScSZ-TR	Ex-SD	GDC-AR
T_s	750°C	760°C	950°C	990°C	1020°C
T_{max}	900°C	1000°C	1117°C	1190°C	1240°C
T_e	1070°C	1130°C	1272°C	1260°C	1440°C

Cobalt-doped GDC has the lowest sintering temperature of all materials. ScSZ from Treibacher sinters at slightly higher temperatures, whereas the cathode tubes shrink at the highest temperature of all tested components, except for as-received undoped ceria from Nextech, Lot-Nr. 318-033 (GDC AR). The higher sinter temperature of nickelate tubes leads to tensile stresses in the deposited layers at temperatures $T_s(\text{layers}) < T < T_s(\text{tube})$, as GDC and ScSZ layer would shrink but are restrained by the substrate. While GDC has shown to cope rather well with constrained sintering [108], zirconia electrolyte layers easily spall or delaminate from a substrate when sintered under tension.

In the present case, the shrinkage of GDC-CD at lower temperature helps to alleviate tensile stresses in the ScSZ layer, but the "later" shrinkage of the nickelate tubes is not optimal and leads to tensile stresses in both layers. A lower sintering temperature can be achieved in a certain range by particle size reduction and in a larger range by sinter additives.

GDC-layers deposited from water or isopropanol-based suspensions showed good mechanical adherence to the substrate even after insufficient shrinkage during sintering in this work, while ScSZ-layers spalled from the substrates after constrained sintering as described elsewhere [108].

It was therefore tried to simplify the system involving tubes with shrinkages $\leq 14\%$ and deposit only a GDC electrolyte layer from isopropanol-based suspension instead of GDC/ScSZ double layers. The GDC layers still sinter under constrained conditions as the substrate's shrinkage is less than what the GDC layer would need for complete densification, but it can lead to reasonably densified layers. In Table 6.4, an overview of the designated cell designs from the respective fabrication method is given. Tubes of type CIP-VITO, CIP-ZARA, CIP-EPFL and T-SC were only used for the simplified system: NNO (Cathode) - GDC (Electrolyte) - NiO/GDC (Anode). As GDC becomes an electronic conductor above 600°C [103], this system is limited to temperatures below 600°C where the nickelate material shows better electrical conductivities but much reduced oxygen kinetics due to high activation energies [133][24][34]. Extruded tubes of type Ex-SD were used for the originally targeted system: NNO (Cathode) - GDC (Interlayer) - ScSZ (Electrolyte) - NiO/YSZ(or Ni/GDC) (Anode).

Chapter 6. Nickelate Tubes

Table 6.4: Proposed cell configuration for each fabrication type. C=Cathode, I=Interlayer, E=Electrolyte, A=Anode

Tube Type	Shrinkage to 1300°C	Proposed System
CIP-VITO	10-12%	NNO(C) / GDC(E) / Ni-GDC(A)
CIP-ZARA	11%	NNO(C) / GDC(E) / Ni-GDC(A)
CIP-EPFL	14%	NNO(C) / GDC(E) / Ni-GDC(A)
Ex-SD	18%	NNO(C) / GDC(I) / ScSZ(E) / Ni-GDC(A)
		NNO(C) / GDC(I) / ScSZ(E) / Ni-YSZ(A)
T-SC	12%	NNO(C) / GDC(E) / Ni-GDC(A)

7 Chemical Compatibility

In this chapter, chemical reactivity of adjacent layers in the utilised tube design is shown and evaluated.

7.1 GDC-NNO interfaces

In this section, the reactivity of NNO with GDC will be evaluated, as it is one important factor for the fabrication route, especially sintering temperature and dwell time, of cosintered NNO-GDC half cells (case: cathode-supported cells) and NNO-electrodes sintered on already densified supports (case: anode-and electrode-supported cells).

7.1.1 Diffusion couples

Diffusion reaction couples of GDC/NNO powder mixtures were prepared and exposed to different temperature / time combinations. Therefore, the GDC powder 318-033 and fourth batch nickelate powder were mixed in 50:50 vol% quantities and uniaxially pressed to pellets of 9 mm diameter and ca. 4-5 mm of height. The compaction pressure was 157 MPa during 2 minutes. Intact pellets were extracted from the pressing mould and subsequently exposed to different reaction temperatures, in the range of 700-1300°C, and dwell times, in the range of 2-24 hours. The heating and cooling rate for the exposed pellets was 3 K/min. The different sample reaction conditions are shown in Table 7.1.

The temperature range 700-800°C can be considered realistic for SOFC-application which is why the dwell times at these temperatures was extended to 24 hours. For temperatures $\geq 900^\circ\text{C}$, the reaction happens during sintering. The dwell time for samples in the temperature range 900-1300°C was consequently limited to a typical sintering dwell time of 2 hours. The reacted pellets are shown in Fig. 7.1. Colour changes were visible to the naked eye. The colour changed from black to a greyish dark green from 700-900°C, and distinctly from dark to light green from 1000-1300°C. Similar results were obtained by Lalanne [31], who has tested reactivity between NNO and electrolytes at exposition durations as long as 1 month and found distinct colour

Table 7.1: Overview of reaction temperature - dwell time combinations that were used for GDC-NNO reaction couples.

Sample Nr.	Reaction Temperature	Reaction Time
1	700°C	24h
2	800°C	24h
3	900°C	2h
4	1000°C	2h
5	1100°C	2h
6	1200°C	2h
7	1300°C	2h

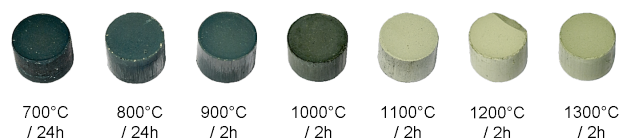


Figure 7.1: Reaction couples exposed to different temperature-time combinations.

changes for reaction temperatures above 900°C. X-ray diffraction (XRD) was conducted to identify the phases responsible for the colour change. The measurements were done in a classical θ -2 θ mode with 2 θ between 20-90° with a 0.02°-stepsize and 2 sec/step data collection time on a Bruker 8 Discovery diffractometer. The results were interpreted using the EVA-software code with ICCD-data sheets to identify the best fitting phases. The found phases and the respective ICCD-data sheet numbers are shown in Table 7.2. The XRD-scans and the indicated

Table 7.2: Identified phases and the utilised ICCD data base entries.

Phase	$\text{Nd}_{1.95}\text{NiO}_{4+\delta}$	10GDC	$\text{Nd}_{0.4}\text{Ce}_{0.6}\text{O}_{1.8}$	$\text{Nd}_{0.5}\text{Ce}_{0.5}\text{O}_{1.75}$	NiO	$\text{Nd}_4\text{Si}_3\text{O}_{12}$
ICCD-Nr.	01-089-0131	01-075-0161	01-075-0155	01-075-0156	01-089-7101	00-042-0171

present phases from 700-1100°C are shown in Fig. 7.2. Up to 900°C, no distinct reaction took place. Lalanne [31] has found the formation of phases such as NdNiO_3 already at 800 and 900°C after 1 month of dwell. The kinetics of the reaction at these temperatures however is slow enough to be considered irrelevant for typical sintering durations. After dwelling at 1000°C for 2 hours, additional peaks due to the formation of a reaction product between GDC and NNO appear. For temperatures $\geq 1100^\circ\text{C}$, this product is the main crystalline phase, as NNO and GDC peaks completely disappeared for $T > 1000^\circ\text{C}$ and $T > 1100^\circ\text{C}$ respectively. The peaks for the reaction product fitted best to the mixed oxide $\text{Nd}_x\text{Ce}_{1-x}\text{O}_{2-x/2}$ of cubic symmetry. Peaks at higher diffraction angles of $\text{Nd}_{0.4}\text{Ce}_{0.6}\text{O}_{1.8}$ (cf. Table 7.2) were slightly shifted to lower 2 θ values with respect to the observed pattern and peaks of $\text{Nd}_{0.5}\text{Ce}_{0.5}\text{O}_{1.75}$ were slightly shifted

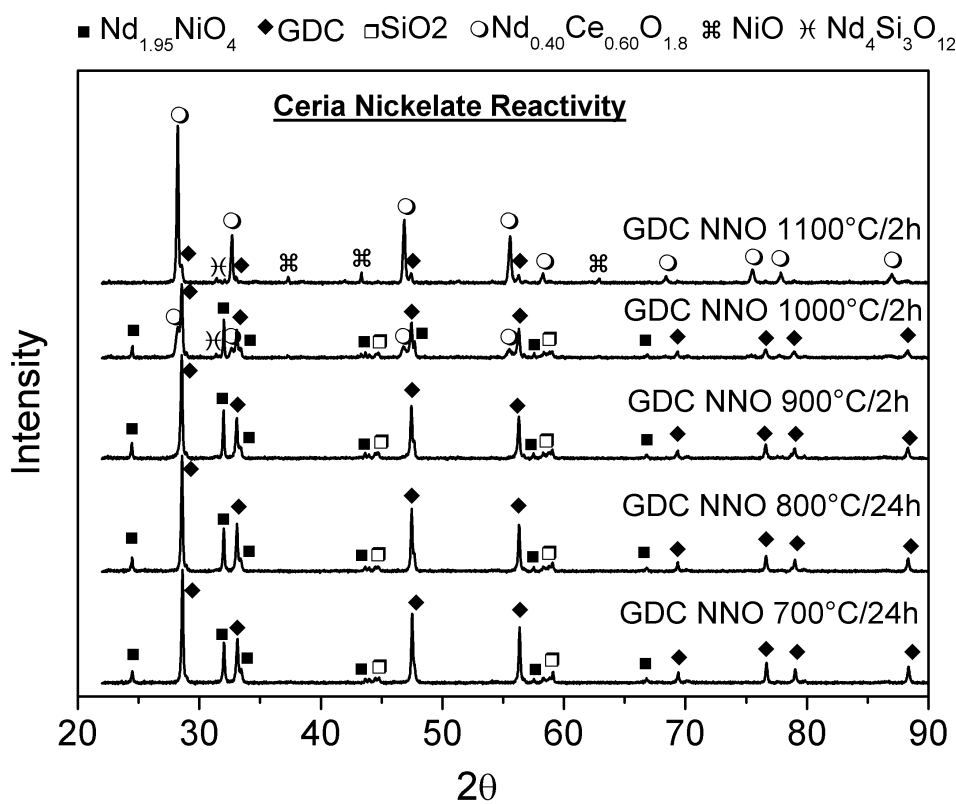


Figure 7.2: XRD-scans and phases of reaction couples exposed to 700-1100°C.

to higher 2θ values, indicating an intermediate stoichiometry of $\text{Nd}_{0.40-0.50}\text{Ce}_{0.60-0.50}\text{O}_{1.80-1.75}$. A Si-amount of ca. 1 at% is present as endogeneous impurity in neodymium nickelate powder. As it is poorly crystallised, the peak heights are small and the phase difficult to distinguish. From 1000-1300°C on, peaks of $\text{Nd}_4\text{Si}_3\text{O}_{12}$ are visible, as Si reacts with Nd to form neodymium silicate according to equation 5.2. The XRD-results for reaction couples exposed to temperature 1100-1300°C are shown in Fig. 7.3.

$\text{Nd}_x\text{Ce}_{1-x}\text{O}_{2-x/2}$ is the main crystalline phase and additional peaks of NiO and $\text{Nd}_4\text{Si}_3\text{O}_{12}$ prove that NNO is partially desintegrated. $\text{Nd}_x\text{Ce}_{1-x}\text{O}_{2-x/2}$ can be described as a Nd-doped CeO_2 , which can be considered a reasonable conductor as shown by Hagiwara et al. [134]. Therefore, its phase formation is not the critical factor in the determination of NNO sinter temperature for optimum performance. The XRD-results were further analysed in Bilbao, Spain, by Ri-

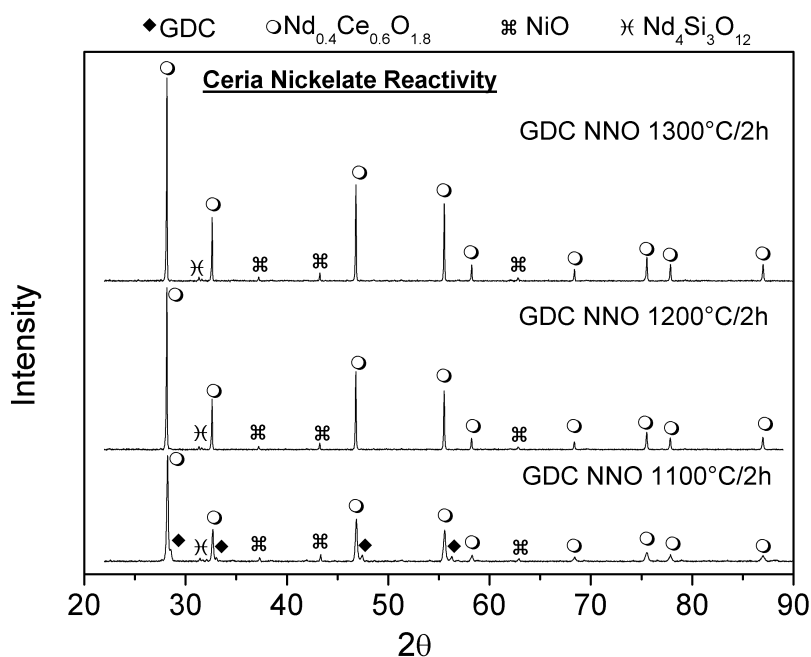


Figure 7.3: XRD-scans and phases of reaction couples exposed to 1100-1300°C.

etveld refinement by Aitor Larrañaga in a collaboration to quantify the amounts of the formed phases. The results are shown in Fig. 7.4. The amount of formed $\text{Nd}_x\text{Ce}_{1-x}\text{O}_{2-x/2}$ is higher than what could have been expected from the XRD patterns. While the mixed oxide is the main crystalline phase for $T \geq 900^\circ\text{C}$ in Rietveld analysis, its peaks in XRD patterns are only clearly distinguishable for $T \geq 1000^\circ\text{C}$. The difference can be explained by partial peak overlapping, which may overestimate the amount of $\text{Nd}_x\text{Ce}_{1-x}\text{O}_{2-x/2}$.

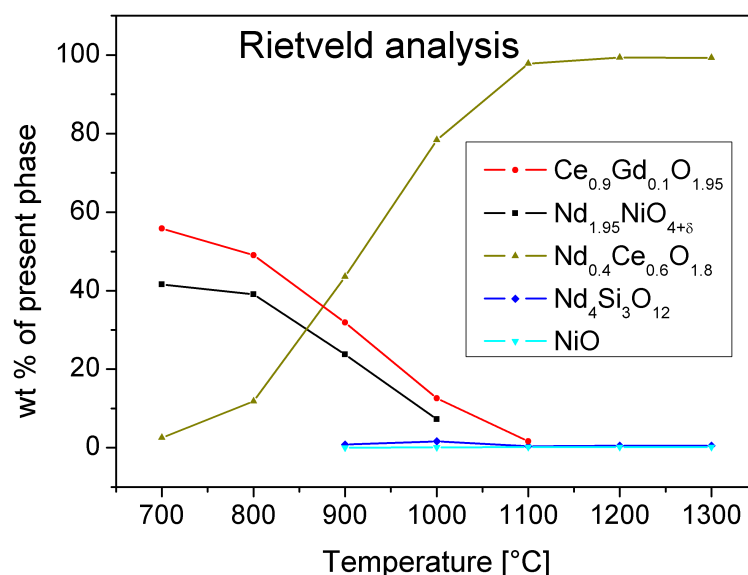


Figure 7.4: Rietveld refinement results of phase quantities in GDC-NNO reaction couples.

7.1.2 Symmetrical 3-electrode cells

Further proof of reactivity between GDC and NNO was found by post-mortem SEM-EDX analysis of cross-sections of symmetrical NNO/GDC/NNO pellets used for electrochemical tests (cf. chapter 8). The microstructure of NNO electrodes sintered at temperatures of 1000-1300°C/2h on already densified GDC pellets is shown in Fig. 7.5. The nickelate electrode particles appeared fine-grained for $T=1000^\circ\text{C}/2\text{h}$ and $T=1100^\circ\text{C}/2\text{h}$, whereas slightly coarser particles were seen for $1200^\circ\text{C}/2\text{h}$ and distinct particle coarsening was observed for $1300^\circ\text{C}/2\text{h}$, as oversintering led to substantial grain growth. For NNO-electrodes sintered at $1000^\circ\text{C}/2\text{h}$, delaminations such as shown in Fig. 7.5a were observed. The lacking adhesion of NNO to GDC pellets was probably caused by missing reactivity, as the NNO electrode easily detached from the GDC-pellet's surface.

Element quantifications were performed by SEM-EDX in rectangular regions of ca. $0.5\ \mu\text{m}$ rectangle thickness, starting from the GDC-NNO interface up until ca. $2\ \mu\text{m}$ into GDC and NNO. The results are shown in Fig. 7.6.

After 2h at 1000°C , no substantial reaction was observed. Small amounts of Nd and Ce may have actually diffused, but the measurement in the first rectangular section may also very well be influenced by the adjacent material as the interface was not perfectly straight-lined.

After sintering at $1100^\circ\text{C}/2\text{h}$ and $1200^\circ\text{C}/2\text{h}$, a reaction layer of ca. $0.5\ \mu\text{m}$ thickness had formed on both sides of the interface. The amounts of Nd and Ce inside the reaction layer approach each other as the temperature increases, however, the reaction layer must be considered to consist of two phases, i.e. $\text{Nd}_x\text{Ce}_{1-x}\text{O}_{2-x/2}$ and the bulk material, as the reaction is kinetically

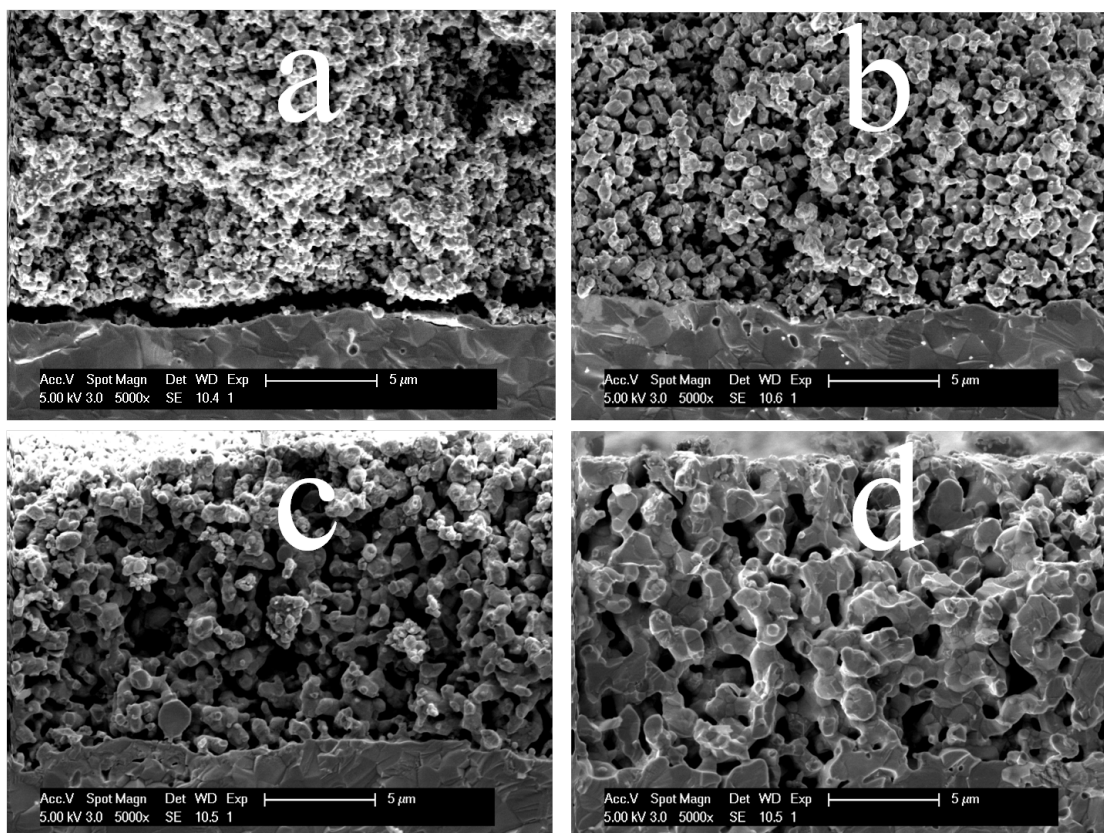


Figure 7.5: The microstructure of NNO-electrodes in GDC-NNO-GDC symmetrical pellets. a: 1000°C/2h, b: 1100°C/2h, c: 1200°C/2h, d: 1300°C/2h

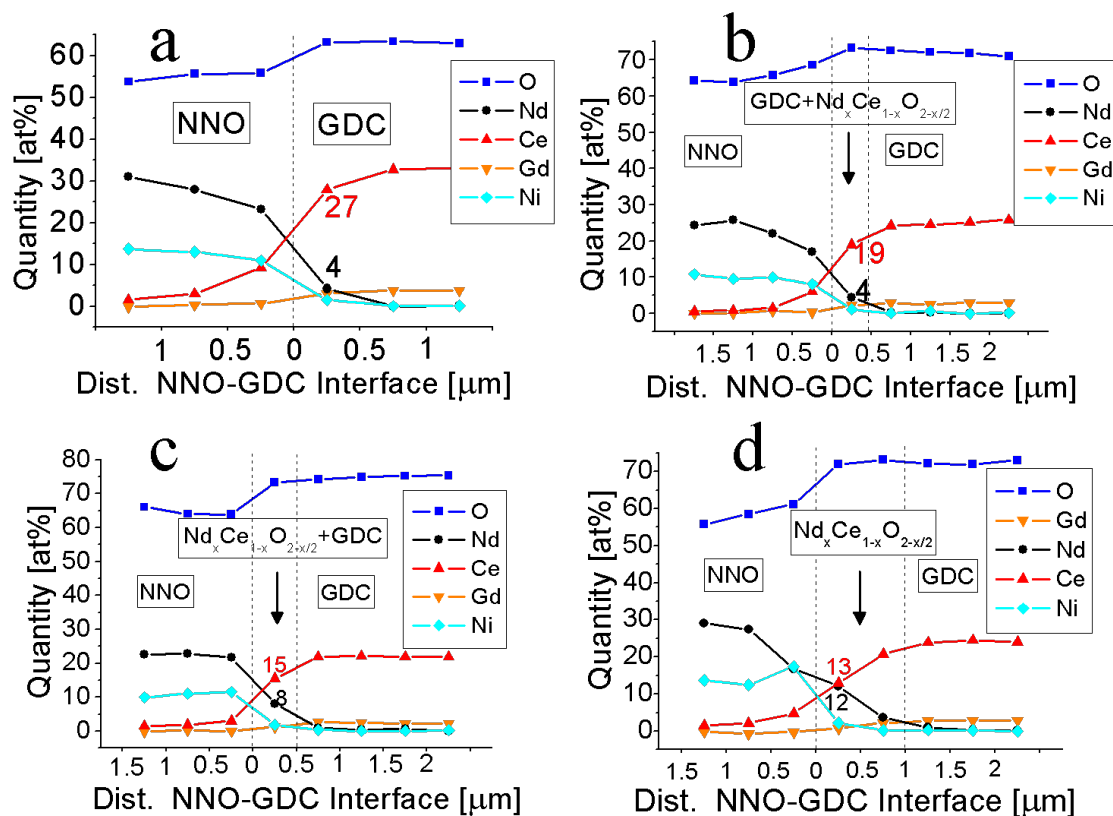


Figure 7.6: SEM-EDX element quantifications across the GDC-NNO interface in symmetrical GDC-NNO-GDC 3-electrode pellets. Quantifications were done in rectangular areas of $0.5 \mu\text{m}$ thickness. a: $1000^\circ\text{C}/2\text{h}$, b: $1100^\circ\text{C}/2\text{h}$, c: $1200^\circ\text{C}/2\text{h}$, d: $1300^\circ\text{C}/2\text{h}$. The red and black numbers indicate the Ce- and Nd-content in the reaction layer, respectively.

hindered in comparison to diffusion couples. This is due to the smaller contact zones between GDC and NNO particles in a layered arrangement compared to diffusion couple pellets, where more GDC-NNO interface area exists due to intimate powder particle mixing.

After sintering at 1300°C/2h, a reaction zone of ca. 1 µm was formed on both sides of the former interface. The concentrations of Nd and Ce, that were quantified inside the reaction layer on the GDC side of the interface, amounted to 12 and 13 at% respectively. Assuming the measured amounts of elements are completely incorporated in the mixed oxide, the respective element quantities lead to a stoichiometry of Nd_{0.48}Ce_{0.52}O_{1.76}, which is in the range predicted by XRD measurements on diffusion couples.

The post-mortem SEM-EDX analysis of GDC/NNO/GDC 3-electrode cell cross-sections also showed the precipitation of Ni from Nd_{1.95}NiO_{4+δ} at the NNO/GDC interface by element mapping, which is also evidenced by an increase in Ni-concentration towards the interface in the quantification by EDX (cf. Fig. 7.6d). Maps of Nd, Ni and Ce of an NNO-electrode sintered at 1300°C/2h on a GDC-pellet are shown in Fig. 7.7. Ni separation at the interface is distinctly visible, as spots of high Ni-concentration coincide perfectly with spots of low Nd-concentration. Ce diffusion into NNO was confirmed as well.

7.2 GDC-Zirconia interfaces

In this section, the reactivity of 10GDC with yttria- and scandia-doped zirconia will be investigated. This is an important parameter as the reaction products possess ionic conductivities of 1-2 orders of magnitude smaller than 10GDC or ScSZ and should therefore be avoided. As adjacent GDC- and ScSZ-layers are cosintered, the reactivity is also higher than for layers that are sintered on already densified substrates [135].

The 10GDC powder of nominal composition 90mol%CeO₂-10mol%GdO_{1.5} used in this study was from Fuel Cell Materials, Lot-Nr.318-033. 10 ScSZ powders of nominal composition 89mol%ZrO₂-10mol%Sc₂O₃-1mol%CeO₂- from Praxair (ScSZ PR) and Treibacher (ScSZ TR) were used. 10YSZ of nominal composition 90mol%ZrO₂-10mol%Y₂O₃ was from Tosoh's TZ-10YS series, Lot-Nr.S104515P. The characteristics of the used powders are shown in Table 7.3. Powder mixtures of 50-50 vol% were prepared by mixing the respective powder quantities

Table 7.3: Characteristics of the used electrolye powders.

	10GDC	10YSZ	ScSZ PR	ScSZ TR
d _{v,10} [µm]	0.09	0.14	0.63	0.09
d _{v,50} [µm]	0.25	0.44	1.03	0.21
d _{v,90} [µm]	1.15	1.11	1.83	0.45
SSA [m ² /g]	11	6	10	14

in a mortar for 10 minutes. The powder mixtures were compacted by uniaxial pressing in a cylinder-shaped pressing mould with a diameter of 9 mm. The compaction pressure of

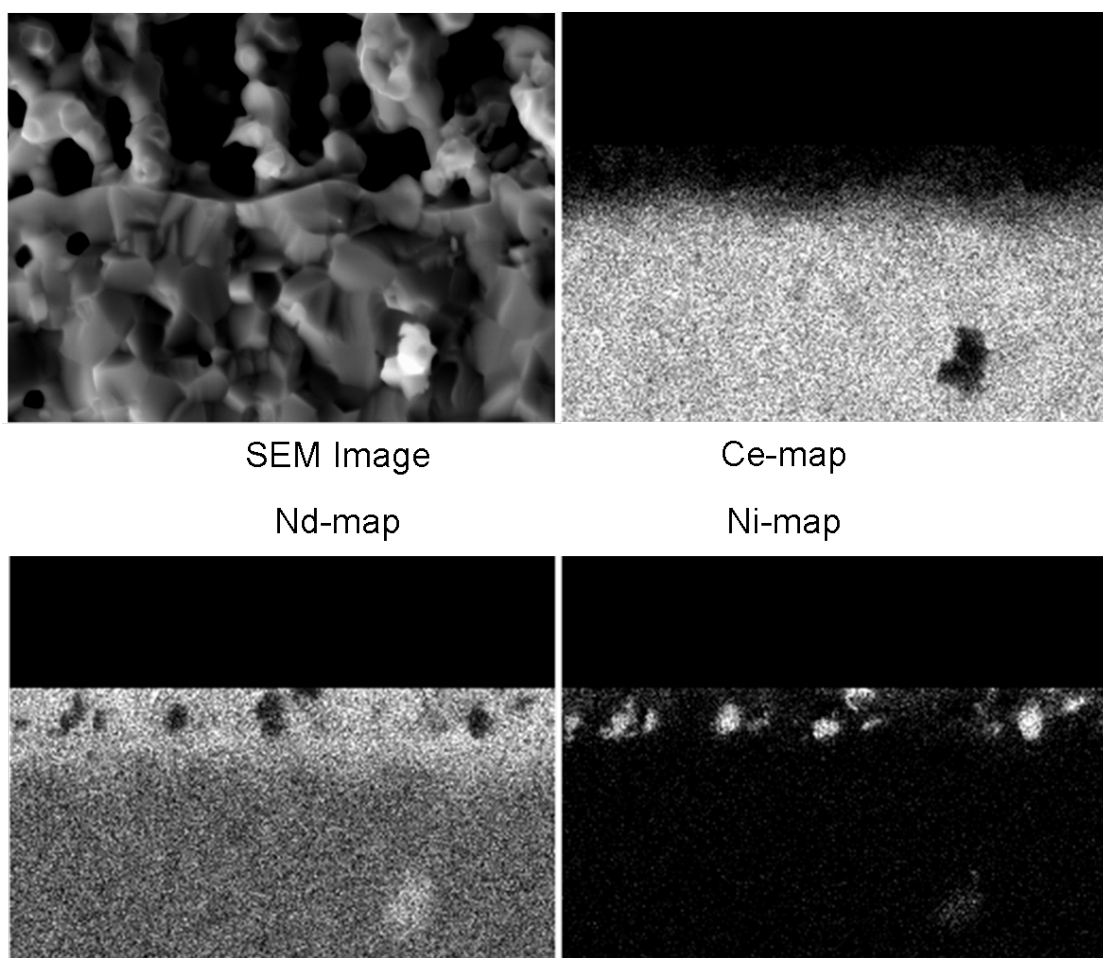


Figure 7.7: SEM-EDX element concentrations maps across the GDC-NNO interface in symmetrical GDC-NNO-GDC 3-electrode pellets sintered at 1300°C/2h.

157 MPa was applied during 2 minutes before it was slowly decreased. Intact pellets of ca. 4 mm height were extracted from the mould and subsequently exposed to different reaction temperatures, in the range of 1250-1350°C, and dwell times, from 1-8 hours under air. For the reaction process, the pellets were placed in an alumina crucible on a powder bed of the same composition as the pellet itself. Heating and cooling was done with a rate of 3 K/min. The reacted pellets were analysed by XRD on a Bruker D 8 Discover. The scans were made with standard θ - 2θ mode with 2θ between 20-90° with a 0.02°-stepsize and 1 sec/step data collection time. The used ICCD-cards for phase identification are shown in Table 7.4.

Table 7.4: Present electrolyte phases and the utilised ICCD data base entries.

Phase	10GDC	10ScSZ	10YSZ
ICCD-Nr	01-075-0161	01-089-5478	00-030-1468

Rietveld refinement was done after the scans were repeated with better signal/noise ration by the collaboration with Dr. Aitor Larrañaga in Bilbao, Spain.

In the refinement routine, 50 vol% 10GDC - 50 vol%zirconia mixtures were presupposed. After the reaction, two solid solutions were present, a zirconia-rich and a ceria-rich one. For these two phases, the occupational factor of phase 1 was cycled until the refinement was stable and a certain stoichiometry of phase 1 solid solution was defined. The ATZ parameter (molecular weight times atomic number) was readjusted and the weight percentages of both phases recalculated. Then, the Zr/Ce ratio for phase 2 was calculated in order to obtain a total amount of 50 vol% 10GDC-50 vol%zirconia. This calculation affected the ATZ parameter of phase 2, which changed the weight percentage of both phases. With these new phase quantities, the Zr/Ce ratio in phase 2 was recalculated which changed the ATZ factor which changed the phase weight percentage and so on. The procedure was repeated until the differences between each cycle were negligible.

7.2.1 GDC-10ScSZ

The result of the XRD analysis is shown in Fig.7.8. It can be seen that for all selected reaction temperature / time combinations the 2θ peak positions of 10GDC and ScSZ PR were shifted with respect to the peaks for the as-received powders. A shifting peak position signifies a changing lattice constant which is in this case due to cation diffusion. The shift generally increased with rising reaction temperature and/or time and was more pronounced for ScSZ than for 10GDC, which means that ceria diffused quicker into ScSZ than zirconia diffused into 10GDC, which was reported by other authors [136, 137, 138, 139]. As Ce-diffusion was faster than diffusion of Zr in the opposite direction, it led to decreasing 10GDC-peak heights, as 10GDC was slowly decomposed, and an increasing amount of ScSZ with incorporated Ce and hence increasing peak heights. This was confirmed by the results of Rietveld refinement shown in Fig. 7.9. The Zr-rich solid solution reached almost complete intermixture of the

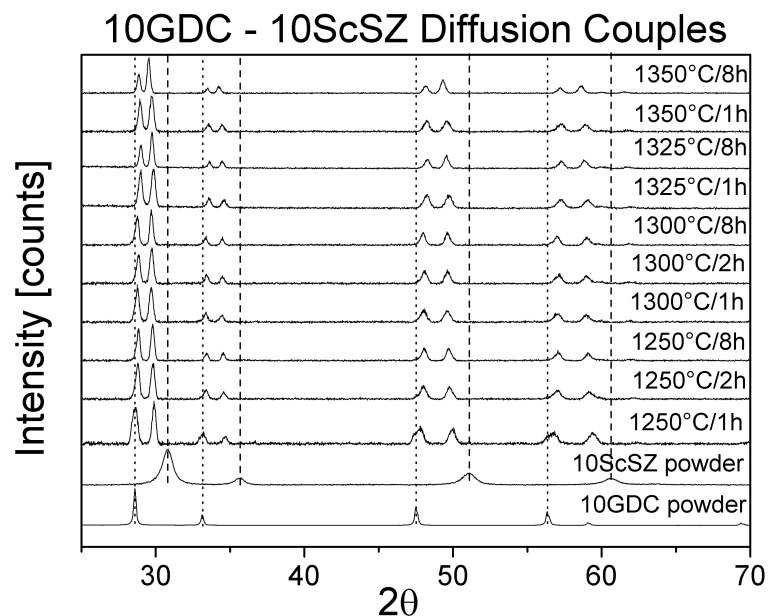


Figure 7.8: XRD-scans and peak shifts of 10GDC and 10ScSZ over the whole investigated range.

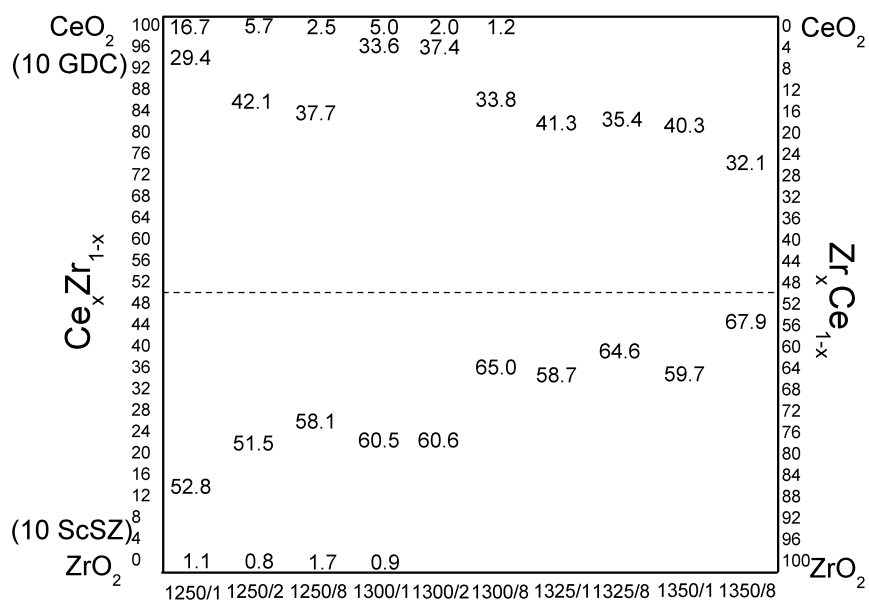


Figure 7.9: Calculated amounts and composition of solid solutions for all investigated 10GDC-10ScSZ reaction couples.

A-site, or $\text{Zr}_{0.5}\text{Ce}_{0.5}$, at 1350°C , whereas the Ce-rich solid solution still possessed more than 70% Ce on its crystallographic A-site.

As ScSZ PR was rather coarse and sintered at higher temperatures, the influence of ScSZ-granulometry on the measurement was analysed by using ScSZ TR in one 10GDC-ScSZ TR reaction couple exposed to 1300°C for 2 hours. As ScSZ TR is very sinteractive and fine-grained, the two cases/ScSZ-materials can be considered contrarian. The results of Rietveld refinement in comparison to ScSZ PR are shown in Fig. 7.10. While the reactivity of ScSZ TR with 10GDC

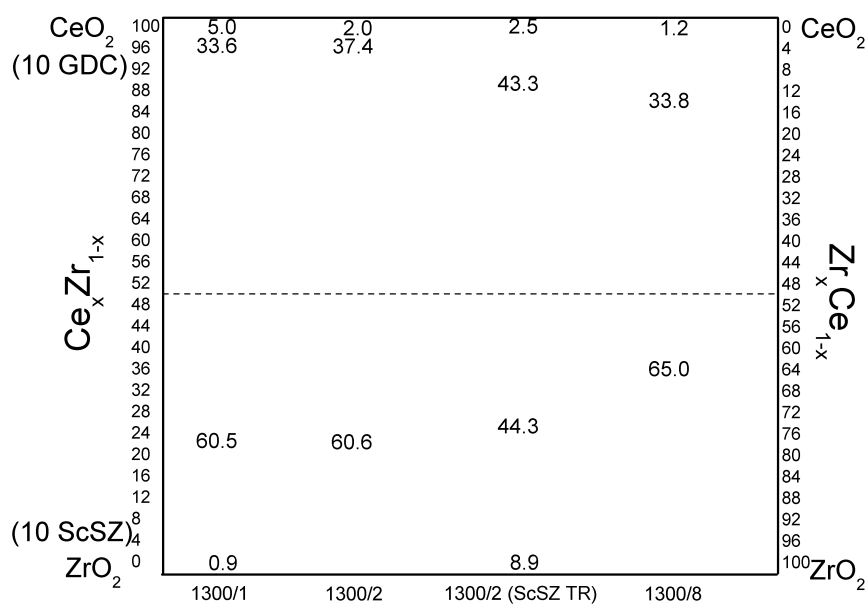


Figure 7.10: Calculated amounts and composition of solid solutions for ScSZ PR and ScSZ TR used in the diffusion couple at $1300^\circ\text{C}/2\text{h}$ and the surrounding reaction couples.

was slightly higher than for ScSZ PR, the difference was still relatively small which can be explained by the cation diffusion lengths. For 10GDC-YSZ interfaces, diffusion lengths of several micrometers for Ce and Zr were found at 1300°C [137]. As the diffusion length was several times greater than the grain diameter, the influence of the grain size on the reactivity was relatively small in the investigated range of conditions.

7.2.2 GDC-10YSZ

The results of XRD-analysis are shown in Fig. 7.11. It can be seen that the peak shift and change of the peak shape was much more pronounced than for 10ScSZ. The composition of the solid solutions after the reaction are analysed by Rietveld and shown in Fig. 7.12. The refinement of the occupational factor, as it was done for 10GDC-ScSZ mixtures, could not be performed for 10GDC-10YSZ due to the strong overlap. Deconvolution of the overlapped (111)-plane diffraction signal was used to calculate the cell parameters, and hence their

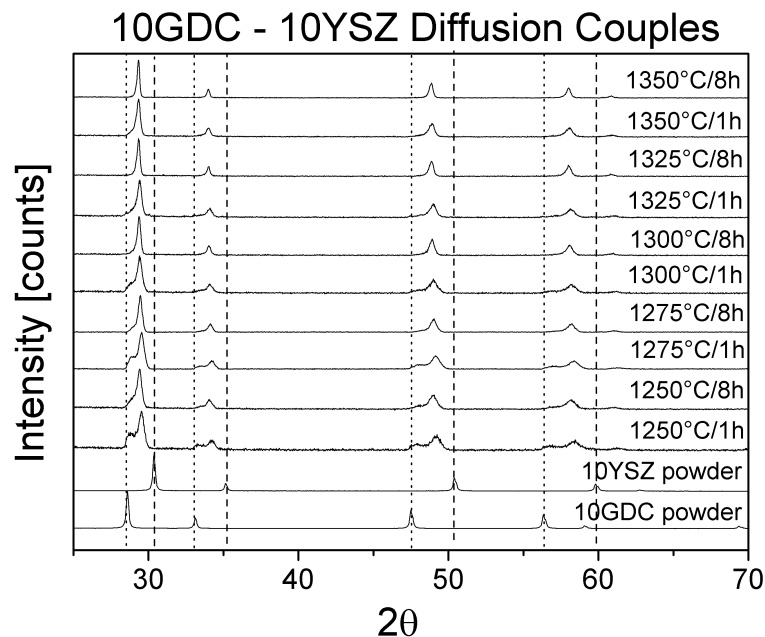


Figure 7.11: XRD-scans and peak shifts of 10GDC and 10YSZ over the whole investigated range.

volumes, as well as to simulate the intensities which can be extrapolated to a phase percentage. The deconvolution of the overlapped peaks for 1250°C/1h is shown in Fig. 7.12. The lattice parameter was used to calculate the composition, i.e. the stoichiometry $\text{Ce}_x\text{-Zr}_{1-x}$, assuming Vegard's rule, which was already validated [140, 141] for this system. The results of these calculations are shown in Fig. 7.13.

It can be seen that already at 1250°C, almost complete intermixing of the A-site occurs for 10GDC as well as for 10YSZ. This means that the incorporation of Zr- and/or Y-cations into 10GDC and the incorporation of Ce- and/or Gd-cations into 10YSZ is facilitated with respect to the 10GDC-ScSZ reaction couple.

In the fluorite structure (cation coordination number 8 [142]), the ionic radii of the cations in the investigated zirconia compounds are $\text{Zr}^{4+}=0.84\text{\AA}$, $\text{Sc}^{3+}=0.87\text{\AA}$, $\text{Y}^{3+}=1.02\text{\AA}$. As the ionic radii of cations in 10ScSZ are closer than for 10YSZ, higher lattice strain in 10YSZ than in ScSZ may be an explanation for the increased diffusivity/reactivity.

In summary, 10GDC and ScSZ may be cosintered up to short sinter dwell times (≤ 2 hours) at 1250°C, whereas the temperature of cosintered 10GDC- and YSZ-layers should be kept well below 1250°C. A lower sintering temperature evokes higher challenges to guarantee gas-tightness of the electrolyte layer after sintering. Therefore, the sintering profile constitutes a compromise between reactivity/diffusion and sintering/densification considerations.

The Kirkendall effect due to different diffusion speeds of Ce- and Zr-cations was routinely observed at the interface of adjacent GDC- and ScSZ TR layers after sintering at 1300°C/2h, as

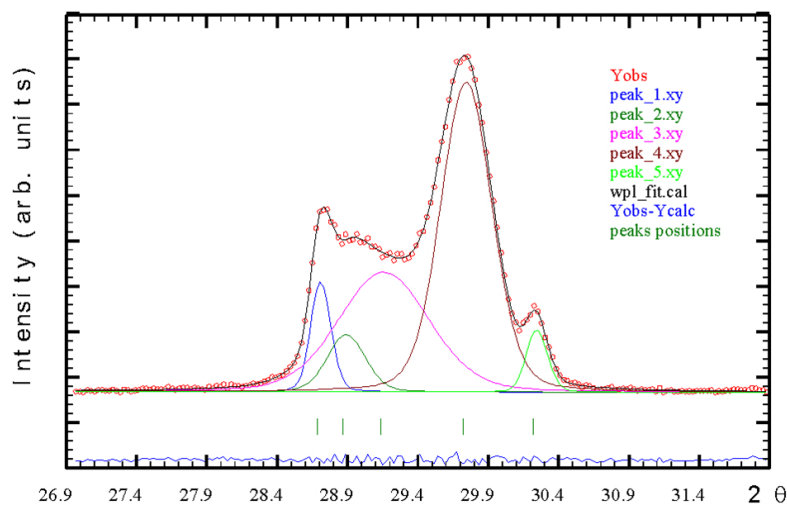


Figure 7.12: Deconvolution of the overlapped peak for the 10GDC-YSZ reaction couple at 1250°C/1h. "peak_1" corresponds to GDC, "peak_5" corresponds to 10YSZ, and "peak_2-4" correspond to GDC-YSZ solid solutions. The differential plot "Yobs-Ycalc" shows excellent agreement.

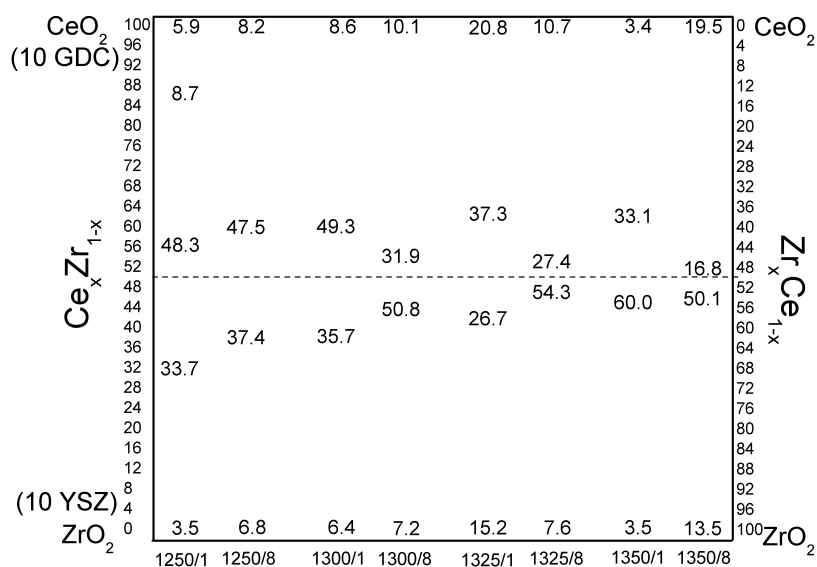


Figure 7.13: Calculated amounts and composition of solid solutions for all investigated 10GDC-10YSZ reaction couples.

shown in Fig. 7.14.

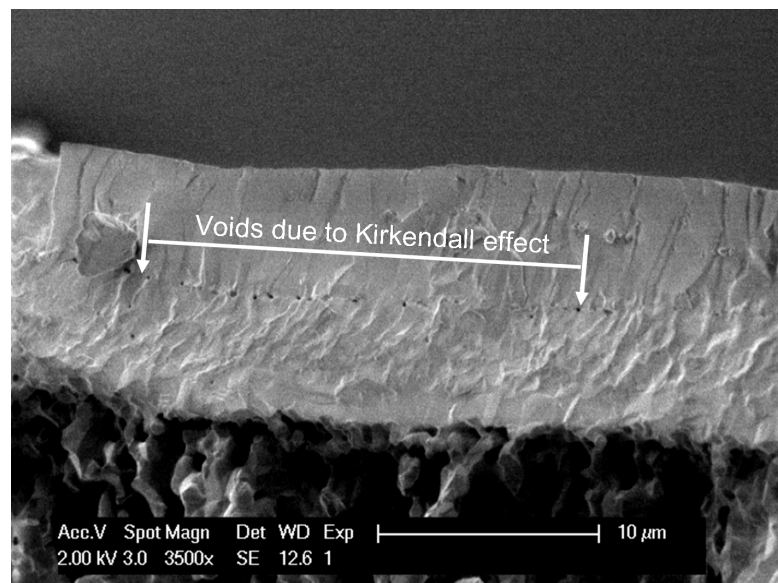


Figure 7.14: Kirkendall effect, pore formation at the GDC-ScSZ interface due to different diffusion speeds.

7.3 ZrO_2 -NNO interfaces

The chemical interactions between zirconia and neodymium nickelate were studied by Lalanne [31]. Contrarily to GDC-NNO, where the composition of reaction products was largely unidentified, in the case of YSZ-NNO the perovskite-structured NdNiO_3 was found for ageing conditions between 800-900°C. Furthermore, the formation of $\text{Nd}_2\text{Zr}_2\text{O}_7$ was observed for reaction temperatures $\geq 900^\circ\text{C}$, and constituted the only reaction product for $T \geq 1000^\circ\text{C}$. The latter can be assumed to be a poor conductor due to its pyrochlore structure of lower lattice symmetry. This implies that the sinter conditions for NNO-cathodes on ZrO_2 electrolyte must be limited to lower temperatures to avoid substantial reaction, thereby limiting the mechanical adhesion of NNO to the electrolyte. Consequently, delaminations between NNO and YSZ were observed for sinter temperatures $< 1100^\circ\text{C}$ [133].

The positive influence of a GDC interlayer was observed elsewhere [36], leading to enhanced contact areas between NNO and GDC as compared to NNO/YSZ and enhanced performance with increasing cathode sinter temperature up to 1150°C.

A further explanation for the improvement of thermomechanical and electrochemical properties is provided by the TECs of the different materials (cf. Fig. 5.39). GDC has a TEC intermediate between NNO and YSZ, thereby alleviating thermal stresses, which leads to lesser risk of mechanical failures such as delamination. However, even for NNO-cathodes sintered on GDC-electrolyte pellets, temperatures of $> 1000^\circ\text{C}$ were experimentally found necessary to avoid delaminations (cf. Fig. 7.5 a, b).

8 Electrochemical Characterisation of the used nickelate

In this section, the electrochemical characterisation of NNO-GDC interfaces will be shown. The focus was hereby mainly on the characterisation of the GDC/NNO interface by exchange current density measurements and the variation of preparation conditions such as sintering temperature of NNO, current collection method etc. as impedance spectroscopy has already been conducted in detail on $\text{Nd}_2\text{NiO}_{4+\delta}$ cathode thin films on YSZ electrolyte pellets by Mauvy [22, 34] as well as $\text{La}_2\text{NiO}_{4+\delta}$ cathodes on SDC electrolyte pellets by Perez-Coll [32]. Nevertheless, impedance spectroscopy was also performed and the results compared to literature values. Long term tests were made to study the influence of Cr-deposition on the degradation of NNO-electrodes.

8.1 Motivation

The exchange current density is the central parameter to describe the quality of an electrode-electrolyte interface with respect to its electrochemical activity. A higher current exchange density translates to a higher electrochemical activity and lower activation losses due to the ionic charge transfer through the electrode-electrolyte interface. Besides the important information about the optimum sintering temperature of NNO on GDC and the related exchange current density, which is a central parameter to quantify and simulate the losses in a single cell due to activation polarisation of the GDC-NNO interface, these measurements also showed sensibility of nickelates to Cr-deposition and reactivity with GDC by post-mortem analysis.

The mechanism of Cr-positioning of cathodes involves the diffusion of volatile gaseous Cr-species such as CrO_3 (in dry atmosphere) or $\text{CrO}_2(\text{OH})_2$ (in wet atmosphere) [143] and reaction with Sr- and Mn-containing cathode materials to form chromate phases such as SrCrO_4 at the cathode surface. Since nickelates are Sr, Mn- free cathode materials, they were expected to show much improved resistance against Cr-degradation. This hypothesis was verified in the scope of this work and published [144].

8.2 1st series of measurements

GDC powder by Nextech, Lot-Nr. 318-033, was used to produce pellets by uniaxial pressing. B-1000 from Duramax, Lot-Nr. 5647353, was added as binder which allowed the removal of crack-free pellets from the mould after compaction at 80 MPa. The pellets were sintered at 1300°C /2h as simulated tube fabrication temperature and had a sinter density of 85-90%. As-received neodymium nickelate powder was mixed in a mortar with a 3 wt% solution of ethyl cellulose in terpineol until a homogeneous suspension was obtained.

One layer of NNO-suspension was deposited through a circular screen of a diameter of 8 mm congruently on both sides of the GDC-pellets. Furthermore, a reference electrode of the same nature was deposited by brush painting on the face of the working electrode following the suggestions for correct electrode placement by Nagata et al. [145], which implies that the distance between working and reference electrode was at least 5 times the electrolyte's thickness.

Following the deposition and drying, the electrodes were sintered at 1300°C /2h to simulate the cofiring temperature of micro-tubular cells. Gold meshes were hot pressed onto the electrodes at 1040°C under a load of ca. 5 N/cm². The complete single cell is shown in Fig. 8.1. An air flow

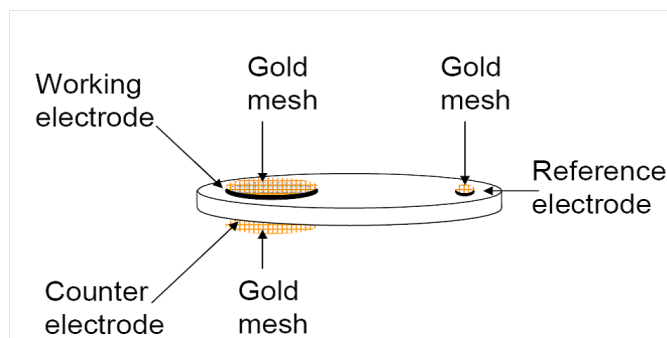


Figure 8.1: Symmetrical 3-electrode single cell setup of the first series of measurements.

of 400 ml/min was connected to both sides of the pellet. Current-voltage characteristics were measured in galvanostatic mode between 0-250 mA/cm² with a Tacussel PJT 35-2 measuring device, where the voltage between working- and counter electrode (ΔU_{WC}) as well as between working- and reference electrode (ΔU_{WR}) was recorded. Electrochemical impedance spectroscopy (EIS) and IV characteristics were repeatedly recorded during the run after different durations. EIS was recorded at OCV with an IM6 impedance analyser (Zahner, DE) with 10 mV of excitation amplitude. IV characteristics were recorded with ΔU_{WR} as the voltage and currents between 0-100 mA, so that the working electrode functioned as cathode.

Long-term tests during 1000 hours under polarisation of 250 mA/cm² with repeated IV-curve and EIS-measurements were executed under dry and wet (3% H₂O) air atmosphere to study the influence of different Cr-evaporation rates on the degradation of nickelate electrodes. All tests were performed at 700°C. The setup for long term tests is shown in Fig. 8.2.

After the 1000h-test was completed, post-test analysis was conducted by scanning electron microscopy (SEM) imaging of pellet cross-sections as well as EDX. Furthermore, a lamella was

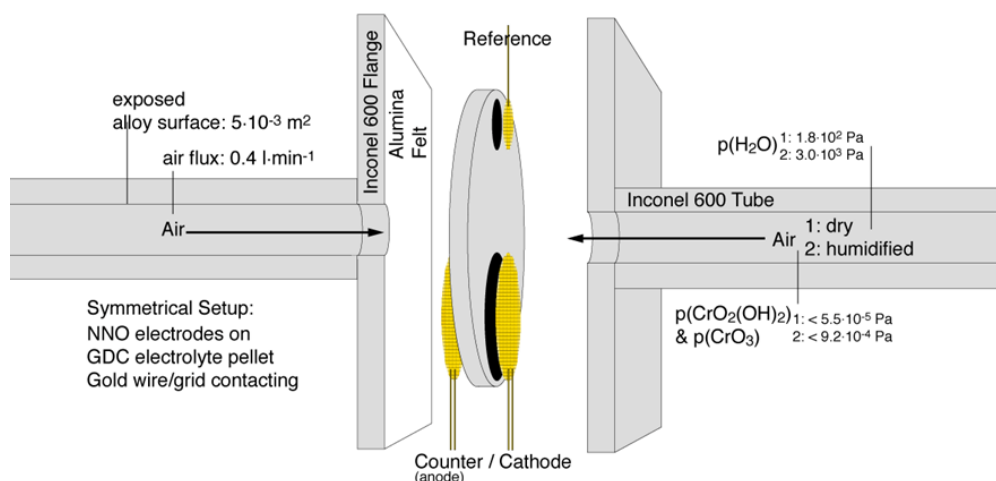


Figure 8.2: The test rig used for long term tests. Humid air increases the Cr-evaporation rate from stainless steel balance-of-plant materials as indicated. Image taken from Schuler et al. [144]

extracted by focussed ion beam (FIB) from the pellet and analysed by transmission electron microscopy (TEM) with EDX.

An example of a typical impedance spectrum at OCV and 700°C is shown in Fig. 8.3, with the voltage being measured between working and reference electrode (ΔU_{WR}). Two contributions, at medium frequency (MF) and low frequency (LF), were detected which were partially overlapped. It was shown in the literature [34] that mixed ionic electronic conductors (MIEC) generally display a MF-contribution which arises from charge-transfer processes at the MIEC electrode-electrolyte interface. The LF-contribution is generally associated with processes at the electrode surface. For nickelates, the charge transfer reaction of oxygen reduction on the electrode surface is assumed to be the rate-determining step at high oxygen partial pressures and molecular oxygen dissociation at low partial pressures [34]. The polarisation resistance R_P of the NNO cathode ($R_P = R_{LF}$) at the beginning of the test was more than two times higher than what Mauvy [22] has measured for symmetrical NNO-YSZ-NNO cells. Improvements of the NNO powder dispersion, current collection method and sintering temperature were therefore targeted in a second series of experiment (see below).

In long term experiments under dry air flow, an evolution of LF- and MF-semicircles with time was observed. Both increased with time, however the LF increased more distinctly and finally incorporated the MF-contribution. This is shown in Fig. 8.4. The voltage between working- and counter electrode (ΔU_{WC}) as well as between working- and reference electrode (ΔU_{WR}) is plotted against the test duration in Fig. 8.5. Both voltages ΔU_{WC} and ΔU_{WR} slightly decreased with time which suggests activation rather than degradation. However, the activation was due to an improving contact with time as evidenced by the decreasing ohmic resistance (high frequency intercept with the real axis in Fig. 8.4), which overcompensated the increased interface- and polarisation resistances.

After the end of long-term tests, post-analysis was performed by SEM and SEM-EDX. Further-

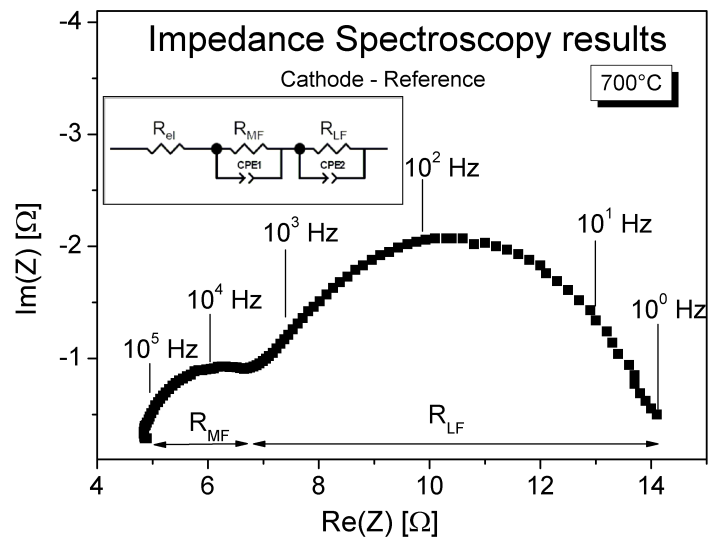


Figure 8.3: EIS result at OCV and 700°C. The voltage was ΔU_{WR} and 10 mA was used as amplitude. Contributions at medium frequency and low frequency are partially overlapped. The frequencies are indicated in the graph.

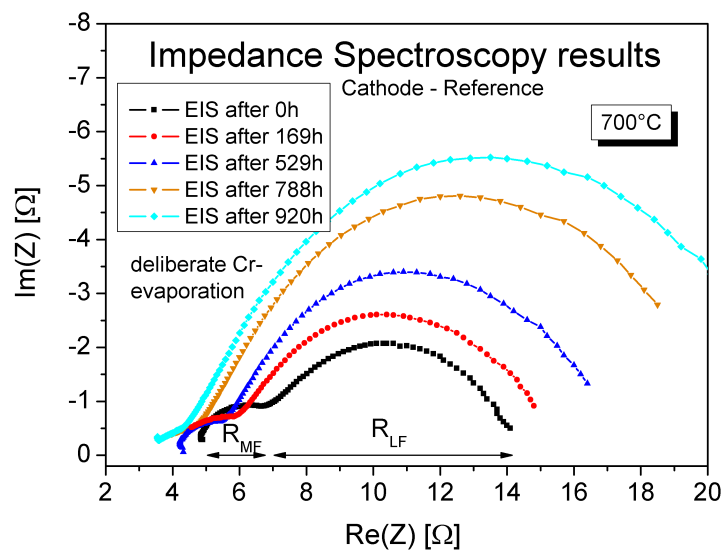


Figure 8.4: Evolution of MF- and LF-contribution over time at OCV and 700°C after the indicated durations. The voltage was measured between working and reference electrode and 10 mA was used as amplitude. The overlap between LF- and MF-semicircles was reinforced as the diameter of the LF-contribution distinctly increased with time.

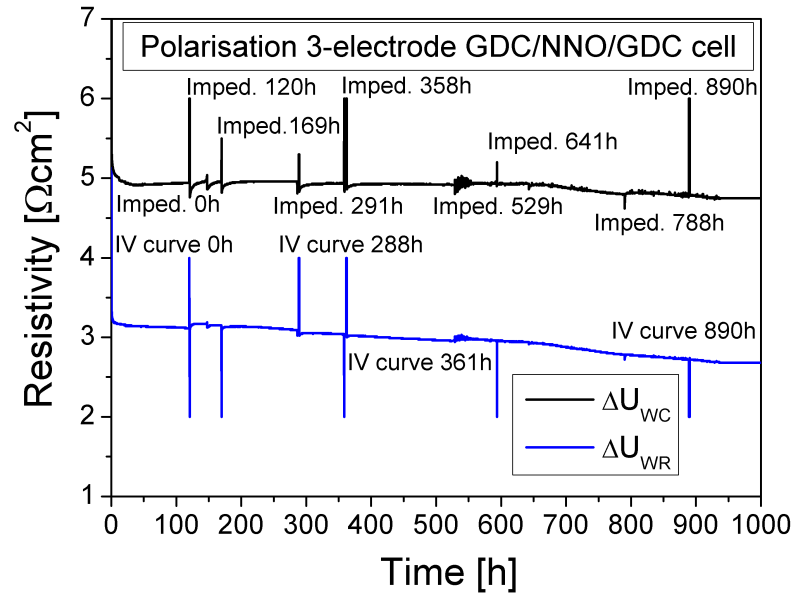


Figure 8.5: Evolution of voltages ΔU_{WC} and ΔU_{WR} over time. The polarisation was 500 mA/cm².

more, a lamella was extracted by focussed ion beam (FIB) and analysed by TEM equipped with EDX. A cross-sectional image recorded by TEM and element mapping by TEM-EDX is shown in Fig. 8.6. In Fig. 8.6, substantial amounts of Cr can be found at the surface of NNO grains. Some NNO-particle regions showing a contrast in TEM-images possess distinct amounts of Si, which is present in neodymium silicate compounds such as $\text{Nd}_4\text{Si}_3\text{O}_{12}$ as described in section 5.1.2. The parts of grains which show Si traces are not covered by Cr at the surface. As Cr-coverage of electrode surfaces was found to be related to electrochemical activity of the electrodes [146], it can be assumed that $\text{Nd}_4\text{Si}_3\text{O}_{12}$ does not contribute electrochemically to the cathode activity.

This means that Si-contaminations reduce the effective electrode surface area by reaction with Nd from NNO to $\text{Nd}_4\text{Si}_3\text{O}_{12}$ according to equation 5.2. NiO-precipitates are also found in Fig. 8.6, underlining the decomposition of NNO and the validity of equation 5.2. It becomes clear that the increase in polarisation and interface resistance is caused by Cr-deposition at NNO-particles' surfaces and NNO/GDC interfaces. The exact composition of the Cr-rich phase could not be revealed by EDX due to the presence of multiple laterally overlapping phases, however NdCrO_4 is the thermodynamically stable phase [147] at the operation conditions. IV-curves, which were regularly registered at 700°C during the 1000h-test, can be used to calculate the cathode overpotential η_{cath} according to

$$\eta_{\text{cath}} = \Delta U_{WR} - I * R_{\text{cell}} \quad (8.1)$$

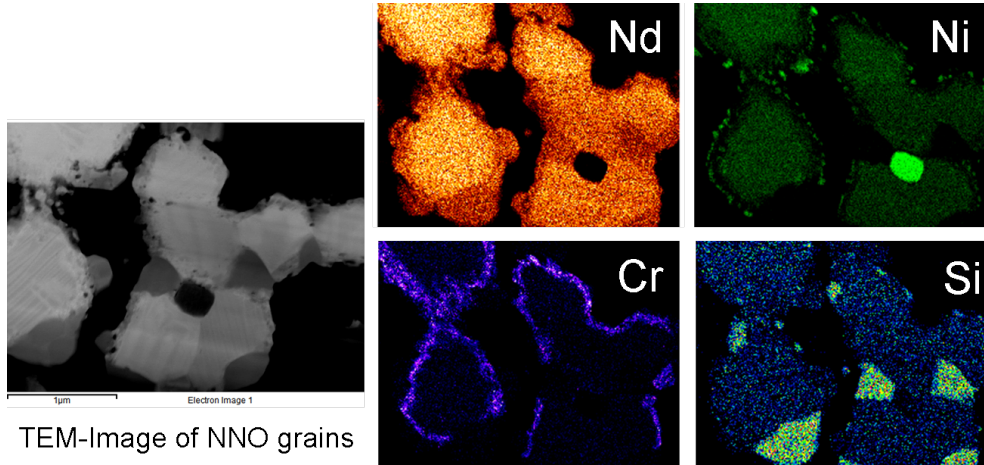


Figure 8.6: Analysis results of TEM-imaging and TEM-EDX of a pellet cross-section lamellae extracted by FIB. Cr- and Si-rich regions can be distinguished.

where ΔU_{WR} is the voltage between working and reference electrode, I is the current run through the cell and R_{cell} is the ohmic loss of the cell determined from the high-frequency intercept with the real part of Z of the impedance spectra. When η_{cath} is plotted against the logarithmic current density i [A/cm^2], the curve becomes a straight line for high current densities as η_{cath} becomes proportional to $\log i$, which means that the Butler-Volmer equation [148] gathering the complex electrode reactions is reduced to the Tafel equation. When the straight sections are extrapolated to $\eta_{cath}=0$, the intercept with the x-axis ($\log i$) represents the exchange current density i_0 . This graphical identification of i_0 is shown for 4 IV curves recorded during the 1000h test after different durations in Fig. 8.7. The exchange current density decreased from 15 to ca. 7 mA/cm^2 over the whole test duration. The resistance of LF- and MF-contributions for NNO at 700°C is plotted against test duration in Fig. 8.8a and the exchange current density is plotted against time in Fig.8.8b. The LF- and MF-impedances increase with test duration and the exchange current density decreases with time as Cr-deposits contaminate the NNO particle surface and GDC-NNO interface. The dependence on test duration is slightly stronger for the LF-contribution than for the MF-contribution, as the coverage of free NNO particle surfaces with Cr-deposits (cf. Fig. 8.6) influences the whole gas-electrode interface but only parts of the gas-accessible GDC/NNO interface. The increase of MF-contribution and the decrease of exchange current density with time show exactly the same dependence on test duration time, i.e. $t^{0.10 \pm 0.02}$.

This corroborates that the MF-contribution stems indeed from the charge transfer reaction at the electrode-electrolyte interface, which is also largely responsible for the current exchange density. It was shown [32, 149] that parameters such as electrical conductivity of the electrolyte also contribute to the charge-transfer reaction at the electrolyte/electrode interface. As shown in Fig. 8.8, the LF-part of impedance increases with time to the power of $t^{0.15 \pm 0.05}$ and the sum of LF+MF increases with $t^{0.14 \pm 0.04}$.

Horita [143] has analysed the influence of Cr-contamination on mixed ionic electronic conducting (MIEC) electrodes of composition $La_{0.8}Sr_{0.2}FeO_{3-x}$ (LSF) at 800°C and 300h of ex-

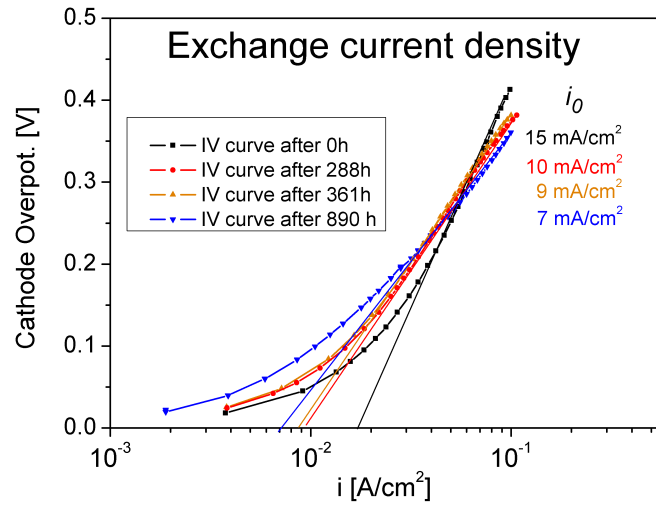
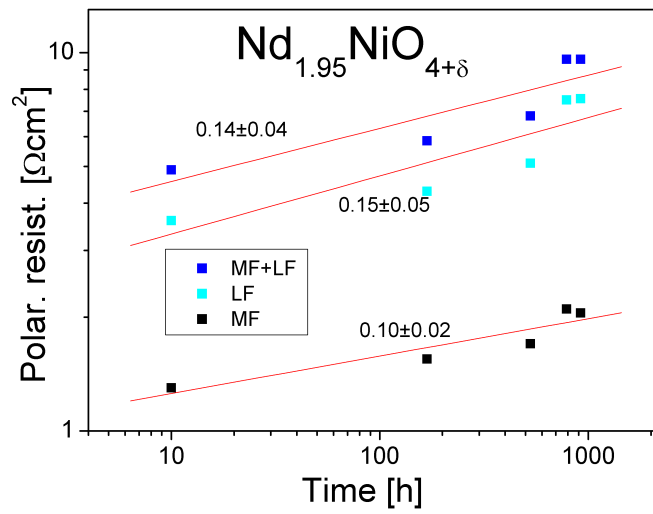


Figure 8.7: The evolution of exchange current densities during the long-term test.

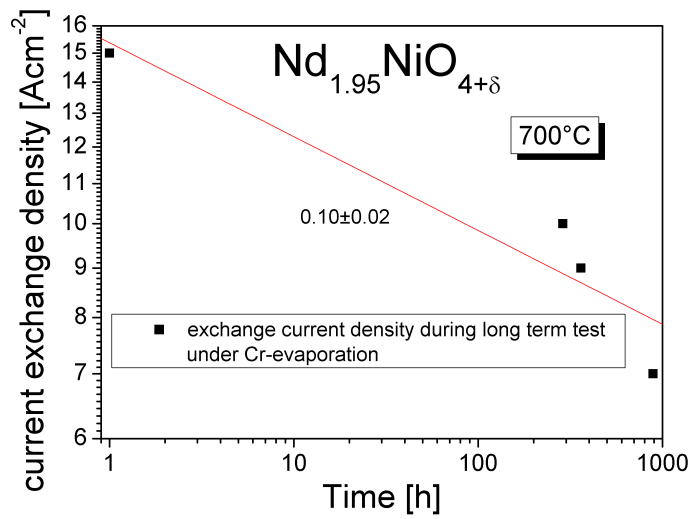
position and found an increase of the polarisation resistance with $t^{0.25}$. It can be seen that the slopes of interpolated straight lines for LF- and MF-contributions of NNO are smaller than what was found for LSF, which may point to slightly higher Cr-tolerance. However, the test temperatures are different which implies different Cr-evaporation rates. Further data at different temperatures is needed to compare NNO to other cathode materials in terms of Cr-degradation. Yang [30] has measured chemical oxygen surface exchange coefficients (k_{chem}) of NNO and $\text{La}_{0.6}\text{Sr}_{0.4}\text{CoO}_{3-x}$ (LSC) materials and found more substantial degradation of k_{chem} in the presence of a Cr-source for LSC than for NNO at 600°C.

8.3 2nd series of measurements

GDC powder of the same origin as in the first series was used. PVA, Mowiol 8-88 Lot-Nr. DEBC118952, was added dropwise as aqueous solution to the powder until it flowed smoothly. The treated powder was compacted to pellets under uniaxial load of 160 MPa. Intact pellets of 24 mm diameter were obtained after compaction. The green pellets were sintered at 1450°C/2h in air with 3 K/min heating and cooling rate and were $\geq 95\%$ dense. NNO was dispersed in a 3 wt% solution of ethyl-cellulose in terpineol and milled in a triple-roll milling device for 2 hours before being screen-printed as described in section 8.2. The milling was exercised to improve the granulometry towards a more fine-grained homogeneous PSD. The sintering temperature of the deposited layers was now varied between 1000°C and 1300°C in 100°C intervals. The sintering was carried out under stagnant air atmosphere with a dwell time of 2 hours per sample. The sintered electrodes were contacted by LSC, Praxair. LSC was dispersed in a 3 wt% solution of ethyl-cellulose in terpineol in a mortar and deposited onto the electrodes by



(a)



(b)

Figure 8.8: The degradation as a function of test duration (exposure to Cr contamination). Slopes of interpolated straight lines are indicated in the graph. (a) Degradation of LF- and MF-contributions as well as their sum with time as measured by EIS. (b) Decrease of exchange current density with time.

painting. The 3-electrode design is shown in Fig. 8.9. The electrochemical tests were identical

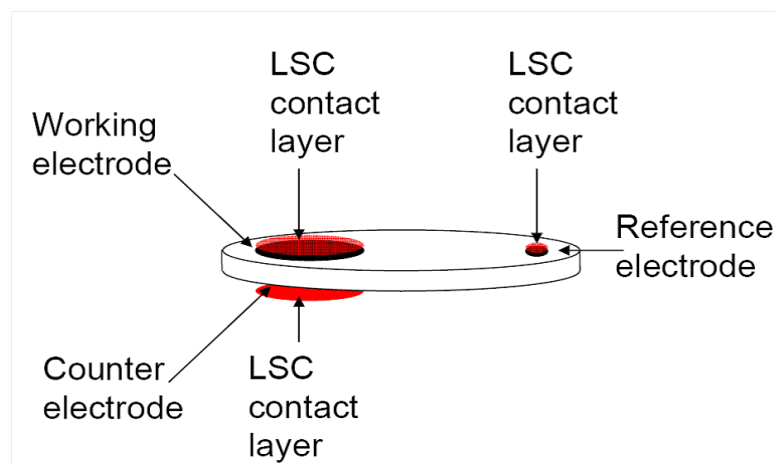


Figure 8.9: The 3-electrode setup for the second test series.

to the ones for the first series described in section 8.2, except no long-term tests were run. The installed pellets were simply heated to 700°C, tested and cooled down again for post-mortem analysis.

The impedances measured at OCV and 700°C for NNO electrodes sintered at different temperatures is shown in Fig. 8.10. Electrodes sintered at 1000°C showed much higher polarisation resistances ($R_p = R_{LF}$) than NNO-layers sintered at 1100-1300°C. Differences in ohmic resistance existed due to small variations in thickness and densities. Single suppressed LF-semicircles were observed, an MF-semicircle was not clearly seen but could be vaguely distinguished for NNO electrodes sintered at 1300°C. It is reasonable to assume that the MF-contribution was simply incorporated into the bigger LF-semicircle.

As the MF-contribution is caused by charge-transfer across the electrolyte-electrode interface, the formation of an interfacial reaction layer influences the magnitude of the MF-semicircle, which would explain the fact that an MF-contribution was only distinguishable for samples with NNO-electrodes sintered at the highest temperature, 1300°C, where the thickest interlayer has formed. The polarisation resistance R_p is fitted according to the equivalent circuit shown in Fig. 8.10 for all samples and plotted against the NNO sintering temperature in Fig. 8.11. NNO-electrodes sintered at 1200°C show the lowest values of R_p with 1.1 Ωcm^2 , which is slightly lower than results by Mauvy of NNO-electrodes on YSZ-pellets [22].

The IV-characteristics were measured for all samples and the cathode overpotentials η_{cath} were calculated by equation 8.1. In order to determine the exchange current density i_0 , η_{cath} is plotted as a function of logarithmic current density i as shown in Fig. 8.12.

The values for i_0 follow the same trend as the EIS-results. The highest exchange current density i_0 of 60 mA/cm² at 700°C is found for NNO-electrodes sintered at 1200°C/2h. These findings coincide with results by Haanappel [36], who measured performances of planar single cells with NNO cathodes sintered at different temperatures. The best performance was found for electrodes sintered at 1150-1200°C. At these temperatures, substantial solid state reaction

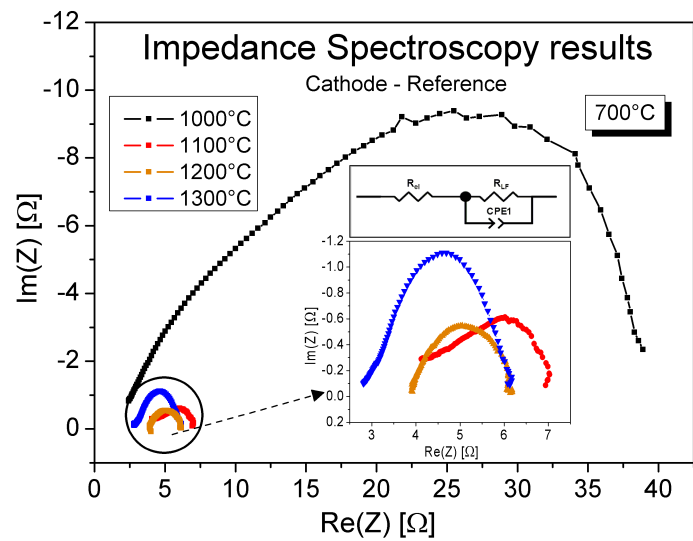


Figure 8.10: The EIS results for NNO electrodes sintered at different temperatures. Y-axis out of proportion for readability.

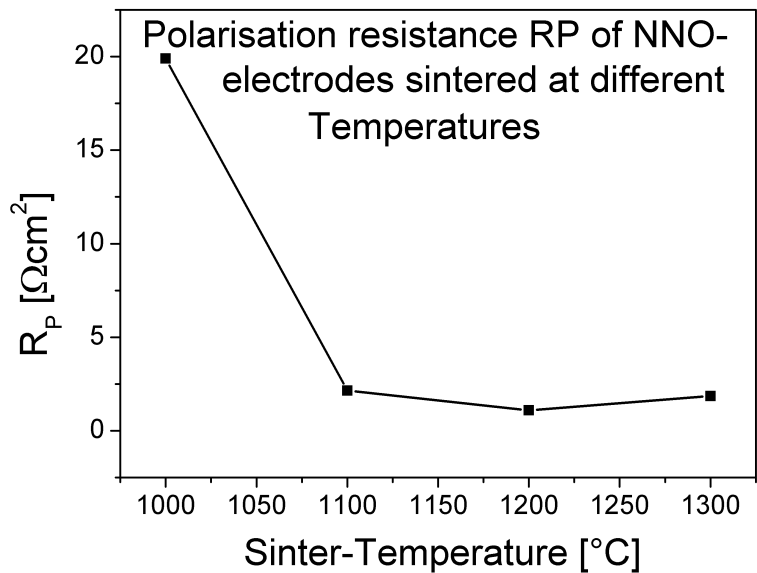


Figure 8.11: Polarisation resistance for NNO-electrodes sintered at different temperatures.

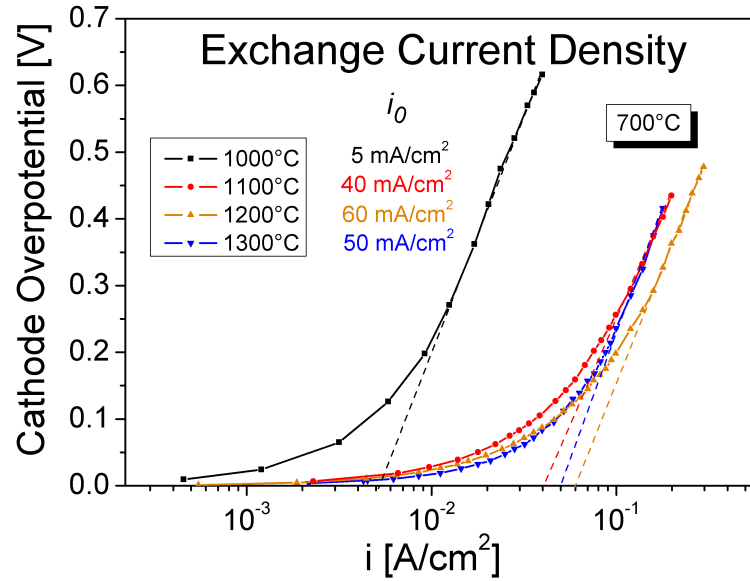


Figure 8.12: The cathode overpotential η_{cath} of NNO-cathodes sintered at different temperatures as a function of current density. The straight parts of the curve at higher current densities are extrapolated to $\eta_{\text{cath}}=0$ to determine the exchange current density i_0 .

between GDC and NNO is already present (cf. chapter 7).

Contrarily to the undesirable formation of pyrochlore phases such as $\text{La}_2\text{Zr}_2\text{O}_7$ between La-containing cathodes and zirconia-electrolytes, the formation of the cubic oxide $\text{Nd}_x\text{Ce}_{1-x}\text{O}_{2-x/2}$ does not seem to compromise the conductivity as severely and is therefore not the determining factor for optimum electrochemical performance. This is due to the higher lattice symmetry of the fluorite type cubic $\text{Nd}_x\text{Ce}_{1-x}\text{O}_{2-x/2}$ as compared to the pyrochlore type cubic lattice of $\text{La}_2\text{Zr}_2\text{O}_7$, which leads to drastically lower oxygen ion conductivity coupled with poor electronic conductivity for the latter.

8.4 Exchange current density

For the two series of electrochemical measurements, exchange current densities between GDC and NNO at 700°C were measured in the range of 15-60 mA/cm². The first series can be considered closer to the real situation in a NNO-supported single cell without activation layer, where GDC layers are directly deposited on NNO cathodes, the microstructure of NNO is unoptimised, both GDC and NNO are cosintered at 1300°C and the current collection is made by gold meshes or wires. The second series shows how the electrochemical response of the system can be improved when GDC is sintered to higher densities, the NNO granulometry is refined, the NNO sintering temperature is decreased to 1200°C and a LSC contacting layer is

applied. For cathode-supported cells, this means that

- The cosintering temperature should decrease to 1200°C to improve the electrochemical properties, even though the performance difference for GDC/NNO interfaces was found to be rather small. Moreover, this implies improvement of the electrolyte densification behaviour as the electrolyte layers must be gas-tight after cosintering. For GDC, Cobalt-doping as introduced in chapter 5 can be used to improve the low-temperature densification behaviour [120] and the interfacial charge-transfer reaction [32], while a fine-grained ScSZ powder should densify sufficiently at 1200°C as shown by its dilatometric shrinkage curve (see page 86). Sinter aids for ScSZ are another possibility.
- The current collection method must be carefully chosen, which is a special challenge on the inside of the tube (cathode side) due to geometrical restrictions.
- The PSD of NNO must be finer-grained to increase the active surface area. Since restrictions of the manufacturing process limit the granulometry (e.g. nano-powders can not be compacted by CIP due to high particle-particle friction), an improved granulometry could be achieved by adding a functional layer of fine-grained NNO between NNO-tube and GDC-interlayer. This would also open possibilities to improve the performance by using NNO-GDC composites for functional layers, which were shown to decrease considerably the electrode polarisation [149]. However, each additional layer during cosintering will complicate the situation during the shrinkage process and needs to be extremely well-tailored with respect to green density, PSD, shrinkage etc.

For anode-or electrolyte-supported cells, the cathodes are typically added after the sintering of the electrolyte. The decoupling of electrolyte densification temperature from cathode sintering temperature facilitates the optimisation of nickelate cathodes, as the optimum temperature and granulometry of electrode preparation can be chosen independently of electrolyte densification restrictions.

The exchange current density of NNO-GDC is compared to other cathode-electrolyte systems in Table 8.1. From it, it can be seen that nickelates showed higher exchange current densities than LSM-YSZ at 700°C, but are lower than for LSCF-cathodes with GDC-electrolyte at 650-700°C. This coincides qualitatively with results by Haanappel et al. [36] on single cell peak power densities with LSM-, LSCF- and NNO-cathodes.

8.4. Exchange current density

Table 8.1: Exchange current densities of different cathode-electrolyte systems.

Temp.	i_0 [mA/cm ²]						
	LSM- 8YSZ [150]	LSM- 8YSZ [151]	LSM- 8YSZ [152]	LSCF- GDC [151])	LSCF- GDC [153]	NNO- YSZ [34]	NNO- GDC this work
650°C				41	44	1.8 (628°C)	
700°C			29 (690°C)		126	10 (718°C)	15-60
750°C		60 (740°C)	40	147 (740°C)	301		
800°C	210	112	70 (810°C)	168	529	31 (820°C)	

9 Fabrication and Testing of Single Cells

This chapter deals with the electrochemical testing of complete single cells and their fabrication route. The cell design for each tube fabrication type was suggested in table 6.4 and used for the fabrication of complete cells. The fabrication details, the setup used for electrochemical testing and its results are presented in the next sections. For all cell types, layers were deposited by dip-coating with a withdrawal speed of $U=300$ mm/min. The GDC- and ScSZ layers were deposited over the whole tube length (ca. 25-30 mm after sintering) whereas the anode was deposited only in the middle of the available electrolyte surface, in order to leave space for alumina extensions. Pressure loss measurements were performed on sintered half-cells. The tubes were sealed on both extremities with teflon tape before dip-coating of the anode-layer, and anode lengths of typically ca. 15 mm (half of the total length) were obtained. The fabrication of each tube type is described in detail in the next sections.

9.1 Fabrication of Complete Single Cells

9.1.1 Fabrication of cell with tubes of type CIP-VITO

Cold-isostatically pressed tubes by VITO were dip-coated into suspensions of GDC-1CD powder in isopropanol solvent, with 2 wt.% TEA dispersant and 5 wt.% PVB binder (wt% of dry solid weight). The suspensions had a solid load of $\phi=5$ vol%. Since as-received Co-doped ceria powder showed some agglomerations, ball-milling of suspensions with $\phi=10$ vol% of GDC-1CD powder dispersed in isopropanol with 2 wt% TEA-dispersant was performed for ca. 15 h prior to dip-coating as described in chapter 5. The dip-coated tubes were dried overnight and sintered vertically at 1300°C/2h under stagnant air. Afterwards, NiO-GDC anodes were deposited by dip-coating in suspensions with a solid load of $\phi=19$ vol%, with all other parameters being equal to the electrolyte suspension. The anode was sintered at 1300°C/2h before the samples were installed for electrochemical testing.

In a first series, a single layer of GDC-1CD was deposited by dip-coating in a suspension with 5 vol% solid load once. The sintered tubes were dip-coated twice in NiO-GDC suspensions without rice starch addition. After sintering of the anode, some cells were fractured perpendicular

to the tube axis to perform cross-section imaging by SEM. A cross-section of an as-sintered cell prior to electrochemical testing is shown in Fig. 9.1. The GDC-electrolyte layer and the anode

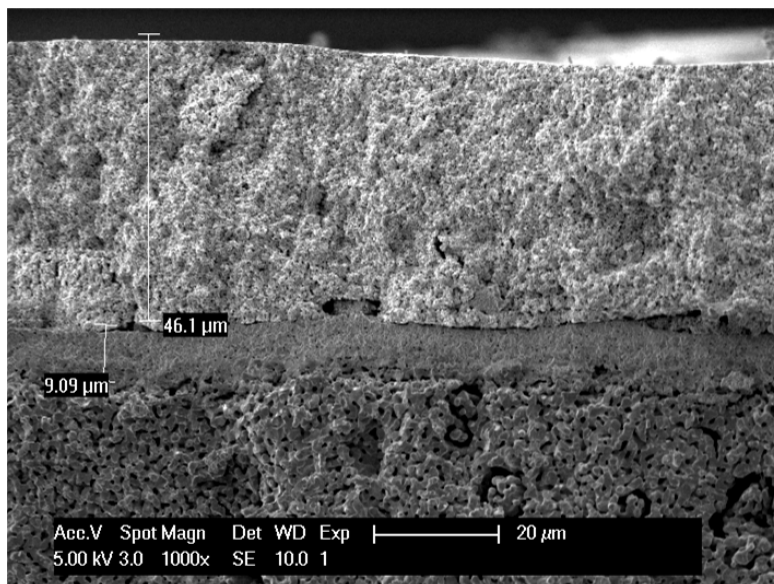


Figure 9.1: Cross-section SEM image of as-sintered cells.

layer showed thicknesses of ca. 9 μm and ca. 50 μm respectively. As ceria becomes an MIEC in reducing atmosphere above 600°C, cells with only GDC electrolyte generally have electrolyte thicknesses of $\geq 15 \mu\text{m}$ [63]. The anode, whose thickness was targeted at ca. 30 μm , was almost twice as thick and rather dense, while the reduction of NiO to Ni introduces a porosity of 22 vol% by the difference of densities [154] and increases the porosity. The results of pressure loss measurements are shown in Fig. 9.2. The pressure loss constant was $\kappa = 1.8 \cdot 10^{-2} \text{ 1/s}$ for tube lengths of 20 mm, which signifies rapid pressure loss, and corresponds to a permeability of $4.5 \cdot 10^{-6} \text{ mol m}^{-2} \text{ Pa}^{-1} \text{ s}^{-1}$.

Zhang [68] and Kim [155] suggested $1.7\text{--}50 \cdot 10^{-9} \text{ mol m}^{-2} \text{ Pa}^{-1} \text{ s}^{-1}$ as acceptable permeabilities for gas-tight electrolytes, which is clearly lower than the observed ones. These results led to changes in the experimental procedure.

In later essays, a GDC-1CD layer was formed by dip-coating twice or thrice in a suspension of 5-6 vol% solid load with the same withdrawal speed. The sintered tubes were dip-coated once in NiO-GDC suspensions with $\phi = 19 \text{ vol } \%$, where rice starch was added to the anode powder to yield a nominal porosity of 40-50 vol% after the reduction of NiO to Ni. After sintering of the anode, some cells were fractured perpendicular to the tube axis to perform cross-section imaging by SEM. A cross-section of an as-sintered cell prior to electrochemical testing is shown in Fig. 9.3.

The pressure loss measurement results of thicker GDC-layers are shown in Fig. 9.4 and compared to the first series with single dipped GDC-layers. The exponential decay constant decreased to $\kappa = 3.4 \cdot 10^{-3} \text{ 1/s}$ and $1.3 \cdot 10^{-3} \text{ 1/s}$ for GDC thicknesses of 11 and 13 μm and sample lengths of ca. 20 mm, which led to calculated permeabilities of $7.8 \cdot 10^{-7}$ and $3.2 \cdot 10^{-7} \text{ mol}$

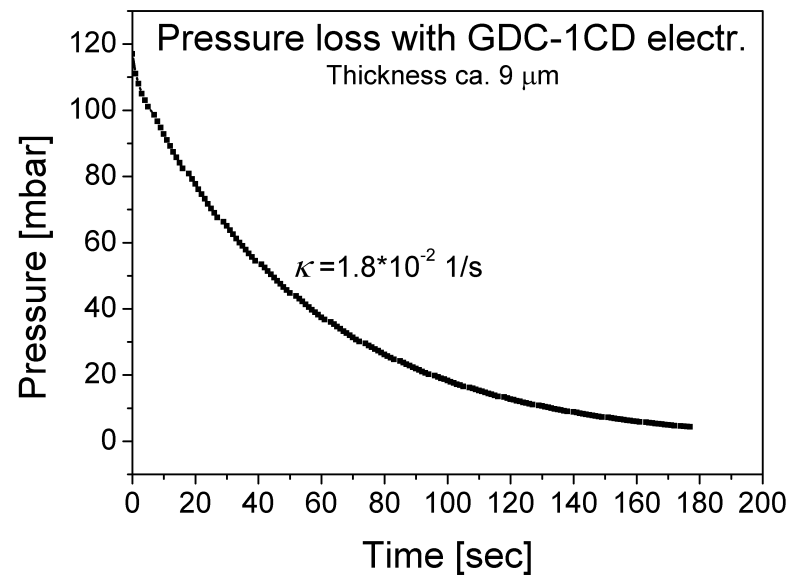


Figure 9.2: Pressure loss of tubes CIP-VITO with a GDC-1CD layer of ca. 9 μm thickness.

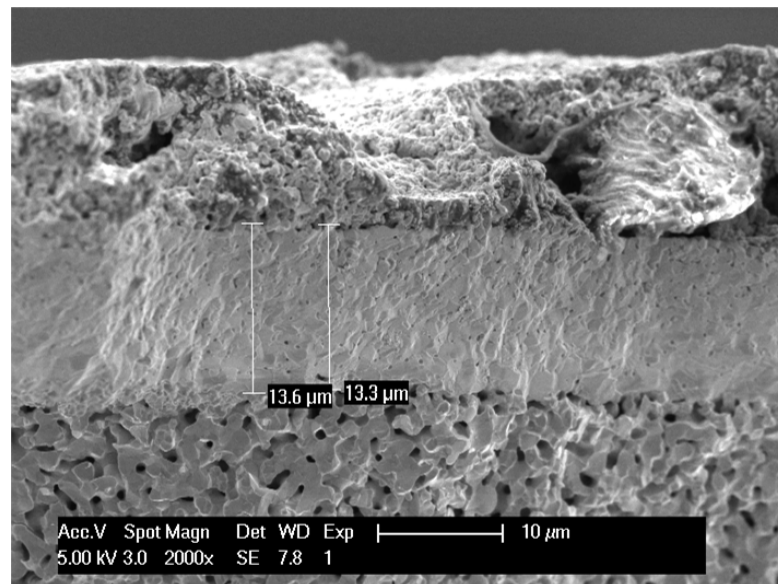


Figure 9.3: Cross-section SEM image of as-sintered cells of the second series.

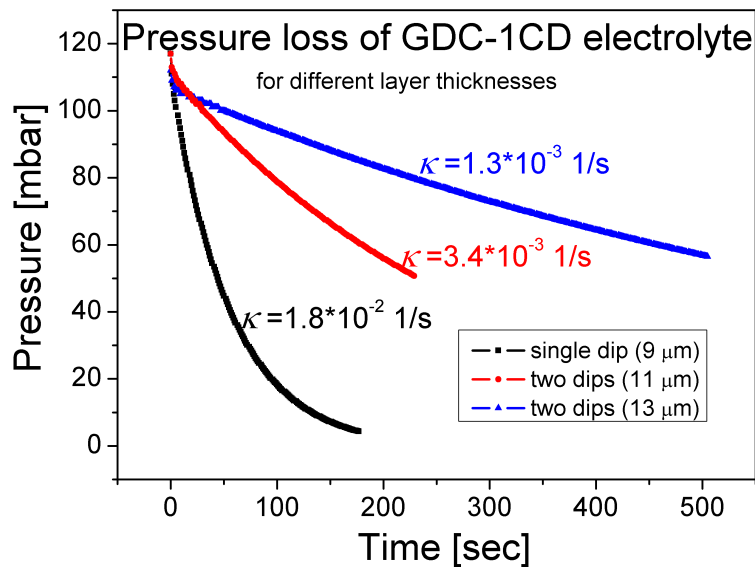


Figure 9.4: Pressure loss measurements of as-sintered cells with GDC electrolyte of 11 and 13 μm thickness.

$\text{m}^{-2}\text{Pa}^{-1}\text{s}^{-1}$ respectively.

Clearly, the permeation decreases with increasing electrolyte thickness, while a GDC electrolyte layer of greater thickness can lead to excessive ohmic losses, especially as the operation temperature of cells with ceria-electrolyte is limited to $\leq 600^\circ\text{C}$ due to the development of substantial electronic conductivity for $T \geq 600^\circ\text{C}$ [103]. As the permeability was slightly higher than for tubes of type T-SC and the same electrolyte thicknesses, the cells were not tested as lacking gas-tightness was the primary concern.

9.1.2 Fabrication of cell with tubes of type CIP-ZARA

Cold-isostatically pressed tubes fabricated in Zaragoza were prepared in the same way as tubes of type CIP-VITO, with single dips in GDC-suspension of 5 vol% solid load. Coated tubes were dried over night and sintered vertically at $1300^\circ\text{C}/2\text{h}$. Pressure loss measurements were performed on sintered half-cells. The pressure loss measurement is shown in Fig. 9.5.

Very poor pressure loss constants of $\kappa = 0.076 \text{ 1/s}$ were obtained for GDC-layer thicknesses of 9 μm as rather permeable electrolyte layers were created. The surface pore size of the tubes of ca. 3 μm due to the utilisation of commercial maize starch pore former led to the infiltration of GDC-CD particles, which, after ball-milling, are ≥ 2 times smaller than the apparent pore diameter. The infiltration of cathode pores by GDC-particles leads to inhomogeneties in the GDC-layer such as pinholes. Due to the poor density of GDC-layers, tubes of type CIP-Zara

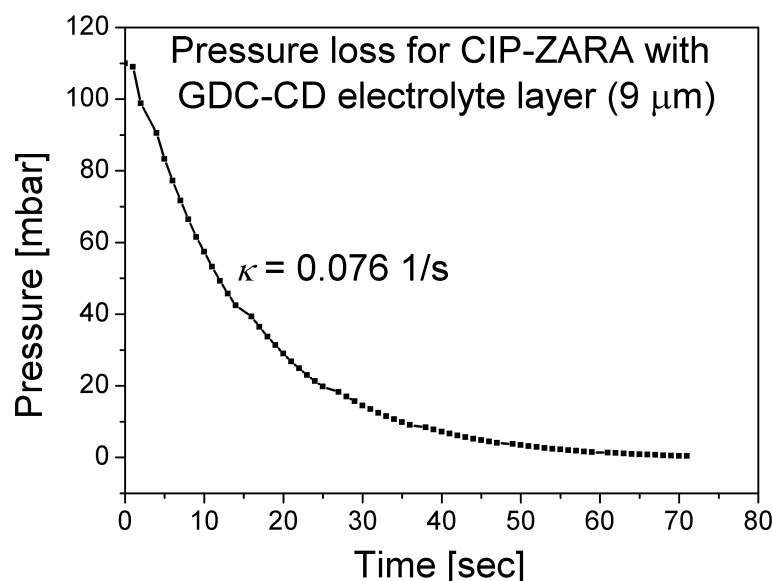


Figure 9.5: Pressure loss measurements performed on as-sintered half-cells of tubes CIP-ZARA dipped once in GDC electrolyte suspension.

were not used for single cell fabrication, as GDC-layers of the same thickness as for other tube types led to drastically higher permeabilities of $3.5 \cdot 10^{-5} \text{ mol m}^{-2} \text{ Pa}^{-1} \text{ s}^{-1}$.

9.1.3 Fabrication of cells with tubes of type T-SC

Complete cells based on slip-casted tubes fabricated at Cereco, Greece were prepared the same way as tubes of type CIP-VITO, where a GDC-electrolyte layer was deposited by dipping once, twice and thrice in GDC-suspensions of 5 vol% solid load and the same composition as the suspension used for CIP-VITO. Fresh wet coatings were allowed to dry over night at ambient conditions before the tubes were sintered in an upright position at $1300^\circ\text{C}/2\text{h}$. The cross-section of as-sintered cells with a single-dipped GDC-electrolyte prior to testing is shown in Fig. 9.6.

A single dip in GDC-suspension corresponded to ca. $9 \mu\text{m}$ electrolyte layer thickness after sintering. Increasing the number of dips in GDC-electrolyte suspension increased the layer's thickness, as 11 and $13 \mu\text{m}$ thick GDC-layers were obtained after dipping twice and thrice in the suspension. The pressure loss constants for different layer thicknesses is shown in Fig. 9.7.

The indicated values of κ led to gas-permeabilities of $6.0 \cdot 10^{-6}$, $1.3 \cdot 10^{-7}$ and $9.0 \cdot 10^{-8} \text{ mol m}^{-2} \text{ Pa}^{-1} \text{ s}^{-1}$ for electrolyte thicknesses of 9, 11 and $13 \mu\text{m}$ after dip-coating once, twice and thrice respectively. The results are superior over permeabilities of coated tubes of type CIP-

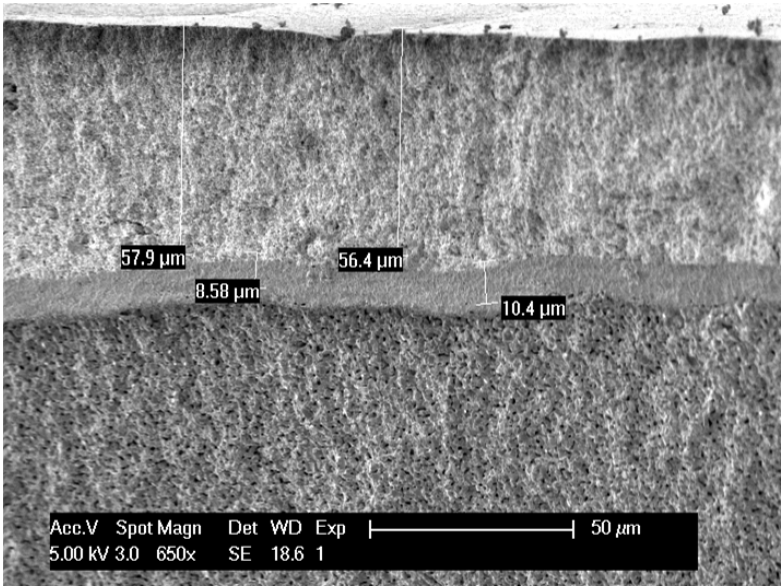


Figure 9.6: Cross-section of as-sintered half-cells with tube supports prepared by slip-casting.

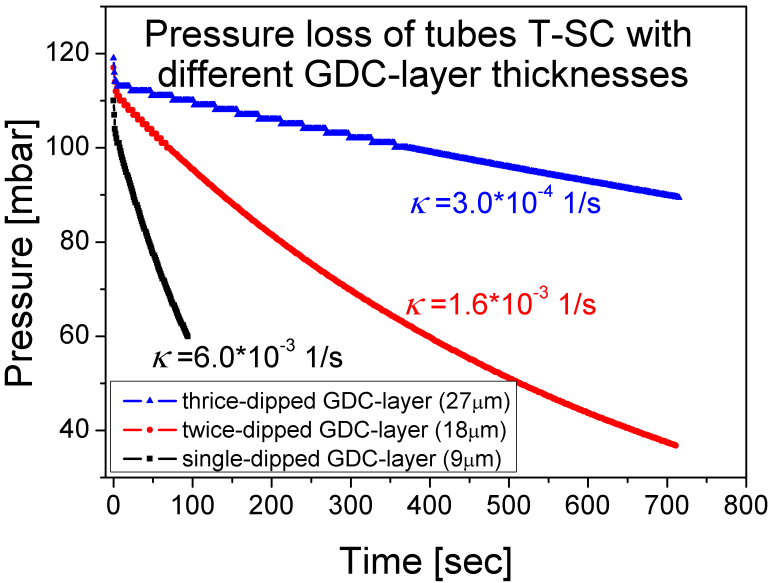


Figure 9.7: Pressure loss constants of sintered half-cells with different GDC-layer thickness on tubes prepared by slip-casting.

VITO with the same GDC-layer thickness due to

- Higher shrinkage of the substrate (less constraints during cofiring)
- Less porosity in the substrate

while diffusional limitations due to lower porosity during the electrochemical testing may overcompensate the improved gas-tightness. The anode was deposited by dipping once in NiO-GDC suspensions of 19 vol% solid load with 2 wt% TEA and 5 wt% PVB in isopropanol solvent, while rice starch was added to the anode powder to yield a nominal porosity of 40-50 vol% after NiO reduction.

9.1.4 Fabrication of cells with tubes of type CIP-EPFL

Tubes prepared by CIP at EPFL were dip-coated twice and thrice in GDC-suspension of 5 vol% solid load of the same composition as for tubes of type CIP-VITO. Similar electrolyte thicknesses, i.e. 11 and 13 μm respectively, as in the case of CIP-VITO and T-SC were obtained. The pressure loss measurements led to permeabilities of $2.9 \cdot 10^{-6}$ and $2.0 \cdot 10^{-6} \text{ mol m}^{-2} \text{ Pa}^{-1} \text{ s}^{-1}$ for 11 and 13 μm GDC-electrolyte thickness. As these values are worse than for tubes of type CIP-VITO and T-SC, the production of single cells was stopped.

9.1.5 Fabrication of cells with tubes of type Ex-SD

The tubes were presintered at different temperatures and dip-coated into GDC- and ScSZ-suspensions before cofiring at 1300°C , which changed the shrinkage of the tubes during cosintering. In all cases, a decrease of shrinkage of the cofired, coated tubes with respect to the uncoated tube, which sintered under "free" conditions, was observed. Tube presintered at 1000°C , which had a linear shrinkage of 18% up to the sintering temperature of 1300°C , shrank only 14% when cofired with GDC- and ScSZ layers, when both GDC- and ScSZ suspensions were optimised to possess 18% sinter shrinkage to 1300°C themselves. The shrinkage of GDC- and ScSZ-layers was determined by measuring the shrinkage of GDC- and ScSZ-pellets prepared by slip-casting from the investigated suspensions, as explained in the powder chapter. The difference in shrinkage between freely sintered tubes and cofired half-cells can be explained by the differences in characteristic sintering temperatures T_s , T_{max} and T_e , or, in simplistic language, "one layer tries to shrink when the other one doesn't (want to)", which caused constrained conditions during cosintering and limited the shrinkage. This phenomenon was especially remarkable for extruded tubes, which had the smallest diameter of all tested tubes, the lowest green density and highest porosity, whereas tubes of bigger diameter and higher green density (CIP-VITO, T-SC, CIP-ZARA) showed almost no difference in shrinkage between sintering and cosintering. The thin-walled green body of higher porosity of the extruded tubes has a lower stiffness than green bodies with less porosity of higher wall thickness, and is more prone to changes in the shrinkage by layers. For example, a single 10 μm thick GDC-layer on a

tube surface represents 3.2% of the total wall thickness for extruded tubes but only 0.1% of the total wall thickness for the tubes of type CIP-VITO.

The presintering temperature of extruded tubes was therefore a parameter of optimisation, and tubes presintered at 900-1000°C were mostly used as they showed a good compromise of mechanical stability and sinter shrinkage. A GDC-layer was deposited by dip-coating with the same conditions as for tubes of type CIP-VITO, hence $\phi=4-6$ vol%, 2 wt% TEA, 5 wt% PVB in isopropanol solvent, where the agglomerated powder was ball-milled prior to dip-coating. The tubes coated with a GDC-interlayer were dried overnight at ambient conditions and dip-coated again in ScSZ-TR electrolyte suspensions. ScSZ-suspensions had a solid load of $\phi=4-6$ vol%, 2 wt% PAA, 5 wt% PVA in water as solvent. Immediately after the deposition, the tubes were transferred to the drying chamber which was set to 25°C/90% RH. The tubes were dried for 24 hours and afterwards extracted from the drying chamber, placed horizontally on a ScSZ-TR powder bed and cosintered at 1300°C/2h. The anode was deposited by dipping once in the respective suspension after the tubes were sealed at their extremities by teflon tape. The coated tubes were dried over night at ambient conditions and sintered again at 1300°C/2h. The selfmade NiO-GDC and the commercial NiO-YSZ powder mixtures were used as anode formulations and yielded a nominal porosity of 22 vol% after NiO reduction assuming no residual porosity after sintering. Rice starch was also added to increase the nominal porosity to 30, 40 and 50 vol% after NiO reduction, respectively.

The typical range of pressure losses for tubes prepared in the described manner is shown in Fig. 9.8. The pressure loss constant κ varied between $2 \cdot 10^{-3}$ and $5 \cdot 10^{-4}$ 1/s, which leads to

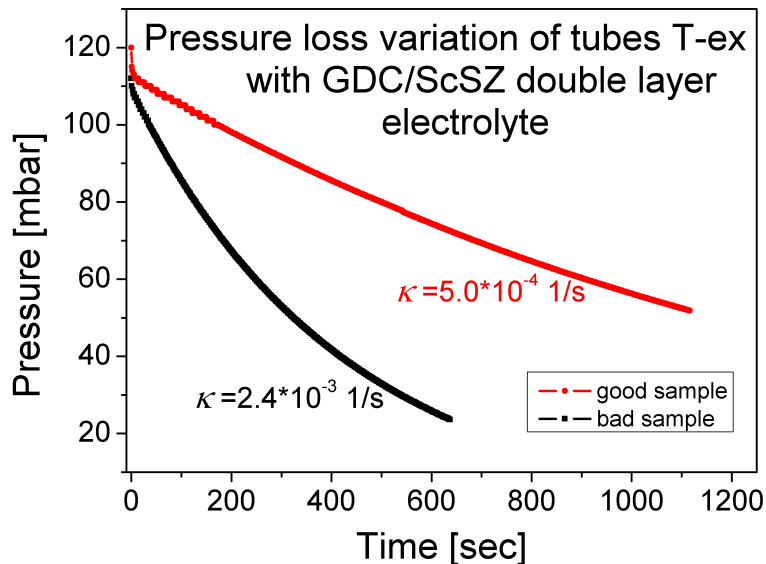


Figure 9.8: Pressure loss results of cells prepared by extruded tubes.

permeabilities in the range of $1.5 \cdot 10^{-6}$ - $3.7 \cdot 10^{-7}$ mol m⁻²Pa⁻¹s⁻¹. A cross-sectional image of a sintered cell prior to testing is shown in Fig. 9.9.

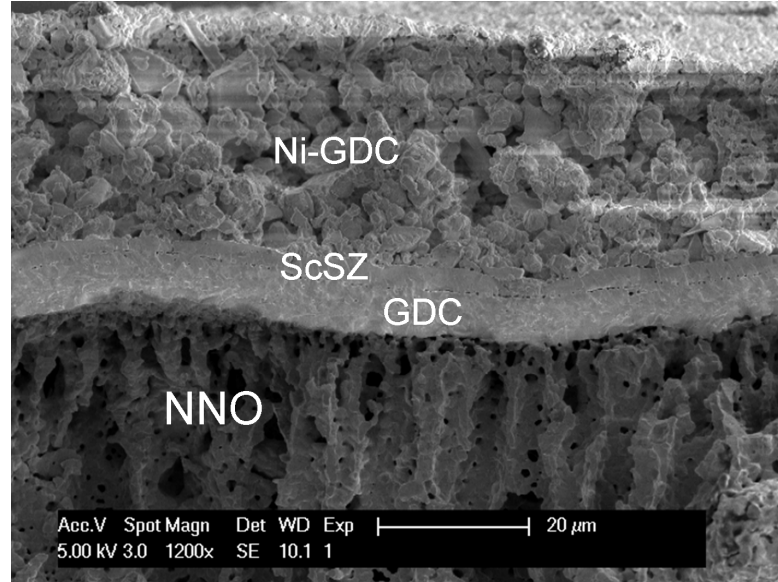


Figure 9.9: Cross-sectional image of complete cells with extruded tubes.

The thickness of the GDC-interlayer and ScSZ-electrolyte layer were between 5-8 μm and 2-4 μm respectively. A higher layer thickness for ScSZ led to spalling during sintering due to tensional stress build-up during sintering. Increasing the thickness of the GDC-interlayer was found to increase the tendency for delamination and spalling, suggesting circumferential stresses which increased with layer thickness. A better match between sintering temperatures between nickelate substrate, GDC and ScSZ must be obtained to increase the ScSZ-film thickness that can withstand thermal stresses during cofiring without failure.

9.2 Measurement Setup

The different taken steps to install a sample in the measurement device are shown in Fig. 9.10. First, the tube is electrically connected by gold wire of 0.3 mm diameter or by silver mesh, depending on the tube type. For extruded tubes, gold wire is wrapped around the anode and platinum paste, Heraeus CL11-5349, is painted on the surface for better thermomechanical connection while the gold wire on the cathode side is simply mechanically connected to the cell by drawing a slightly curved wire through the inner hole of the tube. Without Pt-paste, the gold wire, whose thermal expansion coefficient (TEC) is higher than the anode material's TEC, detached from the anode surface and led to loose contact.

The current on both electrode sides of tubes with bigger diameter, i.e. CIP-VITO, CIP-LTP and T-SC, was collected by a silver mesh which was beforehand connected to gold wires by point-brazing. The silver mesh was folded around a tubular object of slightly bigger diameter and then inserted into the tubes to achieve more efficient current collection (a), but could

not be used for extruded tubes due to the mechanical stresses imposed on the fragile tubes during the connection. The sample, while being placed on a V-shaped metallic support, was inserted into two alumina tubular extensions and ceramic paste from Aremco, Ceramabond 885, was applied to the alumina-sample interfaces (b). A third alumina tube was placed as a "bridge" between the two alumina extensions to act as a mechanically stabilising connection to minimise shear forces, which led immediately to cracking. The "bridge" is also connected to the extensions by ceramic paste (c). After an hour of drying at ambient conditions, the sample on the support is placed in a furnace where the ceramic paste is cured at 93, 260 and 371°C, each step with a dwell time of 2 hours. The heating rate between each step of 50°C/h was carefully chosen due to thermal stresses of differently expanding materials.

A complete cell after curing is shown in 9.10d. While a single ceramic tube of 3.5 mm diameter was sufficiently stable as "bridge" for cells from extruded tubes (e), which, due to their smaller cell diameter, have smaller and lighter alumina extensions, the weight of alumina extensions for tubes CIP-VITO, CIP-EPFL and T-SC made the setup too unstable. Due to limitations of the quartz tube size, the diameter of the "bridge" could not be increased above 3.5 mm. A half-pipe shaped semi-tube was prepared by cutting a full tube along the tube axis and was glued to the alumina extensions for mechanical support (f), which led to stable setups which just fitted in the quartz tube.

The installation process is shown in Fig. 9.11. The sample is placed inside a furnace with inserted quartz tube (a). The quartz end pieces with screw thread are attached and the gold cables from the anode extracted through an offset extension (b). The caps, in which single-hole washers of a diameter slightly bigger than the alumina extensions are inserted (c), are carefully conducted along the alumina extensions and then slightly screwed on the quartz end pieces (d). The gas connections are carefully connected to the alumina extensions (e) with as little force as possible exerted on them to prevent shearing forces acting on the sample. The elastic hoses connected to the offset extensions which lead the gold cables are blocked by hose clamps (f). Finally, the caps are sealed by silicon glue, RTV-1 E43 from Wacker, Germany (g) and the gas conducts connected to the open extensions (h).

The installed samples were heated to 700°C, where an air flow of 100 ml/min was conducted into the cathode gas compartment. On the anode side, an argon flow of 80 ml/min during 10 minutes was used to purge all oxygen before the gas flow was abruptly changed to pure dry hydrogen. The OCV under argon depends on the residual oxygen content in the anode gas stream and the cell's gas tightness and was generally in the range of 60-80 mV, according to the electrolyte and sealing quality, i.e. gas-tightness. After the gas stream was changed to pure dry hydrogen, the potential rose abruptly and overshoot in the first seconds, decreased instantaneously afterwards and rose slowly again within the next ca. two hours to a constant value as shown in Fig. 9.12. Since the anode is a thin layer, its reduction should take place very quickly and its slow rise is an indication of diffusive limitations. After the OCV was established, electrochemical characterisation was performed by IV curve measurements and impedance spectroscopy which are shown in the next section.

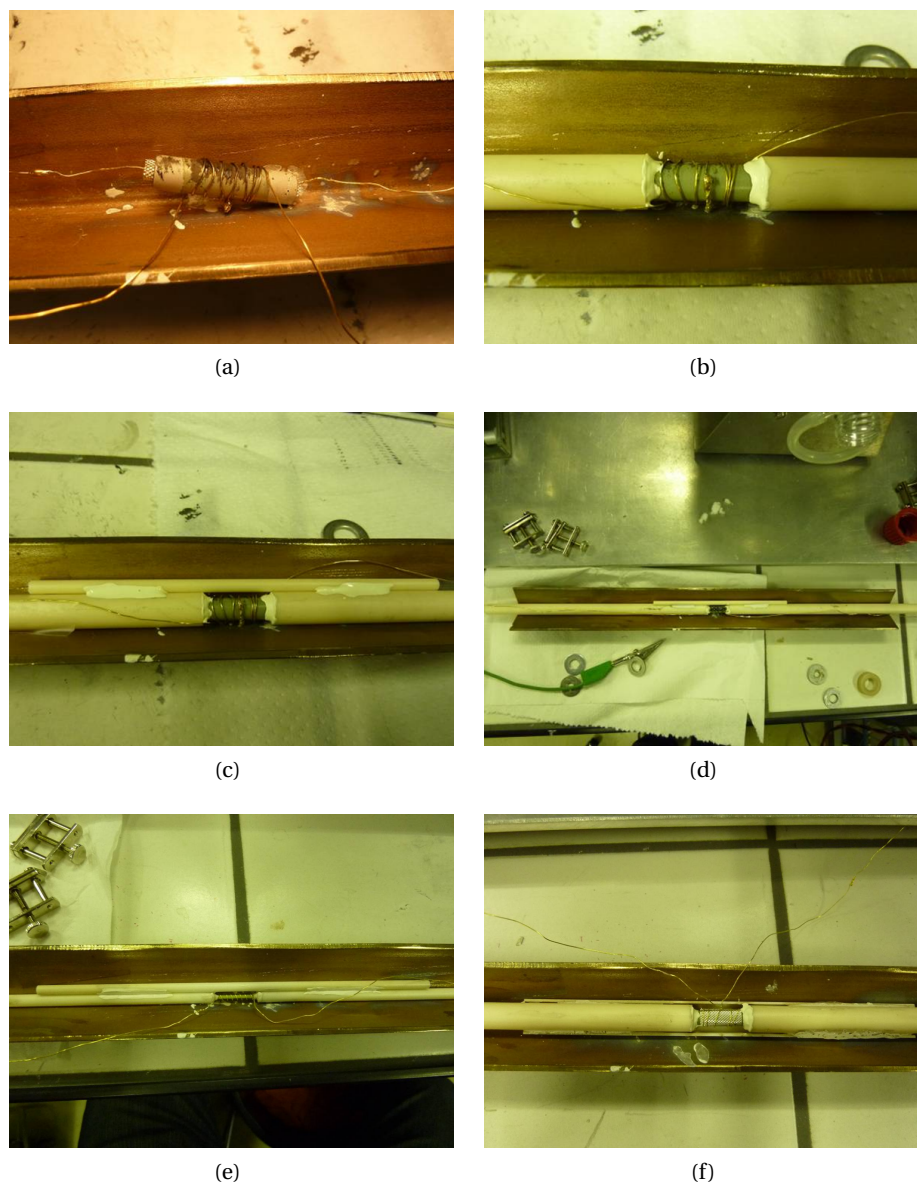


Figure 9.10: Preparational steps of a sample for electrochemical testing (a)Electrical connection (current collection) by gold wires. (b)Sealing of the sample by ceramic glue. (c)Connection of both extensions by a third tube ("bridge"). (d)A complete sample for electrochemical testing. (e)The bridge as mechanical support for tubes of type Ex-SD. (f)The half-pipe as mechanical support for tubes of types CIP-VITO and T-SC.

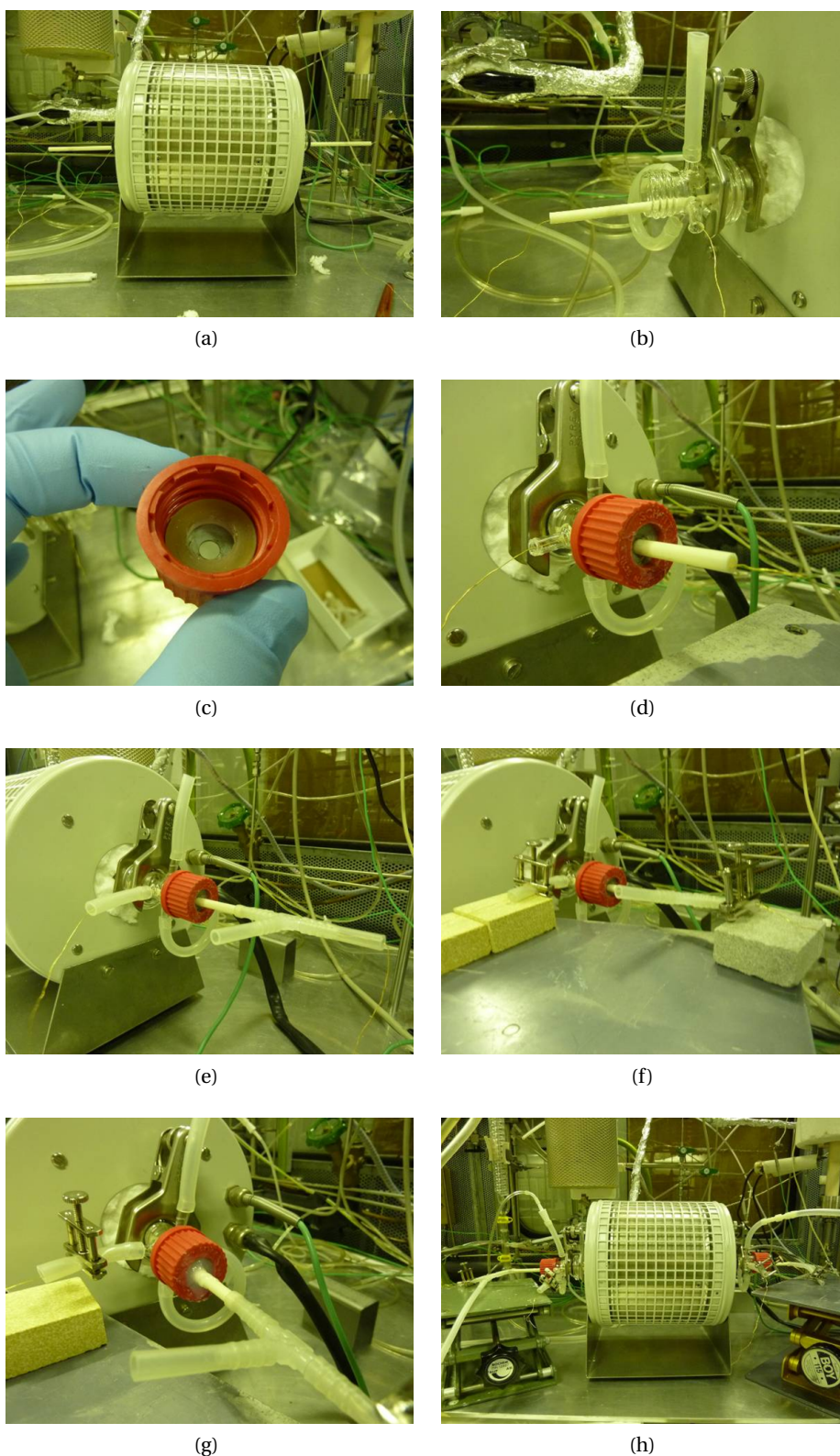


Figure 9.11: Installation of a sample for electrochemical testing (a) Sample inside quartz tube in tubular furnace. (b) Extraction of anode current collectors through quartz end pieces. (c) Caps with single-hole washers. (d) Connection of caps to quartz tube. (e) Addition of elastic end pieces for gas connection. (f) Blocking of elastic hoses by hose clamps. (g) Sealing of caps by silicon glue. (h) Connection of gas conducts.

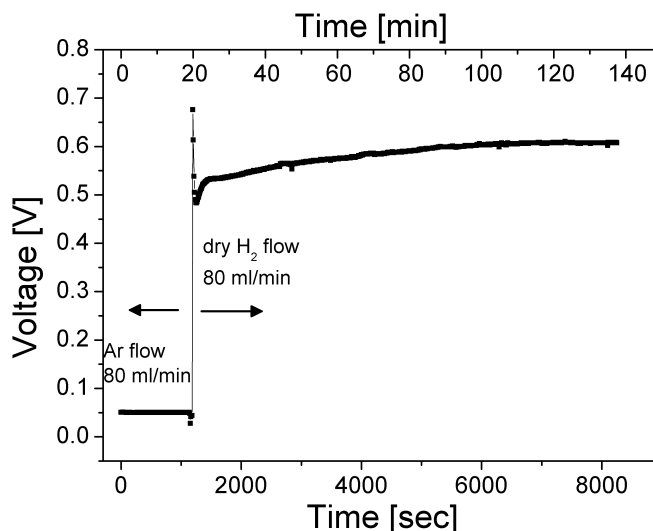


Figure 9.12: Establishment of OCV after anode gas is changed to pure hydrogen gas flow.

9.3 Electrochemical Results

9.3.1 Cells based on extruded tubes (Ex-SD)

The variation of stable OCVs at 700°C obtained after equilibration of the voltage under dry hydrogen atmosphere for the different samples is shown in Fig. 9.13. A scatter of 600-1100 mV is evidenced, which leads to a confidence range of 0.8 ± 0.2 V. While dry hydrogen should theoretically lead to even higher OCVs, values above 1050 mV can be considered reasonable with respect to leakage. As the fabrication conditions were the same for all investigated tubes, the rather low reproducibility can be attributed to tube surface grooves and roughness on the micrometer-scale which leads to layer defaults such as pinholes.

After the establishment of the OCV, IV-curves were recorded in a potential range between the OCV and 0.5 V. Current densities were calculated as the ratio of current and active anode surface area. A typical IV curve is shown in Fig. 9.14.

Power densities were calculated as the product of cell voltage and current density. The voltage showed a linear decrease up to ca. 35 mA/cm², which corresponded to an ASR of ca. 1.3 Ωcm². The cell performances were strongly limited by diffusion, as the voltage decreased abruptly at ca. 35 mA/cm². This would suggest rather dense electrodes which limit the gas transport. Post-test analysis evidenced a rather dense anode microstructure as partly visible in Fig. 9.9 for samples analysed before the test, but even more pronounced after the test as shown in Fig. 9.15a. In addition, a rather dense Pt-layer covering the anode was evidenced and is shown in Fig. 9.15b. After the first series of measurements, rice starch was added as pore former to increase the anode porosity, however no substantial improvement could be noticed.

The electrochemical impedance spectroscopy (EIS) analysis for anodes both with and without

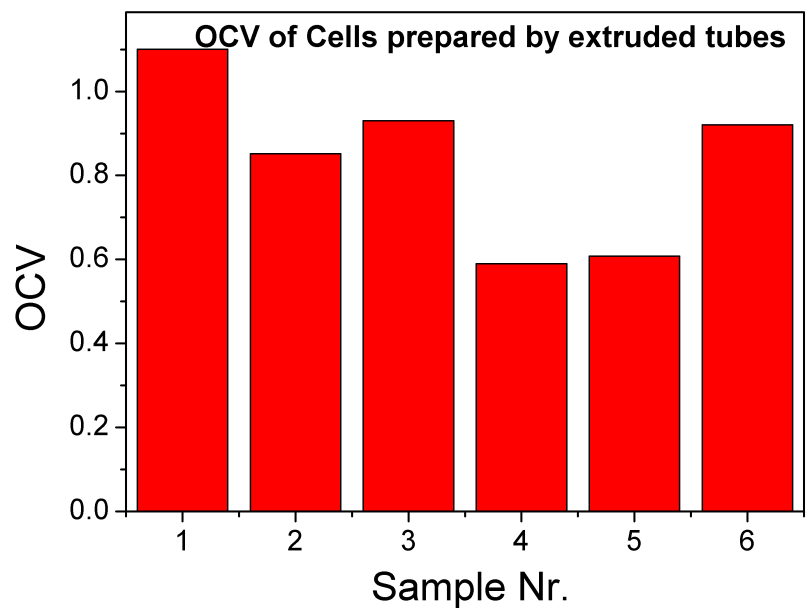


Figure 9.13: Variation of OCV for cells based on extruded tubes.

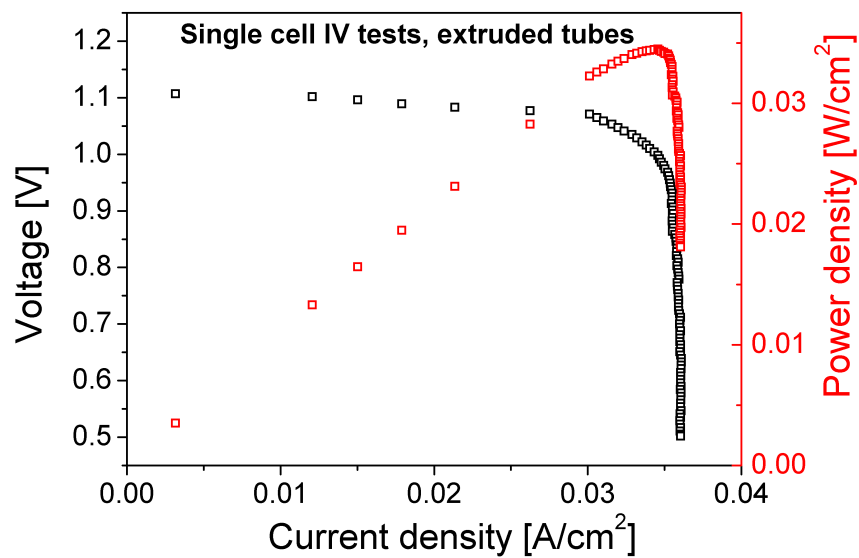


Figure 9.14: Typical IV curve for cells based on extruded tubes.

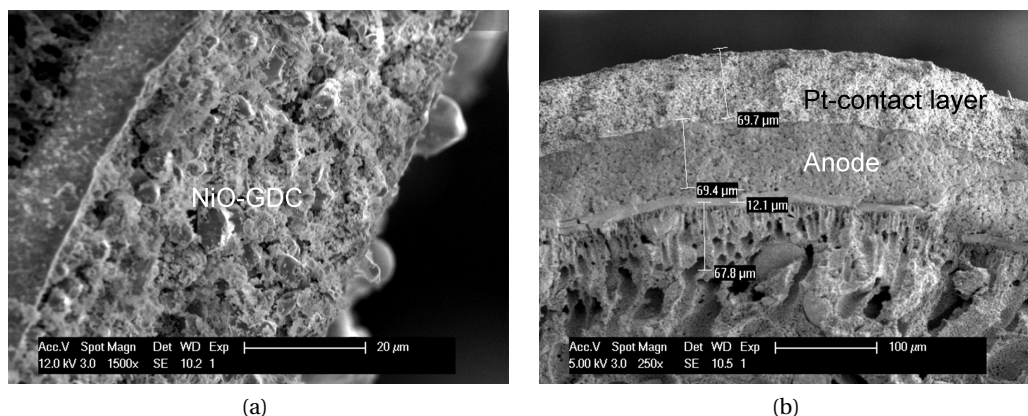


Figure 9.15: Post-mortem cross-section of cells based on extruded tubes. (a)Dense microstructure of the anode layer (b)Pt-layer on the anode surface

rice starch addition could not be effected below frequencies of ca. 3 kHz, as the impedance grew substantially and the measurement stopped. The high-frequency parts of the Nyquist-type plots measured for the tested cells were rather indistinct, but generally showed the trend of a huge polarisation resistance. This is supposedly due to densification of the Pt-contacting layer on the anode side, which is already quite dense at 700°C operating temperature. An additional thermal treatment at 900°C led to even higher impedance, which indicates further densification of Pt, as the electrode materials have been exposed to higher temperature before and the ceramic seal was not in direct contact to the electrodes and showed no signs of reaction. Even when Pt-paste was only deposited as small stripes along the anode surface, the whole anode surface showed a characteristic silvery appearance after the test, indicating substantial Pt-diffusion.

Different current collection methods on the anode side must be used in the future to improve the cell performance.

9.3.2 Cells based on tubes prepared by slip-casting(T-SC)

As the setup involving tubes of greater diameter was challenging, only cells of slip-cast tubes, T-SC, were measured. Additionally, the tested cells were not the ones showing the lowest permeabilities which leaves some space for possible improvements. The tested cells had an GDC-electrolyte layer thickness of ca. 11 µm. The open circuit voltage (OCV) was ca. 0.3 V at 600°C. The absence of Pt as current collector was immediately perceivable, as EIS measurements could be successfully performed over the whole frequency range of 0.1-5·10⁵ Hz, even though the signal was very noisy in the lower frequency range. EIS results are shown in Fig. 9.16. Substantial polarisation losses were evidenced, which are probably related to the anode microstructure. As the rise at lower frequencies is nearly vertical, an almost pure capacitor is evidenced, which highlights the limitations mentioned before. Furthermore, the current collection method of wrapped Ag-meshes proved sufficient for a stable voltage signal

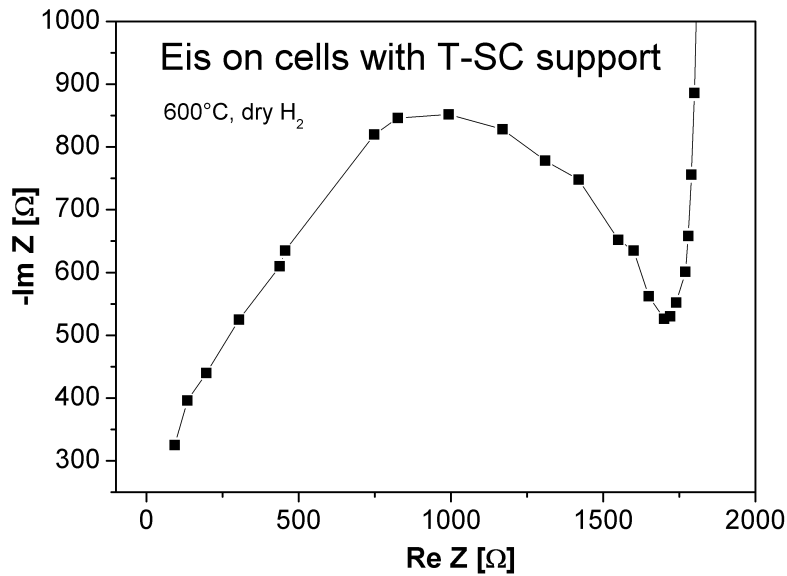


Figure 9.16: EIS measurement for cells based on slip-cast tubes. The y-axis is compressed for better readability.

but is probably still not efficient enough on the anode side, as silver has a higher TEC than the cell materials and probably loses some contact during heating. The IV-characteristics of the cell at 600°C are shown in Fig. 9.17 and were rather similar to the cells prepared by extrusion, as a limiting current density led to a drastic voltage drop. Due to the higher active electrode area and the lower OCV, a much lower power density of only few mW/cm² was obtained. In summary, the anode microstructure and the current collection method were very strongly limiting parameters for the electrochemical performance. The differences in shrinkage behaviour of cathode and electrolyte materials led to electrolyte layers showing residual porosity which impeded a correct OCV as gas interdiffusion decreased the difference in oxygen partial pressure between the two gas compartments.

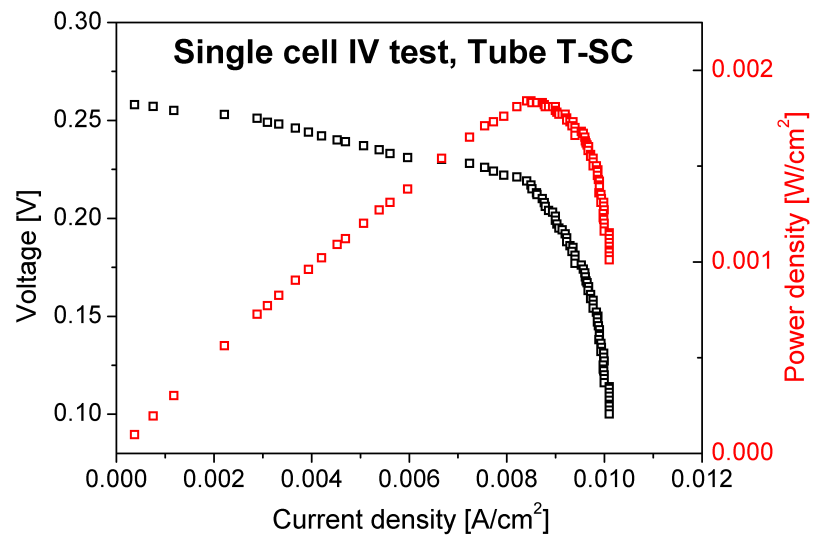


Figure 9.17: IV curve for cells based on slip-cast tubes.

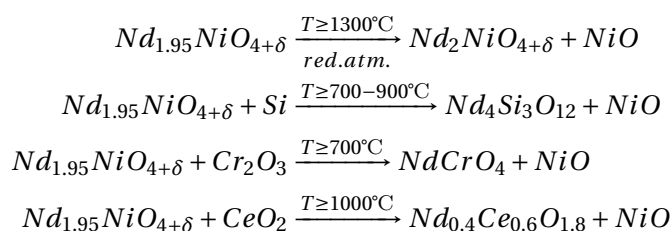
10 Summary, Conclusions and Outlook

In this thesis, a number of different aspects concerning the fabrication and functioning of micro-tubular SOFC with mechanical cathode support were investigated. Neodymium nickelate was tested in this work as an alternative cathode material for the intermediate temperature range of 650-750°C. Different experimental tests and setups were used to evaluate several properties such as chemical reactivity, sintering shrinkage, exchange current density with GDC electrolyte and electrochemical performance of complete cells.

In the following, the main results for each of the investigated topics will be resumed followed by the general conclusion drawn from this work and an outlook with improvements of the system will be given at the end of the chapter.

10.1 Chemical Reactivity

In this work, several reactions of neodymium nickelate with different constituents were identified, where some of the reaction are evitable by proper powder processing and system design, some can be eliminated by external devices such as filters and some are inevitable but do not endanger severely the operation of the system. All the observed reactions of neodymium nickelate are shown in the equations below.



The first reaction is triggered by reducing atmospheres or by reaction temperatures above 1300°C. It can be avoided by complete gas-tightness of the electrolyte and of the sealing material at operating conditions. In normal fuel cell operation, the gas atmosphere at the cathode side is sufficiently oxygen-rich to prevent the establishment of reducing atmospheres,

especially in a stack/system where typically air flow excess is used for thermal management. The reaction also occurs at temperatures which are too elevated for operation but can prevail during the sintering process as the chemical stability of the sub-stoichiometric material is restricted to lower temperatures. This can be circumvented by an adapted fabrication process with limited sintering temperature, which requires well-matched shrinkages of all cofired materials.

The second reaction is initiated by the presence of silicium. This impurity was introduced during the processing of calcined powder to ensure a defined granulometry. Cost-cutting milling media materials such as zirconia silicate are not as abrasion-resistant as ZrO_2 and can contaminate the powder, while an improved powder purity would automatically inhibit the reaction.

The third reaction happens because of the evaporation of volatile Cr-species from metallic interconnects with ensuing deposition on the cathode. Although neodymium nickelate can show signs of improved resistance against Cr-poisoning compared to other cathode materials reported in the literature, degradation still occurs and can only be inhibited by effective Cr-filters, protective scales on the metallic interconnector surface or Cr-free cost-intensive materials.

The fourth reaction takes place at the NNO-GDC interface. While different reports have shown optimum performance of nickelate cathodes for a sintering temperature of 1150-1200°C, the cited reaction starts at even lower temperatures. The presence of the mixed oxide at the interface is consequently inevitable for optimum performance but does not severely degrade the electrical conduction such as the pyrochlore structured $\text{La}_2\text{Zr}_2\text{O}_7$ or the perovskite SrZrO_3 at LSM-YSZ interfaces [156].

All reactions develop due to the high mobility of neodymium in the compound. The replacement of neodymium by another cation [24] or the preparation of higher-ordered Ruddlesden-Popper phased nickelate compounds [33] may decrease the reactivity while keeping the electrochemical activity on a sufficient level.

Additionally, the reactivity of adjacent GDC-interlayer and zirconia electrolyte layers was investigated by diffusion couples. 10 mol% yttria-stabilised zirconia showed substantial reaction with GDC with almost complete intermixture of cations at temperatures as low as 1250°C, whereas ScSZ-GDC showed much reduced reaction even at temperatures as high as 1300°C. However, a reaction occurred for both zirconia materials in the whole investigated temperature range of 1250-1350°C. Considering the optimum sintering temperature of nickelate cathodes of 1150-1200°C, the cofiring temperature for cathode-supported cells should be decreased to 1200°C, which would require excellent powder processing, highly matched sinter profiles and high support shrinkages [95].

10.2 Shrinkage

The shrinkage of nickelate powders and tubes, slip-cast ceria and zirconia pellets was investigated. The nickelate material typically showed shrinkages of 11-13% to 1300°C in the case of compacted pellets and tubes which were prepared by dry methods such as cold-isostatic pressing. Wet-chemical processing such as extrusion showed higher shrinkages, but is highly dependent on the slurry composition, as tubes prepared by slip-casting from water-based suspensions also achieved only 13% sinter shrinkage up to 1300°C.

Commonly used commercial GDC-powder shrank 11-12% to 1300°C and showed densities of 80-85%. The addition of Cobalt as sintering aid decreases the sintering temperature. The relative sinter shrinkage remained almost unchanged by the addition of Cobalt but was strongly influenceable by the choice of solvent and dispersant. Dispersants in organic media, which were less effective due to the absence of electrostatic repulsive forces, led to lower green body densities and increased sinter shrinkages.

Zirconia powders generally show higher shrinkage than ceria powders to full density. Sinter active scandia-stabilised zirconia powder by Treibacher AG showed the highest green densities and the lowest sinter shrinkages to 1300°C in water-based suspensions with PAA-dispersant. The sinter shrinkage was still ca. 18% and could not be decreased any further. The powder however was well densified at 1300°C and the sinter temperature can potentially even decrease to the 1200°C target according to its dilatometric shrinkage curve.

As the ceria and zirconia layers have to be cosintered in order to achieve good mechanical adherence, the zirconia sinter shrinkage is the critical parameter for sufficient densification and has to be at least matched by the tube's shrinkage. Typically, the shrinkage during the cofiring process decreased compared to the free sinter shrinkage. As 18% shrinkage were necessary for zirconia layers during cosintering, the actual shrinkage of free tubular substrates during sintering should be even higher. This requires very sinter-active cathode powders of high specific surface area and low particle size.

Zirconia tends to spall when it is sintered under constrained conditions, more precisely when tensile stresses prevail in the zirconia layer. This could be seen in this work as the thickness of ScSZ layers could not exceed ca. 3 µm without the occurrence of delaminations. The substrate should be sinter-active enough to shrink before the ScSZ-layer in order to exert compressive stresses in the zirconia layer during sintering. The presence of the ceria interlayer which shrinks before ScSZ partially relieves the tensile stresses in ScSZ, however the substrate sintering temperature still exercises the biggest influence on the stress state in the zirconia layer due to the substrate's thickness with respect to total cell size and therefore its high proportion of the overall stress state.

10.3 Exchange Current Density

The exchange current density describes the current density exchanged across an interfaces and was measured for nickelate-ceria systems. The value depends on the operation temperature, the electrical conductivity and the density of the electrolyte [32], the granulometry of the

electrode and the current collection efficiency among other parameters. In this context, two extreme cases of a "poor" interface state with low current collection efficiency, low electrolyte density and coarse granulometry of the nickelate cathode as well as a "good" interface with an improved current collection method, higher electrolyte density and finer nickelate granulometry were tested and revealed exchange current densities at 700°C of 10 and 50 mA/cm², respectively.

Sintering temperatures of 1100-1300°C led to 35-50 mA/cm² for fine-grained nickelate electrodes whereas electrodes sintered at 1000°C had poor mechanical contact to GDC pellets and resulted in distinctly worse current densities. While these results indicate a slight upgrade over conventional LSM cathode-YSZ electrolyte interfaces, the improvement can still be increased by using Cobalt-doped GDC-electrolytes as cobalt-rich phases segregate at the grain boundaries and form highly-conductive grain-boundary layers [32, 120]. The exchange current densities at 700°C are slightly higher than for LSM cathodes, but lower than values measured for LSCF-GDC interfaces, which suggests that the temperature of operation should not be decreased to ≤600°C for nickelate cathodes, where LSCF cathode activity is probably superior.

This shows that the temperature window for the utilisation of nickelates is between 650-750°C, which is mirrored in the literature [36] by electrochemical results of tested planar single cells with LSM, LSCF and nickelate cathodes. Cr-poisoning of nickelate cathodes was also evidenced by the evolution of EIS semi-circles and the exchange current density i_0 , which decreased from 15 to 8 mA/cm² during long-term tests of 1000 hours duration.

10.4 Electrochemical Performance of Single Cells

Tubes of different fabrication routes were used for different cell designs. All tubes with shrink-ages less than 18% were used for single cells with a single GDC electrolyte layer, as GDC can be sintered to almost full density under constrained conditions [108]. Tubes of fabrication routes which showed more than 17% shrinkage up to the sinter temperature were used for single cells with GDC interlayer and ScSZ electrolyte.

Different test series were prepared, where improvements based on the results of the previous tests were incorporated in newer series. For tubes prepared by extrusion, gold wires were used as current collector and Pt-paste was painted on the anode surface to improve the contact during heating, as gold expands more than the anode material and detached without the presence of Pt-paste, leading to loose contact on the anode side.

Tubes of bigger diameter were more robust and the simple insertion of a gold wire into the cathodic tube was insufficient for stable current collection. Consequently, silver meshes were used as cathode current collectors. Rectangular silver meshes were cut and gold wires were connected to the silver meshes by point-brazing. The silver meshes were rolled around tubular objects and inserted into the tube for cathode current collection and wrapped around the anode for anode current collection.

Tubes prepared by extrusion showed permeabilities of $4\text{--}12 \times 10^{-7} \text{ mol m}^{-2} \text{Pa}^{-1} \text{s}^{-1}$, which led to open circuit voltages (OCV) of 0.6–1.1 V under dry hydrogen atmosphere at 700°C and evidenced some residual porosity in the cell. Cross-section images showed some signs of delamination of the ScSZ layer, probably due to slightly constrained sintering, which was responsible for the experienced gas leakage. The thickness of GDC and ScSZ layers was ca. 6 and 3 μm respectively. The power density under dry hydrogen at 700°C was 0.03 Wcm^{-2} at 0.035 Acm^{-2} .

Tubes prepared by cold-isostatic pressing at VITO (CIP-VITO) showed permeabilities of $3\text{--}8 \times 10^{-7} \text{ mol m}^{-2} \text{Pa}^{-1} \text{s}^{-1}$ for GDC electrolyte layer thicknesses of 11–13 μm . The electrochemical performance was not tested as cells made from tubes of type T-SC showed lower permeabilities.

Tubes prepared by cold-isostatic pressing at the University of Zaragoza (CIP-ZARA) showed bigger surface pore sizes than the other tube types due to the utilisation of commercial maize starch as pore former. As the pore size was at least twice as big as the deposited particles of the GDC interlayer, the pores were infiltrated by the particles and inhomogeneous green layers resulted in insufficient gas-tightness. Therefore, the fabrication route was abandoned and the focus shifted to other tube types.

Tubes prepared by cold-isostatic pressing at the laboratory of powder technology (LTP) at EPFL (CIP-EPFL) were fabricated with lower compaction pressure to yield tubes of lower green density, and consequently higher sinter shrinkages, and showed ca. 14 % of linear thermal shrinkage up to the sintering temperature of 1300°C. As this was still not sufficient to avoid spalling of deposited and cofired ScSZ layers, only GDC electrolyte layers were deposited. The measured permeability of cells with GDC-1CD electrolyte was $2\text{--}3 \times 10^{-6} \text{ mol m}^{-2} \text{Pa}^{-1} \text{s}^{-1}$, which is much higher than the permeability of cells prepared from tubes T-SC. Therefore, the electrochemical performance was not tested.

Tubes prepared by slip-casting at Cereco (T-SC) Cells made from tubes of type T-SC were prepared by dip-coating of GDC-electrolyte layers, which showed a thickness of 11–13 μm . The permeabilities of complete cells were $9\text{--}11 \times 10^{-8} \text{ mol m}^{-2} \text{Pa}^{-1} \text{s}^{-1}$, which were the best among all tubes. Electrochemical cell tests were performed using a half-pipe shaped cell support and silver mesh as current collectors on the anode and cathode side. An OCV of 0.3 V at 600°C under dry hydrogen was obtained, as residual porosity and electronic conductivity of the electrolyte prevented the establishment of the correct OCV. The power density under dry hydrogen at 700°C was only a few mWcm^{-2} as substantial diffusion limitations occurred.

10.5 Outlook

Cathode-supported micro-tubular cells are very interesting from a system's point of view but generally are limited by their rather constricted performance, which is partially a result of difficulties during the fabrication of these cells related to cosintering at low firing temperatures.

This has led to very few literature contributions compared to anode- or electrolyte-supported cells and consequently many parameters and relations have yet to be explored.

As the shrinkage of the cathode tube is the key parameter for successful densification of the cofired electrolyte layers, more research has to be done to develop cost-efficient industry-suitable fabrication methods for nickelate tubes. During the work, a lot of time was invested to find materials which allow densification at temperatures low enough for cosintering purposes. Scandia-stabilised zirconia (ScSZ) powder from Treibacher was considered sinter-active enough to densify at temperatures below 1300°C and pellets were found to be >95% dense after sintering at 1300°C. As the temperature of its maximum densification rate was 1117°C, complete densification can be envisaged at 1200°C. Zhao [95] has demonstrated that ScSZ from Daiichi, which is slightly less sinteractive than powder from Treibacher, could be densified at 1250°C in a cofiring process when the substrate's shrinkage was sufficiently high. Cosintering of ScSZ electrolyte layers with ceria interlayers and nickelate tubes at 1200°C would improve both interfaces in terms of electrochemical activity and interfacial phase formation.

Gadolinia-doped ceria powder can be used for low temperature densification by the addition of Cobalt as sintering aid, as maximum shrinkage rates of 2 wt% Co-doped ceria powder were observed at 900°C. As the sintering temperature of Co-doped ceria is lower than that of ScSZ, zirconia goes into compression which helps the densification. However, nickelate powder has to be processed to enable sintering at temperatures as low as ceria to minimize the mismatch of shrinkage curves. Therefore, the granulometry of nickelate powder must be shifted to smaller particle sizes and/or sintering aids for nickelate powder must be developed. As very fined-grained powder in the nanometer-range is difficult to compact by dry methods such as CIP due to enhanced particle surface friction, wet-chemical methods such as extrusion or dip-coating are necessary to develop further. Moreover, they enable the fabrication of tubes with low green density and still high enough mechanical stability due to the presence of binder and other additives, whereas tubes of low green density prepared by dry methods such as CIP are prone to cracking. A smaller nickelate particle size would also improve the electrochemical activity as shown by the measurement of exchange current densities with milled and as-received nickelate powder.

For the deposition of ScSZ layers by dip-coating, water-based suspensions were used as the employment of water-soluble PAA-dispersant led to the highest ScSZ green density and consequently the lowest sinter shrinkage to full density. However, water-based suspensions were very thin fluid which can lead to inhomogeneous green layers, especially considering the nickelate tube's surface roughness, which was in the range of a few micrometers and therefore on the same scale as the deposited layer's thickness. Gelatin can be imagined as a further additive to increase the suspension's viscosity and further decrease its surface tension, which was shown for tape-casting paste development [157]. Suspensions with organic dispersants and isopropanol solvent had substantially lower green density due to less efficient particle dispersion and were far from dense after sintering at 1300°C.

Another critical field of work involves the tube dimensions and porosity. The nickelate family of materials typically possesses conductivities of 80-100 S/cm at 700°C, where 100 S/cm is considered the limiting conductivity for fuel cell operation. As the conductivity is a function

of density, a lower porosity than for anode-supported cells of higher electrical conductivity should be targeted. This can lead to elevated polarisation losses due to diffusion limitations, especially at high current densities. The diffusion losses depend mainly on the porous tube's pore channel diameter and the tube's wall thickness, i.e. diffusion distance, and tortuosity. The pore size is limited by the granulometry of the powder deposited on the tube's surface as pore sizes distinctly greater than particle sizes lead to infiltrated pores and inhomogeneous layers with defects such as pinholes during the coating process. As the tube pore size is typically limited to ca. 1 μm in diameter, its wall thickness and tortuosity should be limited to less than 400 μm and 5, respectively. Tubes of greater diameter also need higher wall thicknesses for mechanical support, however tube wall thicknesses of 400 μm should be sufficient to stabilise tubes up to ca. 6-8 mm of diameter, especially at lower porosity.

In order to demonstrate the potential of neodymium nickelate as cathode material, the single cell performance was evaluated by calculating losses due to diffusion, interfacial charge transfer and electrical conduction using analytical expressions for anode and cathode concentration and activation overpotentials as well as ohmic losses published by Chan et al. [158]. The polarisation losses due to oxygen diffusion through the porous cathode support tube were calculated using the diffusion parameters of pore size, porosity and tortuosity shown in chapter 6. The calculation of diffusion losses was published [132] for extruded and compacted tubes (Ex-SD and CIP-VITO). Here the calculation of concentration potential is done assuming extruded tubes of small diameter (Ex-SD) working at 700°C, with all relevant parameters being shown in Table 10.1.

For the calculation of anode diffusion losses, the tortuosity and the pore size radius were estimated to be 5 and 1 μm respectively and the porosity was determined by calculations and image analysis to be 34 vol%. For activation losses, the key parameter in the calculation is the exchange current density. For the interface GDC-NNO, experimentally measured (cf. chapter 8) exchange current densities of 15 mA/cm^2 were used. For the interface ScSZ-Ni/YSZ on the anode side, 100 mA/cm^2 were assumed. The double layer electrolyte interface between GDC and ScSZ was presumed to have a negligible contribution to the total activation losses.

Ohmic losses due to limited conductivity were calculated by assuming that the conductivity is proportional to the density of the material, and published conductivities at 700°C of 0.05 S/cm for 10GDC [159, 135] and for ScSZ [160] were taken as conductivities at 100% density. The conductivity of Ni-YSZ anodes at 700°C was given by Wang [129] for dense NiO-YSZ microstructure, hence 23% porosity after the reduction of NiO to Ni [154], leading to a relative porosity of $23/34=0.68$. The conductivity of neodymium nickelate of stoichiometry $\text{Nd}_{1.95}\text{NiO}_{4+\delta}$ was taken as 100 S/cm at 700°C [24] at full density. The ohmic losses of the current collectors were assumed to be negligible and perfect current paths perpendicular to the respective layer's surface were assumed, where especially the latter can be considered a simplification. All relevant parameters are again shown in Table 10.1.

The results of these calculations are shown in Fig. 10.1. Further parameters involving system conditions were a specific fuel flow of $6 \text{ ml}\cdot\text{cm}^{-2}\cdot\text{min}^{-1}$, an active anode surface area of 0.97 cm^2 and an air excess flow of $\Lambda=5$. As can be seen from Fig. 10.1, the specific fuel flow is too

Table 10.1: Parameters used for the calculation of the expected single cell performance. All Parameters taken from literature were for 700°C. P_A represents total pressure at the anode side, P_C represents total pressure at the cathode side.

Polarisation resistance, cathode				
NNO	ϵ	τ	$\langle r \rangle$	P _C
	60%	6	0.9 μm	1 bar
Polarisation resistance, anode				
Ni-YSZ	ϵ	τ	$\langle r \rangle$	P _A
	34%	5	1 μm	1 bar
Activation overpotential, cathode-side				
NNO/GDC	i_0			
	15 mA/cm2			
Activation overpotential, anode-side				
Ni-YSZ/ScSZ	i_0			
	100 mA/cm2			
Ohmic losses, all cell components				
	ϵ	σ	Source	Thickness
NNO	60%	100 S/cm	[24]	300 μm
GDC	5%	0.05 S/cm	[159, 135]	10 μm
ScSZ	5%	0.05 S/cm	[160]	10 μm
Ni-YSZ	34%	890 S/cm	[129]	30 μm

low to attain the maximum power density, as the fuel utilisation reaches 100% at lower current densities already. Higher fuel flows would be required to reach the peak power density.

In reality, the output probably will be lower, as perfect current collection and geometries are assumed and no interfacial phases due to sintering are included which would add contributions to the ohmic losses. Nevertheless the potential for improved electrochemical performance with respect to results on LSM-supported cells [96] is visible.

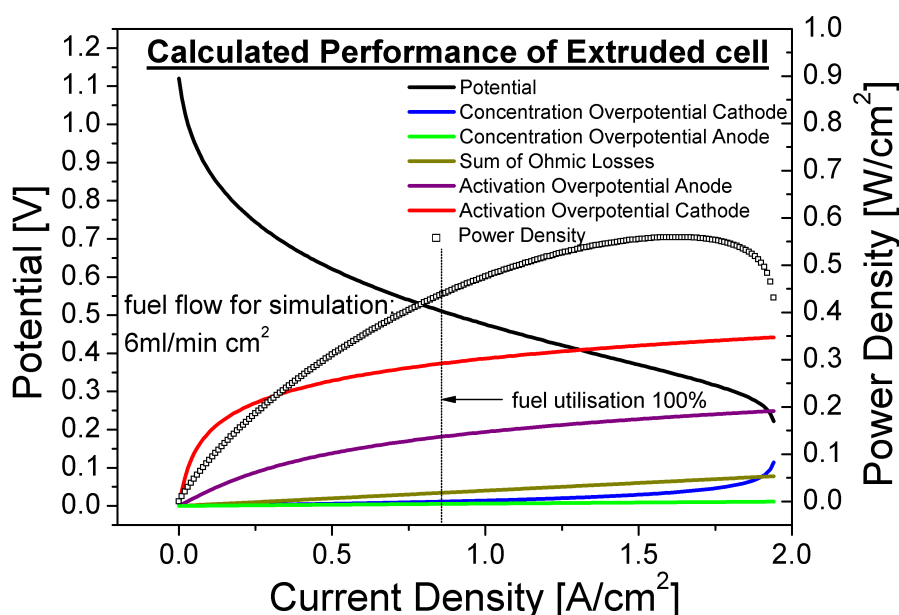


Figure 10.1: Calculated IV-curve for cells based on extruded tubes (Ex-SD). All overpotentials are also shown as a function of current density. The peak power density is beyond the limits of a fuel flow of $6 \text{ ml} \cdot \text{cm}^{-2} \cdot \text{min}^{-1}$, as the fuel utilisation approaches 100% at lower current densities.

In the bigger picture, nickelate-supported micro-tubular SOFC can be imagined in portable applications such as cell-phones or as laptop battery substitute, where frequent start-up/shut-down cycles and changes in electrical load require a high redox stability of the system, which would not be guaranteed by anode-supported cells, while the high working temperature of electrolyte-supported cells limits their applicability in the field of portable applications. The temperature window around 700°C is particularly interesting for new cathode materials, as

- Cathode-supported cells have shown competitive performance (cf. page 39) at this temperature and
- The reduction of operating temperature to ca. 700°C is in the focus of interest to reduce fabrication costs (cf. page 23).

Chapter 10. Summary, Conclusions and Outlook

Further domains of application for nickelate-supported tubular cells can be found in high-temperature electrolysis [161] and stacks in the 1-5 kW range for combined heat and power (CHP) for single-family houses in remote areas with off-grid power generation as well as integrated systems of combined gas turbine/microtubular SOFC devices for increased efficiency [89]. The latter is particularly important in the context of shortage of resources and the pursuit of sustainability.

Bibliography

- [1] W. R. Bowen and F. Jenner. The calculation of dispersion forces for engineering applications. *Advances in Colloid and Interface Science*, 56:201–243, 1995.
- [2] J. Gregory. Approximate expressions for retarded vanderwaals interaction. *Journal of Colloid and Interface Science*, 83(1):138–145, 1981.
- [3] [http://www.dispersion.com/zeta potential.html](http://www.dispersion.com/zeta%20potential.html). Zeta potential, short tutorial., 2011.
- [4] F. Perche. *Adsorption de polycarboxylates et de lignosulfonates sur poudre modèle et ciments*. PhD thesis, EPFL, 2004.
- [5] L. Bergstrom, C. H. Schilling, and I. A. Aksay. Consolidation behavior of flocculated alumina suspensions. *Journal of the American Ceramic Society*, 75(12):3305–3314, 1992.
- [6] P. Bowen, C. Carry, D. Luxembourg, and H. Hofmann. Colloidal processing and sintering of nanosized transition aluminas. *Powder Technology*, 157(1-3):100–107, 2005.
- [7] R. Krechetnikov and G. M. Homsy. Dip coating in the presence of a substrate-liquid interaction potential. *Physics of Fluids*, 17(10):–, 2005.
- [8] J. W. Krozal, A. N. Palazoglu, and R. L. Powell. Experimental observation of dip-coating phenomena and the prospect of using motion control to minimize fluid retention. *Chemical Engineering Science*, 55(18):3639–3650, 2000.
- [9] C. J. Brinker and G.W. Scherer. *Sol-gel science: the physics and chemistry of sol-gel processing*. San Diego: Academic Press, Inc, 1990.
- [10] F. Juillerat. *Self-assembled Nanostructures prepared by colloidal chemistry*. PhD thesis, EPFL, 2006.
- [11] J.-M. Haussonne, P. Bowen, C. Carry, and J. Barton. *Céramiques et Verres, Principes et techniques d'élaboration, Traité des Matériaux Vol. 16*, volume 16. Presses Polytechniques et Universitaires Romandes, Lausanne, 2005.
- [12] U. Aschauer. *Atomistic Simulation in Powder Technology - from growth control and dispersion stabilization to segregation at doped interfaces*. PhD thesis, EPFL, 2008.

Bibliography

- [13] <http://www.netzsch-thermal-analysis.com/en/products/dilatometer/>, 2011.
- [14] http://en.wikipedia.org/wiki/File:Solid-oxide-fuel_cell.svg, 2011.
- [15] B. C. H. Steele and A. Heinzl. Materials for fuel-cell technologies. *Nature*, 414(6861):345–352, 2001.
- [16] R. A. George. Status of tubular SOFC field unit demonstrations. *Journal of Power Sources*, 86(1-2):134–139, 2000.
- [17] <http://www.nfcrf.uci.edu/2/activities/ResearchSummaries/materials/Electrolyte-and-Full-Materials-Sets/Index.aspx>, 2011.
- [18] T. Suzuki, M. H. Zahir, T. Yamaguchi, Y. Fujishiro, M. Awano, and N. Sammes. Fabrication of micro-tubular solid oxide fuel cells with a single-grain-thick yttria stabilized zirconia electrolyte. *Journal of Power Sources*, 195(23):7825–7828, 2010.
- [19] J. T. S. Irvine, J. W. L. Dobson, T. Politova, S. G. Martin, and A. Shenouda. Co-doping of scandia-zirconia electrolytes for SOFCs. *Faraday Discussions*, 134:41–49, 2007.
- [20] M. Hirano, T. Oda, K. Ukai, and Y. Mizutani. Effect of Bi₂O₃ additives in Sc-stabilized zirconia electrolyte on a stability of crystal phase and electrolyte properties. *Solid State Ionics*, 158(3-4):215–223, 2003.
- [21] C. W. Sun, R. Hui, and J. Roller. Cathode materials for solid oxide fuel cells: A review. *Journal of Solid State Electrochemistry*, 14(7):1125–1144, 2010.
- [22] F. Mauvy, J. M. Bassat, E. Boehm, J. P. Manaud, P. Dordor, and J. C. Grenier. Oxygen electrode reaction on Nd₂NiO_{4+δ} cathode materials: impedance spectroscopy study. *Solid State Ionics*, 158(1-2):17–28, 2003.
- [23] B. W. Arbuckle, K. V. Ramanujachary, Z. Zhen, and M. Greenblatt. Investigations on the structural, electrical, and magnetic-properties of Nd_{2-x}Sr_xNiO_{4+δ}. *Journal of Solid State Chemistry*, 88(1):278–290, 1990.
- [24] E. Boehm, J. M. Bassat, P. Dordor, F. Mauvy, J. C. Grenier, and P. Stevens. Oxygen diffusion and transport properties in non-stoichiometric Ln(2-x)NiO(4+δ) oxides. *Solid State Ionics*, 176(37-38):2717–2725, 2005.
- [25] H. Chaker, T. Roisnel, M. Potel, and R. Ben Hassen. Structural and electrical changes in NdSrNiO_{4-δ} by substitute nickel with copper. *Journal of Solid State Chemistry*, 177(11):4067–4072, 2004.
- [26] Y. Toyosumi, H. Ishikawa, and K. Ishikawa. Structural phase transition of Nd₂NiO_{4+δ} (0.106 ≤ δ ≤ 0.224). *Journal of Alloys and Compounds*, 408:1200–1204, 2006.
- [27] V. V. Kharton, A. P. Viskup, A. V. Kovalevsky, E. N. Naumovich, and F. M. B. Marques. Ionic transport in oxygen-hyperstoichiometric phases with K₂NiF₄-type structure. *Solid State Ionics*, 143(3-4):337–353, 2001.

- [28] S. J. Skinner and J. A. Kilner. Oxygen diffusion and surface exchange in $\text{La}_{2-x}\text{Sr}_x\text{NiO}_{4+\delta}$. *Solid State Ionics*, 135(1-4):709–712, 2000.
- [29] A. Egger, W. Sitte, F. Klauser, and E. Bertel. Long-term oxygen exchange kinetics of $\text{Nd}_2\text{NiO}_{4+\delta}$ in H_2O - and CO_2 -containing atmospheres. *Journal of the Electrochemical Society*, 157(11):B1537–B1541, 2010.
- [30] M. Yang, E. Bucher, and W. Sitte. Effects of chromium poisoning on the long-term oxygen exchange kinetics of the solid oxide fuel cell cathode materials $\text{La}_{0.6}\text{Sr}_{0.4}\text{CoO}_3$ and Nd_2NiO_4 . *Journal of Power Sources*, 196(17):7313–7317, 2011.
- [31] C. Lalanne. *Synthèse et mise en forme de nouveaux matériaux de cathode pour piles ITSOFC : réalisation et tests de cellules*. PhD thesis, Université Bordeaux, 2005.
- [32] D. Perez-Coll, A. Aguadero, M. J. Escudero, P. Nunez, and L. Daza. Optimization of the interface polarization of the La_2NiO_4 -based cathode working with the $\text{Ce}_{1-x}\text{Sm}_x\text{O}_{2-\delta}$ electrolyte system. *Journal of Power Sources*, 178(1):151–162, 2008.
- [33] R. Sayers, J. Liu, B. Rustumji, and S. J. Skinner. Novel K_2NiF_4 -type materials for solid oxide fuel cells: Compatibility with electrolytes in the intermediate temperature range. *Fuel Cells*, 8(5):338–343, 2008.
- [34] F. Mauvy, C. Lalanne, J. M. Bassat, J. C. Grenier, H. Zhao, L. H. Huo, and P. Stevens. Electrode properties of $\text{Ln}_2\text{NiO}_{4+\delta}$ ($\text{Ln} = \text{La}, \text{Nd}, \text{Pr}$) - AC impedance and DC polarization studies. *Journal of the Electrochemical Society*, 153(8):A1547–A1553, 2006.
- [35] F. Mauvy, C. Lalanne, S. Fourcade, J. M. Bassat, and J. C. Grenier. Impedance spectroscopy study of $\text{Nd}_2\text{NiO}_{4+\delta}$, LSM and platinum electrodes by micro-contact technique. *Journal of the European Ceramic Society*, 27(13-15):3731–3734, 2007.
- [36] V. A. C. Haanappel, C. Lalanne, A. Mai, and F. Tietz. Characterization of anode-supported solid oxide fuel cells with Nd_2NiO_4 cathodes. *Journal of Fuel Cell Science and Technology*, 6(4):0410161–0410166, 2009.
- [37] K. Yashiro, N. Yamada, T. Kawada, J. Hong, A. Kaimai, Y. Nigara, and J. Mizusaki. Demonstration and stack concept of quick startup/shutdown SOFC (qSOFC). *Electrochemistry*, 70(12):958–960, 2002.
- [38] I. P. Kilbride. Preparation and properties of small diameter tubular solid oxide fuel cells for rapid start-up. *Journal of Power Sources*, 61(1-2):167–171, 1996.
- [39] J. Staniforth and K. Kendall. Cannock landfill gas powering a small tubular solid oxide fuel cell - a case study. *Journal of Power Sources*, 86(1-2):401–403, 2000.
- [40] J. Staniforth and K. Kendall. Biogas powering a small tubular solid oxide fuel cell. *Journal of Power Sources*, 71(1-2):275–277, 1998.

Bibliography

- [41] C. Finnerty, G. A. Tompsett, K. Kendall, and R. M. Ormerod. SOFC system with integrated catalytic fuel processing. *Journal of Power Sources*, 86(1-2):459–463, 2000.
- [42] C. M. Finnerty, N. J. Coe, R. H. Cunningham, and R. M. Ormerod. Carbon formation on and deactivation of nickel-based/zirconia anodes in solid oxide fuel cells running on methane. *Catalysis Today*, 46(2-3):137–145, 1998.
- [43] C. M. Finnerty, R. H. Cunningham, K. Kendall, and R. M. Ormerod. A novel test system for in situ catalytic and electrochemical measurements on fuel processing anodes in working solid oxide fuel cells. *Chemical Communications*, 8:915–916, 1998.
- [44] K. Kendall, C. M. Finnerty, G. Saunders, and J. T. Chung. Effects of dilution on methane entering an SOFC anode. *Journal of Power Sources*, 106(1-2):323–327, 2002.
- [45] G. J. Saunders and K. Kendall. Reactions of hydrocarbons in small tubular SOFCs. *Journal of Power Sources*, 106(1-2):258–263, 2002.
- [46] G. J. Saunders, J. Preece, and K. Kendall. Formulating liquid hydrocarbon fuels for SOFCs. *Journal of Power Sources*, 131(1-2):23–26, 2004.
- [47] C. Mallon and K. Kendall. Sensitivity of nickel cermet anodes to reduction conditions. *Journal of Power Sources*, 145(2):154–160, 2005.
- [48] <http://www.adelan.co.uk>.
- [49] N. M. Sammes, R. J. Boersma, and G. A. Tompsett. Micro-SOFC system using butane fuel. *Solid State Ionics*, 135(1-4):487–491, 2000.
- [50] C. E. Hatchwell, N. M. Sammes, and K. Kendall. Cathode current-collectors for a novel tubular SOFC design. *Journal of Power Sources*, 70(1):85–90, 1998.
- [51] C. Hatchwell, N. M. Sammes, I. W. M. Brown, and K. Kendall. Current collectors for a novel tubular design of solid oxide fuel cell. *Journal of Power Sources*, 77(1):64–68, 1999.
- [52] M. Lockett, M. J. H. Simmons, and K. Kendall. CFD to predict temperature profile for scale up of micro-tubular SOFC stacks. *Journal of Power Sources*, 131(1-2):243–246, 2004.
- [53] K. Kendall and M. Palin. A small solid oxide fuel cell demonstrator for microelectronic applications. *Journal of Power Sources*, 71(1-2):268–270, 1998.
- [54] T. Alston, K. Kendall, M. Palin, M. Prica, and P. Windibank. A 1000-cell SOFC reactor for domestic cogeneration. *Journal of Power Sources*, 71(1-2):271–274, 1998.
- [55] G. A. Tompsett, C. Finnerty, K. Kendall, T. Alston, and N. M. Sammes. Novel applications for micro-SOFCs. *Journal of Power Sources*, 86(1-2):376–382, 2000.
- [56] N. M. Sammes and Y. H. Du. Fabrication and characterization of tubular solid oxide fuel cells. *International Journal of Applied Ceramic Technology*, 4(2):89–102, 2007.

- [57] J. Van herle, R. Ihringer, N. M. Sammes, G. Tompsett, K. Kendall, K. Yamada, C. Wen, T. Kawada, M. Ihara, and J. Mizusaki. Concept and technology of SOFC for electric vehicles. *Solid State Ionics*, 132(3-4):333–342, 2000.
- [58] Y. H. Du and N. M. Sammes. Fabrication and properties of anode-supported tubular solid oxide fuel cells. *Journal of Power Sources*, 136(1):66–71, 2004.
- [59] T. L. Nguyen, T. Honda, T. Kato, Y. Iimura, K. Kato, A. Negishi, K. Nozaki, M. Shiono, A. Kobayashi, K. Hosoda, Z. F. Cai, and M. Dokiya. Fabrication and characterization of anode-supported tubular SOFCs with zirconia-based electrolyte for reduced temperature operation. *Journal of the Electrochemical Society*, 151(8):A1230–A1235, 2004.
- [60] N. M. Sammes, Y. Du, and R. Bove. Design and fabrication of a 100 w anode supported micro-tubular SOFC stack. *Journal of Power Sources*, 145(2):428–434, 2005.
- [61] P. Sarkar, L. Yamarte, H. S. Rho, and L. Johanson. Anode-supported tubular micro-solid oxide fuel cell. *International Journal of Applied Ceramic Technology*, 4(2):103–108, 2007.
- [62] V. Gil, R. Campana, A. Larrea, R. I. Merino, and V. M. Orera. Ni-GDC microtubular cermets. *Solid State Ionics*, 180(11-13):784–787, 2009.
- [63] V. Gil, J. Gurauskis, R. Campana, R. I. Merino, A. Larrea, and V. M. Orera. Anode-supported microtubular cells fabricated with gadolinia-doped ceria nanopowders. *Journal of Power Sources*, 196(3):1184–1190, 2011.
- [64] R. Campana, R. I. Merino, A. Larrea, I. Villarreal, and V. M. Orera. Fabrication, electrochemical characterization and thermal cycling of anode supported microtubular solid oxide fuel cells. *Journal of Power Sources*, 192(1):120–125, 2009.
- [65] R. Campana, A. Larrea, J. Pena, and V. M. Orera. Ni-YSZ cermet micro-tubes with textured surface. *Journal of the European Ceramic Society*, 29(1):85–90, 2009.
- [66] R. Campana, A. Larrea, R. I. Merino, I. Villarreal, and V. M. Orera. Mini-tubular ysz based SOFC. *Boletin De La Sociedad Espanola De Ceramica Y Vidrio*, 47(4):189–195, 2008.
- [67] M.A. Laguna-Bercero, R. Campana, A. Larrea, J. A. Kilner, and V. M. Orera. High efficiency reversible solid oxide microtubular fuel cells. *ECS Transactions*, 25(2):865–872, 2009.
- [68] X. Z. Zhang, B. Lin, Y. H. Ling, Y. C. Dong, G. Y. Meng, and X. Q. Liu. An anode-supported micro-tubular solid oxide fuel cell with redox stable composite cathode. *International Journal of Hydrogen Energy*, 35(16):8654–8662, 2010.
- [69] <http://www.protonex.com/>.
- [70] J. L. Martin, C. Martin, and R. J. Kee. Portable SOFCs under 300 watts operating on hydrocarbon fuels. In *7th European SOFC Forum*, volume A052, Lucerne, 2006.
- [71] <http://www.ultra-ami.com/>.

- [72] <http://www.acumentrics.com/sofc-products-fuel-cell-technology.htm>.
- [73] L. Blum, W. A. Meulenbergh, H. Nabielek, and R. Steinberger-Wilckens. Worldwide SOFC technology overview and benchmark. *International Journal of Applied Ceramic Technology*, 2(6):482–492, 2005.
- [74] Y. Mizutani. Current state of R&D on micro tubular solid oxide fuel cells in japan. *Mini-Micro Fuel Cells: Fundamentals and Applications*, -:407–418, 2008.
- [75] R. H. Song, J. H. Kim, D. Y. Chung, H. J. Son, K. S. Yun, J. H. Lim, S. B. Lee, D. H. Peck, and D. R. Shin. Development of a 500W-class anode-supported flat-tube solid oxide fuel cell stack in KIER. In *7th European SOFC Forum*, volume B045, 2006.
- [76] M. Yokoyama, K. Nagai, K. Ukai, and Y. Mizutani. Microtube SOFC module and its electrochemical evaluation. *7th European SOFC Forum*, 2006.
- [77] M. Awano, Y. Fujishiro, T. Suzuki, T. Yamaguchi, and K. Hamamoto. Development of advanced ceramic reactors. In *7th European SOFC Forum*, volume B044, Lucerne, 2006.
- [78] T. Yamaguchi, T. Suzuki, S. Shimizu, Y. Fujishiro, and M. Awano. Examination of wet coating and co-sintering technologies for micro-SOFCs fabrication. *Journal of Membrane Science*, 300(1-2):45–50, 2007.
- [79] T. Suzuki, T. Yamaguchi, Y. Fujishiro, and M. Awano. Improvement of SOFC performance using a microtubular, anode-supported SOFC. *Journal of the Electrochemical Society*, 153(5):A925–A928, 2006.
- [80] T. Suzuki, T. Yamaguchi, Y. Fujishiro, M. Awano, and Funahashi Y. Micro tubular SOFCs for micro ceramic reactor system. *Fuel Cell Forum Lucerne 2006*, 2006.
- [81] T. Suzuki, T. Yamaguchi, Y. Fujishiro, and M. Awano. Current collecting efficiency of micro tubular SOFCs. *Journal of Power Sources*, 163(2):737–742, 2007.
- [82] T. Suzuki, Y. Funahashi, T. Yamaguchi, Y. Fujishiro, and M. Awano. Design and fabrication of lightweight, submillimeter tubular solid oxide fuel cells. *Electrochemical and Solid-State Letters*, 10(8):A177–A179, 2007.
- [83] T. Suzuki, T. Yamaguchi, Y. Fujishiro, and M. Awano. Fabrication and characterization of micro tubular SOFCs for operation in the intermediate temperature. *Journal of Power Sources*, 160(1):73–77, 2006.
- [84] Y. W. Sin, K. Galloway, B. Roy, N. M. Sammes, J. H. Song, T. Suzuki, and M. Awano. The properties and performance of micro-tubular (less than 2.0 mm OD) anode supported solid oxide fuel cell (SOFC). *International Journal of Hydrogen Energy*, 36(2):1882–1889, 2011.

-
- [85] Y. Funahashi, T. Shimamori, T. Suzuki, Y. Fujishiro, and M. Awano. Fabrication and characterization of components for micro tubular SOFCs. *Fuel Cell Forum Lucerne* 2006, 2006.
- [86] Y. Funahashi, T. Shimamori, T. Suzuki, Y. Fujishiro, and M. Awano. Fabrication and characterization of components for cube shaped micro tubular SOFC bundle. *Journal of Power Sources*, 163(2):731–736, 2007.
- [87] Y. Funahashi, T. Shimamori, T. Suzuki, Y. Fujishiro, M. Awano, and T. Araki. Simulation study for the series connected bundles of microtubular SOFCs. *Journal of Fuel Cell Science and Technology*, 7(5):0510121–0510125, 2010.
- [88] T. Suzuki, Z. Hasan, Y. Funahashi, T. Yamaguchi, Y. Fujishiro, and M. Awano. Impact of anode microstructure on solid oxide fuel cells. *Science*, 325(5942):852–855, 2009.
- [89] S. Hashimoto, H. Nishino, Y. Liu, K. Asano, M. Mori, Y. Funahashi, and Y. Fujishiro. Development of evaluation technologies for microtubular SOFCs under pressurized conditions. *Journal of Fuel Cell Science and Technology*, 5(3):–, 2008.
- [90] S. Hashimoto, H. Nishino, Y. Liu, K. Asano, M. Mori, Y. Funahashi, and Y. Fujishiro. The electrochemical cell temperature estimation of micro-tubular SOFCs during the power generation. *Journal of Power Sources*, 181(2):244–250, 2008.
- [91] K. Galloway and N. M. Sammes. Long term performance stability of individual micro-tubular SOFCs operating in the intermediate temperature regime. In *ECS 216*, Vienna, 2009.
- [92] K. V. Galloway and N. M. Sammes. Performance degradation of microtubular SOFCs operating in the intermediate-temperature range. *Journal of the Electrochemical Society*, 156(4):B526–B531, 2009.
- [93] Y. Liu, S. I. Hashimoto, H. Nishino, K. Takei, M. Mori, T. Suzuki, and Y. Funahashi. Fabrication and characterization of micro-tubular cathode-supported SOFC for intermediate temperature operation. *Journal of Power Sources*, 174(1):95–102, 2007.
- [94] Y. Liu, S. I. Hashimoto, K. Takei, M. Mori, and Y. Funahashi. Development and characterization of cathode-supported SOFCs by single-step cofiring fabrication for intermediate temperature operation. *Journal of Fuel Cell Science and Technology*, 5(3):–, 2008.
- [95] C. H. Zhao, R. Z. Liu, S. R. Wang, Z. R. Wang, J. Q. Qian, and T. L. Wen. Fabrication and characterization of a cathode-supported tubular solid oxide fuel cell. *Journal of Power Sources*, 192(2):552–555, 2009.
- [96] T. Yamaguchi, S. Shimizu, T. Suzuki, Y. Fujishiro, and M. Awano. Evaluation of micro LSM-supported GDC/ScSZ bilayer electrolyte with LSM-GDC activation layer for intermediate temperature-SOFCs. *Journal of the Electrochemical Society*, 155(4):B423–B426, 2008.

Bibliography

- [97] T. Yamaguchi, S. Shimizu, T. Suzuki, Y. Fujishiro, and M. Awano. Fabrication and evaluation of cathode-supported small scale SOFCs. *Materials Letters*, 62(10-11):1518–1520, 2008.
- [98] T. Yamaguchi, S. Shimizu, T. Suzuki, Y. Fujishiro, and M. Awano. Fabrication and characterization of high performance cathode supported small-scale SOFC for intermediate temperature operation. *Electrochemistry Communications*, 10(9):1381–1383, 2008.
- [99] T. Yamaguchi, S. Shimizu, T. Suzuki, Y. Fujishiro, and M. Awano. Demonstration of the rapid start-up operation of cathode-supported SOFCs using a microtubular LSM support. *Journal of the Electrochemical Society*, 155(11):B1141–B1144, 2008.
- [100] T. Yamaguchi, S. Shimizu, T. Suzuki, Y. Fujishiro, and M. Awano. Development and evaluation of a cathode-supported SOFC having a honeycomb structure. *Electrochemical and Solid State Letters*, 11(7):B117–B121, 2008.
- [101] T. Yamaguchi, S. Shimizu, T. Suzuki, Y. Fujishiro, and M. Awano. Fabrication and evaluation of a novel cathode-supported honeycomb SOFC stack. *Materials Letters*, 63(29):2577–2580, 2009.
- [102] K. Yamahara, C. P. Jacobson, S. J. Visco, and L. C. De Jonghe. Catalyst-infiltrated supporting cathode for thin-film SOFCs. *Solid State Ionics*, 176(5-6):451–456, 2005.
- [103] O. Yamamoto. Solid oxide fuel cells: fundamental aspects and prospects. *Electrochimica Acta*, 45(15-16):2423–2435, 2000.
- [104] I. Villarreal, M. Rivasa, L.M. Rodriguez-Martinez, L. Otaegi, A. Zabala, N. Gomez, M. A. Alvarez, I. Antepara, N. Arizmendiarrrieta, J. Manzanedo, M. Olave, A. Urriolabeitia, N. Burgos, F. Castro, and A. Laresgoiti. Tubular metal supported SOFC development for domestic power generation. ECS 216, 2009.
- [105] L.M. Rodriguez-Martinez, L. Otaegi, M. A. Alvarez, M. Rivas, N. Gomez, A. Zabala, N. Arizmendiarrrieta, I. Antepara, M. Olave, A. Urriolabeitia, I. Villarreal, and A. Laresgoiti. Degradation studies on tubular metal supported SOFC. ECS 216, 2010.
- [106] P. Blennow, J. Hjelm, T. Klemensø, Å. Persson, K. Brodersen, A. Kumar Srivastava, H. Lund Frandsen, M. Lundberg, S. Ramousse, and M. Mogensen. Development of planar metal supported SOFC with novel cermet anode. *ECS Transactions*, 25(2):701–710, 2009.
- [107] M. C. Tucker, G. Y. Lau, C. P. Jacobson, L. C. DeJonghe, and S. J. Visco. Stability and robustness of metal-supported SOFCs. *Journal of Power Sources*, 175(1):447–451, 2008.
- [108] M. C. Tucker. Progress in metal-supported solid oxide fuel cells: A review. *Journal of Power Sources*, 195(15):4570–4582, 2010.

- [109] V. Lawlor, S. Griesser, G. Buchinger, A. G. Olabi, S. Cordiner, and D. Meissner. Review of the micro-tubular solid oxide fuel cell Part i. Stack design issues and research activities. *Journal of Power Sources*, 193(2):387–399, 2009.
- [110] K. Kendall. Progress in microtubular solid oxide fuel cells. *International Journal of Applied Ceramic Technology*, 7(1):1–9, 2010.
- [111] K. S. Howe, G. J. Thompson, and K. Kendall. Micro-tubular solid oxide fuel cells and stacks. *Journal of Power Sources*, 196(4):1677–1686, 2011.
- [112] F. Zhao, C. Jin, C. H. Yang, S. W. Wang, and F. L. Chen. Fabrication and characterization of anode-supported micro-tubular solid oxide fuel cell based on BaZr(0.1)Ce(0.7)Y(0.1)Yb(0.1)O(3-delta) electrolyte. *Journal of Power Sources*, 196(2):688–691, 2011.
- [113] S. Hashimoto, Y. Liu, K. Asano, F. Yoshiba, M. Mori, Y. Funahashi, and Y. Fujishiro. Power generation properties of microtubular solid oxide fuel cell bundle under pressurized conditions. *Journal of Fuel Cell Science and Technology*, 8(2):0210101–0210106, 2011.
- [114] Y. Liu, N. Liu, and X. Y. Tan. Preparation of microtubular solid oxide fuel cells based on highly asymmetric structured electrolyte hollow fibers. *Science China-Chemistry*, 54(5):850–855, 2011.
- [115] C. Jin, J. Liu, L. H. Li, and Y. H. Bai. Electrochemical properties analysis of tubular NiO-YSZ anode-supported SOFCs fabricated by the phase-inversion method. *Journal of Membrane Science*, 341(1-2):233–237, 2009.
- [116] T. Suzuki, T. Yamaguchi, Y. Fujishiro, M. Awano, and Y. Funahashi. Recent development of microceramic reactors for advanced ceramic reactor system. *Journal of Fuel Cell Science and Technology*, 7(3):0310051–0310055, 2010.
- [117] Y. Liu, K. Yasumoto, S. Hashimoto, K. Takei, M. Mori, Y. Funahashi, Y. Fijishiro, A. Hirano, and Y. Takeda. Development of ceria based SOFCs with a high performance La(0.6)Sr(0.4)Co(0.2)Fe(0.8)O(3-delta)-Ce(0.9)Gd(0.1)O(1.95)-Ag composite cathode. *Journal of Fuel Cell Science and Technology*, 7(6):0610031–0310035, 2010.
- [118] T. Suzuki, Y. Funahashi, T. Yamaguchi, Y. Fujishiro, and M. Awano. New stack design of micro-tubular SOFCs for portable power sources. *Fuel Cells*, 8(6):381–384, 2008.
- [119] Clariant. *Mowiol Polyvinyl Alcohol*. Clariant GmbH, Sulzbach, 1999.
- [120] C. Kleinlogel and L. J. Gauckler. Sintering and properties of nanosized ceria solid solutions. *Solid State Ionics*, 135(1-4):567–573, 2000.
- [121] R. Greenwood and L. Bergstrom. Electroacoustic and rheological properties of aqueous Ce-ZrO₂ (Ce-TZP) suspensions. *Journal of the European Ceramic Society*, 17(4):537–548, 1997.

Bibliography

- [122] F. Shojai, A. B. A. Pettersson, T. Mantyla, and J. B. Rosenholm. Electrostatic and electrosteric stabilization of aqueous slips of 3Y-ZrO₂ powder. *Journal of the European Ceramic Society*, 20(3):277–283, 2000.
- [123] H. G. Pedersen and L. Bergstrom. Forces measured between zirconia surfaces in poly(acrylic acid) solutions. *Journal of the American Ceramic Society*, 82(5):1137–1145, 1999.
- [124] F. Q. Tang, X. X. Huang, Y. F. Zhang, and J. K. Guo. Effect of dispersants on surface chemical properties of nano-zirconia suspensions. *Ceramics International*, 26(1):93–97, 2000.
- [125] Y. L. Zhang, H. F. Gao, D. K. Peng, M. Y. Meng, and X. Q. Liu. Dip-coating thin yttria-stabilized zirconia films for solid oxide fuel cell applications. *Ceramics International*, 30(6):1049–1053, 2004.
- [126] L. Bergstrom. Hamaker constants of inorganic materials. *Advances in Colloid and Interface Science*, 70:125–169, 1997.
- [127] A. Mai, V. A. C. Haanappel, F. Tietz, and D. Stover. Ferrite-based perovskites as cathode materials for anode-supported solid oxide fuel cells - Part ii. Influence of the CGO interlayer. *Solid State Ionics*, 177(19-25):2103–2107, 2006.
- [128] D. Ray. *Characterization of 10mol% Sc₂O₃-1mol% CeO₂-ZrO₂ Ceramics as electrolyte material for lower temperature solid oxide fuel cells*. PhD thesis, North Carolina A&T State University, 2007.
- [129] J. Wang and L. Gao. Surface and electrokinetic properties of Y-TZP suspensions stabilized by polyelectrolytes. *Ceramics International*, 26(2):187–191, 2000.
- [130] M. Prica, S. Biggs, F. Grieser, and T. W. Healy. Effect of calcination temperature on the electrokinetic properties of colloidal zirconia. *Colloids and Surfaces a-Physicochemical and Engineering Aspects*, 119(2-3):205–213, 1996.
- [131] H. Hayashi, T. Saitou, N. Maruyama, H. Inaba, K. Kawamura, and M. Mori. Thermal expansion coefficient of yttria stabilized zirconia for various yttria contents. *Solid State Ionics*, 176(5-6):613–619, 2005.
- [132] H. Luebbe, J. Rossen, S. Diethelm, J. Van Herle, H. Hofmann, P. Bowen, F. Snijkers, and T. Betz. Fabrication and characterisation of cathode support-tubes for micro-tubular SOFC application. *ECS Transactions*, 25(2):10, 2009.
- [133] C. Lalanne, G. Prosperi, J. M. Bassat, F. Mauvy, S. Fourcade, P. Stevens, M. Zahid, S. Diethelm, J. Van herle, and J. C. Grenier. Neodymium-deficient nickelate oxide Nd_{1.95}NiO_{4+d} as cathode material for anode-supported intermediate temperature solid oxide fuel cells. *Journal of Power Sources*, 185(2):7, 2008.

- [134] T. Hagiwara, Z. Kyo, A. Manabe, H. Yamamura, and K. Nomura. Formation of C-type rare earth structures in the $\text{Ce}(1-x)\text{Nd}(x)\text{O}(2-\delta)$ system: a factor in the decrease in oxide-ion conductivity. *Journal of the Ceramic Society of Japan*, 117(1372):1306–1310, 2009.
- [135] X. D. Zhou, B. Scarfino, and H. U. Anderson. Electrical conductivity and stability of Gd-doped ceria/Y-doped zirconia ceramics and thin films. *Solid State Ionics*, 175(1-4):19–22, 2004.
- [136] T. Horita, N. Sakai, H. Yokokawa, M. Dokiya, T. Kawada, J. Van Herle, and K. Sasaki. Ceria-zirconia composite electrolyte for solid oxide fuel cells. *Journal of Electroceramics*, 1(2):155–164, 1997.
- [137] A. Tsoga, A. Gupta, A. Naoumidis, D. Skarmoutsos, and P. Nikolopoulos. Performance of a double-layer CGO/YSZ electrolyte for solid oxide fuel cells. *Ionics*, 4:234–240, 1998.
- [138] A. Tsoga, A. Gupta, A. Naoumidis, and P. Nikolopoulos. Gadolinia-doped ceria and yttria stabilized zirconia interfaces: Regarding their application for SOFC technology. *Acta Materialia*, 48(18-19):4709–4714, 2000.
- [139] A. Tsoga, A. Naoumidis, and D. Stover. Total electrical conductivity and defect structure of $\text{ZrO}(2)\text{-CeO}(2)\text{-Y}(2)\text{O}(3)\text{-Gd}(2)\text{O}(3)$ solid solutions. *Solid State Ionics*, 135(1-4):403–409, 2000.
- [140] H. Mitsuyasu, Y. Nonaka, and K. Eguchi. Analysis of solid state reaction at the interface of yttria-doped ceria/yttria-stabilized zirconia. *Solid State Ionics*, 113:279–284, 1998.
- [141] N. Sakai, T. Hashimoto, T. Katsube, K. Yamaji, H. Negishi, T. Horita, H. Yokokawa, Y. P. Xiong, M. Nakagawa, and Y. Takahashi. Miscibility gap in $\text{CeO}_2\text{-ZrO}_2\text{-YO}_{1.5}$ system as an electrode of solid oxide fuel cell. *Solid State Ionics*, 143(2):151–160, 2001.
- [142] <http://www.hbcnetbase.com/>.
- [143] T. Horita, Y. P. Xiong, H. Kishimoto, K. Yamaji, M. E. Brito, and H. Yokokawa. Chromium poisoning and degradation at $(\text{La,Sr})\text{MnO}(3)$ and $(\text{La,Sr})\text{FeO}(3)$ cathodes for solid oxide fuel cells. *Journal of the Electrochemical Society*, 157(5):B614–B620, 2010.
- [144] J. A. Schuler, H. Luebbe, A. Hessler-Wyser, and J. Van herle. Nd-nickelate based solid oxide fuel cell cathode sensitivity to Cr-, Si-contamination. In *9th European Fuel Cell Forum*, volume B0503, Lucerne, 2011.
- [145] M. Nagata, Y. Itoh, and H. Iwahara. Dependence of observed overvoltages on the positioning of the reference electrode on the solid-electrolyte. *Solid State Ionics*, 67(3-4):215–224, 1994.
- [146] J. A. Schuler, P. Tanasini, A. Hessler-Wyser, C. Comninellis, and J. Van Herle. Cathode thickness-dependent tolerance to Cr-poisoning in solid oxide fuel cells. *Electrochemistry Communications*, 12(12):1682–1685, 2010.

Bibliography

- [147] H. Schwarz. Über die chromate(v) der seltenen erden .3. neodymchromat(v), NdCrO_4 . *Zeitschrift Fur Anorganische Und Allgemeine Chemie*, 322(3-4):129–136, 1963.
- [148] H. Y. Zhu and R. J. Kee. A general mathematical model for analyzing the performance of fuel-cell membrane-electrode assemblies. *Journal of Power Sources*, 117(1-2):61–74, 2003.
- [149] D. Perez-Coll, A. Aguadero, M. J. Escudero, and L. Daza. Effect of DC current polarization on the electrochemical behaviour of $\text{La}_2\text{NiO}_{4+\delta}$ and $\text{La}_3\text{Ni}_2\text{O}_{7+\delta}$ -based systems. *Journal of Power Sources*, 192(1):2–13, 2009.
- [150] Y. Matsuzaki and I. Yasuda. Electrochemical properties of a SOFC cathode in contact with a chromium-containing alloy separator. *Solid State Ionics*, 132(3-4):271–278, 2000.
- [151] P. Leone, M. Santarelli, P. Asinari, M. Cali, and R. Borchellini. Experimental investigations of the microscopic features and polarization limiting factors of planar SOFCs with LSM and LSCF cathodes. *Journal of Power Sources*, 177(1):111–122, 2008.
- [152] A. Barbucci, P. Carpanese, G. Cerisola, and M. Viviani. Electrochemical investigation of mixed ionic/electronic cathodes for SOFCs. *Solid State Ionics*, 176(19-22):1753–1758, 2005.
- [153] F. Qiang, K. N. Sun, N. Q. Zhang, X. D. Zhu, S. R. Le, and D. R. Zhou. Characterization of electrical properties of GDC doped A-site deficient LSCF based composite cathode using impedance spectroscopy. *Journal of Power Sources*, 168(2):338–345, 2007.
- [154] M. Radovic and E. Lara-Curzio. Mechanical properties of tape cast nickel-based anode materials for solid oxide fuel cells before and after reduction in hydrogen. *Acta Materialia*, 52(20):5747–5756, 2004.
- [155] S. D. Kim, S. H. Hyun, J. Moon, J. H. Kim, and R. H. Song. Fabrication and characterization of anode-supported electrolyte thin films for intermediate temperature solid oxide fuel cells. *Journal of Power Sources*, 139(1-2):67–72, 2005.
- [156] J. W. Seo, J. Fompeyrine, A. Guiller, G. Norga, C. Marchiori, H. Siegwart, and J. P. Locquet. Interface formation and defect structures in epitaxial $\text{La}_2\text{Zr}_2\text{O}_7$ thin films on (111)Si. *Applied Physics Letters*, 83(25):5211–5213, 2003.
- [157] F. Snijkers, A. de Wilde, S. Mullens, and J. Luyten. Aqueous tape casting of yttria stabilised zirconia using natural product binder. *Journal of the European Ceramic Society*, 24(6):1107–1110, 2004.
- [158] S. H. Chan, K. A. Khor, and Z. T. Xia. A complete polarization model of a solid oxide fuel cell and its sensitivity to the change of cell component thickness. *Journal of Power Sources*, 93(1-2):130–140, 2001.

-
- [159] K. R. Reddy and K. Karan. Sinterability, mechanical, microstructural, and electrical properties of gadolinium-doped ceria electrolyte for low-temperature solid. *Journal of Electroceramics*, 15(1):45–56, 2005.
- [160] D. S. Lee, W. S. Kim, S. H. Choi, J. Kim, H. W. Lee, and J. H. Lee. Characterization of ZrO₂ co-doped with Sc₂O₃ and CeO₂ electrolyte for the application of intermediate temperature SOFCs. *Solid State Ionics*, 176(1-2):33–39, 2005.
- [161] F. Chauveau, J. Mougín, J. M. Bassat, F. Mauvy, and J. C. Grenier. A new anode material for solid oxide electrolyser: The neodymium nickelate Nd(2)NiO(4+delta). *Journal of Power Sources*, 195(3):744–749, 2010.
- [162] E. A. Mason and A. P. Malinauskas. *Gas Transport in Porous Media: The Dusty-Gas Model*, volume 89-92. Elsevier, 1983.
- [163] I. S. Grigoriev, E. Z. Meilikhov, and A. A. Radzig. *Handbook of Physical Quantities*. CRC Press, 1996.
- [164] R. Krishna and J. A. Wesselingh. Review article number 50 - The Maxwell-Stefan approach to mass transfer. *Chemical Engineering Science*, 52(6):861–911, 1997.

Contact

PhD – Materials science

Henning Lübbe
Avenue des Oiseaux 9
CH-1018 Lausanne
Schweiz
Tel.: +41(0)21 / 5500480
Mobil: +41(0)77 / 4483641
henning-luebbe@web.de

- PhD and Master degree in materials science
- Specialised in ceramic powder technology and electrochemistry (fuel cells, batteries)
- Routinely contact with industrial partners
- Fluent in English, French and German

Education

- 2007 – 2011 PhD at EPFL in Lausanne (CH) in materials science, ceramic powders for Solid Oxide Fuel Cells
- 2001 – 2007 Studies in materials science at the University of Stuttgart (D), Master degree in material science engineering, specialisations: fuel cell technology, non-destructive testing
- 1994 – 2001 Secondary school with final examinations in 2000 and subsequent alternative civilian service, Berlin (D)

Experience and Internships

- 2007 – 2011 PhD-thesis at EPFL Lausanne (CH)
- Creation of a tubular fuel cell with innovative materials in collaboration with industrial partners
 - Characterisation, treatment as well as shaping of ceramic powders, deposition of thin films, sintering, mechanical and electrochemical tests
 - Testing and evaluation of ionic and electronic conductors by impedance-spectroscopy and current-voltage-characteristics
 - By means of the collaboration of 2 work groups, I am at the interface of powder technology and industrial energy engineering
 - [Several publications](#) and supervision of multiple projects
 - „[C.F. Schönbein Contribution to Science Medal](#)”, European Fuel Cell Forum 2011
- 2005 – 2006 Internship at the SHANGHAI INSTITUTE OF CERAMICS, Shanghai (CHN)
- Synthesis and characterisation of luminescent material for flat screen panel application.
 - Proof that material did not satisfy industrial interest.
 - spoke casual mandarin on a daily basis.
- 2003 – 2005 Student trainee at ROBERT BOSCH GmbH, Stuttgart (D), department: Diesel systems
- Power tests and synthesis of ceramic glow plugs for Diesel engines.
 - Responsibility for power test.
 - extensive hands-on skills in X-ray imaging.

- 2004 Internship at the GERMAN AEROSPACE CENTRE, Stuttgart (D), 6 months
Institute of technical thermodynamics, domain: solid oxide fuel cells
- Quality assurance and analysis of ceramic powders for fuel cell application

Expertise

Powder technology, deposition and analysis:

- Analysis per scanning electron microscopy (SEM), energy-dispersive X-ray spectroscopy (EDX), X-ray diffraction (XRD), thermogravimetric analysis (TGA) as well as impedance spectroscopy and current-voltage characteristics
- Granulometry measurements by different methods such as laser diffraction, dilatometry
- Shaping by slip-casting, cold-isostatic pressing (CIP) and uniaxial pressing (UP)
- Deposition by dip-coating, screen-printing

Software:

MS Office, Origin, Image J, LabView, ZView+Zahner (Impedance spectroscopy), Illustrator

Languages

German (Mother tongue)
English (fluent, C2)
French (fluent, C1)
Spanish (good basics, B1)
Mandarin (good basics, A2)

Activities

Basketball ([Member of a team in third](#) swiss league)
Guitar
Travels (many travels in Europe, North- and Central America, Australia, China, Kenia)

Personal situation

Age: 30 years
Marital status: single
Nationality: German
Place of birth: Berlin (D)

Publication list

Articles

1. Luebbe H., Van herle J., Hofmann H., Bowen P., Aschauer U., Schuler A., Snijkers F., Schindler H.-J., Vogt U., Lalanne C., "Cathode-supported micro-tubular SOFCs based on $\text{Nd}_{1.95}\text{NiO}_{4+\delta}$: Fabrication and characterisation of dip-coated electrolyte layers", *Solid State Ionics*, 180(11-13), 2009
2. Luebbe H., Rossen J., Diethelm S., Van herle J., Hofmann H., Bowen P., Snijkers F., Betz T., "Fabrication and characterisation of cathode support-tubes for micro-tubular SOFC application", *ECS Transactions*, 25(2), 2009
3. Luebbe H., Schuler, J.A., Larrañaga A., Arriortua M.I., Van herle J., "Reactivity of zirconia electrolytes and ceria interlayer used as electrolyte double layers in cathode-supported micro-tubular SOFCs", in preparation
4. Luebbe H., Larrañaga A., Arriortua M.I., Van herle J., "Electrochemical performance optimisation for neodymium nickelate - gadolinia doped ceria electrolyte by controlled interfacial reactivity", in preparation
5. Luebbe H., Nakajo A., Van herle J., "Thermal stresses during post-sinter cooling of cathode-supported micro-tubular SOFCs with neodymium nickelate cathode and scandia-doped zirconia (ScSZ) electrolyte ", in preparation
6. Luebbe H., Van herle J., Hofmann H., Bowen P., Campana R., Snijkers F., Betz T., "Cathode-supported micro-tubular SOFCs: Fabrication and electrochemical characterisation", in preparation

Conference Talks

1. Luebbe H., Favrat D., Van herle J., Hofmann H., Bowen P., Schuler A., Snijkers F., Schindler H.-J., Vogt U., Lalanne C., "Micro-tubular Solid Oxide Fuel Cells using nickelate cathodes: Characterisation of the electrolyte and first results on performance", *Electroceramics XI*, 2008, Manchester, United Kingdom

2. Luebbe H., Van herle J., Schuler A., Snijkers F., Betz T., Larrañaga A., "Micro-tubular Solid Oxide Fuel Cells with nickelate cathode support", ECS 220, 2011, Boston, USA

Conference Posters

1. Luebbe H., Van herle J., Bowen P., Hofmann H., Snijkers F., Schindler H.-J., Vogt U., Lalanne C., "Microtubular SOFCs based on nickelate cathode support and low cost fabrication", Nano Europe, 2008, St. Gallen, Switzerland
2. Luebbe H., Diethelm S., Van herle J., Bowen P., Hofmann H., Snijkers F., Betz T., Lalanne C., "Micro-tubular SOFCs on nickelate cathode support", Electroceramics XI, 2009, Vienna, Austria
3. Luebbe H., Diethelm S., Van herle J., Bowen P., Hofmann H., Snijkers F., Betz T., Lalanne C., "Microtubular SOFCs on nickelate cathode support", European Fuel Cell Forum, 2010, Lucerne, Switzerland

Conference Abstracts/Proceedings

1. Luebbe H., Favrat D., Van herle J., Hofmann H., Bowen P., Schuler A., Snijkers F., Schindler H.-J., Vogt U., Lalanne C., "Micro-tubular Solid Oxide Fuel Cells using nickelate cathodes: Characterisation of the electrolyte and first results on performance", Electroceramics XI, Manchester, UK, 2008, 34317
2. Luebbe H., Van herle J., Diethelm S., Hofmann H., Bowen P., Snijkers F., "Fabrication and characterisation of cathode support tubes for micro-tubular SOFC application", ECS 216, Vienna, Austria, 2009, B1574
3. Luebbe H., Diethelm S., Betz T., Hofmann H., Van herle J., "Micro-tubular SOFC on nickelate cathode support: Dip-Coating of GDC interlayers", European Fuel Cell Forum, Lucerne, Switzerland, 2010, 110
4. Schuler, J.A., Luebbe H., Hessler-Wyser A., Van herle J., "Nd-Nickelate Solid Oxide Fuel Cell Cathode Sensitivity to Cr and Si Contamination", European Fuel Cell Forum, Lucerne, Switzerland, 2011, B0503

A Appendix

A.1 Diffusion-Test

The mathematical derivation of the equations used for the determination of average pore radius $\langle r \rangle$ contributing to the diffusion process as well as the tortuosity τ of the porous network is presented here.

The Dusty-Gas Model that describes the transport of a gas mixture in a porous medium is the scientific basis for the diffusion measurement. For the case of a gas species 1 in an isothermal binary gas mixture, Mason [162] describes the radial flow of species 1 with the formula

$$N_1 = -\psi \frac{P}{RT} \frac{D_{1K} D_{12}}{D_{12} + (1 - x_1)(D_{1K} - D_{2K})} \frac{\delta x_1}{\delta z} \quad (\text{A.1})$$

where ψ is the ratio of porosity ϵ divided by tortuosity τ

$$\psi = \frac{\epsilon}{\tau} \quad (\text{A.2})$$

of the porous body, which determines the effective diffusion coefficient according to

$$D_{j,K}^{eff} = D_{j,K} \left(\frac{\epsilon}{\tau} \right) \quad (\text{A.3})$$

as written by Chan [158]. In equation A.1, N_1 [mol m⁻²s⁻¹] represents the radial gas flow of species 1, P [Pa] represents the gas pressure, R the ideal gas constant, T [K] the absolute temperature, D_{12} [m²s⁻¹] the mutual diffusion coefficient of binary gas mixture 1-2 and D_{jK}

Appendix A. Appendix

$[\text{m}^2\text{s}^{-1}]$ is the Knudsen diffusion coefficient of gas species j . Here, it is now assumed that the concentration x_1 is the mean value \tilde{x}_1 between the concentrations on the outside ($x_{1,ext}$) and inside ($x_{1,inn}$) of the tube, hence

$$x_1 \approx \tilde{x}_1 = x_{1,ext} - \frac{\Delta x_1}{2} \quad (\text{A.4})$$

with $\Delta x_1 = x_{1,ext} - x_{1,inn}$. Writing equation A.1 in differential form with $\Delta x_1 = \partial x_1$ and $\Delta z = \partial r$ yields

$$N_1 = -\psi \frac{P}{RT} \frac{D_{1K}D_{12}}{D_{12} + (1 - \tilde{x}_1)(D_{1K} - D_{2K})} \frac{\partial x_1}{\partial r} = \alpha \frac{\partial x_1}{\partial r} \quad (\text{A.5})$$

Since \tilde{x}_1 depends only on constants as defined in equation A.4, it is possible to include it in the constant α which is indepent of x_1 and r . Furthermore, steady state operation in cylindrical coordiantes is charaterised by

$$\frac{1}{r} \frac{\partial}{\partial r} (r N_1) = 0 \quad (\text{A.6})$$

and therefore multiplying equation A.5 with r yields

$$r * N_1 = \text{const.} \equiv N_{1,r} = r \alpha \frac{\partial x_1}{\partial r} \quad (\text{A.7})$$

Here, $N_{1,r}$ is a constant with the unit $[\text{mol m}^{-1}\text{s}^{-1}]$. Integration by separating the variables leads to

$$N_{1,r} * \int_{r_{inn}}^{r_{ext}} \frac{1}{r} dr = \alpha * \int_{x_{1,inn}}^{x_{1,ext}} dx_1 \quad (\text{A.8})$$

The integrated equation

$$N_{1,r} = \alpha \frac{\Delta x_1}{\ln \frac{r_{ext}}{r_{inn}}} \quad (\text{A.9})$$

can be inversed to yield a linear equation in δx_1^{-1} of the form

$$\frac{2\pi L}{f} = A' \cdot \frac{1}{\Delta x_1} + A'' \quad (\text{A.10})$$

which was shown in the manuscript, equation 6.3. The slope A' and y-axis intercept A'' of equation A.10 are

$$A' = -\frac{RT \ln \frac{r_{ext}}{r_{inn}}}{P\psi D_{1K} D_{12}} [D_{1,2} + (1 - x_{1,ext})(D_{1K} - D_{2K})] \quad (\text{A.11})$$

and

$$A'' = -\frac{RT \ln \frac{r_{ext}}{r_{inn}}}{P\psi D_{1K} D_{12}} \left[\frac{1}{2} (D_{1K} - D_{2K}) \right] \quad (\text{A.12})$$

respectively. Consequently, ψ can be determined from either A' or A'' by rearranging equation A.11 or A.12 with respect to ψ . The molar flow f [mols⁻¹] should not be confused with the radial flow per cross-section N_1 [molm⁻²s⁻¹] or the constant $N_{1,r}$ which are interconnected by

$$f = 2\pi L r * N_1 = 2\pi L * N_{1,r} \quad (\text{A.13})$$

which was also used for the inversion of equation A.9. In equation A.13, L represents the length along which diffusion across the tube occurs (cf. Fig. 6.13). As the binary gas-mixture consisted of oxygen-argon in the diffusion experiment, the relation

$$D_{1,2}(T) = D_{O_2-Ar}(T) = 0.167 \frac{cm^2}{s} \left(\frac{T}{273} \right)^{1.736} \quad (\text{A.14})$$

from Grigoriev [163] was used to describe the mutual diffusion. The Knudsen diffusion

coefficient of gas species j was calculated [164] by

$$D_{j,K}(T) = \frac{2}{3} \langle r \rangle \sqrt{\frac{8RT}{\pi M_j}} \quad (\text{A.15})$$

where M_j is the molar mass [kgmol^{-1}] of gas species j . The mean pore radius $\langle r \rangle$ of pores contributing to diffusion can be obtained by

$$\langle r \rangle = D_{1,2} \left[\left(\frac{A'}{2A''} + x_{1,ext} - 1 \right) (D_{1,K}^* - D_{2,K}^*) \right]^{-1} \quad (\text{A.16})$$

where $D_{j,K}^*$ is defined as

$$D_{j,K}^* = \frac{D_{j,K}}{\langle r \rangle} = \frac{2}{3} \sqrt{\frac{8RT}{\pi M_j}} \quad (\text{A.17})$$

Plotting $\frac{2\pi L}{f}$ against $\frac{1}{\Delta X_1}$ yields A' as the slope and A'' as the y-axis intercept according to equation A.10, while the mean pore radius can be determined by equation A.16 and the tortuosity by equation A.2 where the porosity ϵ has to be measured independently and ψ can be obtained by rearranging equations A.11 or A.12 with respect to ψ .